Universität der Bundeswehr München
Fakultät für Elektrotechnik und Informationstechnik

# Compact Microwave Antennas and Antenna Combinations for Terrestrial and Satellite Services on Vehicles

Iuliia Goncharova

Vollständiger Abdruck der von der Fakultät für Elektrotechnik und Informationstechnik der Universität der Bundeswehr München zur Erlangung des akademischen Grades einer

DOKTOR–INGENIEURIN

genehmigte Dissertation.

Vorsitzender: Univ.-Prof. Dr.-Ing. Dieter Gerling
Gutachter:
1. Univ.-Prof. Dr.-Ing. Stefan Lindenmeier
2. Univ.-Prof. Dr.-Ing. Arne Jacob

Die Dissertation wurde am 04.06.2018 bei der Universität der Bundeswehr München eingereicht und durch die Fakultät für Elektrotechnik und Informationstechnik am 13.06.2018 angenommen. Die mündliche Prüfung fand am 18.12.2018 statt.

Ich versicherte an Eides statt, dass ich die der Fakultät für Elektrotechnik und Informationstechnik der Universität der Bundeswehr München vorgelegte Dissertation mit dem Thema

*Compact Microwave Antennas and Antenna Combinations for Terrestrial and Satellite Services on Vehicles*

ohne fremde Hilfe erstellt, bei der Abfassung keine anderen als die im Literaturverzeichnis angeführten Hilfsmittel benutzt und die wissenschaftlichen Leistungen eigenständig erbracht habe.

M. Sc. Iuliia Goncharova

# Thanksgiving

This thesis would not be written without some people whom I want to express my sincerely appreciation.

First of all, I thank to Prof. Dr.-Ing. habil. Stefan Lindenmeier for his giving me an opportunity to extend my theoretical knowledge and to implement them in the praxis while receiving a PhD at Institute of High Frequency Technology and Mobile Communication at the University of Bundeswehr Munich. He provided me with interesting and absorbing themes and concepts for work. Their elaboration under his careful supervision brought me a lot of discovers and pleasure. I am also grateful to him for his interest in my scientific development and supporting me in publication and in visiting of useful conferences.

I thank also to Prof. Dr.-Ing. habil. Wilfrid Pascher for his support in electromagnetic theory and in mathematics.

My thanks are also derived on the insitute's workshop to workshop's head Mr. Oliver Kindt and to fine-precision mechanics Mr. Markus Mittermeier for their quick and responcible manufacturing of the high-quality hardware demonstrators and for their oppenness for new trends and technologies.

The work of laboratory technicians, Ms. Sandra Hirlmeier and Ms. Nicole Lach, is also worth to be appreciated. Especially, their collaboration in the production and assembly of circuit boards for the antennas under investigation.

I am feeling thankful to my colleagues which were opened for fruitful professional discussions and for a pleasant working atmosphere.

My special thanks are to my husband for his giving me a continuous inspiration to live and to work. Also I am very gratifule to my parents who gave me a possibility to obtain such interresting profession, for their overall support during my study and PhD application.

# Acronyms list

| | |
|---|---|
| AM | Amplitude modulation [radio] |
| BSF | Bottom-side fixation |
| CCHA | Capacitively coupled helical antenna |
| CDMA | Code division multiple access |
| CPW | Coplanar waveguide |
| DAB | Digital audio broadcasting |
| ESD | Electro static discharge |
| FDMA | Frequency division multiple access |
| FM | Frequency modulation |
| GEO | Geostationary orbit |
| GNSS | Global navigation satellite systems |
| GPS | Global positioning system |
| HEO | Elliptical geosynchronous orbit |
| HIA | High impedance amplifier |
| HP | Horizontal polarization |
| LHCP | Left-hand circular polarization |
| LTE | Long term evolution [technology] |
| MBD | Main beam direction |
| MIMO | Multiple in multiple out |
| NFS | Near field source |
| PPS | Precise positioning service |
| RHCP | Right-hand circular polarization |
| RG | Realized gain |
| RP | Radiation pattern |
| SAW | [Filter on] surface acoustic waves |

| | |
|---|---|
| SPS | Standard positioning service |
| SDARS | Satellite digital audio radio service |
| TDD | Time-division duplex |
| TSF | Top-side fixation |
| VP | Vertical polarization |
| WLAN | Wireless local area network |
| XPD | Cross-polarization discrimination |

# Symbols list

| | |
|---|---|
| $\varepsilon$ | permittivity, [F/m] |
| $\theta$ | elevation angle, counted from zenith, [°] |
| $\lambda$ | wave length, [m] |
| $\mu$ | permeability, [H/m] |
| $\varphi$ | azimuthal angle, [°] |
| $\psi$ | phase of the current, [°] |
| $\omega$ | radial frequency, [rad/s] |
| $\hat{e}_\theta, \hat{e}_\varphi$ | unit vectors |
| $E$ | electric field intensity, [V/m] |
| $H$ | magnetic field intensity, [A/m] |
| $k$ | propagation constant, [rad/m] |
| $h, l, \Delta l, l'$ | length, [m] |
| $r$ | distance to the point in far-field zone, [m] |
| $\underline{\hat{V}}$ | vector magnetic potential |
| $Z_0$ | wave impedance of the vacuum, $Z_0 = 120\pi$ Ohm |
| $Z_w$ | wave impedance, [Ohm] |

# Content

# Abstract

Recent developments in cellular communication - like elaboration of Long Term Evolution (LTE) standard - allow large data rates up to 3 Gb/s in down link and connectivity of modern people even while driving. However, a renewal of base-station and at end-user equipment is certainly needed for using the advantages of the LTE service. Thus, along with other hard-ware changes, a user-end shall contain at least two broadband antennas since this standard implies Multiple-In-Multiple-Out technique (MIMO) and carrier aggregation.

Last years show a trend of hiding the increased number of vehicular antennas as much as possible by placing them either upon a roof underneath a shark-fin cover or integrated in car's body. However for even complicated systems, there is a strictly limited mounting space, therefore car antennas must be very compact while providing the required radiation properties. A dense placement in multiple-antenna modules poses an additional obstacle – mutual coupling between aerials. It is especially critical in that modules which contain transmitting antennas for cellular communication and sensitive aerials for satellite reception.

All these challenges and developments have motivated to research a new wideband compact antenna for the LTE communication on car. The investigation was conducted in different operation scenarios: in a stand-alone case, in a 2x2 MIMO-module and in combinations with receiving radiators for other services like terrestrial radio, navigation and satellite broadcast.

The researched aerial for LTE (so called 3-D or «Nefer»-antenna) consists of two structures, which are joined together at an excitation point. Due to the independence of the antenna's parts one from another, this 3-D radiator reaches demanded impedance and radiation properties within LTE low, middle and upper bands covering the frequencies of the currently-available cellular communication.

In a 2x2 MIMO module, the 3-D radiators of this dual-band principle enable stable connection to the LTE-800-MHz network with enough mean throughput of 24 Mbit/s (state on 2012) which was measured during the drive-test in live network.

Since a typical antenna module for a personal vehicle includes several radiators for distinct services, the 3-D aerial (single and in 2x2 MIMO-system as well) has been combined and carefully investigated in several modules with aerials for satellite radio and navigation made according to the scarabaeus concept. In these combinations, 3-D radiators for cell-phone service are well-decoupled from antennas for satellite signal reception. Decoupling can be even improved by means of band-rejection filters for the critical frequencies and by optimization of filtering properties of the

antennas for satellite services as it is shown in the thesis. In the researched combinations, the Nefer-antennas keep their omnidirectional pattern with only slight deviations and reach sufficient impedance matching to 50-Ohm line.

Thus, the thesis proposes a high-efficient compact and reliable solution for LTE service on a personal vehicle which can even be used in complicated multiple-antenna modules.

Alongside with the main topic on antennas for cellular communication, some researches on scarabaeus aerials for satellite reception were conducted. These investigations were required because of the recent improvements in navigation – like opening of the GPS-L2C band for civil use and development of interoperable L1C-singal – and due to the strengthened requirements on decoupling from terrestrial interferers. These researches are reflected in the thesis too.

# Zusammenfassung

Die jüngsten Entwicklungen im Mobilfunk - wie die Ausarbeitung des Long Term Evolution (LTE)-Standards - ermöglichen große Datenraten bis zu 3 Gb/s (down link) und die Konnektivität moderner Menschen sogar während der Fahrt. Allerdings ist dazu sicherlich eine Erneuerung der Basisstationen und der Endgeräte notwendig, um die Vorteile des LTE-Dienstes nutzen zu können. So muss ein Endgerät gleichzeitig mit anderen Hardware-Änderungen mindestens zwei Breitbandantennen aufweisen, da dieser Standard unter anderem Multiple-In-Multiple-Out-Technik (MIMO) und Carrier Aggregation einschließen.

Die letzten Jahre zeigen einen Trend, die große Anzahl von Fahrzeugantennen so weit wie möglich zu verstecken. Normalerweise werden die Strahler entweder auf einen Dach unter eine Haifischflossenabdeckung untergebracht oder in die Karosserie integriert. Allerdings ist der Bauraum sogar für komplizierte Systeme stark begrenzt, daher müssen Fahrzeugantennen sehr kompakt sein und gleichzeitig die erforderlichen Strahlungseigenschaften aufweisen. Eine dichte Antennenanordnung in Mehrfachantennenmodulen stellt mit der gegenseitigen Kopplung zwischen den Strahlern ein zusätzliches Hindernis dar. Besonders kritisch ist es in Modulen, die Sendeantennen für Mobilfunk und empfindliche Antennen für Satellitenempfang enthalten.

All diese Entwicklungen und Herausforderungen haben dazu motiviert, eine neue breitbandige kompakte Antenne für die LTE-Kommunikation im Auto zu erforschen. Die Untersuchung wurde in verschiedenen Betriebsszenarien durchgeführt: im Einzelbetrieb, in einem 2x2 MIMO-Modul und in Kombinationen mit Strahlern für andere Dienste wie terrestrischen Rundfunk, Navigation und Satellitenradio.

Die erforschte Antenne für den LTE-Dienst (sog. 3D- oder „Nefer"-Antenne) besteht aus zwei Strukturen, die an dem Antennenfußpunkt zusammengeschaltet sind. Aufgrund der Unabhängigkeit der Antennenteile von einander erreicht dieser 3D-Strahler die geforderten Impedanz- und Strahlungseigenschaften innerhalb der LTE-unteren, -mittleren und oberen Bänder, womit alle Frequenzen des derzeit verfügbaren Mobilfunkes abgedeckt sind.

In einem 2x2 MIMO-Modul ermöglichen die 3D-Strahler nach dem Dual-Band-Prinzip eine stabile Verbindung zum LTE-800-MHz-Netzwerk mit einem mittleren Durchsatz von 24 Mbit/s (Stand 2012), der während eines Drive-Tests im Live-Netzwerk gemessen wurde.

Da ein typisches Antennenmodul für Personenkraftwagen mehrere Strahler für unterschiedliche Dienste beinhaltet, wurde die 3D-Antenne (einzeln und auch im

2x2 MIMO-System) in mehreren Varianten mit Antennen für Satelliten Radio und Navigation, die nach dem Skarabäus-Konzept aufgebaut sind, kombiniert und sorgfältig untersucht. In diesen Kombinationen sind die 3D-Strahler für Mobilfunk gut von Antennen für den Satellitensignalempfang entkoppelt. Die Entkopplung kann darüber hinaus durch Bandsperrefilter für die kritischen Frequenzen und durch Optimierung der Filtereigenschaften der Antennen für Satellitendienste verbessert werden, wie in der Arbeit gezeigt. In den untersuchten Kombinationen behalten die Mobilfunkantennen ihr Rundstrahlverhalten mit nur geringen Abweichungen bei und erreichen eine ausreichende Impedanzanpassung an die 50-Ohm-Leitung.

So schlägt die Arbeit eine hocheffiziente, kompakte und zuverlässige Lösung für den LTE-Service an einem Fahrzeug vor, die auch in komplizierten Mehrantennenmodulen eingesetzt werden kann.

Neben dem Schwerpunktthema Antennen für den Mobilfunk wurden einige Forschungen zu Skarabäusantennen für den Satellitenempfang durchgeführt. Diese Untersuchungen wurden aufgrund der jüngsten Verbesserungen in der Navigation - wie der Öffnung des GPS-L2C-Bandes für den zivilen Gebrauch und der Entwicklung eines interoperablen L1C-Singals - und aufgrund der gestiegenen Anforderungen an die Entkopplung von terrestrischen Störern erforderlich. Auch diese Forschungen spiegeln sich in der Arbeit wider.

# Chapter 1

# Introduction and Thesis Overview

What does a modern human need? What has the highest price for him? Time. In order to save time, society continually improves means of personal and public transportation. For a long time ago, since starting with horses and carriage, now we are using high-speed automobiles and trains that can reach inconceivable speeds. In the 19th century, a journey from Munich to Augsburg took around 8 hours [1] whereas now it takes only about one hour. During that long journey, the contemporary people took books and newspapers to pass the time that they spent on the trip rationally. Modern people – per se – think in the same way: even during such a short one-hour journey, we try to fill our time with useful and entertaining pastimes to use our treasured time optimally.

Books and newspapers are very good only for those peoples who are travelling as passengers. However, the driver needs a different entertainment. Thus, in the 20th century audio broadcasting gained acknowledgement in the automotive surrounding. Even today, it maintains its popularity. Of course, there are some changes in radio; for example, it uses other frequencies, modulation and sometimes another type of broadcasting. Thus, in Europe radio is a terrestrial service while in the US it is transmitted by satellites. The latter enables covering large territories and saving investments especially in regions with a low degree of crowding. Audio broadcasting supplies its listeners with music of different art, news, various talk shows and current information about road and traffic situations. Precious information about the latter is also provided by global or local navigation systems that consider traffic congestions and closed streets during the calculation of the optimal way. Probably only a few of us can imagine living without such a useful service, which helps to reach one's destination quickly by car or foot while using a smartphone. Phones also allows to rationally use time during a trip. We discuss business, converse with our friends about plans for an evening or solve other important problems through cellular communication. All of these can be done even while driving due to hand-free systems that are implemented in modern cars. A more reliable connection to the

base stations during driving is realized by means of additional cellular antennas, which are integrated in the automobile.

The spectrum of the activities for passengers can be enhanced with the use of an integrated smartphone or tablet as a device that enables access to unlimited internet data. Soon, even drivers will be 90% free from driving due to the implementation of autonomous driving systems.

All of the aforementioned services are extremely important for modern society and for humans of the future. Therefore, they are essential parts of automobiles nowadays.

Although these systems differ one from another in their constellation and function, they have one common trait: all wireless systems cannot operate without antennas. Thus, navigation, terrestrial and satellite radio, cellular communication require corresponding devices that receive and transmit their signals. A continuous changing of these services gives steadily new impulses for the research and development of the corresponding aerials for each unit in their system, such as base stations, satellites and end-user equipment like smartphones or integrated antennas for cars.

Typically, an automotive antenna system includes several aerials for simultaneous access to different services. The radiators must be space-efficient and highly decoupled one from another since even for complicated systems, there is a strictly-limited mounting space underneath a protection cover (for roof-top mounting) or in a deepening in the car's body (for hidden mounting).

Investigations that will be discussed in this thesis cover compact and space-efficient antennas and antenna combinations for all mentioned services, namely cellular communication, navigation and satellite audio broadcasting in automotive applications. They concern new requirements for each separate service from antenna point of view and propose some solutions to improve decoupling between the aerials in the combinations, as well as locking satellite antennas from reception of the terrestrial signals from the interferers.

The presented work is arranged as follows.

The thesis starts with an overview of some technical aspects of the LTE communication system and the satellite services (satellite broadcasting and navigation), with a focus on those specialities that are relevant for antenna researchers. Furthermore, *Chapter 2* reports the results of publications on the existing antenna solutions for cellular communication based on LTE, satellite broadcasting and navigation that

can be used in the automotive sphere and for combinations of these antennas. Some particularities of antenna integration in cars will subsequently be highlighted.

The motivation of the work and definition of the goal will be detailed in the last subsection of this chapter.

*Chapter 3* discusses small-size dual-band antennas for LTE communication technology, starting with a concept explanation through theoretical considerations and simulation to a functional demonstrator. The measurement results appear to be in very good agreement with the theory and simulation, showing the high realized gain of the antennas within two wide-frequency bands (from 698 MHz to 960 MHz and from 1.5 GHz to 2.7 GHz) [2]. At the same time, the radiators of this 3-D design principle are relatively compact, which allows placing other antennas underneath the same cover; for example, compact aerials of scarabaeus principle [3]. The results of such investigations will be discussed in chapter 5.

*Chapter 3* includes confirmation of the antennas' applicability on automobiles through a simulation on a common car. Here, an LTE MIMO module of two antennas is also presented that are designed based on the investigated 3-D dual-band concept. The combination reveals reliable performance in a MIMO system, showing low correlation coefficient and sufficient gain.

Thus, the wide-band 3-D antennas for cellular communication based on LTE technology enable the realization of the LTE communication on a car with a minimum of radiators.

Before the combinations of the 3-D radiators for LTE communication with the antennas for satellite reception were investigated, further research of scarabaeus antennas for satellite signal reception was conducted to improve their radiation properties according the current specifications and for the cases of their combination with terrestrial radiators for cellular communication. The results of these researches will be shown in *Chapter* 4.

First, a scarabaeus antenna for satellite digital audio radio broadcasting (SDARS) was considered to enhance its decoupling from the LTE service and from other terrestrial interferers. *Chapter* 4 demonstrates the simulation and measurement results of the functional demonstrator with improved rejection of terrestrial signals outside its operational bandwidth, which is reached by means of the changes in its construction.

*Chapter* 4 also contains a discussion of several wide- and dual-band antennas for global navigation satellite systems (GNSS). The description starts with a single-

band antenna for reception of the existing GPS-L1 signal and the future -L1C interoperable signal. The aerial has a special shape to use all available volume underneath a small conical cover and allows its combination with further vertical structures that can be placed in its centre. However, the shape of the GPS antenna is not complicated.

Here, results of investigations of several dual-band antennas for simultaneous operation in GPS L1 & L2 systems and the future GLONASS, Galileo and BeiDou-2 systems are discussed. The chapter reports about two different concepts to realize the dual-band functionality: the double-ring design, which contains two separate metal antennas for two different frequency bands; and a single-ring concept, which allows simultaneous reception by means of only a single metal element. The latter involves the use of a simple resonance network.

A combination of the antenna for satellite broadcasting with improved decoupling from the LTE communication and the single-ring GNSS antenna for GPS L1 & L2 closes the discussion in this chapter.

*Chapter 5* reports investigations on the combinations of the antennas for terrestrial services with the antennas for the satellite reception, which are hidden underneath typical shark-fin-shaped covers for roof-top mounting. Herein, a way to reduce the mutual coupling between the antennas of these two types is discussed.

The chapter begins with the theoretical background for the optimal combination. Furthermore, description of a combination of a 3-D antenna for cellular communication with aerials for satellite signal reception (for GPS and SDARS) follows. This module has been extended by an antenna for terrestrial radio, which is mounted outside the shark-fin cover. Although these two modules contain only one antenna for cellular communication, they can be successfully complemented by second wide-band radiator to enable the use of LTE service. This statement is proven by a short investigation, which is also reported in this chapter.

Research into a combination of a very compact GNSS antenna and an aerial for terrestrial broadcasting closes this chapter.

Recent developments show a trend of hiding the antennas from the car's outer surface. Investigations of aerials for satellite signal reception in the hidden mounting will be reported in *Chapter 6.* Here, a stand-alone aerial and a diversity antenna combination for the reception of the satellite broadcasting will be described. This investigation reveals an undeniable advantage of the diversity module over the single aerial, especially in such a restricted mounting position in a deepening in a car's roof, providing for the structures to be highly decoupled one from another.

The antennas and antenna modules in this work were designed and simulated in a CST Microwave Studio environment. For a circuit simulation, Advanced Design System was used.

# Chapter 2

# State of the Art of Car Antennas for Cellular Communication, Satellite Broadcasting and Navigation

Modern cars are being developed hand by hand with the newest technologies. The results of the progress not only in mechanical engineering, material science and ergonomics but also in safety, driving assistance, mobile communication and entertainment are being implemented into cars nowadays. Thus, the use of navigation makes driving easier while satellite and terrestrial audio broadcasting make it more comfortable, as well as provide useful information about a road situation. Cellular communication on the car allows the driver to have a standing connection to the outer world. The realization of all such services requires a number of wireless communication systems, which cannot be imagined without antennas.

Differences in the system constellations of the services mentioned above lead to a necessity to use a multitude of antennas on an automobile. A typical antenna module includes one or two radiators for mobile communication, an aerial for the positioning system, antennas for satellite and terrestrial broadcasting or different combinations of these radiators. In solutions of two and more antennas, coupling between them – especially between the LTE-transmission path and the sensitive reception part for the satellite services – is a serious obstacle for the placement of antennas in proximity to one another while keeping their demanded performance at once. Moreover, even in a single-antenna case, the car's body destructively influences the radiation properties of the radiator.

A next brief description of the LTE communication technology, satellite broadcasting and global navigation systems is targeted to highlight their peculiar properties from an antenna perspective. Furthermore, the most appropriate antenna types and combinations for LTE cellular communication, satellite broadcasting and navi-

gation in automotive application will be briefly discussed. The problems of antenna integration on a car will also be considered in this section.

# 2.1 Technical Aspects of LTE Cellular Communication, Satellite Broadcasting and Navigation Systems in Automotive Applications

## 2.1.1 LTE Communication Technology

Long-term evolution (LTE) is a cellular wireless communication standard which involves the use of both paired (for frequency-division duplex, FDD) and unpaired spectrum (for time-division duplex, TDD), and a carrier aggregation that leads to a wide range of operational frequencies.

LTE technology was established in 2009, and one year later it was called the 4$^{th}$ generation of cellular communication [4]. Subsequently, several improved releases have been announced. The newest LTE-Advanced Release-13 provides many enhancements, whereby in particular it ensures high data rates up to 3 Gbps in downlink and 1.5 Gbps in uplink [5], [6]. Such high data rates have been achieved by using a carrier aggregation and 2x2 (4x2 and 4x4 since 2017) MIMO technology. Therefore, at the receiving end at least two radiators are demanded, and each must provide simultaneous reception in two wide-frequency bands.

Data stream from a base station of the LTE service is transmitted by four pairs of directional aerials. Each pair is a cross-combination of two antennas with linear polarization, which are additionally tilted by 45° to the earth surface for radiating linearly polarized waves with ±45° slant, thus enhancing the channel quality. In order to provide an omnidirectional coverage, three sectoral antennas have been mounted on each base station. Since cellular communication is a terrestrial service, its signals appear near to the earth level. Thus, they occur at elevation angles roughly between 90°and 85° (counted from zenith), except for a receiver is too close to the transmitter.

The LTE signals can be transmitted within 45 narrow frequency bands, which are listed in Table 1 [7]. For each data transmission, two of them are simultaneously utilized due to the carrier aggregation [6]. All LTE bands can be categorized in three wide ranges: LTE lower (698 MHz – 960 MHz), LTE middle (1.428 GHz – 2 GHz) and LTE upper (2.01 GHz – 2.69 GHz) ranges. There are further developments of LTE standard at frequencies between 3400 MHz and 3800 MHz.

For all of these reasons, ***an LTE antenna for worldwide application should:***

- act within two wide-*frequency ranges: from 698 MHz to 960 MHz and from 1.427 GHz to 2.69 GHz*;
- possess an *omnidirectional* radiation pattern with main beam direction at $\theta$ = [85°; 90°];
- provide high gain in horizontal plane;
- possess high radiation efficiency; and
- provide low mismatch loss, i.e. be sufficiently matched to the 50-Ohm signal path (with reflection coefficient at least -6 dB or better).

Table 1: Operation frequencies of LTE communication technology across the world

| | Band Nr. | Uplink, MHz | Downlink, MHz |
|---|---|---|---|
| LTE lower range | 12 | 698 – 716 | 728 – 746 |
| | 17 | 704 – 716 | 734 – 746 |
| | 13 | 777 – 787 | 746 – 756 |
| | 14 | 788 – 768 | 758 – 768 |
| | 18 | 815 – 830 | 860 – 875 |
| | 19 | 830 – 845 | 875 – 890 |
| | 20 | 832 – 862 | 791 – 821 |
| | 5 | 824 – 849 | 869 – 894 |
| | 6 | 830 – 840 | 875 – 885 |
| | 8 | 880 – 915 | 925 – 960 |
| LTE middle range | 11 | 1427.9 – 1447.9 | 1475.9 – 1495.9 |
| | 21 | 1447.9 – 1462.9 | 1495.9 – 1510.9 |
| | 24 | 1626.5 – 1660.5 | 1525 – 1559 |
| | 4 | 1710 – 1755 | 2110 – 2155 |
| | 3 | 1710 – 1785 | 1805 – 1880 |
| | 2 | 1850 – 1910 | 1930 – 1990 |
| | 35 | 1850 – 1910 | |
| | 39 | 1880 – 1920 | |
| | 33 | 1900 – 1920 | |
| | 37 | 1910 – 1930 | |
| | 36 | 1930 – 1990 | |
| | 1 | 1920 – 1980 | 2110 – 2170 |
| LTE upper range | 34 | 2010 – 2025 | |
| | 40 | 2300 – 2400 | |
| | 38 | 2570 – 2620 | |
| | 41 | 2496 – 2690 | |
| | 7 | 2500 – 2570 | 2620 – 2690 |
| LTE new range | 22 | 3410 – 3500 | 3510 – 3600 |
| | 42 | 3400 – 3800 | |
| | 43 | 3600 – 3800 | |

### 2.1.2 Satellite Broadcasting and Navigation Systems

***Satellite Digital Audio Radio Service*** (SDARS) was established in 2001 in North America by two providers: Sirius Satellite Radio and XM Satellite Radio. In 2007, they joined to form SiriusXM Radio. Prior to this, the companies developed their specific systems, which have still been maintained.

Satellites of the lower frequency band of the satellite broadcasting (Sirius part) operate at frequencies between 2320 MHz and 2332.5 MHz, while those of the upper band (XM part) transmit signals at frequencies from 2332.5 MHz to 2345 MHz [8]. The Sirius part uses one Geostationary Orbit (GEO) satellite and three Elliptical Geosynchronous Orbit (HEO) satellites, whereas the XM space segment comprises two GEO satellites. Therefore, the broadcasted left-hand polarized (LHCP) signals from these satellites appear at elevation angles between 0° and 75°. In cities, the satellite signals are retransmitted by terrestrial repeaters at 2326.25 MHz and 2338.75 MHz by vertically-polarized waves near to horizon.

A further important satellite service in automotive applications is navigation. It has already been widely implemented on the cars and will be one of the most important parts of future automobiles based on recent successful investigations in the autonomous driving.

A ***Global Navigation Satellite System*** (GNSS) is a common denomination for satellite positioning systems that are available across the world. Nowadays, only a Global Positioning System (GPS) from the US provides navigation over the globe, offering several services for civil use such as Standard Positioning Service (SPS) and Precise Positioning Service (PPS) [9]. SPS and PPS are both available at the carrier frequency of 1575.42 MHz with different signal bandwidths, namely 2.046 MHz for SPS [10] and 20.46 MHz for PPS [11]. In March 2016, the US government opened further frequencies for civil use (exactly 1227.60 MHz with a bandwidth of 20.46 MHz) for improving the on-Earth positioning accuracy [11].

There are also several GNSS under development, such as GLONASS from Russia and Galileo from the European Union. The operation capacities of these systems are planned to be completed by 2020 [12], [13]. China will extend its local positioning system BeiDou to BeiDou-2 for global navigation in the near future [14]. All of these systems are planned to operate at different frequencies with different bandwidths, whereby GLONASS will function at frequencies between 1598.0625 MHz and 1605.0625 MHz [12], while BeiDou-2 will be available at the carrier frequency of 1561.098 MHz with a bandwidth of 4.092 MHz [15]. Galileo in L1 band is planned to operate at 1575.42 with a 24.552 MHz bandwidth [16].

Signals transmitted from the satellites of all GNSSs have right-hand circular polarization (RHCP) and occur at elevation angles between 0° and 30°. BeiDou-2, Galileo and GPS make use of a code division multiple access (CDMA) [10, 15, 13], while GLONASS uses a frequency-division multiple access (FDMA) [12], which leads to some differences in signal processing only.

The US and Europe have recently developed a common civil signal L1C centered about a nominal frequency 1575.42 MHz with a bandwidth of 30.49 MHz to enable interoperability between international satellite navigation systems [17], thus making the antenna development slightly easier. This service is also planned to be available by 2020 [9].

Considering the information above, the following can be specialized for antennas for navigation and satellite broadcasting.

***An antenna for GNSS service must:***

- provide a hemispherical radiation pattern for *RHCP waves* with the main reception at elevation angles near to zenith. LHCP must be strongly discriminated;
- operate at 1561 MHz, 1575 MHz and from 1598 MHz to 1606 MHz;
- show high efficiency; and
- possess a low reflection coefficient (at least -10 dB or better).

***Antennas for SDARS have to***

- receive *LHC* polarized signals at the frequencies between 2.32 GHz and 2.345 GHz;
- obtain a directional radiation pattern with the main reception at elevation angles around ±75°;
- discriminate RHCP by minimum 10 dBic;
- provide a stable reception of VP waves at elevation angles near to the horizon;
- highly reject VP signals out of the SDARS band at angles close to the horizon; and
- be highly efficient and possess a low reflection coefficient (at least -12 dB)

Furthermore, in combinations with aerials for cellular communication, the antennas for satellite signal reception must be highly decoupled from the former by at least *-20 dB (transmission coefficient, $S_{ij}$)* especially at LTE frequencies due to a full-duplex configuration of the cellular network, which also implies transmission from the user side.

Next, the most appropriate antenna types for the reception of satellite signals and for operation at LTE cellular communication system in stand-alone case as well as in combinations will be considered.

## 2.2 Antenna Types for Terrestrial Communication and Satellite Reception in Cars

There are a number of antennas being investigated and developed for cellular communication and satellite signal reception that are suitable for a roof-top mounting on a car, as reviewed, for example, in [18], [19], [20], [21] and [22]. Below, some traditional and new aerial types will be briefly discussed.

### 2.2.1 Antenna Types for LTE Cellular Communication

For ***LTE cellular communication***, multi-resonant monopoles and helical antennas, inverted F- antennas as well as reconfigurable antennas are used for the reason that the LTE communication technology is a service in several wide-frequency bands with omnidirectional coverage from the antenna perspective. These aerial types have various shapes and design types: planar printed on a substrate, 3D metal parts such as wires or other metal constructions, or 3D structures manufactured by the recent technologies, namely by molded interconnect device (MID) technology or inkjet printing.

Some examples of a planar *multiresonant monopole* are found in [18], [23], [24] and [25]. *Multiresonant monopole* is a combination of several monopoles, each for a certain frequency band, with a common driving point. Figure 2.1-a schematically shows a triple-resonant monopole including three functional parts for three frequency bands. The longest part (folded monopole) dominates the structure at the lowest frequency $f_1$, while the other two parts enable operation at the medium (the second in the length part, $f_2$) and highest (the shortest part, $f_3$) required frequencies. Measured results of a tri-band monopole for a cellular phone and Wi-Fi – which are presented in [18] – allow considering such a design for utilization in LTE service.

A *helical antenna* with uniform or non-uniform pitch is able to operate within two bands [26]. Extended by a monopole with a common feed, it gives a third resonance and thus enables service within three frequency bands [18]. The architecture of a helical-monopole combination (helix with uniform pitch) is schematically shown in Figure 2.1-b. Although the helical antennas and their combinations can be

relatively compact, they possess very narrow bandwidth [18] and thus cannot fully satisfy the bandwidth requirements of the LTE service.

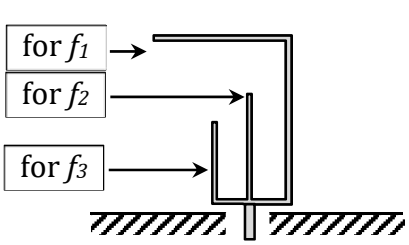


(a) Multiresonant monopole ($f_1 < f_2 < f_3$).

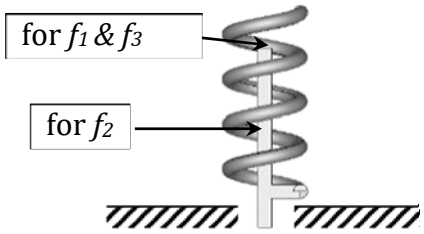


(b) Multiband helical-monopole combination ($f_1 < f_2 < f_3$).

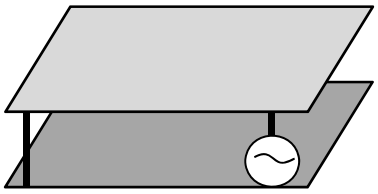

(c) Inverted-F antenna (further slots provide multiple resonances).

Figure 2.1: Schematic representation of multiresonant antennas for LTE.

Further high-profile LTE vehicular antennas are investigated by authors of [27] and [28]. These radiators are made in the form of flat metal structures printed on a 3D body. In [27], a combination of a bow tie antenna and a folded monopole with a common excitation point is proposed. It is a wideband antenna that reveals good impedance properties (reflection coefficient is better than -7 dB) and a monopole-like radiation pattern in the LTE-800-MHz band and at frequencies between 1.7 GHz and 3.5 GHz. The antenna design is meant to be printed by MID technology on a shark-fin-shaped housing made of an expensive MID material. A more cost-efficient solution is presented in [28]. In this paper, a wideband monopole with an additional radiator (T-shaped monopole) is considered to be manufactured by inkjet printing and subsequently attached to the outer surface of a plastic cylinder. The antenna shows wideband impedance properties and near-constant omnidirectional radiation pattern operating at the frequencies from 700 MHz to 960 MHz and from 1.5 GHz to 4.5 GHz with maximum gain between 4 dBi (at LTE lower frequencies) and 8.1 dBi (at the LTE new band, 3.6 GHz). It can be successfully used on a public transport but cannot be utilized at personal automobiles due to its large height (68 mm).

Although the last two solutions reveal good performance, they demand a relatively large mounting volume and their architectures are highly dependent on the shape of a considered housing.

There are also reports on low-profile 3D solutions that are suitable for LTE communication on a vehicle, especially on *Planar Inverted F-antennas (PIFA).* A schematic representation of a simple PIF structure is shown in Figure 2.1-c. Extended with slots and slits, it generates multiple resonances and provides a wide impedance bandwidth as detailed, for example, in [29], [30], [31], [32], [33]. Although modified versions of PIFA can even operate in an ultra-wide band, they possess low gain in the horizontal plane at $\theta$ = 85° - 90°, which indicates a trade-off between the aerial performance and its volume (particularly concerning the height of a radiator).

In the following, a brief overview of antennas used for the reception of satellite signals will be provided.

### 2.2.2 Antenna Types for the Reception of Satellite Navigation Services and Satellite Broadcasting in Cars

For the ***satellite signal reception*** in a car, a patch, frame, annular ring, helical, crossed-dipole or crossed-frame antenna can be utilized, which are schematically shown in Figure 2.2. The antennas of these types are suitable for satellite signal reception due to the hemispherical shape of their radiation pattern for co-polarized waves and their polarization selective properties.

As already mentioned above, navigation services are continually under development and improvement, which leads to dramatic transformations in the antennas used for them. Thus, since 2011 requirements on the cross-polarization discrimination (XPD) level have been tightened. Furthermore, since 2016 the US government has opened a navigation signal in L2 band for civil use on Earth. These changes have given an impetus to a large number of research studies in this field. Thus, for example, in [34] a compact single-band frame antenna with high gain and XPD is proposed for GPS in L1 band. Its schematic representation is shown in Figure 2.2-f. Although this radiator operates well, it receives navigation signals only in a single band that was sufficient until 2016 but is not at the present time. The author of [35] reports a low-profile square patch antenna (its sketch is shown in Figure 2.2-a) with a sufficient level of XPD but with low gain and only single-band reception in the GPS-L1 band.

Some works on dual-band antennas for GNSS in L1 and L2 bands with high XPD that satisfy the current requirements on aerials for navigation will be briefly described below.

In [36], a dual-band circularly-polarized (CP) crossed asymmetrical dipole antenna is introduced. The antenna shows high performance within two frequency bands of GPS service, reaching maximum RHCP gain of 7.5 dBic (L1 band) and 6.3 dBic (in L2 band) with a low reflection coefficient below -10 dB. However, the antenna is relatively large and needs a deep wide cavity as a reflector.

Another 3D solution for dual-band operation is a well-operating crossed-dipole antenna, as discussed in [37]. Its schematic view is shown in Figure 2.2-e. This aerial achieves a low value axial ratio along with a high RHCP gain of around 4 dBic and acceptable impedance matching to 50 Ohm (simulation results) in both bands of GPS service; however, like the aerial from [36], it requires a large mounting volume of 90 mm x 90 mm x 15.5 mm.

For navigation, a helical aerial with CP – which is schematically depicted in Figure 2.2-d – can be utilized. The authors of [38] present its modified and improved version: a printed tapering quadrifilar helical antenna. It shows high radiation performance at frequencies from 1.16 GHz to 1.61 GHz but it occupies a huge volume of 74 mm x 74 mm x 82 mm and thus it cannot be used on cars, although it might be a good candidate for other applications where the occupied volume is not so critical, such as for geodesy.

Although the height of circularly-polarized antennas can be reduced by means of patch technology, their width and length remain almost the same as those of the 3D solutions mentioned above. For example, the authors of [39] have shown a low-profile multi-layer antenna with a good operation in L1 and L2 bands, which is only 5.7 mm high, although it is 45.4 mm wide and 56.8 mm long. Moreover, patch radiators need an expensive low-loss material as a substrate, otherwise they will suffer from high thermal losses.

The authors of [40] have presented a wide-band CP antenna system that includes an orbicular patch made of an FR-4 substrate and a metal patch located above the first element at a distance of 4 mm. The combination is fed through two pins with a 90° phase difference. The antenna combination shows good impedance matching and radiation properties in both frequency bands. This radiator – as well as other flat but wide samples shown in this overview – can be applied in the systems where the antenna height is very critical but there is sufficient space in length and width, since the antenna's overall dimensions are 90 mm x 90 mm x 5.8 mm (without considering a circuit board with a feeding network).

In [41], a dual-band CP annular-ring microstrip antenna for GNSS is proposed. Its simplified version is sketched in Figure 2.2-b. The antenna operates at both L1

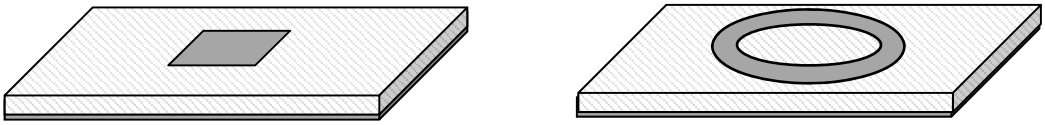

(a) Patch antenna.



(b) Annular-ring patch antenna.

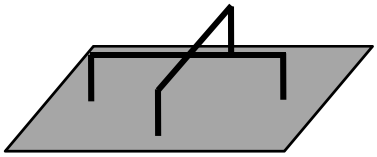

(c) Crossed-frame antenna.

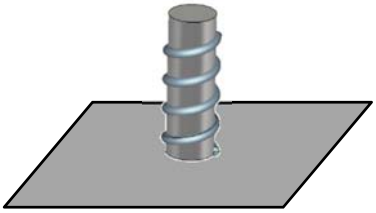

(d) Helical antenna.

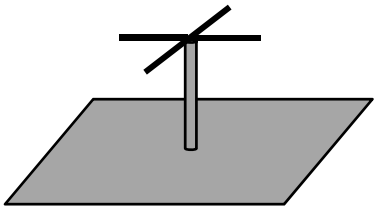

(e) Crossed-dipole antenna.

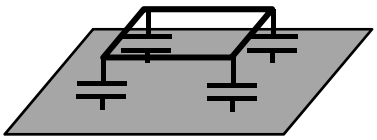

(f) Frame (scarabaeus) antenna.

Figure 2.2: Schematic representation of antennas for satellite signal reception.

and L2, bands reaching a RHCP gain higher than 5.2 dBic high XPD even at the elevation angles near to the horizon. Although the proposed antenna is highly performant, it needs a large mounting volume.

In [42], a slot-loaded proximity-fed compact antenna is presented. The antenna design employs a circular patch for signal reception in L1 band and additional slots that are implemented in the patch for operation in L2 band. The slot-loaded patch is stacked on a high-dielectric constant ceramic puck. The design is very compact (diameter is 25 mm, height is near 11 mm) and shows very good radiation and impedance properties. However, the antenna is made of an expensive high-frequency laminate and high-dielectric ceramic.

From the overview of existing antennas for navigation, it is obvious that further research is required on a compact and simultaneously cost-efficient solution with dual-band operation and high XPD in L1 and L2 bands.

The satellite broadcasting system has its own constellation and other specialties that distinguish it from navigation systems, as shown in section 2.1.2. In particular,

it involves terrestrial repeaters with operation on vertically-polarized waves for reinforcement of the service quality in cities. Therefore, antennas for SDARS are usually a combination of two antenna types: one for the reception of circularly-polarized signals (CP) and another for the reception of vertically-polarized waves (VP).

In [43], a combination of a frame structure for satellite signal reception and a monopole for VP signals is shown. The satellite part is designed of two crossed vertical frames (simple sketch is depicted in Figure 2.2-c) fed by currents with a 90° phase shift. In the centre of the cross, a capacitively-loaded monopole is located. The results of further investigations on the improvement of radiation properties and mounting volume for this antenna design are published in [44]. In this paper, a low-profile (of 9 mm height) highly-performant crossed-frame antenna is presented, albeit it needs some simplification in the manufacturing procedure.

In [45], a combination of a printed dipole with an integrated balun for satellite signal reception with an array of spiral monopoles for the reception of terrestrial signals is introduced. The combination obtains a wide-beam radiation pattern with sufficient gain and impedance matching in the SDARS band. However, the newest trend in automotive antennas requires a much compacter solution.

The author of [46] describes an 'inverted radiating' patch. Here, a radiating element of a convenient corner-truncated patch is wrapped down, and the upper and down parts are connected via metalized holes, allowing a size reduction to 30 mm x 30 mm x 4 mm. Although the antenna shows good properties, its wide operational bandwidth causes an interaction with services available at frequencies near to SDARS band and it suggests the use of an expensive substrate.

Another compact solution is shown in [47]. In this paper, a compact frame antenna made as a 3D metal construction for the reception of satellite and terrestrial SDARS signals is presented (Figure 2.2-f). The antenna is only 20 mm x 20 mm x 10 mm due to the shortening capacitances, which are realized as a part of the metal structure. This compact radiator possesses high LHCP gain at elevation angles where satellite signals occur and high VP gain at the elevation angles near to the horizon, as well as a high XPD level and excellent efficiency due to its panel design. Due to the continually-changing requirements to SDARS aerials, this antenna needs further improvement, particularly in terms of bandwidth. The work done on the antenna enhancement is reported in further sections of this thesis.

Further antennas for satellite signal reception that can be used in automotive vehicles can be found in [48] and [49] (a compact ring antenna with capacitive slots)

Subsequently, combinations of antennas for terrestrial communication and satellite signal reception will be reviewed.

### 2.2.3 Multiple-Antenna Modules for LTE Cellular Communication and the Reception of Navigation and Satellite Broadcasting for Cars

Although there are many commercial multiple-antenna solutions for LTE cellular communication and the reception of navigation and satellite radio in automobiles that are integrated underneath a single cover, there are only a few publications in which the radiation properties of the antennas and mutual coupling effects are discussed, for example [50], [51], [52].

Thus, in [50] a flat roof automobile antenna module for LTE, GPS and SDARS is presented. The module includes a PIFA for cellular communication, a square loop antenna for navigation by means of GPS and a circular loop antenna for the reception of the satellite broadcasting. The antennas show a good performance even in such dense mounting. The radiator for LTE possesses gain of around 1 dBi at elevation angles between 60° and 70° (these angles are typical for antennas with VP which are measured on a finite ground plane; see section 3.3.3). It is 4 dBi lower than that of a quarter-wave monopole, caused by the very low profile of the presented PIFA. Both aerials for satellite signal reception obtain a required gain for the corresponding services. However, a strong mutual coupling is observed between the radiator for LTE and the antenna for GPS, which can be concluded from the figure for current distribution on the LTE radiator. The coupling between the aerial for cellular communication and the antenna for satellite broadcasting is also noticeable, but it is weaker than in the former case. The mutual coupling manifests in a deformation of the radiation pattern of both satellite aerials and the blockage of the weak satellite signals by the strong LTE signals, which are radiated by the cellular antenna in its transmitting mode. There are clearly further actions required to lock the satellite antennas from the cellular one.

## 2.3 Problems of Antenna Integration in Cars

For several decades, a single antenna on the vehicle (mast antenna) has protruded from the car's exterior, whereas in recent years a trend of hiding the increased number of vehicular antennas as much as possible can be observed. There are several possibilities of antenna integration in a car, as shown in Figure 2.3. In general, satellite antennas can be mounted on a top of a roof (positions 1 and 2), on a trunk (pos. 3), fixed on an inner surface of a windshield (pos. 4, 5) or integrated

into side mirrors (pos. 6). For omnidirectional LTE antennas, the diversity of mounting positions is limited by two or three at most. For an LTE antenna, the most suitable mounting is either upon a roof underneath a plastic housing (pos. 1) or a partially-hidden integration in a deepening in the roof underneath a flat plastic cover (pos. 2). These positions are the most appropriate ones since there an omnidirectional coverage can be realized and a sufficient conducting ground plane is available. However, strict requirements are posed upon the LTE antennas concerning their mounting volume.

Typically, an automotive antenna system includes several aerials for simultaneous access to different services. However, for even complicated systems, there is a strictly-limited mounting space underneath a protection cover (for roof-top mounting) or in a deepening in the car's body (for hidden mounting). Therefore, antennas for automotive applications in stand-alone cases as well as in combination must be very compact while providing the required radiation properties like a wide bandwidth for LTE radiators or hemispherical radiation patterns for SDARS and GNSS aerials. A restricted mounting volume requires constructing compact multiresonant and wide-band antennas for the efficient use of the available space.

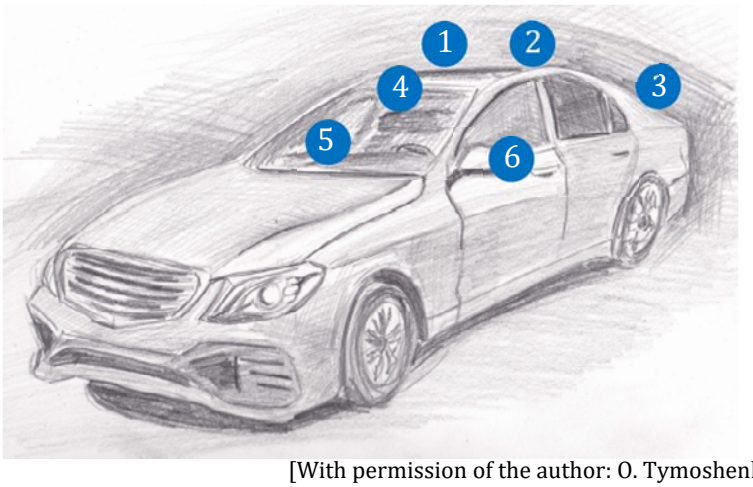


[With permission of the author: O. Tymoshenko]

Figure 2.3: Possible positions for antenna mounting on a common car.

A dense antenna placement in multiple-antenna modules poses an additional obstacle, namely mutual coupling between the aerials. It is especially critical in modules that contain transmitting antennas for cellular communication and sensitive aerials for satellite reception, since LTE communication implies not only reception but also transmission at the user end. There are several options to mitigate this problem, such as spatial separation, special arrangement of the radiators or application of additional filtering networks. In the restricted mounting volume, the first

two possibilities require compact antenna solutions, since a form of a housing and a mounting volume are usually prescribed by car vendors. Moreover, resistance of the satellite antennas towards LTE or WLAN interferers can be improved through a special form of radiation pattern for the satellite antennas with poor gain at elevation angles close to the horizon. Therefore, even in stand-alone cases, satellite antennas have to be locked for LTE signal reception due to the close allocation of their operational bands.

All of these challenges motivate the following.

## 2.4 Goal Definition

Obviously, there is a necessity to find highly-performant, cost-efficient and compact solutions for LTE cellular communication, navigation and satellite broadcasting on an automobile.

The goal of the work is to investigate a new antenna concept for LTE cellular communication for automotive applications, which covers all frequencies of this service. The research will be performed in different operation scenarios: in a stand-alone case, in a MIMO module to realize the LTE service and in combination with antennas for the reception of signals from satellite broadcasting and navigation underneath a common cover. For the last case, the frame (scarabaeus) antennas were chosen for satellite signal reception. However, they demand further investigation and enhancement according to the current specifications from the providers of navigation and satellite broadcasting. For satellite broadcasting, it means designing antenna with a special shape of RP, which prevents reception of signals from terrestrial interferers (LTE base stations and WLAN-2.4GHz access points) outside the SDARS band, as well as enabling high VP and LHCP gain at the required frequencies. For navigation, an antenna shall provide a dual- or wide-band function to enable the precise positioning that is currently demanded.

Furthermore, aerials for satellite reception must be optimized in terms of shape and radiation properties to achieve good performance in case of their combination with radiators for LTE service with reduced coupling between these aerials. The antennas have to have their own design for each of these two satellite services, since SDARS and GNSS have different system constellation and distinctive requirements, as discussed above.

The concepts of both antenna types – for terrestrial and satellite signal reception – were researched at the Institute of High Frequency Technology and Mobile Communication.

# Chapter 3

# Small-Size Dual-Band 3-D Antennas for LTE Cellular Communication

In the current chapter, a highly-performant LTE antenna for operation within wide-frequency bands of the LTE lower, middle and upper ranges will be discussed. The chapter starts by describing the antenna concept, before following mathematical calculations of the constituting parts of the structure. The validity of the presented concept will be shown by means of the simulation and measurement results of a functional demonstrator. A discussion of a MIMO module of two LTE 3-D dual-band antennas will close the chapter.

## 3.1 Concept of Dual-Band LTE Antenna

The design of a small-size dual-band LTE antenna for a roof-top mounting on a car implies the combination of two structures for two frequency bands. These constructions are joined together at an excitation point (Figure 3.1).

One part of the antenna architecture is a cone-shaped structure that possesses a very wide operational frequency bandwidth [2], covering the frequencies of the LTE middle and upper bands. Another part is a structure that is similar to a quarter-wave monopole with a capacitive top load. It is meant to operate within the LTE lower frequency range.

The antenna architecture is adaptive in height and width by a high degree, whereby it can easily be fitted underneath different plastic covers of diverse shape.

Cone-shaped and monopole-like structures both radiate/accept vertically-polarized (VP) waves omnidirectionally in the horizontal plane. Even without applying an additional matching circuit, 3-D dual-band antennas have sufficient impedance matching in all required LTE frequency ranges, as will be further shown.

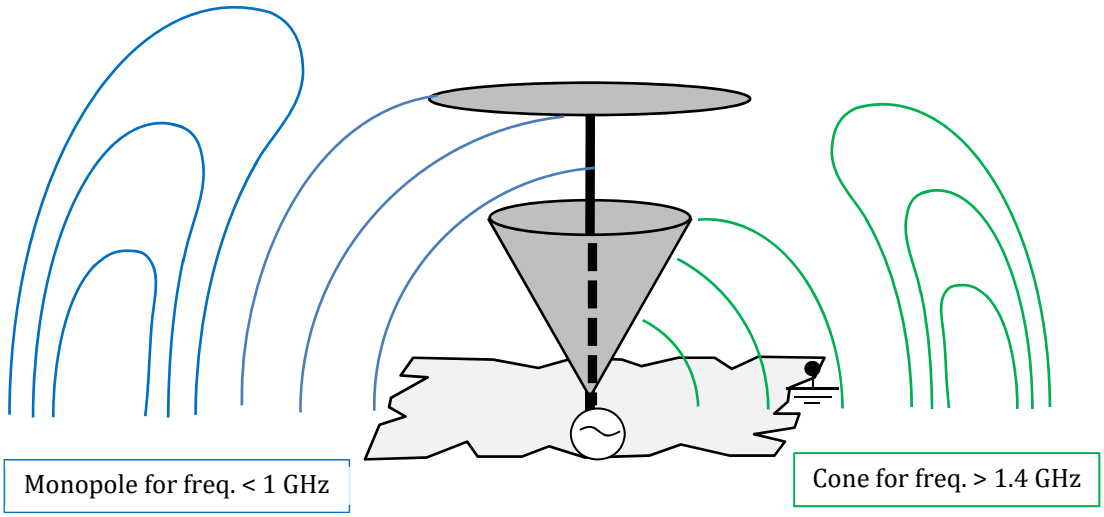


Figure 3.1: A principle structure of dual-band antenna for the LTE cellular communication with sketched electric field distribution.

Next, a theoretical description and calculation of a far field of the radiator will be provided.

## 3.2 Theoretical Considerations

The 3D LTE antenna concept involves two aerial types: a quarter-wave monopole with a roof capacitor and a conical antenna, which are intended for a combination at a common driving point. As far as antennas operate within different frequency ranges, both structures are well isolated electrically one from another and thus they can be analysed separately by considering the structures in turn.

Since the radiator is regarded to be used on a car's roof, the parts of its architecture can be roughly approximated to the structures above an infinite perfectly conducting plane. Therefore, the following antenna types will be discussed below: a quarter-wave monopole, a shortened monopole with a capacitive top load and a conical antenna. All considered aerials are located above an infinite conducting plane.

### 3.2.1 Monopole Antenna

Radiation and impedance properties of a common quarter-wave monopole are already well investigated. Therefore, their derivation will not be shown in this the-

sis. Instead, a brief description of the derivation procedure and corresponding mathematical expressions in closed form will be given. A brief description of the calculation procedure of the field that an antenna radiates can be found in appendix A.2.

## *Radiation Pattern*

A monopole in a first approximation is usually represented as an elongation of a thin inner conductor of an opened coaxial line, which protrudes from an opening in an infinite conducting ground plate. Figure 3.2 shows a sketch of this approach.

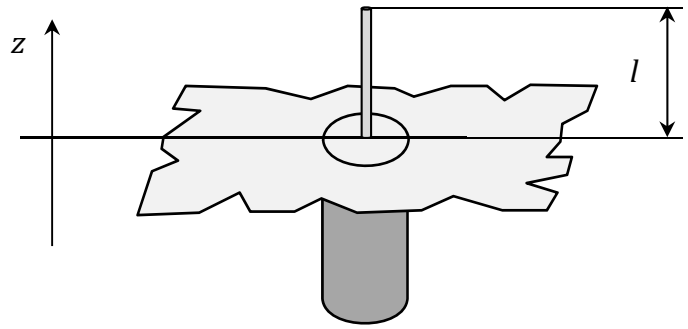


Figure 3.2: Simple representation of the monopole antenna.

Along this aerial, a sinusoidal current flows with the distribution mathematically described by (1). This is a reliable approach for the thin monopoles with a height of around λ/4 [53].

$$I_l(z) = \frac{I_0}{\sin(kl)} \sin\big(k(l-z)\big) \qquad for \quad 0 < z < l, \tag{1}$$

where: $I_0$ – current at the driving point of the monopole;

$k = \omega\sqrt{\mu\varepsilon}$ – propagation constant,

here: $\omega$ – radial frequency, rad/s;

$\varepsilon$ – permittivity of the propagation medium, F /m;

$\mu$ – permeability of the medium, H/m.

The total radiated field is obtained through calculating the vector magnetic potential $\underline{\hat{V}}$ [54] produced by the current with the distribution (1) in a point at the distance *r* and afterwards by using the relation (2) [55] between magnetic potential $\underline{\hat{V}}$

and magnetic field intensity $\underline{\hat{H}}$. Electric field intensity $\underline{\hat{E}}$ is obtained from the known $\underline{\hat{H}}$-field by means of (4). A brief summary of the calculation procedure is provided in appendix A.2.

$$\underline{\hat{H}}(r,\theta,\varphi) = \frac{1}{\mu_0} rot\left(\underline{\hat{V}}(r,\theta,\varphi)\right). \tag{2}$$

After carrying out the whole calculation, the following expression of *magnetic intensity H in far field zone* has been reached:

$$\underline{\hat{H}}_{\varphi}(r,\theta,\varphi) = j\frac{I_0}{2\pi\sin(kl)} \cdot \frac{\cos(kl\cdot\cos(\theta)) - \cos(kl))}{\sin(\theta)} \cdot \frac{e^{-jkr}}{r} \cdot \hat{e}_{\varphi}\,. \tag{3}$$

The electric field intensity of the monopole is calculated by using the following relation between the electric and magnetic fields, which is given in [56] by:

$$\underline{\hat{E}}(r,\theta,\varphi) = \frac{1}{j\omega\varepsilon_0} \cdot rot\left(\underline{\hat{H}}(r,\theta,\varphi)\right), \tag{4}$$

where: $\varepsilon_0$- permittivity of free space, $\varepsilon_0 = 8.85\cdot10^{-12}$ F/m.

After the necessary calculations have been performed, the *electric far field intensity* of the monopole antenna obtains the following form.

$$\underline{\hat{E}}_{\theta}(r,\theta,\varphi) = j\frac{Z_0\cdot I_0}{2\pi\sin(kl)} \cdot \frac{\cos(kl\cdot\cos(\theta)) - \cos(kl)}{\sin(\theta)} \cdot \frac{e^{-jkr}}{r} \cdot \hat{e}_{\theta}\,, \tag{5}$$

where $Z_0$ – wave impedance of a free space ($Z_0 = 120\pi$).

Clearly, the vertical monopole radiates only a $E_\theta$-component of the electric field thus the main (and single) polarization of its field is vertical.

The resultant expressions are similar to those published in other literature, for example in [53, 55, 54, 57].

The radiation pattern of the aerial – which is calculated by (4) – is depicted in Figure 3.3. The main beam direction is at $\theta = 90°$ and there is no radiation/reception in zenith (at $\theta = 0°$). This satisfies the requirements to the radiator for a cellular communication based on LTE technology.

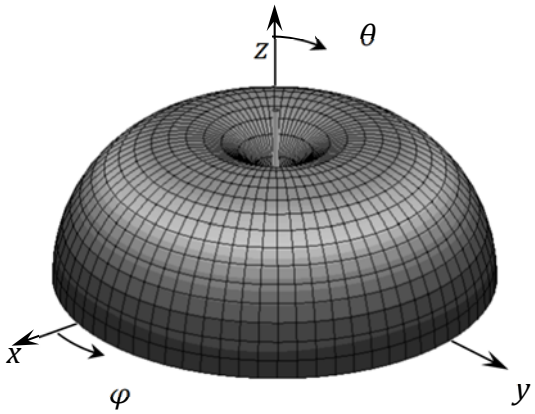


Figure 3.3: Radiation pattern (E-field) of the λ/4-monopole above infinite-ground plane.

## *Input Impedance*

A monopole aerial is a narrow-band antenna that provides demanded impedance matching to a signal path and high gain only close to its resonance frequency, whereas outside this band it reflects most of the power that perfectly satisfies the concept requirements. Such a property is concluded from the equation of input impedance of the infinitely-thin monopole antenna placed above an infinite-ground plane [55]:

$$R_{inp} = \frac{Z_0}{4\pi \cdot \sin^2(kh)}\left\{Cin(2kh) + \frac{1}{2}\sin(2kh)\left[Si(4kh) - 2Si(2kh)\right] + \right.$$
$$\left. + \frac{1}{2}\cos(2kh)\left[2Cin(2kh) - Cin(4kh)\right]\right\}, \tag{6}$$

$$X_{inp} = \frac{Z_0}{4\pi \cdot \sin^2(kh)}\left\{Si(2kh) + \cos(2kh)\left[Si(2kh) - \frac{1}{2}Si(4kh)\right] - \right.$$
$$\left. - \sin(2kh)\left[\ln\left(\frac{h}{b}\right) - Cin(2kh) + \frac{1}{2}Cin(4kh) + \frac{1}{2}Cin\left(\frac{kb^2}{h}\right)\right]\right\}, \tag{7}$$

where: $Cin = \int_0^x \frac{1-\cos(t)}{t}dt$ – modified cosine integral,

$Si = \int_0^x \frac{\sin(t)}{t}dt$ – sine integral,

$h$ and $b$ – length and thickness of the monopole; b → 0.

For an easier interpretation of (6) and (7), input resistance and reactance are plotted in Figure 3.4 for a case of a quarter-wave monopole for the frequency of 800 MHz. Obviously, the antenna is in resonance at around 800 MHz where its input reactance is 0 Ohm and resistance is near 40 Ohm. Out of the resonance, the quarter-wave monopole possesses high-ohmic impedance values, which give high reflection coefficients by including it into the 50-Ohm signal path (Figure 3.4-c). There are several resonances that appear at the frequencies of 800 MHz, 2.4 GHz, 4 GHz and so on, showing periodical character with the cycle length of $\lambda/2$. However, the required radiation properties (omnidirectional RP in horizontal plane; RP with single beam at elevation angle 90° – for vertical plane) of this aerial only appear at the first resonance, since its length here amounts to $\lambda/4$ (optimal height for the wave detach). At the high-order resonances, the radiator height is equal to $¼\cdot\lambda+n\cdot½\cdot\lambda$ for $n$ = 2, 3, … which is greater than the optimal height. An abundant height of the monopole at the high-order resonances leads to undesired top lobes in RP and reduction of antenna gain in horizontal direction (compare Figure 5.17).

The height of a quarter-wave monopole for the LTE lower frequency range is approximately 90 mm, which is much higher than a standard height for roof-top mounting, at most 55 mm. Therefore, the quarter-wave monopole aerial needs some shortening, which reduces the radiation resistance and consequently the antenna efficiency. There are several possibilities to increase the radiation resistance of the shorted radiator and thus improve its efficiency, making it easier to match to the signal path. There are inductive or capacitive loads at the feed point and capacitive top load [58]. In following, the most appropriate options will be considered and their radiation and impedance properties will be described.

## *Capacitively-Loaded Monopole*

The most adequate compensation for the short LTE antenna of the dual-band concept is applying a capacitive top load, which can be easily realized as a part of the monopole-like structure by designing it as a T- or an inverted L-monopole. Sketches of these aerials are depicted in Figure 3.5-a, b. Furthermore, both of these concepts of the compensation will be discussed, starting with the L-monopole (Figure 3.5-a).

### *Inverted L-monopole*

Radiation properties of inverted L-formed monopoles are shown very well in [59] and [60] (regarding driving-point impedance) as well as [61] (concerning radiation pattern) for different types of the current distribution on them. In this thesis, an almost quarter-wave (complete length including a top load) monopole with sinusoidal current distribution will be considered.

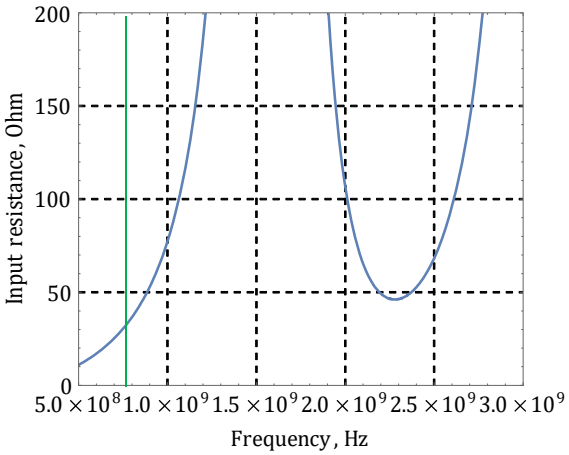


(a) Input resistance.

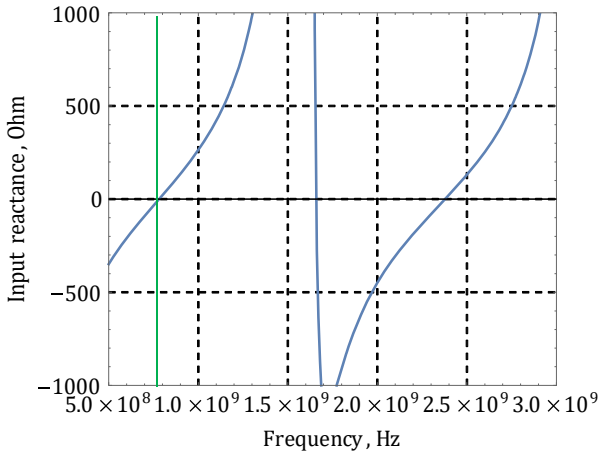


(b) Input reactance.

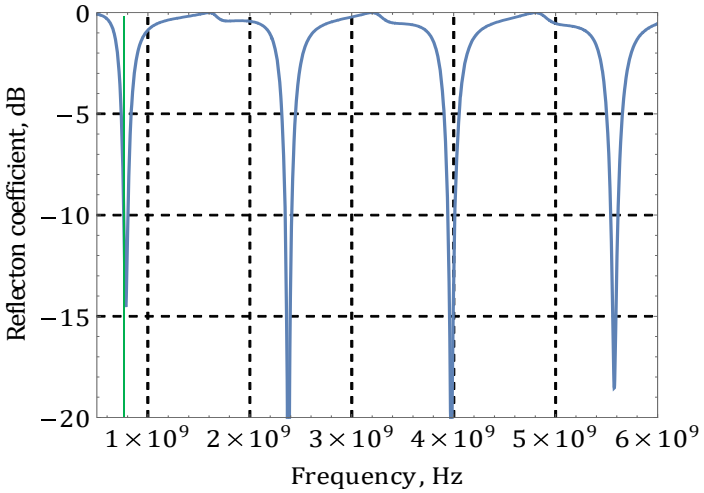


(a) Reflection coefficient ($Z_{ref}$ = 50 Ohm).

Figure 3.4: Input impedance of an ideal λ/4-monopole placed above infinite conducting plane (1st resonance frequency is marked in green).

In Figure 3.5-a, an additional part of length $\Delta l$ works as an elongation of the short monopole of height $h$, whereby a full $\lambda/4$-length is achieved for which the best radiation conditions at the required frequency are valid. Assume, there is a continuous alternative current flowing along both vertical and horizontal parts with the following distribution (8) considering for these parts form a single structure of length $l = h + \Delta l$.

$$\underline{I}_1(z) = \frac{I_0}{\sin(kl)}\sin(k(l-z)) \qquad for \qquad 0 \le z \le h; \qquad \text{- for vertical part;}$$

$$\underline{I}_2(y) = \frac{I_0}{\sin(kl)}\sin(k(\Delta l - y)) \qquad for \qquad 0 \le y \le \Delta l. \qquad \text{- for horizontal part.} \tag{8}$$

According to the superposition theorem, the total electric far field of the L-monopole is a summation of the E-fields produced by its vertical and horizontal parts. Any interaction between these fragments is ignored. Thus, after calculating the aerial's field by the same procedure as for the straight quarter-wave monopole (appendix A.2), an expression (9) for the E-field of the inverted L-monopole was obtained.

$$\underline{\hat{E}}_\theta(r,\theta,\varphi) = j \cdot \frac{I_0 Z_0}{\sin(kl)} \cdot \frac{e^{-jk\cdot r}}{r} \cdot \left[ \frac{e^{-j\cdot k\cdot h\cdot\cos(\theta)}}{\cos(\theta)} \cdot \left\{ j\cdot\sin(k\cdot\Delta l)\cdot\sin(\theta) + \right.\right.$$

$$\left.\left. + \cos(k\cdot\Delta l) - e^{\,j\cdot k\cdot\Delta l\cdot\sin(\theta)} \right\} \cdot \sin(\varphi) + \frac{1}{2\pi} \cdot \frac{\cos(k\cdot h\cdot\cos(\theta)) - \cos(k\cdot h)}{\sin(\theta)} \right] \cdot \hat{e}_\theta;$$

$$\underline{\hat{E}}_\varphi(r,\theta,\varphi) = j \cdot \frac{I_0 Z_0}{\sin(kl)} \cdot \frac{e^{-jk\cdot r}}{r} \cdot \frac{\cos(\varphi)}{\cos^2(\theta)} \cdot e^{-j\cdot k\cdot h\cdot\cos(\theta)} \cdot \tag{9}$$

$$\cdot \left\{ j\cdot\sin(k\cdot\Delta l)\cdot\sin(\theta) + \cos(k\cdot\Delta l) - e^{\,j\cdot k\cdot\Delta l\cdot\sin(\theta)} \right\} \cdot \hat{e}_\varphi;$$

Obviously, from equation (9), the electric far field of the L-shaped monopole comprises both horizontal, $\underline{\hat{E}}_\varphi$, and vertical, $\underline{\hat{E}}_\theta$, components, while the field of the straight monopole has only a vertical constituent. The level of the horizontally-polarized field depends on the length of the capacitive top load $\Delta l$ as well as its elevation above the conducting plane, i.e. the height of the vertical part, although these dimensions depend on each other if the complete length is fixed to one-quarter of the wave.

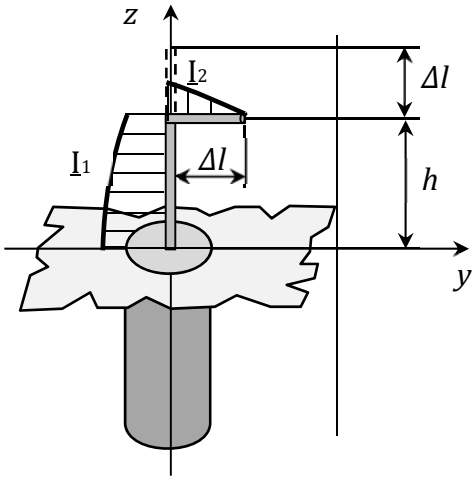


(a) Inverted L-monopole.

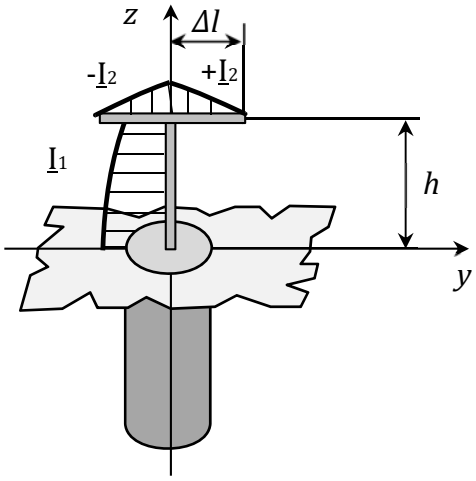


(b) Symmetrical T-monopole.

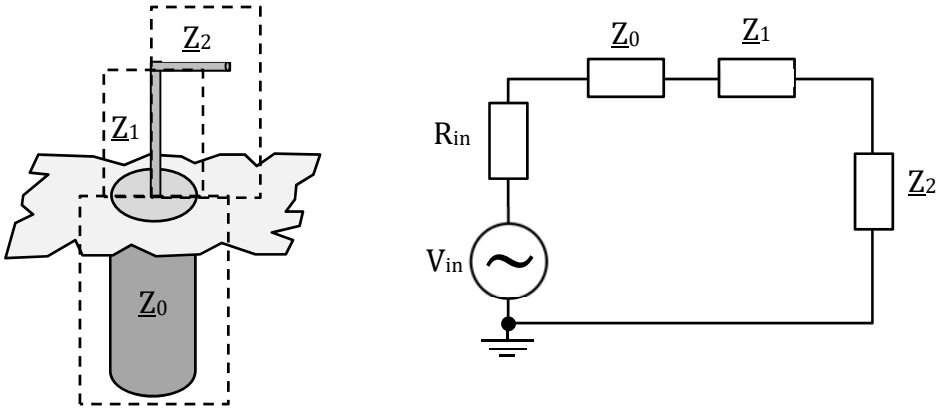


(c) Equivalent scheme of inverted L-monopole.

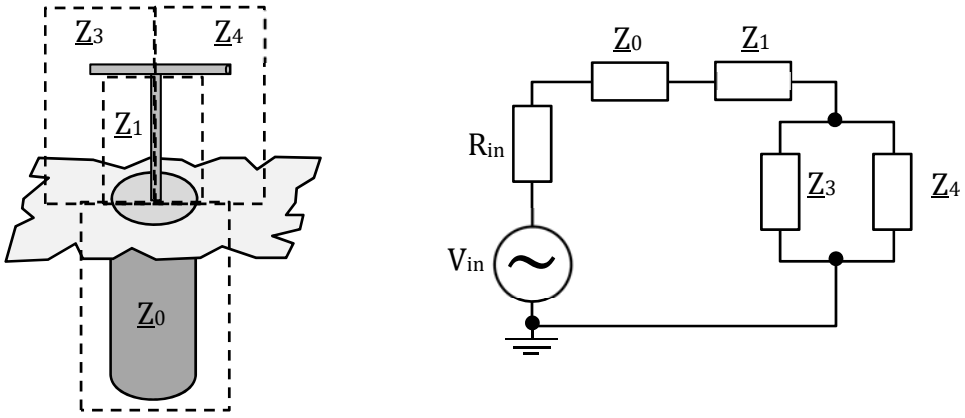


(d) Equivalent scheme of a common T-monopole (different length of the horizontal fragments).

Figure 3.5: Monopole with different capacitive top load. $V_{in}$ – voltage source with its resistance $R_{in}$.

The presence of the horizontal component of the electric field means a slightly strengthened transmission/reception at elevation angles near to the zenith (Figure 3.6-a), which is undesired in cellular communication due to the additional noise reception in zenith. It is as stronger as higher $\Delta l$ is, as Figure 3.6-b shows. Moreover, there is some asymmetry in RP, caused by the geometrical asymmetry of the inverted L-structure.

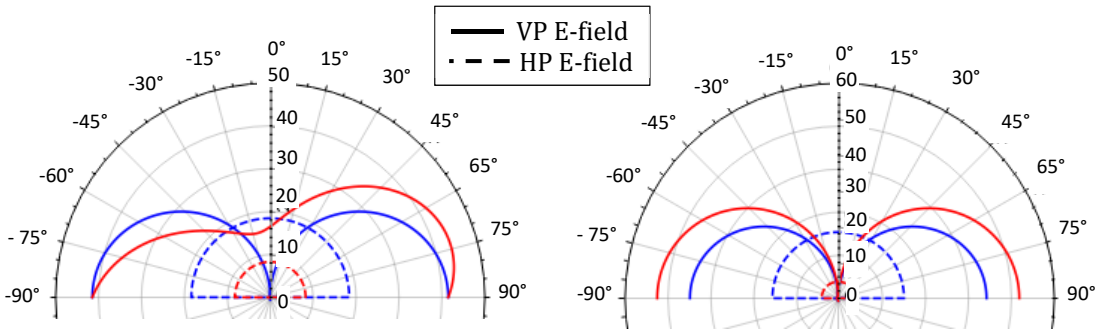


(a) Great circle cuts at phi = 0° (blue) and phi = 90° (red). Monopole dimensions: $\Delta l$ = 0.2·λ/4, $h$ = 0.8·λ/4.

(b) Great circle cuts at phi = 0° for L-monopoles with different dimensions. Red: $\Delta l$ =0.1·λ/4, $h$ = 0.9·λ/4, blue: $\Delta l$ =0.2·λ/4, $h$ = 0.8·λ/4.

Figure 3.6: Radiation pattern (magnitude of E-field) of the inverted L-monopole above infinite-ground plane.

A short monopole possesses very low input resistance (of around 1 Ohm for the length 0.1λ [53] ) while its input reactance is high. It produces high reflection coefficient by including the antenna into a 50-Ohm transmission line. A top load allows to improve input impedance of the short monopole for the better matching to 50-Ohm signal path (considering the resonance frequency) [55]. Its effect is explained roughly by an equivalent scheme of the L-monopole which is given in Figure 3.5-c. An impedance of the radiator can be calculated as a serial connection of the impedances of the vertical and horizontal parts. Since a common monopole antenna is excited by wave TEM, blocks $Z_1$ and $Z_2$ are LC serial resonant circuits (at 1st resonance) or LC ladder networks (at higher resonances [55]). Calculation of this equivalent circuit shows that a magnitude of reactance is several times lower (depends on the ratio $Z_1/Z_2$) than in case of a short monopole with only a vertical part.

Thus, an inverted L-monopole is a well-operating radiator with a relatively low height, which can be successfully used in the user equipment for mobile communication. However, its radiation properties can be further enhanced by adding a second horizontal part from the opposite side to partially compensate the horizontal

component of the electric far field. This construction – which is named as a T-monopole – will be discussed next.

***T-monopole***

One of the possible versions of a T-monopole is schematically shown in Figure 3.5-b. There is a radiator that is symmetrically loaded with two identical horizontal wires of length *Δl.* The length of the vertical wire is *h*.

As in the former case, there is a sinusoidal current on this monopole-like antenna, which is described by (10). Notably, the amplitude of the currents $\underline{I}_2(y)$ and $\underline{I}_2(-y)$ is the same due to the identity of the horizontal wires and their phases being 180° different owing to the wires' arrangement.

$$\underline{I}_1(z) = \frac{I_0}{\sin(kl)}\sin(k(l-z)) \qquad for \qquad 0 \le z \le h;$$

$$\underline{I}_2(y) = \frac{1}{2}\cdot\frac{I_0}{\sin(kl)}\sin(k(\Delta l - y)) \qquad for \qquad 0 \le y \le \Delta l; \tag{10}$$

$$\underline{I}_2(-y) = \frac{1}{2}\cdot\frac{I_0}{\sin(kl)}\sin(k(\Delta l + y)) \qquad for \qquad -\Delta l \le y \le 0$$

This current distribution causes the electric far field given by (11). This expression is obtained by performing the same calculation procedure as in the previous two cases (for the straight and inverted L-monopoles).

$$\underline{\hat{E}}_\theta(r,\theta,\varphi) = j\cdot\frac{I_0 Z_0}{2\pi\sin(kl)}\cdot\frac{e^{-jk\cdot r}}{r}\cdot\left[\frac{\sin(\varphi)}{\cos(\theta)}\cdot\{\cos(k\cdot\Delta l) -\right.$$

$$\left. -\cos(k\cdot\Delta l\cdot\sin(\theta))\}\cdot e^{-j\cdot k\cdot h\cdot\cos(\theta)} + \frac{\cos(k\cdot h\cdot\cos(\theta)) - \cos(k\cdot h)}{\sin(\theta)}\right]\cdot\hat{e}_\theta; \tag{11}$$

$$\underline{\hat{E}}_\varphi(r,\theta,\varphi) = j\cdot\frac{I_0 Z_0}{2\pi\sin(kl)}\cdot\frac{e^{-jk\cdot r}}{r}\cdot\frac{\cos(\varphi)}{\cos^2(\theta)}\cdot e^{-j\cdot k\cdot h\cdot\cos(\theta)}\cdot$$

$$\cdot\{\cos(k\cdot\Delta l) - \cos(k\cdot\Delta l\cdot\sin(\theta)\}\cdot\hat{e}_\varphi;$$

The total electric far field of the T-monopole is graphically shown in Figure 3.7. Obviously, in comparison with the inverted L-monopole of the same dimensions, top radiation is much weaker whereas the radiation at the required angles close to the horizon is much stronger. It is a main and desired effect of the second horizontal fragment. Furthermore, RP is symmetrical due to partial compensation of the fields radiated by the horizontal fragments one by another.

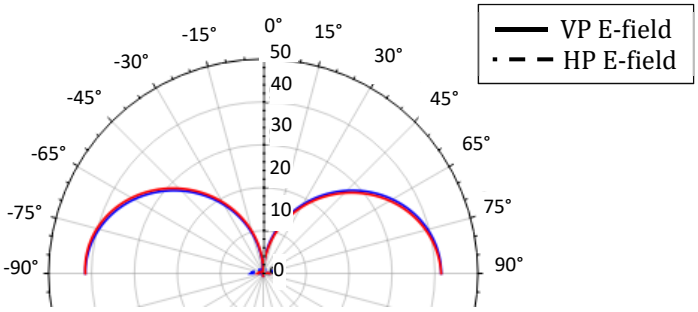


Figure 3.7: Great circle cuts at phi = 0° (blue) and phi = 90° (red) of radiation pattern (magnitude of E-field) of the T-monopole above infinite conducting plane. Monopole's dimensions: $\Delta l = 0.2 \cdot \lambda/4$, $h = 0.8 \cdot \lambda/4$.

The horizontal T-parts allow increasing the input resistance and reducing the reactance of the radiator, like one horizontal part of the L-monopole. Since their effect is stronger than that of the last, the horizontal parts of the T-monopole can be shorter and consequently the whole structure can be compacter than the inverted L-monopole, considering that their input impedances are the same.

It can be roughly explained by calculating the equivalent schemes of these two types of monopole antenna, which are shown in Figure 3.5-c and d. Two horizontal fragments of the T-monopole build a parallel circuit $\underline{Z_3}\underline{Z_4}$ of two LC ladder networks, which is subsequently included in series with the LC ladder circuit $Z_1$. If $Z_3$, $Z_2$ and $Z_4$ are chosen the same, the resonance frequency (condition: Im{Z} = 0) of the equivalent scheme (d) would be by nearly 150 MHz lower than that of the circuit (c). The resonance frequency can be easily tuned by reducing the values of L and C and varying the ratio $\underline{Z_3}/\underline{Z_4}$. Thus, two parts of the T-shaped monopole give a large degree of freedom to tune the radiator for the required frequency and the demanded impedance.

Further diagrams of the input impedance of the inverted L-, T-monopole and a monopole with X-formed top load can be found in [59, 62].

In the following, the radiation and impedance properties of a conical antenna –

which is the second part of the 3D dual-band aerial – will be considered and their mathematical expressions as well as graphical representations will be shown.

### 3.2.2 Conical Antenna

A conical antenna is a modification of a monopole radiator, where the conductor thickness linearly increases with the distance from the excitation point [54] (Figure 3.8). A conical antenna – as well as a biconical aerial – is a wide-band antenna. Its lower operational frequency is limited by the cone height $l$ and aperture angle $2\theta_1$. An upper frequency limit depends on the size of the feed region [54].

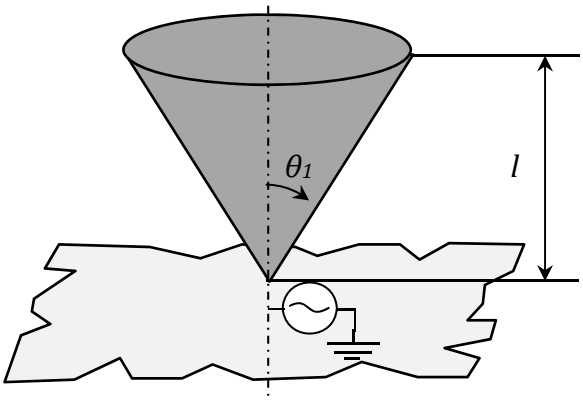


Figure 3.8: Conical antenna.

The radiation properties of the conical radiator – which is located above an infinite conducting plane – can be obtained from those of a symmetrical biconical antenna placed in free space by applying the image principle. The properties of the latter are derived in [56, 54]. Thus, the ***pattern factor*** for the conical antenna of infinite length that is positioned above an infinite conducting plane is written in [56] as (12). Obviously, the radiation pattern of the conical aerial has maxima in the direction $\theta = \pi/2$ and null in zenith [56], which is very similar to RP of the vertical quarter-wave monopole, expressed by (5).

$$C(\theta) = \frac{\sin(\theta_1)}{\sin(\theta)}, \tag{12}$$

where: $\theta_1$ – aperture semi-angle of the cone,
$\theta$ – elevation angle counted from zenith, $\theta_1 \le \theta \le \pi - \theta_1$.

The cut of the cone to some finite length gives a discontinuity, which leads to reflections from the aperture and an excitation of high-order waves of $E_{0n}$- type for n = 1, 2, 3, … . The solutions of the radiated fields as well as for input impedance for the finite biconical antenna can be found in [56]. For a particular case of a good matching between the cone aperture and the free space, an equation for the input impedance of the finite cone radiator can be written as follows in (13) by taking into account that an input impedance of a common monopole-like antenna placed above conducting plane is a half of that of a dipole-like radiator of the double length, which is located in free space [54].

$$Z_{inp} = Z_L \frac{1}{2} \cdot \frac{1 + Z_L Y_A + (1 - Z_L Y_A) \cdot e^{-j2kl}}{1 + Z_L Y_A - (1 - Z_L Y_A) \cdot e^{-j2kl}}, \tag{13}$$

where: $$Y_A = -j \frac{Z_0}{\pi \cdot Z_L^2} \sum_{n=1}^{\infty} \frac{2n+1}{n(n+1)} \frac{\underline{\hat{H}}_n^{(2)}(kl)}{\frac{\partial \underline{\hat{H}}_n^{(2)}(kl)}{\partial (kl)}} \left[P_n(\cos\theta_1)^2\right],$$

n –natural numbers 1, 2, 3, …;

$Z_L$ – impedance of transmission line (signal path);

$\underline{\hat{H}}_n^{(2)}(kl)$ – Riccati-Bessel functions or Riccati-Hankel functions of the second type [63, 64];

$P_n(\cos\theta_1)$ – Legendre polynomial [65].

Figure 3.9 shows an example of impedance properties for a conical antenna of a 0.3λ height (at 1.4 GHz) with an aperture semi-angle of 50°. These diagrams are calculated by equation (13). The aerial height is chosen to be 20% greater than a quarter of the lowest operational wave length, corresponding to [66]. Noticeably, the impedance of the antenna is periodical with a strong decline from the low to high resistance as well as the reactance. Starting from the lowest operational frequency (1.4 GHz), the extremities becomes smoother and closer to 50 Ohm for the resistive part and 0 Ohm for the reactive part. Therefore, the conical antenna is well matched to the 50-Ohm feeding line already from the demanded frequency 1.4 GHz (Figure 3.9-c). Waves of almost all frequencies below the lower limit do not propagate into the feeding line, since there is a strong mismatch between antenna impedance and wave impedance of the line. Noticeably, at frequencies between approximately 490 MHz and 550 MHz, as well as from around 900 MHz to 1100 MHz, the resistance of the

radiator reveals high-ohmic behaviour. It means almost total reflection of the wave, i.e. high isolation of the aerial at the mentioned frequencies, although this can be shifted by changing the geometry of the conical structure. This beneficial particularity can be successfully used in a combination of the cone with other narrow-band antennas for lower frequencies.

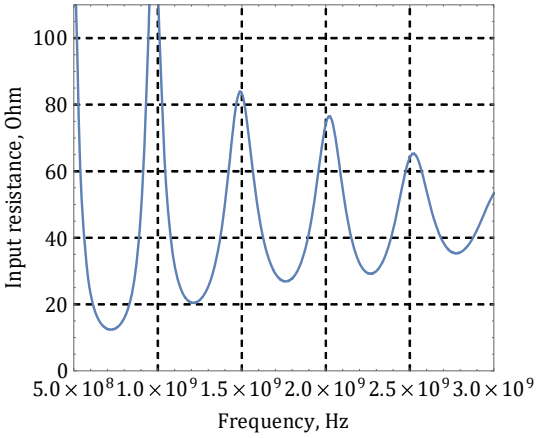


(a) Input resistance.

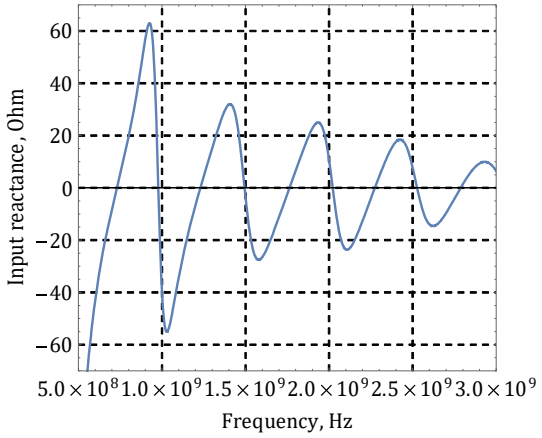


(b) Input reactance.

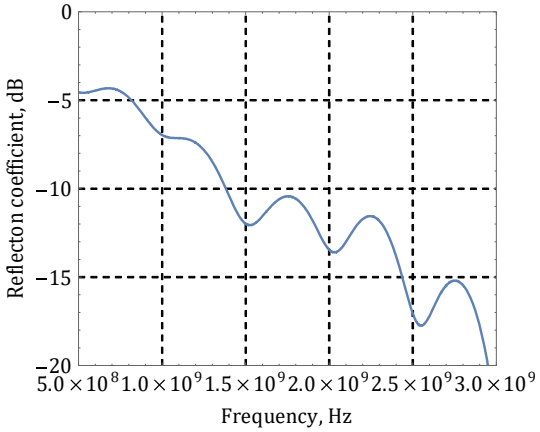


(c) Input reflection coefficient ($Z_{ref}$ = 50 Ohm).

Figure 3.9: Input impedance and reflection coefficient of an ideal conical monopole placed above infinite conducting plane ($\theta_1$ = 50°, $l$ = 0.3λ for 1.5 GHz).

There is no upper frequency limit for an ideal cone antenna with a sharp end. In practice, the upper operational frequency is limited by the geometrical dimensions of the driving point and the accuracy of the soldering.

The discussed impedance and radiation properties of the conical and monopole antennas allow combining these antenna types together at a single excitation point.

The combination principle will be considered in the next subsection, and some mathematical explanation will also be provided.

### 3.2.3 Combination of Conical Antenna with Monopole

The monopole and conical antennas are meant to operate within different frequency bands: the monopole – for the frequencies from 700 MHz to 960 MHz, the cone – starting from 1500 MHz (or 1420 MHz) to 2690 MHz. Out of their operational frequencies, both radiators are poorly-matched to the 50-Ohm signal path, i.e. "closed" for the service (see Figure 3.4 and Figure 3.9). In particular, the quarter-wave monopole for the LTE low band is high-ohmic at almost all frequencies of the LTE middle and high bands except for 2.4 GHz (its 2nd resonance). In turn, the conical antenna has a high-ohmic impedance at the lower frequencies. This fact enables combining both antenna types in one excitation point without their interference on each another. The construction can be equivalently represented by two antenna impedances included in parallel, as shown in Figure 3.10. Clearly, if $Z_{Line} = Z_{monopole}$ and

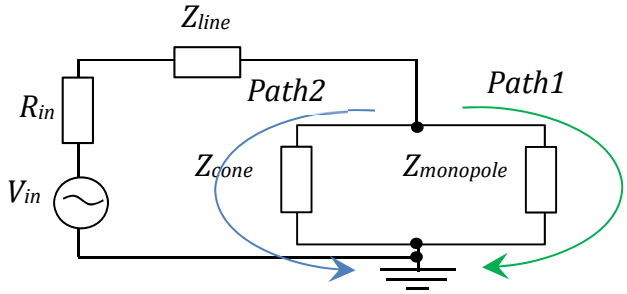


Figure 3.10: Equivalent circuit of the combination of λ/4-monopole with conical antenna.

$Z_{cone} >> Z_{monopole}$, the current flows through $Z_{monopole}$ (path 1 in Figure 3.10) and the other way round: if $Z_{Line} = Z_{cone}$ and $Z_{monopole} >> Z_{cone}$, the current flows through $Z_{cone}$ (path 2).

Moreover, the combination is also allowed by the antennas' geometry and current distribution on them. Therefore, a narrow monopole structure can be positioned inside the conical antenna with almost no influence on the latter's RP, since currents on the conical antenna flow at the outer surface and there are no currents flowing inside the cone, whereby consequently there are no fields propagating there (Figure 3.11). Although the antenna inside is slightly shielded by the cone, the main part of its radiated waves propagates between capacitive top load and the conducting ground plane, causing omnidirectional RP.

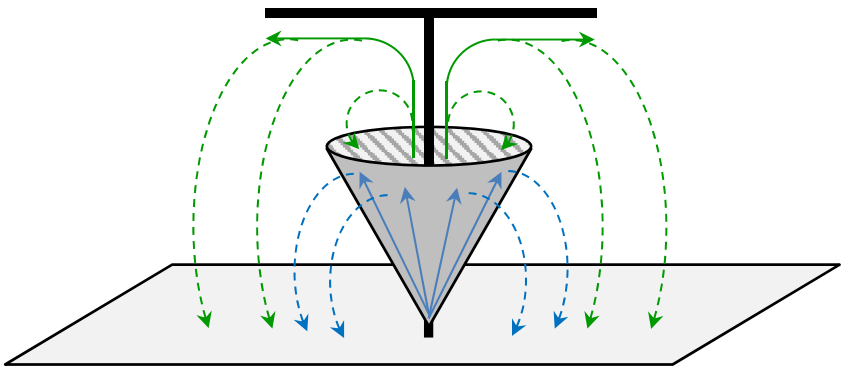

Figure 3.11: Combination of a conical antenna with a capacitively-loaded monopole in a common driving point. (— surface current, ---- electric field).

The validity and operability of the described 3-D dual-band concept for the LTE communication technology has been carefully evaluated and investigated for a multitude of variations and examples in different mounting scenarios and antenna combinations by simulation and measurement of functional demonstrators. Simulated and measured results as well as an antenna geometry will be discussed in the section below.

## 3.3 Dual-band 3D Antenna without Matching Network for LTE Communication Technology

A 3D LTE antenna is designed to be set underneath a standard shark-fin-formed housing. The maximum height of the chosen ESD protection cover is 55 mm in the rear side and it reduces towards the front side. The higher rear part of the cover is very narrow at the top, while the lower front part is relatively wide. A maximum space permitted by the cover for the antenna placement has the following dimensions: height 53 mm; width increases from 1 mm at the top up to 15 mm at the height of 30 mm, with further smooth increasing towards the bottom (Figure 3.12-a); and length is limited to 50 mm, which allows placing further radiators underneath the same cover, since a typical antenna module includes more than one aerial.

The 3D LTE antenna is designed in a way to use the maximum available space so that its overall dimensions coincide with the sizes of the mounting volume, which are shown in Figure 3.12-a. Thus, the antenna is 55 mm high, 15 mm wide and 50 mm long (Figure 3.12-c, d). The lowest part of the structure is 10 mm in width, which ensures good mechanical stability while keeping the performance up to 3 GHz.

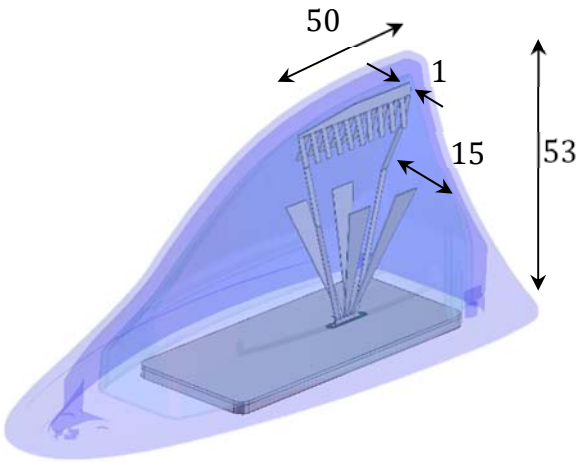


(a) Simulation model with dimensions of mounting volume.

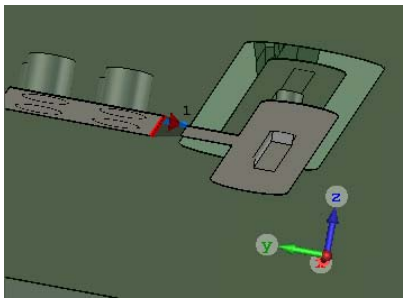


(b) Feeding network (bottom view).

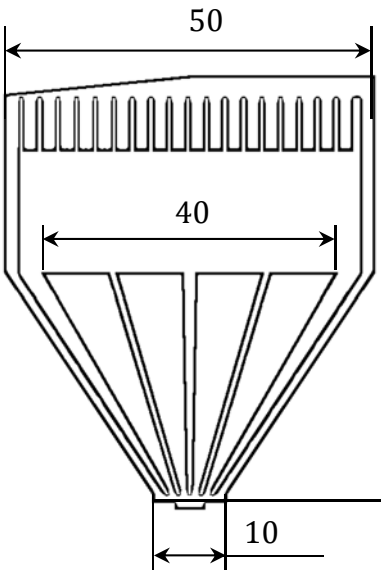


(c) Flat metal part for manufacturing, front view.

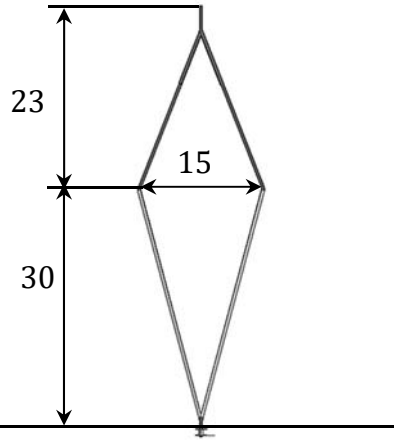


(d) Bent metal part, side view.

Figure 3.12: The LTE 3-D antenna 55 mm underneath design cover and ESD protection housing (all dimensions are in mm). Simulation model and sketch.

The monopole-like structure with the roof capacitor is realized in the form of two inductive wires that hold a ridged roof and press it towards the ESD protection cover. The ridge is made of the strips sloped in opposite directions. This part is dominant in the LTE lower band covering frequencies between 700 MHz and 960 MHz.

The conical antenna part is formed by four strips sloped in alternating ways, and it is supplemented with the lower parts of the inductive wires. The latter help to cover the frequencies down to 1447 MHz. Thus, such a small cone-shaped structure – which is only 30 mm high, 50 mm long and 15 mm wide – operates at frequencies from 1447 MHz to 2700 MHz.

The antenna is inserted into a circuit board through a rectangular slot, so that a small part is protruded from this slot at the bottom side, as shown in Figure 3.12-b. The bottom and top sides of the circuit board are provided with the metal pads around the antenna for soldering the aerial to the circuit board to achieve good stability. The bottom-side pad contains an additional line for the antenna feeding and a small ground pad, which is connected to the top metallization of the circuit board by four via holes. The small ground pad serves for modelling the feeding edge port (in the simulation) and for soldering an outer coating of a feeding coaxial cable to the ground (in case of the realization).

As will be further shown, the antenna fulfils the requirements to its impedance properties without the need for any matching network.

### 3.3.1 Simulation Results

The simulation model includes all relevant parts of the antenna's close environment, such as ESD protection and design covers, as well as a 3 mm-high metal frame maintaining the circuit board (Figure 3.12-a). The model also contains a circular ground plane with bent edges and 1.2 m in diameter, which corresponds to a setup for the measurements in an anechoic chamber (see appendix A.4).

Overall, the theoretical expectations are confirmed by the simulation results. The simulated radiation properties of the 3D LTE antenna at two example frequencies (850 MHz and 2.2 GHz) are shown in Figure 3.13 and Figure 3.14.

At the frequency of 850 MHz, surface current flows mainly along both inductive wires and the roof capacitance. Only a small part of the current distributes on the cone-shaped structure (Figure 3.13-a). Obviously, the conical part is not fully isolated from the monopole part. This is explained by the fact that the conical aerial has very low resistance at some frequencies below its operational band. Thus, in Figure 3.9, the impedance curve of the radiator periodically meets the points with the reactance of nearly 0 Ohm and with the low resistance (of around 20 Ohm and lower) at some

frequencies below the lowest operational frequency limit. Therefore, at these frequencies current flows through the cone, since its resistance is much lower than that of the monopole. An example of such a point is the frequency of 800 MHz for the theoretical calculations of the conical antenna (Figure 3.9) and 850 MHz for the simulation model of the combination (Figure 3.13-a).

The electric field caused by the described surface current is depicted in Figure 3.13-c. Evidently, the low-frequency part of the radiator dominates at 850 MHz, radiating a monopole-like pattern (Figure 3.13-b). The simulated radiation pattern (gain) at 850 MHz reveals an omnidirectional behaviour with negligible small deviations from the circular form. This is valid for all frequencies of LTE lower range.

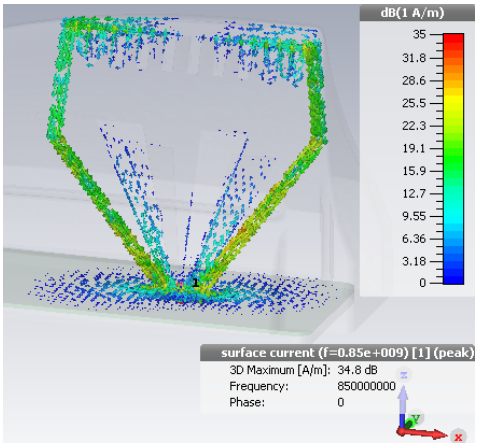


(a) Surface current (snap shot at ψ = 0°).

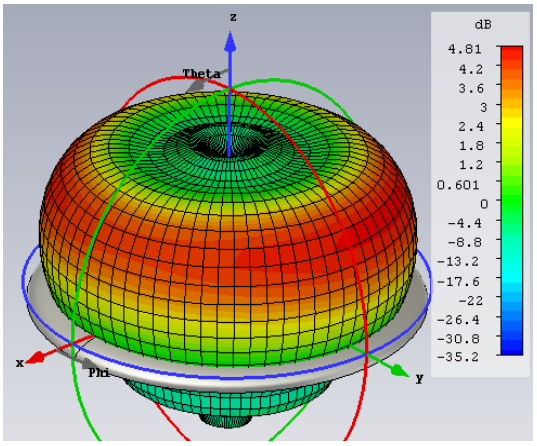


(b) Radiation pattern (VP gain).

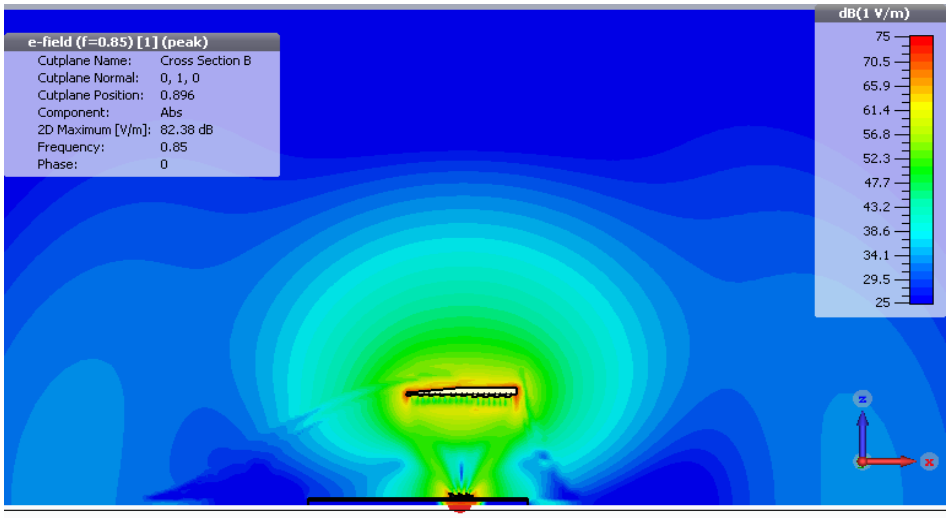


(c) Electric field (snap shot at ψ = 0°).

Figure 3.13: Simulated radiation characteristics of the LTE 3D antenna at 850 MHz.

The maximum antenna gain of 4.81 dBi appears in the direction of 60° elevation (at 850 MHz as well as at other frequencies of the LTE lower frequency range), which is caused by an influence of a ground plane with finite dimensions (see section 3.3.3).

At the example frequency of the LTE upper range – 2.2 GHz, the conical part of the 3D antenna dominates the structure (Figure 3.14). The surface current in Figure 3.14-a is mainly concentrated on the conical part and the lower parts of the inductive wires, causing the electric field shown in Figure 3.14-c. Noticeably, the surface current also distributes along the upper parts of the inductive wires, which is caused by the periodical behaviour of the impedance of the monopole-like part (its reactive

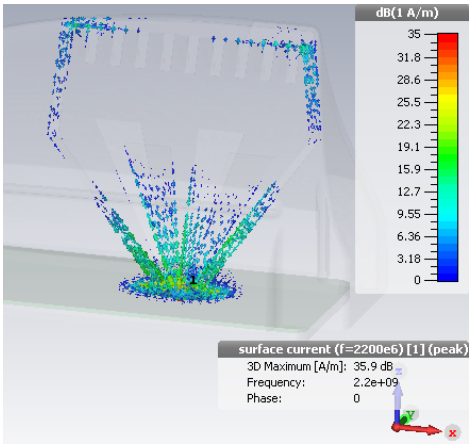


(a) Surface current (snap shot at ψ = 0°).

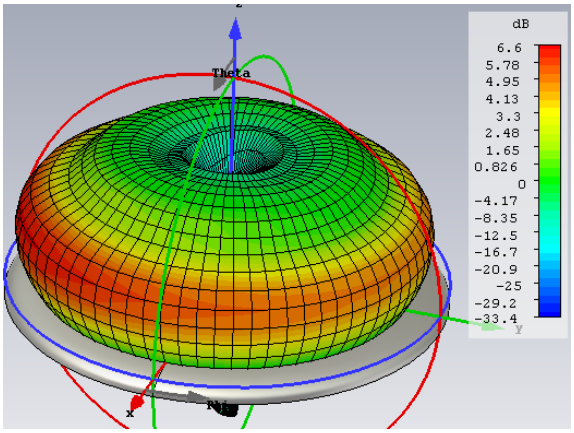


(b) Radiation pattern (VP gain).

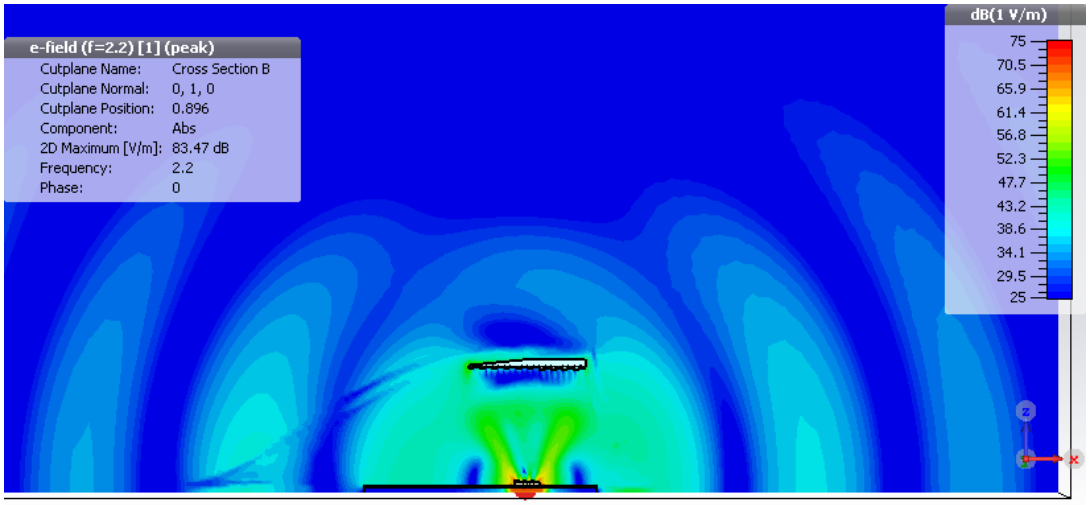


(c) Electric field (snap shot at ψ = 0°).

Figure 3.14: Simulated radiation characteristics of the LTE 3D antenna at 2.2 GHz.

part is 0 Ohm and the resistive one is near to 50 Ohm at the frequencies where the structure is $\lambda/4 + n\cdot\lambda/2$ for $n$ = 1, 2, 3, … in legth; see Figure 3.4). Therefore, it is very well matched to 50-Ohm line and thus some currents also distribute on this structure. The monopole-like part's involvement in the operation at the LTE upper frequencies leads to some deformation of the radiation pattern at these frequencies, which is seen in Figure 3.14-b.

In Figure 3.14-c and in Figure 3.13-c, some refraction of the electric field in the plastic covers can be observed. Noticeably, this effect the stronger the higher the frequency. Nevertheless, there is only a slight influence on antenna gain and efficiency since only a negligibly small part of the power is lost in the covers. There 0.2% and 0.42% of the stimulated power is lost due to the plastic housings at 850 MHz and 2.2 GHz, respectively, as the simulation shows.

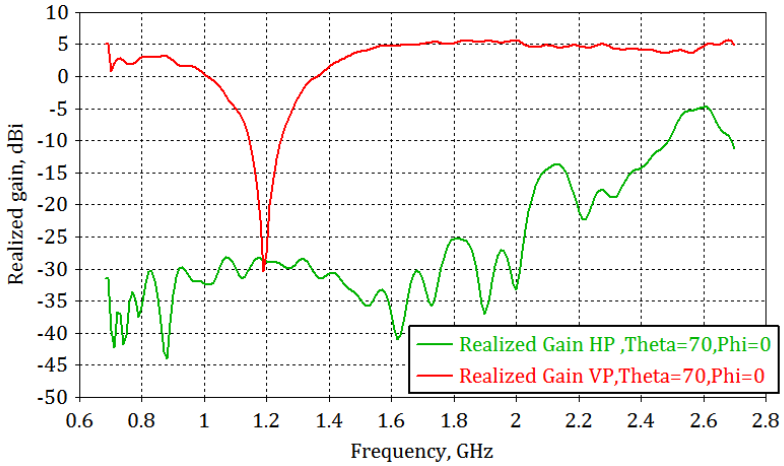


Figure 3.15: Simulated VP and HP realized gains at ($\theta$ = 70°, $\varphi$ = 0°) of the LTE 3-D antenna.

The high-frequency part of the antenna radiates an omnidirectional RP in the horizontal plane, with deviations from the circular form of around ±1 dBi. MBD turns towards the ground in comparison to that at 850 MHz and occurs at an elevation angle of $\theta$ = 70°. The maximum gain of the antenna at the frequency 2.2 GHz is 6.6 dBi.

Obviously, the 3D antenna obtains monopole-like radiation properties at both example frequencies. The same is valid at the frequencies where the cellular communication is currently available (Table 1).

The vertically-polarized (VP) realized gain in MBD amounts to approximately 3 dBi at frequencies between 700 MHz and 960 MHz and around 5 dBi at frequencies from 1427 MHz to 2700 MHz. Horizontally-polarized (HP) realized gain is below -

25 dBi within the LTE lower and middle frequency ranges and lower than -5 dBi at the LTE upper frequencies (Figure 3.15). The presence of the HP field in the LTE high range is caused by the horizontal currents that flow along the antenna's roof. Thus, for example at the frequency 2.6 GHz, the electrical length of the roof is nearly ½·λ. Therefore, it works as a pair of horizontal monopoles fed by the inductive wires which radiate the HP electric field.

Figure 3.15 shows that the 3D antenna is well suited for the reception/transmission of the VP waves due to its high VP gain. The antenna possesses high radiation efficiency of 99% at the required frequencies. Mismatch loss reduces this value to 85% (total efficiency) on average over the demanded LTE frequencies.

### 3.3.2 Measurement Results

A functional demonstrator of the small-size 3D LTE antenna – which does not need any matching network – was built in full compliance with its simulation model.

The photograph of the LTE 3D aerial is depicted in Figure 3.16. Although the antenna is shown only underneath an ESD protection housing, it was measured underneath both ESD protection and design covers. The latter is an opaque stable cover with thick plastic walls. It shields the antennas and electronics inside from mechanical damage and simultaneously contributes to an elegant look of an automobile.

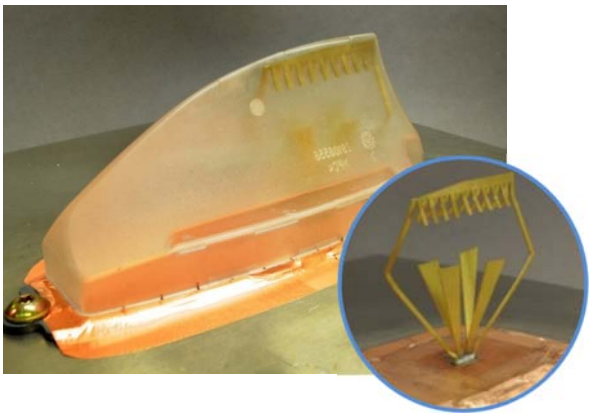

Figure 3.16: Functional demonstrator of the 3D LTE antenna of 55 mm height.

The measurements in the anechoic chamber and the impedance measurement were executed on circular conducting planes 80 cm and 1.2 m in diameter, respectively (for more details, see appendixes A.3 and A.4).

The measurement shows expected results that were predicted by the simulation. Both simulation and measurement results appear in a very good correlation, with only a slight discrepancy at the LTE upper frequencies (Figure 3.17-a), caused by different fixations of the radiator at the bottom side in the simulation environment and in the reality. In the simulation, the radiator is inserted directly into the circuit board and the electrical contact is modelled by overlapping the antenna structure with the metal feeding elements, whereas the realized sample is soldered to the metal pads, which are outcut in the circuit board, building a solder layer. The soldering spot has a noticeable influence especially at higher frequencies. Furthermore, the measured curve shows the presence of a greater parallel capacitance than in the simulation model. This difference is explained by some discrepancy between the simulated and actual properties of the substrate used (FR-4 material). According to the material specification, its dissipation factor and permittivity vary by ±10% from the nominal value [67] within the material, whereas in the simulation model they equal the typically-measured values ($e_r$ = 4.5, $tan\delta$ = 0.015 at 1 GHz) and change only over the frequency. This difference leads to the distinct values of a slot capacitance that appears in the slot between the antenna pad and the top metallization of the circuit board (Figure 3.12-b). Even though the simulated and measured curves slightly differ one from another, they both show sufficient impedance matching to the 50-Ohm signal path without applying any matching network (the impedance values at the demanded frequencies are concentrated within the red circle in Figure 3.17-a, which shows a limit of -6 dB).

Figure 3.17-b demonstrates the measured reflection coefficient over the frequency. At all LTE frequencies, it is lower than -6 dB, which is an acceptable value for a good operation in the LTE system. At frequencies from 1.6 GHz to 2.7 GHz, reflection coefficients are even below -10 dB.

The functional sample of the 3D antenna without matching network radiates/receives the vertically-polarized waves omnidirectionally in horizontal plane. Conical and great circle cuts of its measured radiation pattern (RP) at several frequencies are depicted in Figure 3.18. Noticeably, the main beam direction (MBD) of RP occurs at elevation angles between 60° and 75°, which is similar to the simulation results.

Figure 3.18-a, b shows sections of RP at 850 MHz. At this example frequency of the LTE lower band, the 3D LTE dual-band antenna achieves the maximum realized gain of 4.1 dBi. Its realized radiation efficiency amounts to -1.18 dB. The radiation pattern (VP realized gain) is omnidirectional without any deviation. The main beam direction at this frequency occurs at the elevation angle of 60°.

In the conical cuts of RP at 1.7 GHz (one of the frequencies of LTE middle range), slight deviations of ±0.5 dB from the circular form can be seen (Figure 3.18-c, d). The maximum realized gain occurs at an elevation of 70° and amounts to about 5.4 dBi. The realized radiation efficiency of the antenna at 1.7 GHz equals -0.56 dB.

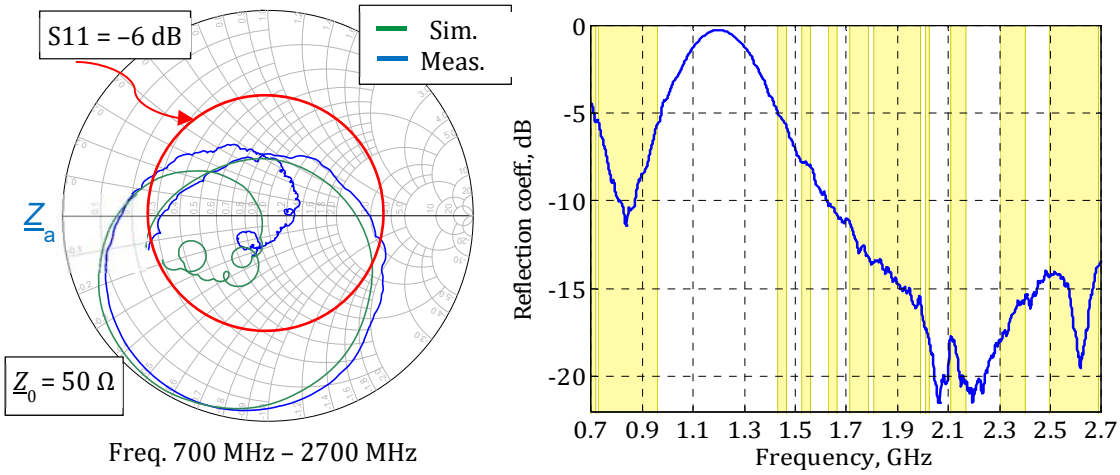


(a) Input impedance. (b) Reflection coefficient.

Figure 3.17: Input impedance and reflection coefficient of the 3-D antenna of 55mm height, which does not require a matching network. In yellow: LTE frequency bands.

At the LTE upper frequencies, the radiation pattern of the antenna is still close to the omnidirectional form. Deviations from a fully-round pattern are only approximately ±1 dBi (Figure 3.18-e, f). The antenna achieves maximum realized gain of 5.67 dBi, with realized radiation efficiency of -0.73 dB.

With increasing frequency, the influence of the finite conducting plane weakens. Therefore, the main beam of the radiation pattern at the LTE upper frequencies is observed at the elevation of around 72°.

The realized gain (linear average over azimuth) of the 3D LTE antenna is compared with that of four λ/4-monopoles in Figure 3.19. The monopoles are designed for different frequency bands corresponding to the required LTE ranges. This comparison shows that the antenna for the LTE service has approximately the same realized gain as that of these λ/4-monopoles, even though the antenna operates in a wider frequency band, covering all bands of four λ/4-monopoles. Thus, the 3D LTE antenna is equivalent to a set of quarter-wave monopoles, each for a certain frequency range.

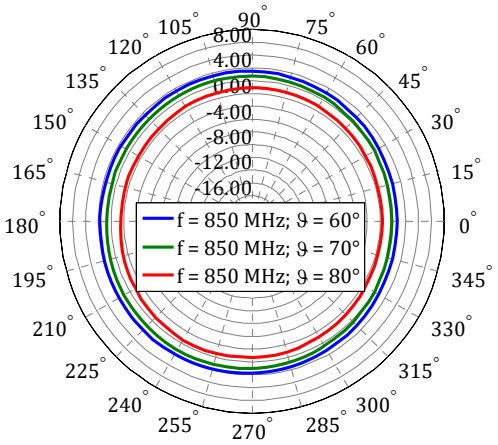


(a) Conical cuts, 850 MHz.

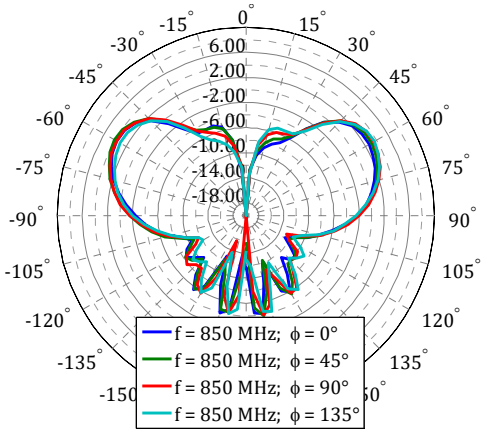


(b) Great circle cuts, 850 MHz.

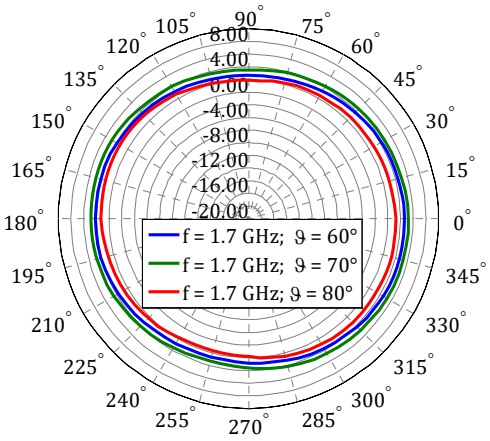


(c) Conical cuts, 1.7 GHz.

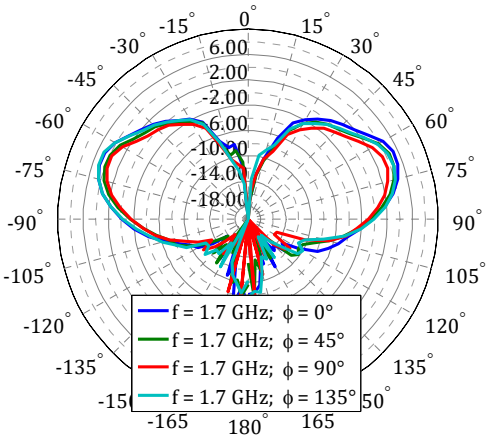


(d) Great circle cuts, 1.7 GHz.

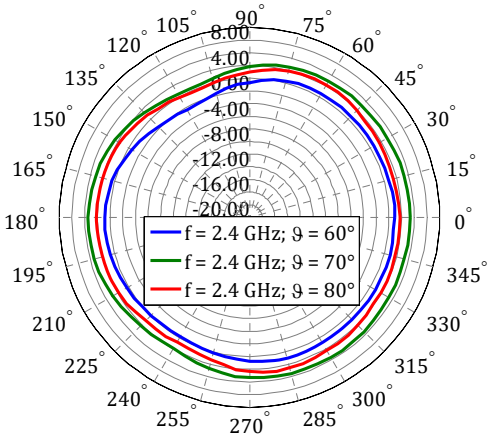


(e) Conical cuts, 2.4 GHz.

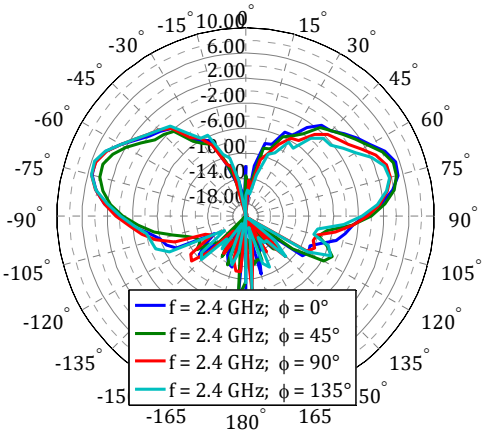


(f) Great circle cuts, 2.4 GHz.

Figure 3.18: Sections of RP (gain) of the LTE 3-D antenna without matching network.

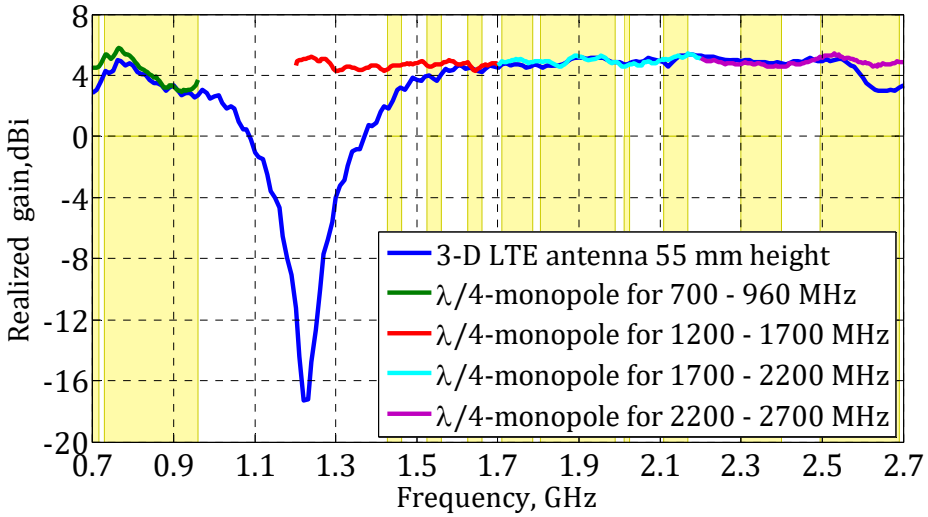


Figure 3.19: Linear average over azimuth realized gain of 3D LTE antenna 55mm height in comparison with that of λ/4 monopoles (yellow - LTE frequency bands).

Since there is no matching circuit has to be used and the structure comprises a pure metal panel, only low thermal losses occur in a signal path and in the antenna itself. In the lower frequency range between 698 MHz and 960 MHz, the realized radiation efficiency of the radiator is on average -1.3 dB and, in the LTE upper range from 1427 MHz to 2700 MHz it is about -0.7 dB. These values include mismatch loss of approximately 0.8 dB at the LTE lower frequencies and nearly 0.2 dB at the LTE upper frequencies and only 0.5 dB of thermal loss for both frequency ranges.

### 3.3.3 Influence of Ground Plane with Finite Dimensions on Radiation Pattern of 3D Antenna and Other Terrestrial Aerials

As far as the ground plane has finite dimensions, the MBD of any terrestrial antenna turns upwards. For frequencies from 698 MHz to 2700 MHz, MBD occurs at elevation angles between 60° and 75° (counted from zenith). For the lower frequencies of this frequency range, the influence of the finite plane is stronger, whereby MBD turns more to the upside than for the higher frequencies. This effect can be pointed out via simulation. The results are shown in Figure 3.20 together with the results of the measurements. This figure demonstrates great circle cuts of the radiation patterns (directivity for a vertically-polarized wave) of the 3D aerial for cellular communication – which is discussed in the current section – for three cases, each for the frequencies 850 MHz and 1700 MHz. Curves (b) and (c) present simulated

results and curve (a) that of the measurements. The third curve (a) shows the radiation pattern of the LTE 3D antenna being placed on an infinite perfectly conducting ground, while the second curve (b) shows the radiation pattern of the same radiator positioned on a finite conducting plane of 1.2 m in diameter. The first curve shows the radiation pattern of the same setup as for (b) in measurement, thus confirming the simulation result.

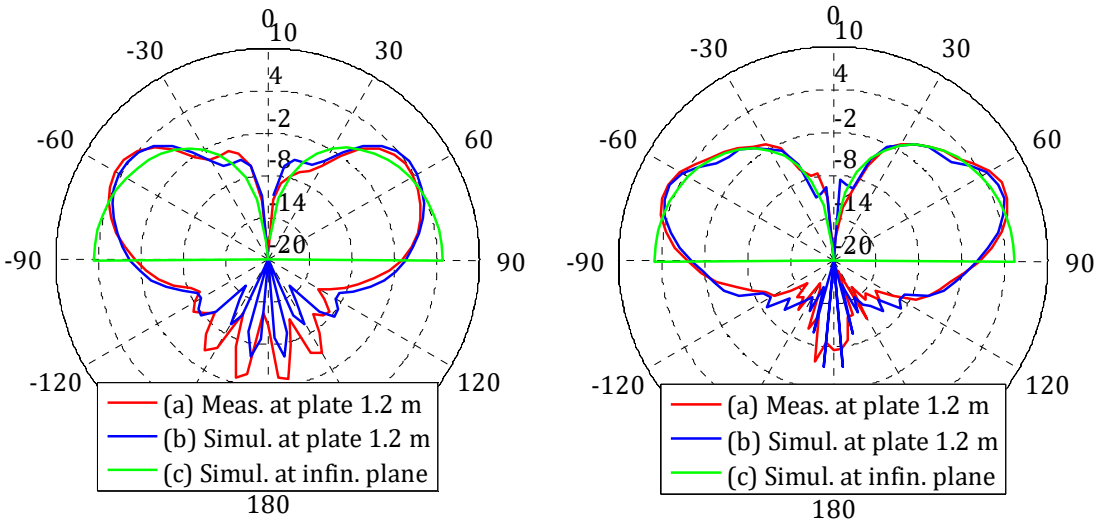


(a) 850 MHz. (b) 1700 MHz.

Figure 3.20: Great circle cuts of RP (directivity) at φ = 0° of the LTE 3D dual-band antenna.

Four λ/4-monopoles were considered to compare the radiation characteristics of the LTE 3D antenna with that of an ideal λ/4-monopole at the same conducting plane with respect to the gain of the VP electric field. The latter are designed for different frequency bands showing optimum achievable performance at all of the required frequencies. For these monopoles – which are mounted on the finite ground plane of 1.2 m in diameter – the MBD of their measured radiation pattern also depends on the frequency. These measurement results are presented in Figure 3.21. In the two examples at frequencies of 850 MHz and 1700 MHz, the λ/4-monopoles have different MBDs at elevation angles of 60° and 70°, respectively. The comparison of Figure 3.20 with Figure 3.21 shows that the 3-D radiator for the LTE service has approximately the same realized gain and a form of RP as those of the quarter-wave monopoles.

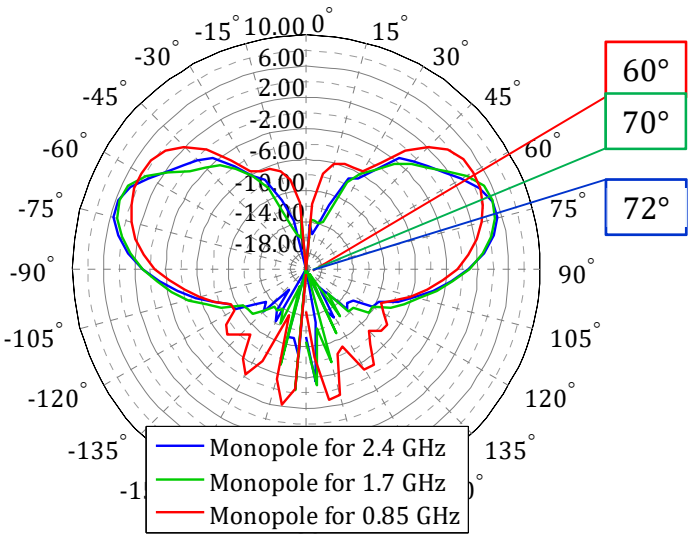


Figure 3.21: Great circle cuts of measured RPs (directivity) of the λ/4-monopoles (at φ = 0°).

The Earth's surface can be approximately described by an infinite conducting plane. Therefore, when the antenna is placed on the roof of a car, MBD of its radiation pattern will be in the horizontal plane as required. However, an additional ripple in the radiation pattern will occur due to the elevated mounting and the non-circular shape of the car's roof.

In what follows, an influence of a car's body on the performance of the 3D LTE antenna – which is placed on a roof of this common automobile – will be considered and simulation results will be discussed.

### 3.3.4 Performance on Car and Discussion of Results

Since the small-size dual-band 3D LTE antenna was designed for automotive applications, it is necessary to check its performance on a car's body. Verification of the antenna adaptability for the usage on cars was conducted by means of simulation. The following simplifications were introduced in the simulation model (Figure 3.22). First, only a metallic body of an automobile was taken into account as long as its influence on the radiation pattern is the most significant. Additionally, a panorama glass in the front of the roof was fully covered by the metal (PEC) since this simulation has as the goal of showing the antenna performance on a common car. The second step was to replace the antenna structure by its radiation properties in the near field, i.e. the antenna is substituted by a near-field radiation source (NFS)

on the certain frequency. These two steps allow reducing the simulation time significantly without loss in the simulation accuracy [68].

The near-field source was placed on the top of the car's roof at a distance of 30 cm from the rear edge and it was tilted by an angle of 3° following the form of the roof.

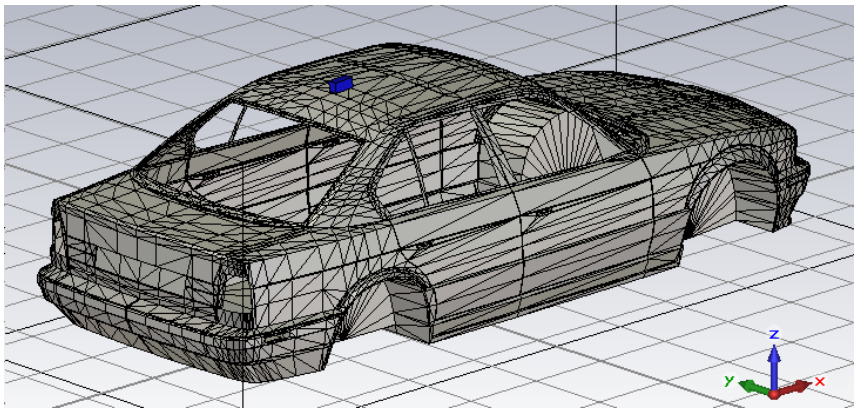


Figure 3.22: Model for antenna simulation on the car.

The simulation results for two example frequencies (850 MHz and 2.4 GHz) are given in Figure 3.23.

The form of PR of the 3D LTE antenna – which does not need a matching network – is noticeably distorted by the car's body, as clearly seen in Figure 3.23-b, d. Nevertheless, radiation patterns maintain their omnidirectional properties, although large ripples of approximately ±2 dBi appear, as is usual for a roof-top mounting.

In the driving direction, the radiator has around 4 dBi directivity between the azimuthal angles ±20°. At angles between 20° and 60°, a directivity reduction down to 0 dBi and even deep fails are observed. Directivities of the antenna in backward and side directions reach a maximum value of 5 dBi, while the lowest value is 0 dBi. At the frequency of 850 MHz, the average directivity (at elevation angle 90°) of the antenna on the car is about 2 dBi, which is 3 dBi lower than that of the same antenna positioned on the infinite conducting plane (Figure 3.23-a).

At 2.4 GHz, the RP of the antenna also shows the ripple and a reduced radiation in the driving and backward directions (Figure 3.23-c). In these directions, the antenna achieves directivity of 2 dBi on average over azimuthal angles (for $\theta$ = 90°), while in the side directions it is almost 5 dBi. Obviously, the body of the automobile has a strong influence on the radiation characteristics of the 3D aerial.

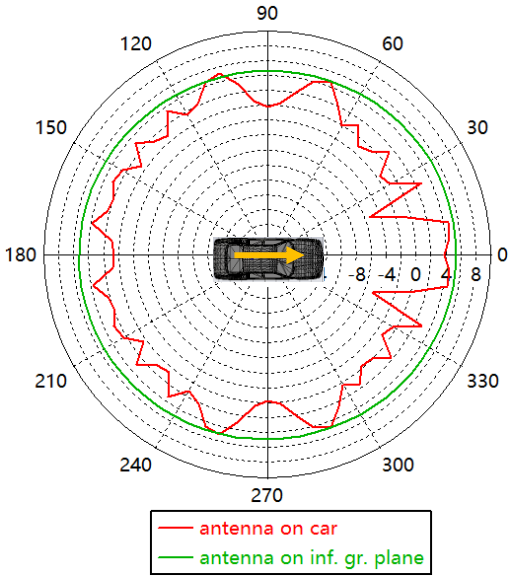


(a) Conical cuts at 850 MHz.

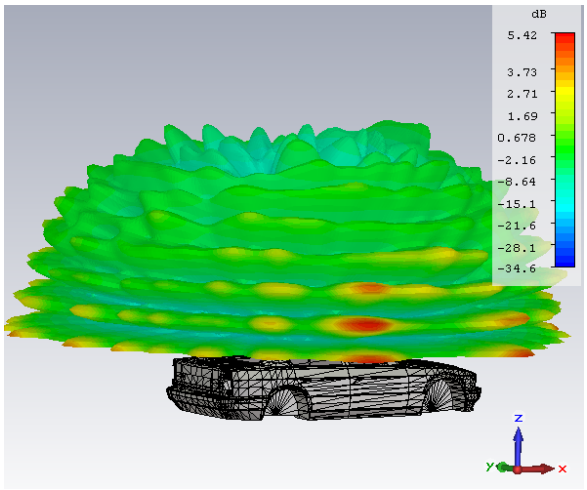


(b) 3D view at 850 MHz.

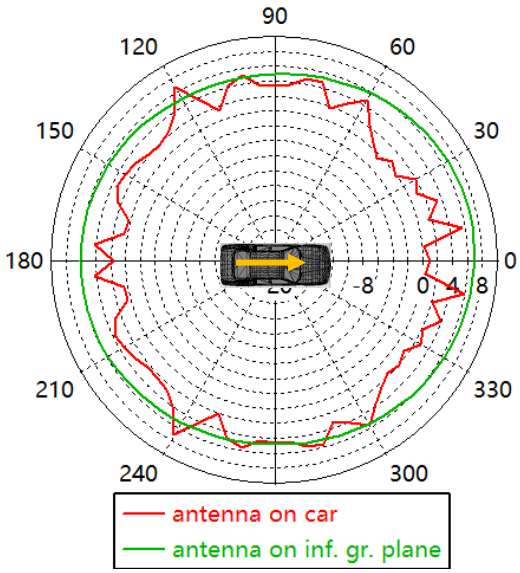


(c) Conical cuts at 2.4 GHz.

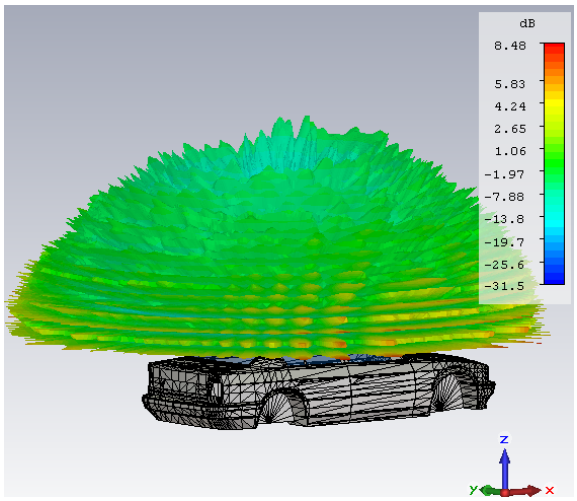


(d) 3D view at 2.4 GHz.

Figure 3.23: RP (directivity) of the 3-D LTE antenna without matching network on the car.

The ripples described and the directivity reduction are caused by reflections and diffractions on the car's body and within it. They are produced by projecting parts of the automobile; for example, by fixation parts of the panorama glass, which is slightly elevated above the roof's plane. The waves that propagate inside the car have significant value (Figure 3.24). A part of electromagnetic waves that are radiated by the LTE antenna penetrate through the windows inside the automobile where they reflect many times and finally propagate back into the free space through the windows. Outcoming waves from the inside of the car with the changed phase and amplitude superpose with the waves coming directly from the LTE aerial that have mostly destructive effect, as seen in Figure 3.23-a, b.

Overall, the antenna demonstrates reliable performance, so it is well suited for utilization in an LTE communication system on a car.

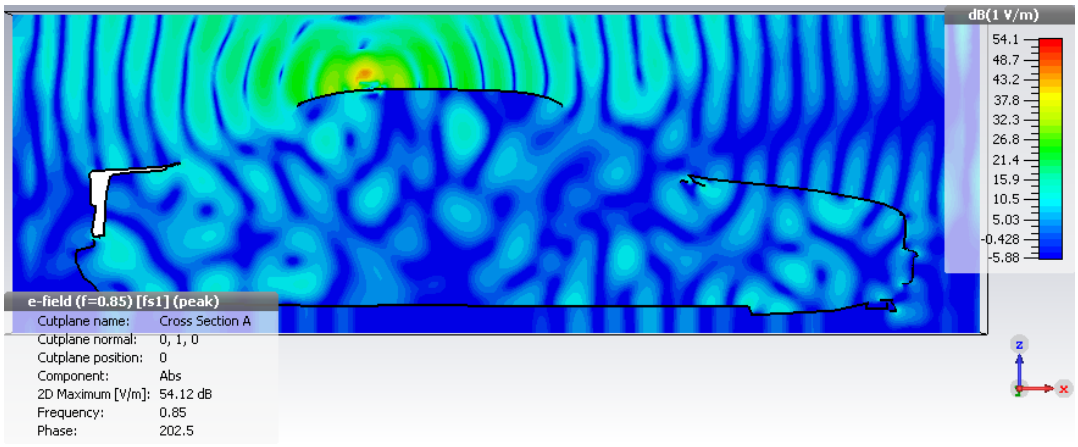


(a) Vertical cut in XZ–plane.

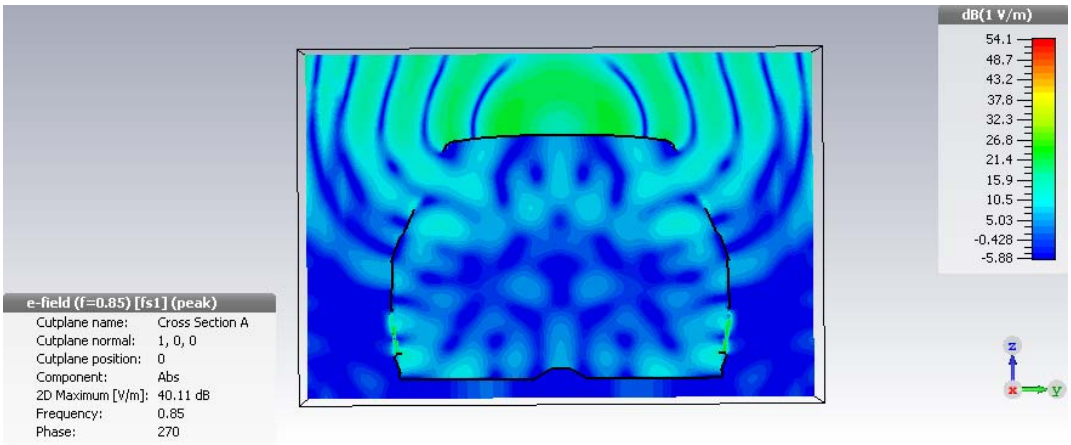


(b) Vertical cut in YZ-plane.

Figure 3.24: Electric field distribution on the car radiated by the 3-D LTE antenna.

## 3.4 MIMO Module of Two LTE 3D Antennas

The recent release of the LTE advanced technology (Release 13) operates with at least a 2x2 MIMO system, which provides high upload and download data rates. Achieving an improvement of these rates is the main goal of the development of new communication technologies and systems. Therefore, two 3D antennas for LTE cellular communication were combined underneath one shark-fin formed cover in a MIMO module. The module functions at the frequencies of LTE lower, middle and upper bands covering the ranges from 700 MHz to 920 MHz and from 1420 MHz to 2700 MHz.

As far as a typical standard shark-fin shaped housing and any other cover have a non-uniform height, which decreases towards the front of the cover, the antennas in the MIMO module are fitted to such different heights and shape corresponding to those of the chosen ESD protection and design covers. The rear part of the module contains a higher 3D radiator No 1 of 53 mm height. In the front part of the housing,

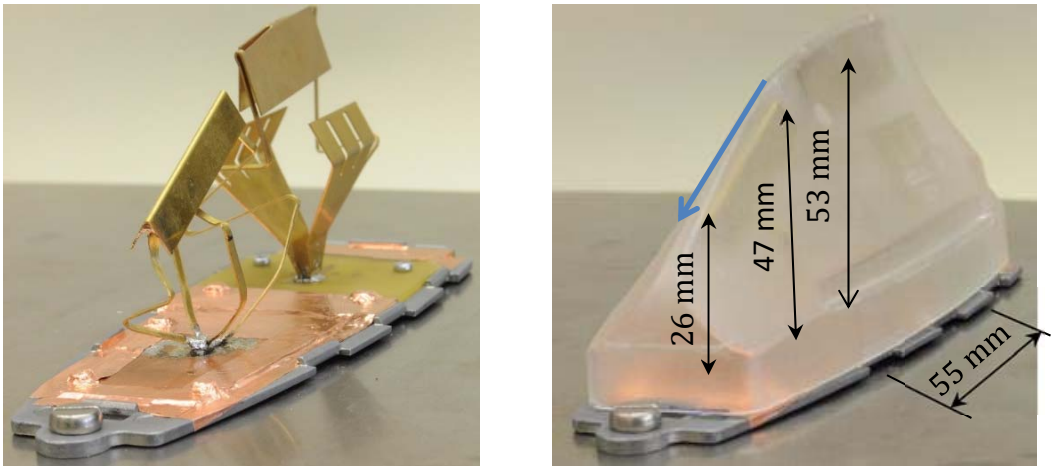


(a) 3-D antennas in the module (b) MIMO module underneath ESD- cover

Figure 3.25: Photograph of the functional MIMO module of two 3-D LTE antennas.

a smaller aerial No 2 with a height varying between 47 mm and 26 mm is placed (Figure 3.25). The antennas are separated by a distance of 55 mm between their excitation points.

Due to its sufficient volume, antenna No 1 does not require a matching network, while antenna No 2 needs an additional matching circuit because of its extremely small overall sizes.

The antennas are fed through two separate ports from the bottom side of the circuit board. The feeding of the front antenna is realized through a 50-Ohm semi-rigid cable, while the rear-side antenna is fed directly by a board-mounted 50-Ohm connector.

### 3.4.1 Simulation and Measurement Results

The MIMO module of two 3D LTE antennas was measured underneath both the ESD protection and design covers according to the measurement setup described in appendixes A.3 and A.4.

The rear-side antenna fulfils requirements for impedance matching without using any additional matching network at frequencies from 700 MHz to 913 MHz and from 1427 MHz to 2690 MHz (Figure 3.26). Therefore, the 3D radiator No 1 of the combination is applicable within all bands of LTE lower, middle and upper frequency ranges, except for the band No 8 (downlink, 925 MHz – 960 MHz), whereas in the stand-alone case its reflection coefficient is below -6 dB even in the band No 8 [69]. Obviously, this slight mismatch is caused by the presence of the second aerial of the MIMO module.

Since the front-side antenna No 2 has a low height (its height only amounts to 0.12λ at 800 MHz) along with the strictly-limited length and width, it requires a

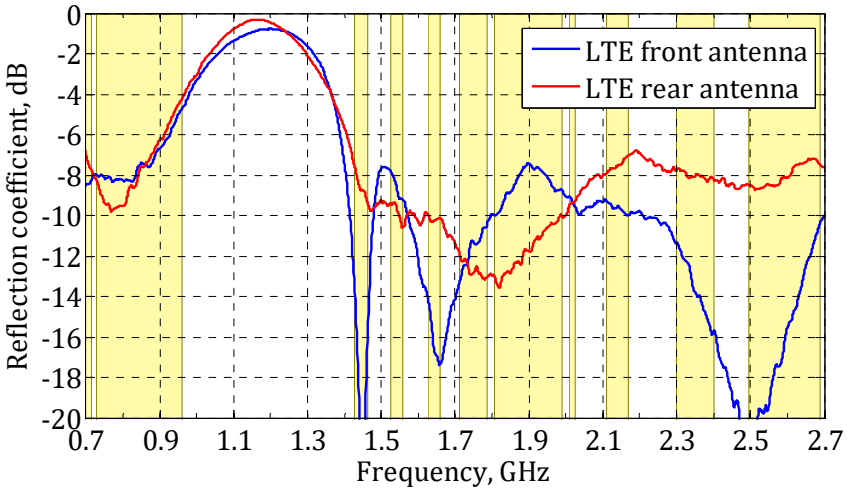


Figure 3.26: Reflection coefficients of LTE 3D antennas of MIMO module (yellow: LTE operational frequency bands).

matching circuit. Accordingly, the antenna reaches the required level of reflection coefficient at the same LTE frequencies as the rear-side antenna No 1 (Figure 3.26).

Due to the close arrangement, coefficients of the power transmission from one antenna to another are between -6 dB and -19 dB (Figure 3.27). At the frequency of 700 MHz, the transmission coefficient reaches the highest value of -6 dB as far as the separation between the antennas in terms of wavelengths ('effective' or electrical separation) is the smallest. With the increased frequency, the effective distance between the antennas increases. Within the LTE middle and upper frequency ranges, transmission coefficients are below -10 dB and -12 dB, respectively. The lowest transmission coefficient of -19 dB is observed at 2.69 GHz, where the effective separation between the MIMO antennas is the largest.

In order to qualify the port decoupling between the LTE antennas No 1 and No 2 in the MIMO module, power transmission from one antenna to another is compared in Figure 3.27 with that of two quarter-wave monopoles, which are separated by 60 mm. There, three monopole pairs were designed, each for a concrete frequency range. The comparison shows that values of transmission coefficients between 3D antennas are approximately the same as those between the quarter-wave monopoles in the reference pairs.

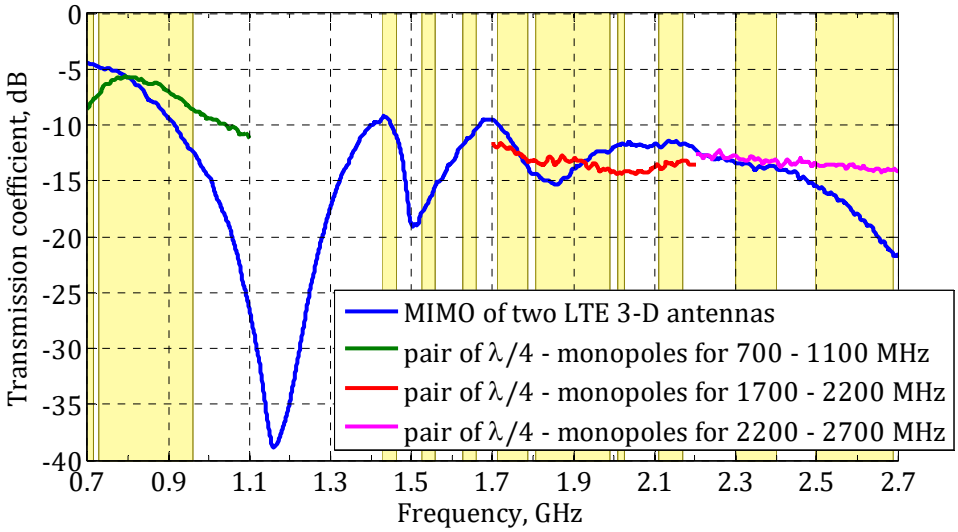


Figure 3.27: Transmission coefficients between 3D antennas in the LTE MIMO module.

The port isolation between antennas within a certain narrow frequency band can be improved by using – for example – a passive decoupling network or inserting parasitic elements, as proposed in [70] and [71]. However, these techniques only

help to improve the port isolation without any enhancement in the form of the radiation pattern.

Snapshots of a simulated electric field distribution of the 3D LTE antennas in the MIMO module at the example frequency of 2.4 GHz show that a portion of an electric field that is radiated by one antenna is received by another antenna of the module (Figure 3.28). Thus, both antennas are working as shielding elements in respect to one another, even if isolation between their ports is more than 14 dB (as it is at 2.4 GHz). Distortions in their radiation patterns – which are illustrated in Figure 3.29 – indicate the mutual coupling between the antennas.

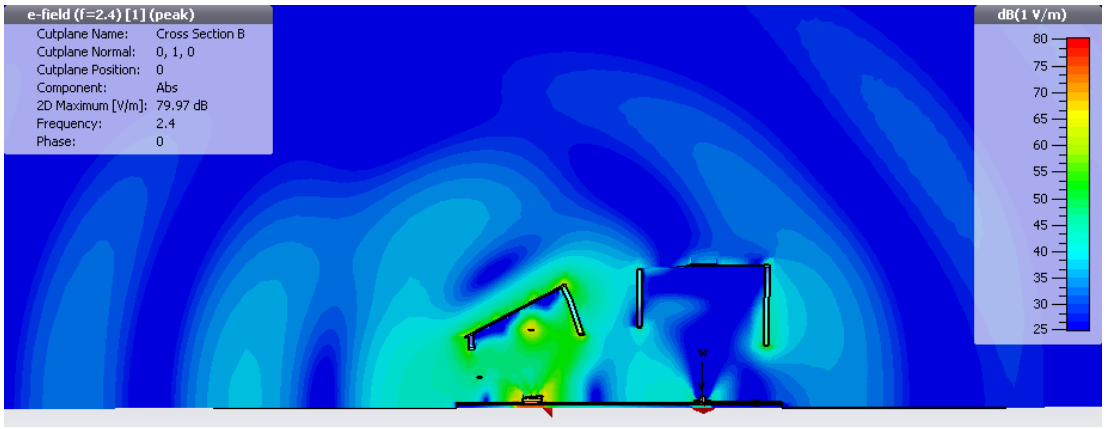


(a) Front-side antenna is fed.

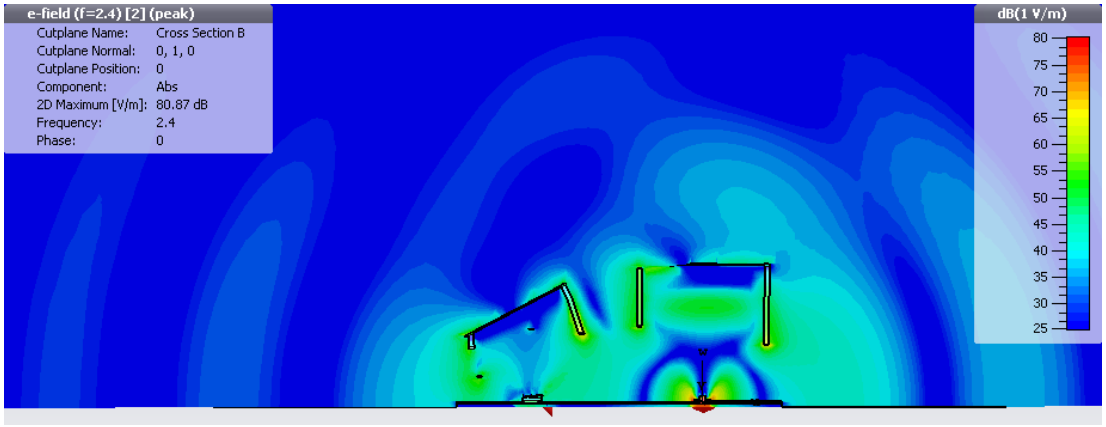


(b) Rear-side antenna is fed.

Figure 3.28: E-field distribution on LTE antennas of the MIMO module at 2.4 GHz.

The rear and front radiators possess an omnidirectional radiation pattern with a gain reduction at several azimuthal angles (Figure 3.29). Both antennas achieve

their maximum gain in the directions opposite to those where the neighbour antenna is positioned and minimum gain in the directions shielded by the neighbour aerial. Thus, the front-side antenna has maximum gain in the driving direction (green arrow in Figure 3.9), whereas that of the rear-side one is in the backward. Such behaviour is observed within the complete LTE frequency range. It is stronger at frequencies where the mutual coupling is higher and it weakens with its reduction

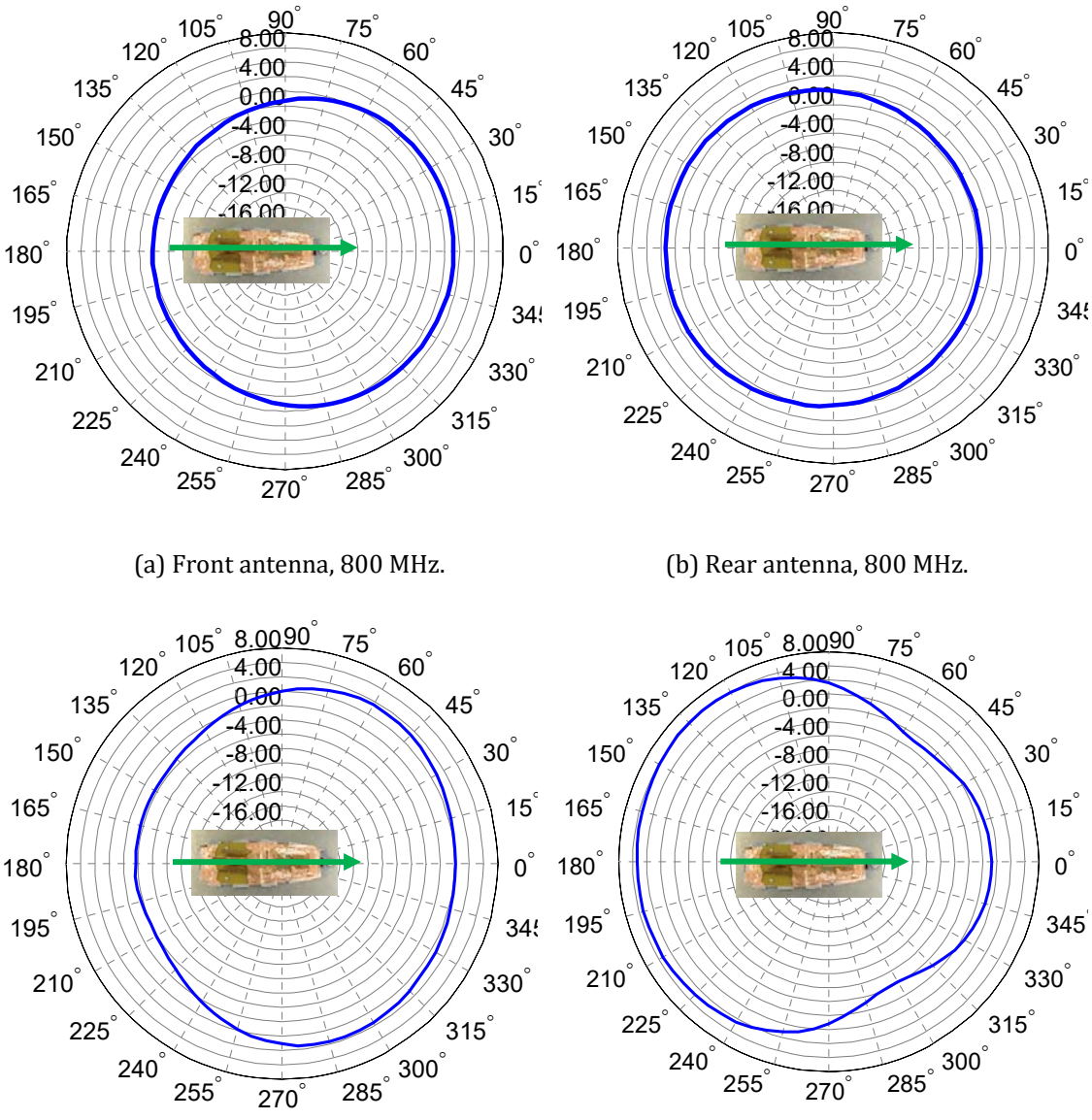


(a) Front antenna, 800 MHz.

(b) Rear antenna, 800 MHz.

(c) Front antenna, 2.4 GHz.

(d) Rear antenna, 2.4 GHz.

Figure 3.29: Conical cuts of RP (realized gain) of the LTE 3-D antennas in MIMO module.

At the frequency of 800 MHz (Figure 3.29-a, b), the front-side antenna has a maximum realized gain of 0 dBi in the driving direction, while in the opposite direction this value decreases down to -4 dBi. Such low values are caused not only by the neighbour aerial but also by the matching circuit, which has around 2.5 dB insertion loss in the LTE low band. The rear-side aerial achieves a maximum realized gain of 4 dBi in the backward direction and 0 dBi in the driving direction.

At 2.4 GHz, the maximum gain of the front-side antenna is around 4 dBi. The rear-side radiator provides nearly 6 dBi of maximum gain. This value is very similar to that of a stand-alone 3-D radiator of 53 mm height (see Figure 3.18). The minimum gain of the front-side antenna is around -4 dBi and the minimum gain of the higher rear-side aerial is approximately -1 dBi. This drop is caused exclusively by the presence of the second radiator.

Overall, the antennas are able to provide a good performance in the LTE network despite the deformation of their radiation patterns.

The 3D radiators of the module show low correlation, which fulfils one of the most important requirements of a common MIMO system. A far-field correlation coefficient is demonstrated in Figure 3.30. In this figure, the highest correlation appears in the LTE low band since the effective separation between the radiators (in terms of wave length) is very small. However, their values are below 0.2 (20%), which is fully acceptable. At the LTE upper and middle frequencies, the correlation coefficient is below 0.05 (5%), which indicates an excellent MIMO performance.

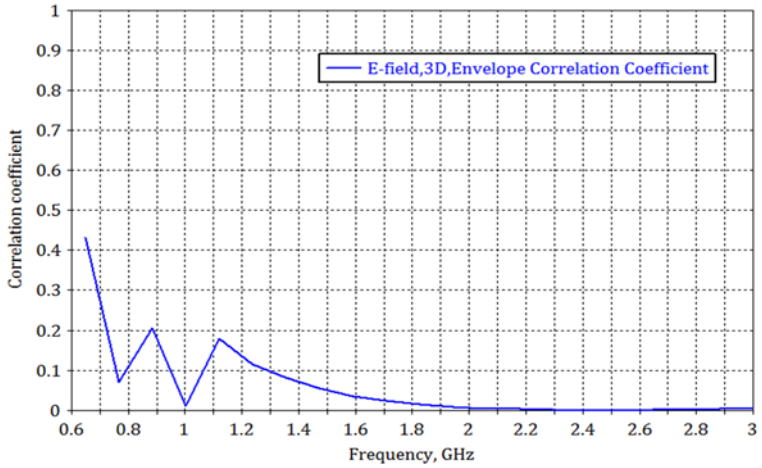


Figure 3.30: Far-field correlation coefficient between 3D antennas in the LTE MIMO module (simulation results).

The next subsection shows further MIMO properties of the discussed 3D LTE module that were developed by a drive test at the LTE-800 MHz network.

### 3.4.2 Drive Test Results

The MIMO module of 3D LTE antennas shown a very good performance in a driving test despite the deformation in their RPs. The test was executed in Munich (Germany) from Verdistraße to Petuelring at LTE Band-20 (800 MHz) 2012. The driving path is illustrated in Figure 3.31. The data rates were measured for both driving directions: forward, from Verdistraße to Petuelring; and backward, from Petuelring to Verdistraße.

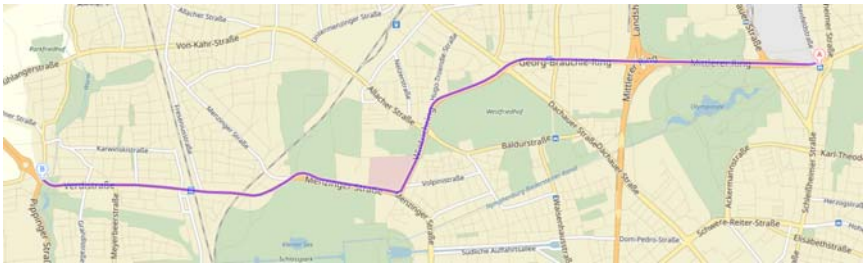

Figure 3.31: 9 km drive test path.

The results of the drive test are presented in Figure 3.32. Noticeably, the antenna module shows slightly different performance for two driving directions, which is caused by change of the channel matrix (variation of the traffic situation, network load and the weather conditions). In the forward and backward directions, the module delivers throughput mainly between 20 Mbit/s and 35 Mbit/s, although in the first case signal fails or mutes (occur in 5% of cases) appear much more often than in other case (< 2%). In both directions, the MIMO module delivers a mean throughput of around 23 Mbit/s together with a high level of mean signal-to-interference-and-noise ratio of 16 dB on average for both antennas. These values indicate a reliable connection to the LTE communication network with sufficient rates of data reception/transmission (state on 2012 – 2014) [72].

The LTE networks are continually under development and the peak up- and downlink data rates are steadily increasing. Therefore, the presented antenna module with MIMO can provide even higher data rates by testing it in the current cellular network.

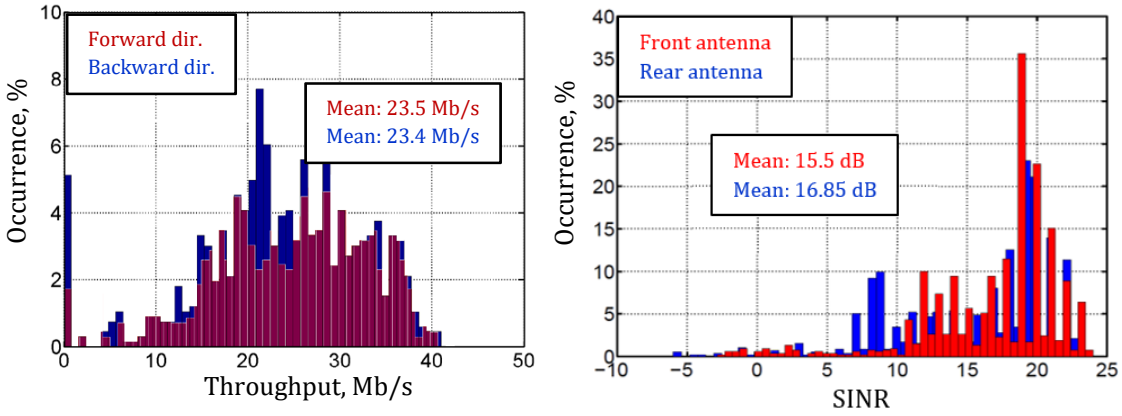


(a) Throughput.

(b) SINR.

Figure 3.32: Drive test results.

***Summary***

In this section, a dual- and wide-band antenna for cellular communication on an automobile has been discussed. The aerial shows a low reflection coefficient (below -6 dB) and high realized gain (around 4.5 dBi) at the frequencies of the LTE low, middle and upper ranges. Due to its panel design, the radiator possesses high radiation efficiency of better than -0.5 dB. The special 3-D design enables easy manufacturing by push-stamping, high reproducibility along with high stability of the construction.

By combining two 3D dual-band radiators in a module, a highly-performant MIMO antenna system for LTE cellular communication was obtained. The antennas appear to be in weak correlation with one another, which indicates a good MIMO performance of the module that was tested in a real scenario, showing sufficient reception data rates.

The theory of the dual-band antenna was also adduced in this section. There is a close correspondence between the calculated and measured far-field and impedance behaviour, thus revealing a correctness of the chosen approach.

The next section contains a description of well-operating antennas for further important services on a car, namely for satellite radio and navigation.

# Chapter 4

# Investigation of Interoperability of Scarabaeus Antennas for Satellite Signal Reception

Alongside cellular communication, there are further services that are very important for the current and future progress in the automotive industry, like satellite radio and navigation. Their system constellation and some points of evolution are briefly described in subsection 2.1.2. In particular, a global navigation system holds tremendous significance nowadays by enabling the fast and relatively safe attainment of the destination point and in the future by giving a possibility for the realization of autonomous driving.

However, there is considerable work done on antennas for satellite reception, the systems' constellation and consequently requirements for the aerials are periodically changing, which gives an impulse for research and new developments of the antennas for satellite signal reception (more information about current trends can be found in subsection 2.1.2). In this thesis, the focus is placed on further investigations and additional improvement of the aerials, which are made according to the already-researched concept of so-called scarabaeus antennas. Their theory was elaborated by the Institute of High-frequency Technology and Mobile Communication of University of the Bundewehr Munich, which has also demonstrated some functional samples in – for example – [47, 73] and [74].

In the current chapter, the discussion will start with an aerial for the reception of US satellite broadcasting. Herein, an antenna with an improved rejection of out-of-band signals will be researched and described, especially concerning vertically-polarized waves from the terrestrial interferers, like base stations of cellular communication or Wi-Fi access points. Furthermore, compact dual- and relatively wide-band antennas for global navigation will be considered. These antennas are meant for the reception of GPS-L1 & L2C, as well as the future interoperable signal L1C and those

from the Galileo, GLONASS and BeiDou-2 systems, which are currently under development. The combinations of these aerials for satellite radio and global navigation will close the investigations within this theme.

## 4.1 Antenna for Satellite Broadcasting with Improved Decoupling from Cellular LTE Communication

A ring antenna for the reception of satellite broadcasting signals – which is presented in [47] – has a relatively wide operational frequency bandwidth. The antenna yields reflection coefficients below -12 dB within a bandwidth of around 170 MHz and XPD of more than 10 dBic within a 70 MHz bandwidth. On the one hand, such a large bandwidth is an advantage for a compact circularly-polarized aerial. On the other hand, the antenna receives not only required waves but also terrestrial signals of other services. Especially in cities, cellular communication based on the LTE technology and WLAN services – which operate at the frequencies near to the SDARS band (Figure 4.1) – have an essential influence on its performance. They lead to the attenuation of a weak satellite signal by a strong terrestrial one that occurs at elevation angles between 30° and 90° (counted from zenith).

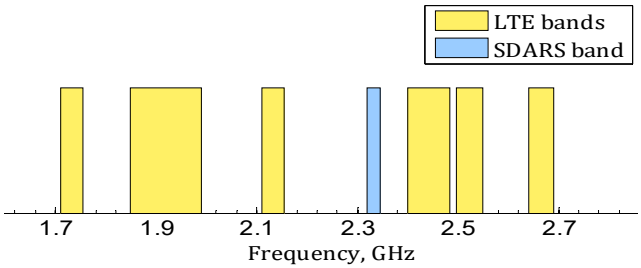


Figure 4.1: Operational frequencies of the SDARS and LTE service (middle and upper ranges) in North Atlantic Region.

This occasion reveals the necessity to modify the SDARS antenna structure to improve its isolation from strong signals of cellular LTE communication and from signals of WLAN services.

### 4.1.1 Principle of Isolation Improvement of SDARS Antenna from LTE Cellular Communication

The operational bandwidth of the ring antenna with the shortened physical length depends to a certain degree on its occupied volume, which is defined by the aerial's height and the perimeter of the top element. Moreover, it depends partially on a value of a shortening capacitance (i.e. on values of its reactance), which is required to get the aerial with the certain dimensions in resonance. The smaller the physical sizes of the aerial, the greater the capacitive reactance (magnitude) is required at each vertical leg and consequently the greater the shortening capacitors that are needed to adjust the aerial for a concrete operational frequency (compare Eq. 3.37 of [73]). It should also be noticed that for a higher frequency, a higher value of a magnitude of the capacitive reactance is required, while for a lower frequency a lower value is needed, providing that the overall dimensions of the antenna remain constant.

Since a reactance of a common capacitor of fixed value is a frequency-dependent function that monotonically increases, there is only a single frequency for which the best situation can be met (reactance of a capacitor coincides with the required one). However, there are a number of frequency points around this optimum for which the conditions are still acceptable ($X_{cap\_freq} \approx X_{res\_freq}$. Note: value of the capacitor is fixed). This range is determined by a gradient of the curve for the reactance of the shortening capacitors, as well as by a slope of the curves for the required values. Moreover, the capacitive coupling of the top ring to the top side of the parallel plate capacitors has a certain influence on the bandwidth of the ring aerials.

Therefore, through the reduction of the antenna height, the level of the received signals by the aerial outside the SDARS band can be suppressed. Thus, the filtering properties of the aerial itself are used.

Furthermore, a deterioration of an impedance matching helps to diminish the reception of VP signals out-of-SDARS-band. For this purpose, an antenna matching network has to be designed to obtain the highest possible reflection at the frequencies below and above the operational band of the satellite broadcasting by keeping the demanded reflection coefficient below -12 dB within the SDARS band.

### 4.1.2 Simulation Results

According to the described principle, a low-profile table-formed antenna of 8 mm height was designed and simulated. Its simulation results are compared in Figure 4.2 with those of a higher (10 mm high) antenna sample considering that both

antennas are identical in width and length. The antennas are simulated under the same conditions: both simulation models contain plastic sockets for supporting their metal parts, both antenna structures are placed on their circuit boards and are lifted up by metal frames. Each construction is located on an infinite conducting plane.

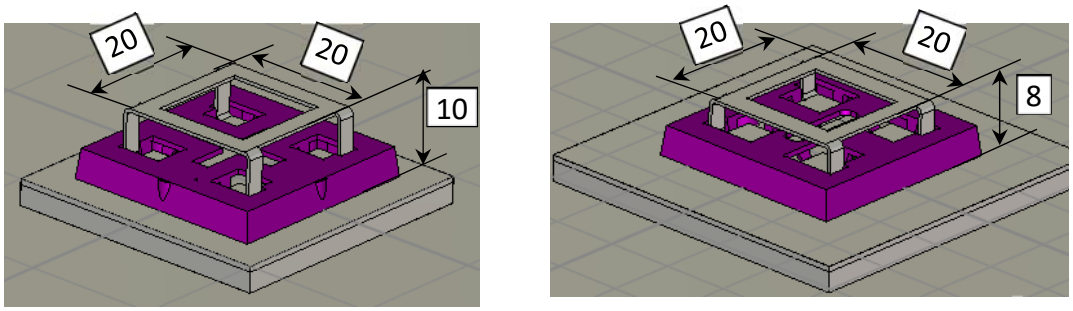


(a) Height 10 mm. (b) Height 8 mm.

Figure 4.2: Simulation models of SDARS antennas. Dimensions are given in mm.

By means of a matching technique proposed in [73], both antennas achieve sufficient matching within the SDARS frequency band (Figure 4.3-b). The antenna of 10 mm height is almost perfectly matched to the 50-Ohm line. Reflection coefficients are below -20 dB. By contrast, a matching network with an 8 mm-high antenna was designed so that the antenna does not obtain the lowest possible but rather accepta-

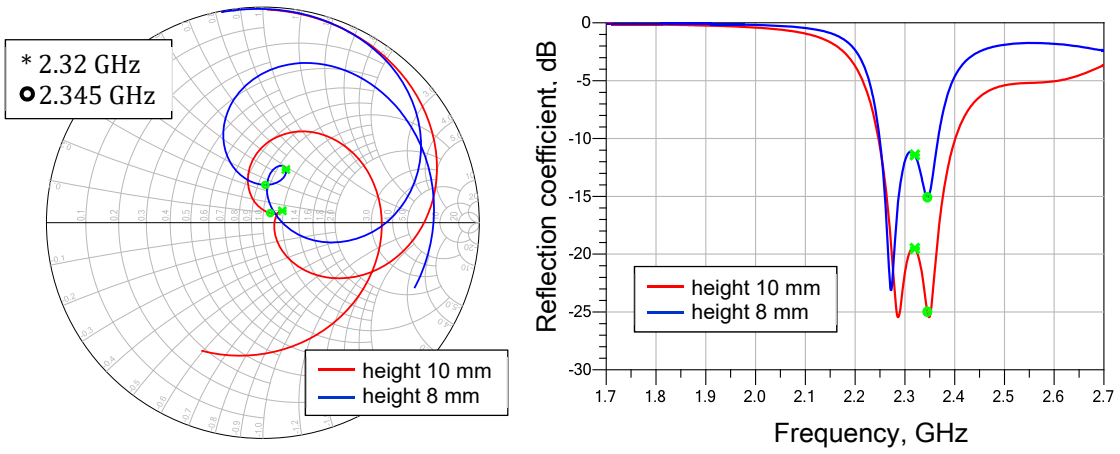


(a) Impedance curves. (b) Reflection coefficient curves.

Figure 4.3: Impedance characteristics of the loop antennas of different height (simulation results).

ble values of the reflection coefficient (below -12 dB) at the frequencies of the satellite broadcasting.

Since the 8 mm-high radiator has a low profile (and consequently large shortening capacitances), its radiation properties and input impedance as well are highly frequency-dependent. It can be seen in Figure 4.3-a where impedances of these two aerials are shown. The impedance curve of the 8 mm-high antenna draws a loop on the Smith chart with a larger radius than that of the radiator of 10 mm height. At the frequencies outside the SDARS band, the 10 mm-high aerial obtains reflection coefficients between -6 and -5 dB, while those of the lower antenna (8-mm-high) are rising from -5 dB at the frequency 2.4 GHz up to -2 dB at 2.6 GHz.

The vertically-polarized realized gains of both aerials for three example elevation angles (in average over azimuth) are depicted in Figure 4.5. Obviously, the 8 mm sample has around 2 dB less gain at frequencies above 2.4 GHz than the higher 10 mm sample. Within the SDARS band, another trend is observed: at the elevation angle of 30°, the VP realized gain of the lower aerial is approximately 0.5 dBi lower than that of the higher sample, at the angle 60°, these values are near the same, while at the angle of 90° the lower antenna achieves distinctly more gain than the higher one. These results coincide with those obtained by the equations for electric far field given in [73].

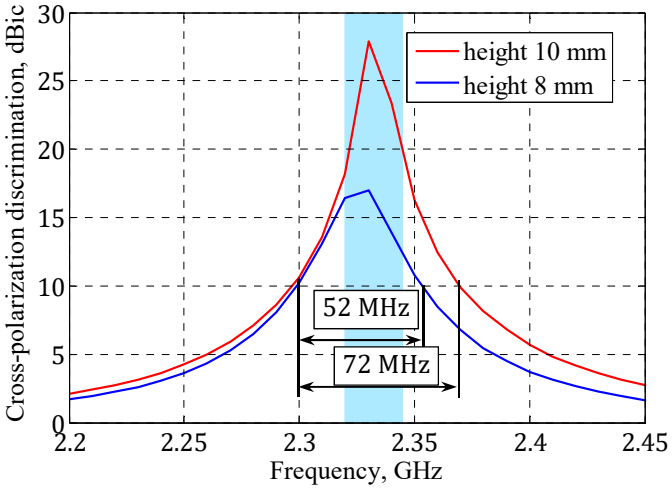


Figure 4.4: Cross-polarization discrimination of the antennas for the satellite broadcasting with different height.

Both effects are positive since the antennas for satellite broadcasting have to provide stable reception of the VP signals from the SDARS terrestrial repeaters, while also rejecting VP waves outside the SDARS band.

Along with these positive effects, an unwanted consequence is the reduction of the operational bandwidth of the low-profile table-formed antenna in terms of the sufficient level of XPD. As Figure 4.4 shows, the bandwidth of the antenna of 10 mm height is 70 MHz, while that of the 8 mm-high aerial is reduced to 56 MHz. However, even this reduced bandwidth is sufficiently wide to compensate for possible frequency shifts, which can be caused by external factors such as tolerances of the material's electrical properties, manufacturing inaccuracy and weather.

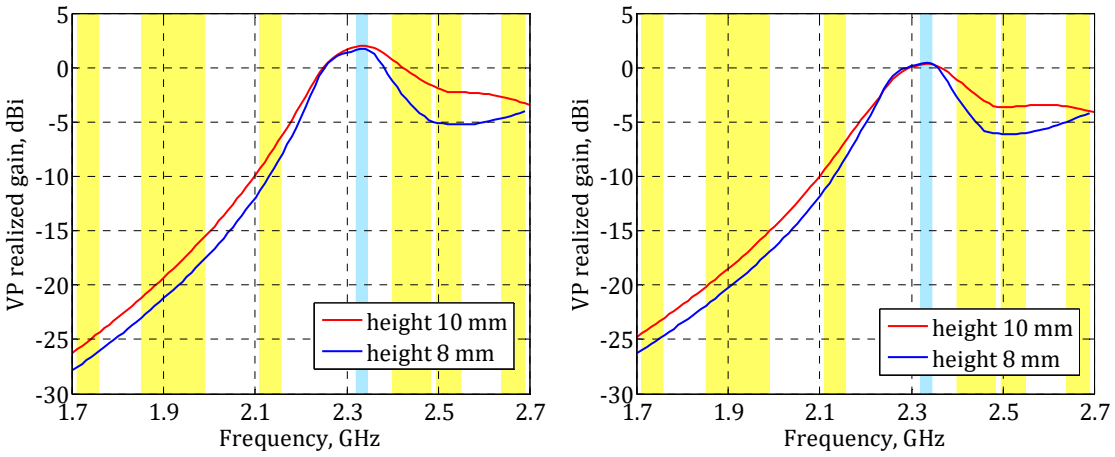


(a) Elevation angle $\theta$ = 30°.

(b) Elevation angle $\theta$ = 60°.

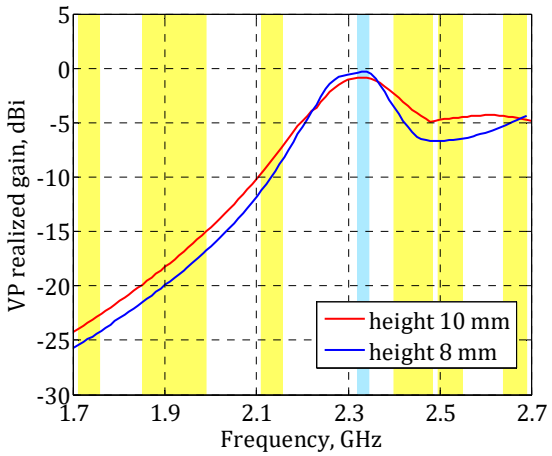


(c) Elevation angle $\theta$ = 90°.

Figure 4.5: Average over azimuth realized gain (vertical polarization) of the SDARS antennas of different height. Simulation results. Yellow - LTE bands, light blue - SDARS band.

A loop antenna with an even lower height (7.5 mm) shows a very good performance within the SDARS frequency band along with the significantly reduced out-of-band reception. This functional sample and its measurement results are described in the following.

### 4.1.3 Measurement Results of Functional Demonstrator

A photograph of the functional low-profile antenna of 7.5 mm height is shown in Figure 4.6.

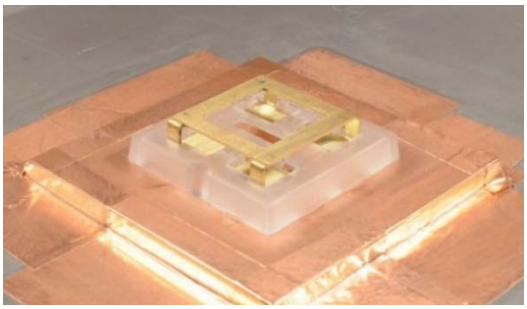

Figure 4.6: Functional demonstrator of the SDARS antenna of 7.5 mm height with improved decoupling from the LTE services.

Prior to the realization, the antenna was designed and optimized by means of CST STUDIO. After some slight adjustments to the required frequency, the manufactured sample was measured in the anechoic chamber by the measurement setup described in appendix A.4.

As other two antennas – which were discussed before – the antenna is capacitively fed through a shortening capacitor of one of its vertical elements. The aerial uses a simple matching network that is designed by the same matching technique as for the former aerial and it comprises a serial capacitor and a parallel inductor. The capacitor is an air-filled parallel plate capacitor, which is formed by a small metal plate (a part of the metal structure) and an outcut in the top side of the circuit board. Through a conducting drill, it is directly connected to a nearly 50-Ohm micro strip line, which is printed on the bottom side of the circuit board. The inductor is made in the form of a microstrip line, which is included in parallel to the 50-Ohm line. The signal output is realized by a coaxial cable, which is soldered to the 50-Ohm microstrip line.

In Figure 4.7, a loop of the antenna impedance is wider than that of the antennas of 10 mm and 8 mm height, which proves the statement about the tendency of the

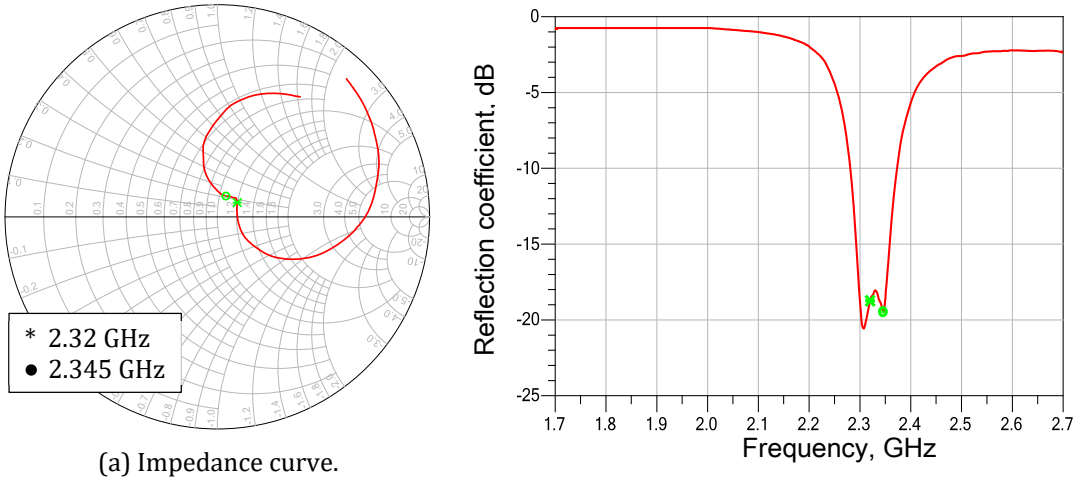


(a) Impedance curve. (freq. 2.1 GHz – 2.45 GHz)

(b) Reflection coefficient.

Figure 4.7: Impedance properties of the SDARS antenna of 7.5 mm height.

bandwidth to decrease with the reduced height. Reflection coefficients at the frequencies above 2.4 GHz are between -5 dB and -2 dB, while within the SDARS frequency band they are below -15 dB (Figure 4.7-b), which satisfies the requirements of the SDARS provider.

The reception of the VP waves is dramatically reduced in comparison to that of the 10 mm-high sample. At 2.4 GHz, the antenna reaches the VP realized gain of only -0.5 dBi at an elevation angle of 30°, -1.8 dBi at 60° and -7.7 dBi at 90° and even

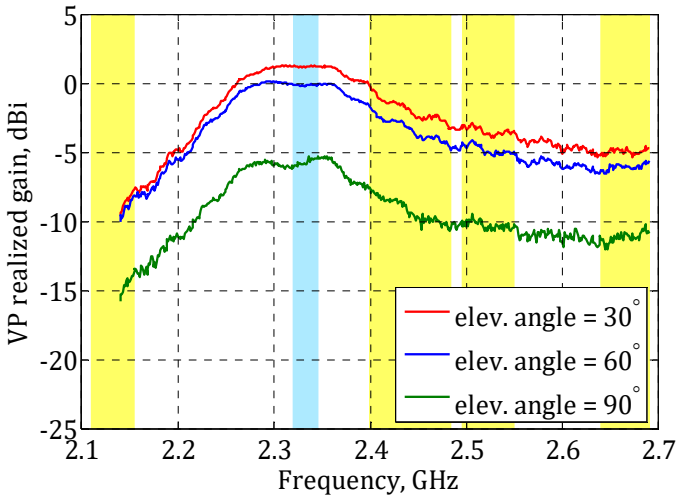


Figure 4.8: VP realized gain of the low-profile SDARS antenna improved decoupling from the LTE communication service.

lower values at higher frequencies (Figure 4.8). The low-profile antenna has a reliable VP performance within the SDARS frequency band and thus it provides stable reception of the signals from terrestrial repeaters of the satellite radio service.

Even with such compact dimensions, the antenna almost fulfils the requirements for the reception in the SDARS band, showing the demanded LHCP realized gain at almost all elevation angles and an excellent level of XPD (Figure 4.9).

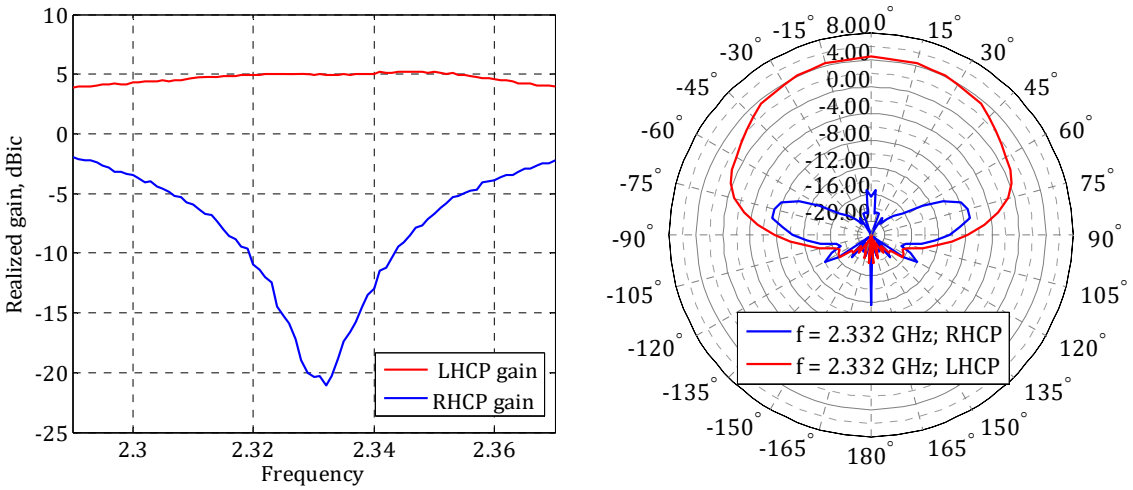


(a) Realized gain in zenith.

(b) Conical cuts of RP (realized gain).

Figure 4.9: Radiation properties of the low-profile SDARS antenna.

The SDARS antenna with improved rejection of the LTE signals yields a nearly constant realized LHCP gain in zenith of approximately 5 dBic over the SDARS band with XPD of more than 25 dBic in zenith at the SDARS mid-band frequency and at least 15 dBic at the band limits. A radiation pattern in Figure 4.9-b shows that the aerial obtains the demanded form of RP and required level of the LHCP realized gain.

The SDARS antenna of 7.5 mm height keeps a good total radiation efficiency of around -1 dB (80 %) within the operational frequency band. This value is by a 0.5 dB lower than that of the 10 mm-high antenna [73], which is caused by the larger shortening capacitors than in the last case – which produces some additional losses – and by the higher mismatch loss due to the intentional poorer matching to the 50-Ohm signal path.

In the following, highly-performant aerials for GNSS will be discussed, which is another very important satellite service for automotive application, particularly for the realization of autonomous driving.

## 4.2 Antenna for Navigation by Interoperable GPS-L1C Signal with Optimized Shape of Its Structure

The volume for an antenna mounting is often extremely small, whereby a GPS aerial with a quadratic structure and its supporting plastic socket – which is presented in [34] – is no longer applicable. Furthermore, the operational bandwidth of the GNSS services is planned to be from 1559 MHz to 1606 MHz, which cannot be covered by the former sample shown in [73]. Therefore, in the current subsection a new interoperable GNSS antenna of scarabaeus type with a shape optimized for the housing and with a new fixation technique for its metal part is presented.

The antenna operates at the centre frequency of 1575.42 MHz with a bandwidth of about 31 MHz, ensuring a reliable reception of the future interoperable navigation signal L1C as well as the current GNSS signals in the L1 band.

The top element of the metal part of this antenna has a near oval shape. This form provides an opportunity to rationally use all available mounting volume, since the chosen housing has oval horizontal sections. Moreover, special constructions designed in the cover enable its application as a supporting element for the aerial's metal part. This eliminates production of an additional plastic socket, which saves volume and allows combining this radiator with further elements even underneath an extremely restricted cover. This design technique can be used for the housings of an arbitrary shape.

### 4.2.1 Antenna Design

The simulation model of the interoperable GNSS antenna and two of its sections are shown in Figure 4.10. The top receiving element of a nearly elliptical shape occupies the maximum available volume, keeping some distance from the walls of the cover (Figure 4.10-a), which is needed to make the antenna resistant towards the possible inhomogeneity of the material of the housing and towards manufacturing tolerances.

The antenna is lifted up and suspended on two ledges on the inner columns, which have projections below and above the top ring to control the antenna's suspension height. The metal part is positioned by the guiding elements, which are designed for each vertical fragment of the antenna. These elements also provide reliable fixation of the aerial by squeezing it into the cover. The feet are disposed by the inner columns, which restrict them at the top and at the inner side, controlling the

distance to the ground plane and their outstanding towards the inside of the antenna.

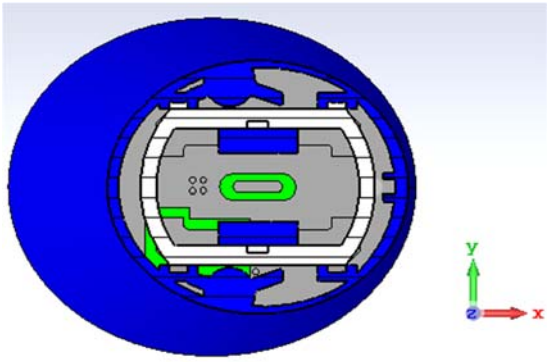


(a) Horizontal section (XY-plane) of the GNSS antenna.

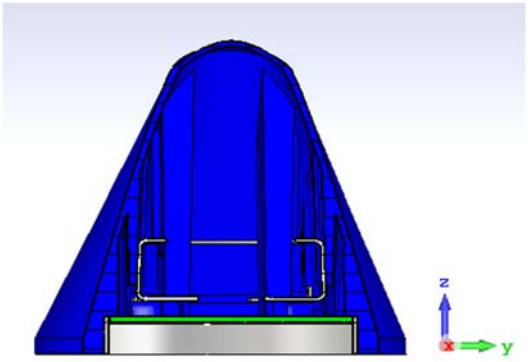


(b) Vertical section (ZY-plane) of the GNSS aerial.

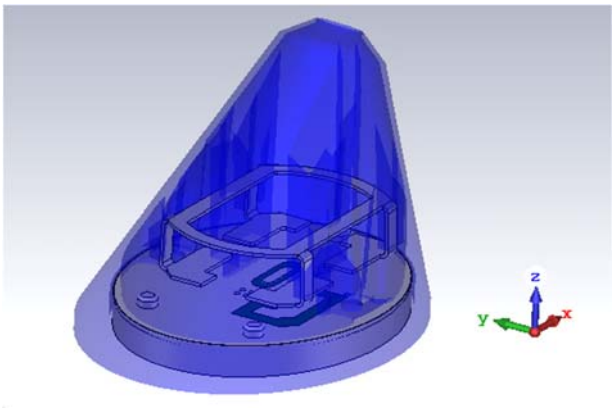


(c) Simulation model.

Figure 4.10: Simulation model of the GNSS antenna with the form optimized for the housing.

The overall dimensions of the antenna are 24 mm (width) by 29 mm (length) and 10 mm (height). The bottom ellipse of the conical housing has a major axis of 58 mm and a minor axis of 48 mm, and the maximum height of the cover is equal to 42 mm.

Underneath the housing, a metal cavity and a circuit board – made of FR-4 – are located (Figure 4.11-c). The simulation model even contains screws that fix the circuit board to the cavity, since they exert an influence on the aerial.

The antenna is fed through one of the shortening elements on which a simple matching network is applied. The network is similar to those used for the SDARS

aerial in subsection 4.1. It contains a serial capacitance – which is realized in the form of a parallel plate air-filled capacitor – and a parallel inductance made from a microstrip line.

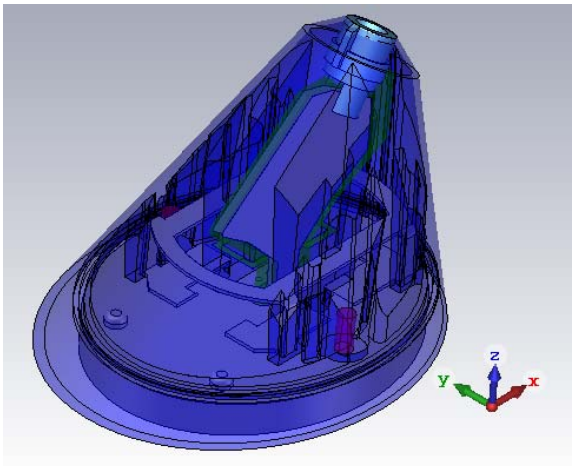


Figure 4.11: Simulation model of the GNSS antenna together with a vertical circuit board in its centre.

The special design of the aerial and the volume underneath the cover allow combining the antenna with further structures. Therefore, the GNSS antenna module was extended by a vertical plate that represents an amplifier for an AM/FM antenna, which is meant to be connected to it through a screw in the top side of the cover. The upper part of the vertical plate is shaped corresponding to the form of the cover to use all available volume, whereas the lower part is designed as narrow as possible to reduce an influence on the GNSS antenna (Figure 4.11). Commonly, this plate can also represent antennas; for example, for the cell-phone service in a narrow band or for WLAN.

### 4.2.2 Simulation Results

The GNSS antenna together with the vertical plate – which was placed in its centre – was simulated and optimized for the operation at GPS-L1 for PPS and L1C signals. It achieves an operational bandwidth of more than 40 MHz in terms of the impedance matching to the 50-Ohm signal path (10 dB level). The antenna obtains XPD up to 35 dBic at the GPS-L1 carrier frequency, more than 10 dBic at the operational frequencies of the existing GPS service in L1 band and it is still applicable at the future interoperable signal L1C, as can be noticed in Figure 4.12.

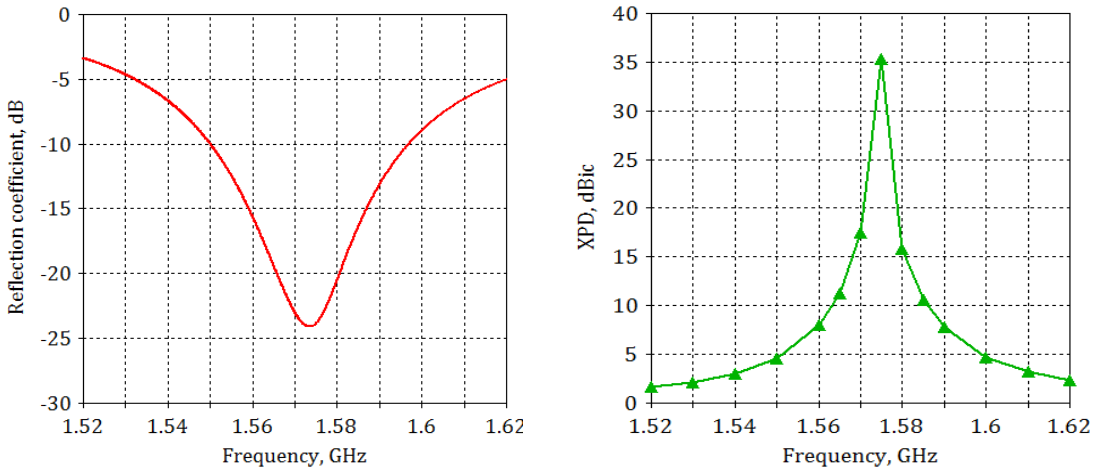


Figure 4.12: Simulation results of the GNSS aerial with a vertical circuit board in its centre.

The radiation patterns at the centre frequency and within the operational bandwidth have the demanded hemispherical form with the main radiation in zenith. The conical cuts of RP are shown in Figure 4.13-a. Noticeably, there is some asymmetry in RP of the GNSS aerial of the combination with the vertical circuit board, whereas the RP of the stand-alone GNSS antenna is almost symmetrical with negligibly small deviations, as can be observed in Figure 4.13-b. Consequently, the distortions in the

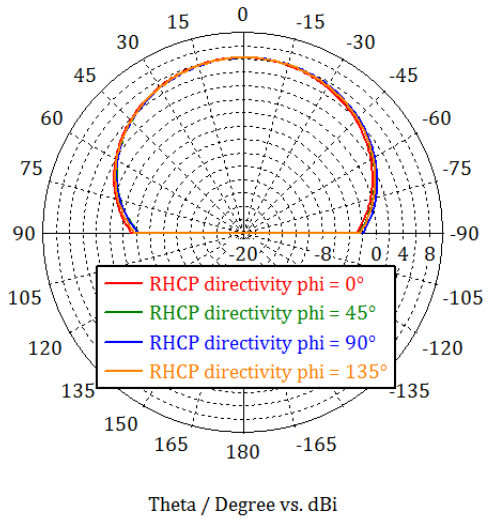


(a) Stand-alone case.

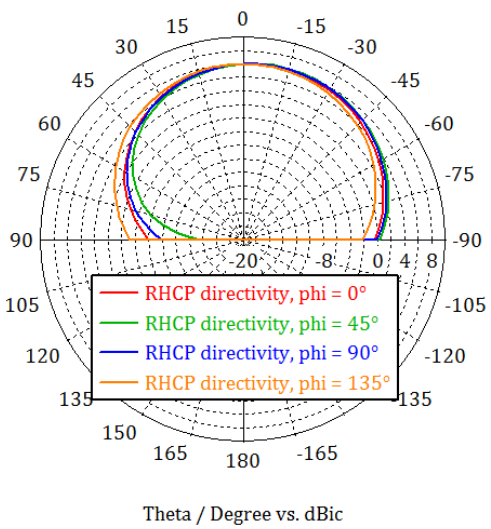


(a) Combination with the vertical plate.

Figure 4.13: Conical cuts of simulated RPs of the GNSS antenna.

RP of the GNSS antenna from the combination are caused exclusively by the presence of the vertical circuit board and the top metal adapter for the mounting of an AM/FM antenna.

### 4.2.3 Measurement Results

In compliance with the simulation model, a functional sample of the GNSS antenna was manufactured (Figure 4.14).

(a) Metal part is embedded into the cover.

(b) Circuit board of the GNSS antenna with the vertical plate for a possible AM/FM amplifier.

Figure 4.14: Functional sample of the interoperable antenna for GPS L1 and L1C signals.

The cover with the fixation and guiding elements was made of an ABS material by means of a 3D printer. Although the printer has a good resolution, the small and sophisticated details of the cover such as fixation elements could not be built as fine as they are in the simulation model. Consequently, there are some differences between the simulated and manufactured samples, which cause the differences between the simulated and measured results. Therefore, after the realization, further adjustments of the antenna to the required frequency were needed. After their implementation, the following results were obtained.

The impedance curve in Figure 4.15-a reveals a resonant behaviour of the measured antenna. The impedances within the required frequency range (from 1565 MHz to 1585 MHz) form a tight loop at the Smith chart and they are concentrated around 50 Ohm, which means an excellent matching to the transmission line. The reflection coefficient within the GPS L1C band is markedly below -17 dB, as observed in Figure 4.15-b. The antenna possesses a 70 MHz bandwidth (for S11 < -10 dB),

which ensures stable operation even if operational conditions were changed, which would result in some shift of the impedance curve.

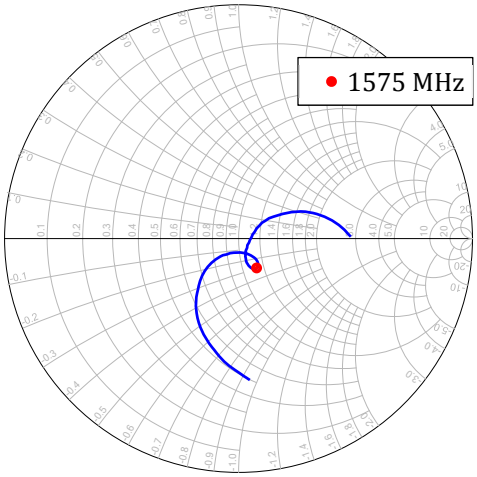


(a) Impedance curve
(freq. 1.52 GHz – 1.63 GHz).

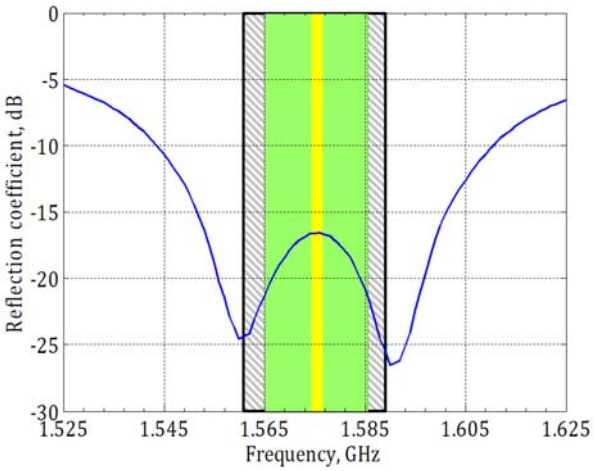


(b) Reflection coefficient
(green: GPS-PPS in L1, yellow: GPS-SPS and Galileo, diagonal hatch: interoperable L1C signal).

Figure 4.15: Impedance properties of the functional antenna for GPS L1 and L1C signals.

The antenna also shows good radiation properties. The realized RHCP gain in zenith is around 4.8 dBic at all frequencies of the L1C signal (Figure 4.16-a). The cross-polarized signals are discriminated by more than 20 dBic at the GPS carrier frequency and by approximately 11 dB at the GPS-PPS range boundaries, as well as by nearly 8 dB at the boundaries of the L1C signal.

The radiation pattern of the GNSS antenna at the signal's carrier frequency – which is depicted in Figure 4.16-b – is slightly distorted by the vertical plate for a possible AM/FM amplifier that was predicted by the simulation (compare Figure 4.13). Nevertheless, the antenna provides at least 2 dBic of the realized RHCP gain at angles up to ±40°.

Even in a very close proximity to the plastic cover and measured together with the vertical plate in its centre, the interoperable antenna attains the total realized efficiency of -1 dB on average over the GPS-L1 and L1C operational frequencies.

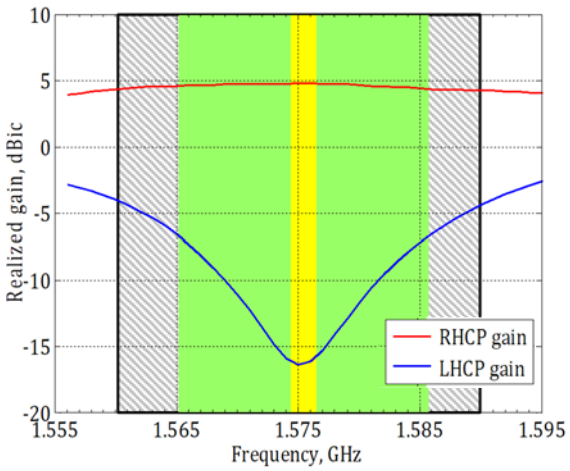


(a) Realized gain in zenith. In green: GPS-PPS in L1 band, yellow: GPS-SPS and Galileo, diagonal hatch: interoperable L1C signal.

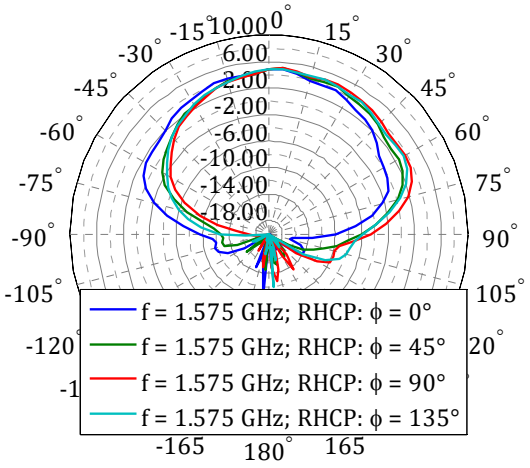


(b) Conical cuts of RP (realized gain) at the L1C carrier frequency.

Figure 4.16: Radiation properties of the functional antenna for GPS L1 and L1C signals.

## 4.3 Double-Ring GPS Antenna for Dual-Band Operation in L1 and L2 Bands in Combination with Antenna for Satellite Broadcasting

By using the L2C signal that was recently opened for civil purposes, the precision of the positioning provided by GPS can be noticeably improved [9]. This signal is transmitted in the L2 band at the carrier frequency of 1227.6 MHz with a bandwidth of 20.46 MHz. Therefore, an extension of GPS receivers for the simultaneous operation in the L1 and L2 bands is required. This extension also concerns a receiving antenna as a part of the system.

In the current subsection, a double-ring antenna concept for a dual-band operation at L1 and L2C signals of the GPS service will be discussed. The applicability of this concept will be shown by simulation and measurement results of two antenna samples from different combinations with an antenna for satellite broadcasting.

In the following, a concept of placing several scarabaeus antennas in a concentric way will be discussed.

### 4.3.1 Concept of Double-Ring GPS Antenna for Dual-Band Operation

The double-ring antenna concept involves a combination with a common footprint of two metal ring antennas with shortening elements (aerials of the scarabaeus type) for two different frequencies, one for L1 band and another ring for L2 band.

The antennas for the signal L1 and L2C have reasonably different physical sizes since the carrier frequencies of these signals are separated by 348 MHz. Therefore, an aerial for the L1 band is much narrower than a radiator for the L2 band. Thus, the smaller (narrower) element is placed in the middle of the wider element (Figure 4.17). Additionally, the outer aerial for the L2C signal is designed to be lower than another metal element to reduce its impact on the inner aerial. The similar technique of combination was implemented by the author of [34] concerning the frame antennas for different frequencies and services and by the author of [75] regarding the combination of several radiators for the same service (pattern and phase diversity for SDARS). The main distinction of the current concept from the techniques described in [34] and [75] is the fact that this combination includes two antennas with similar behaviour of the surface current that is flowing on them and consequently with the similar radiation patterns (for both types of circularly-polarized waves). Although the antennas are meant for different frequencies, decoupling between these aerials is an obstruction of their close location.

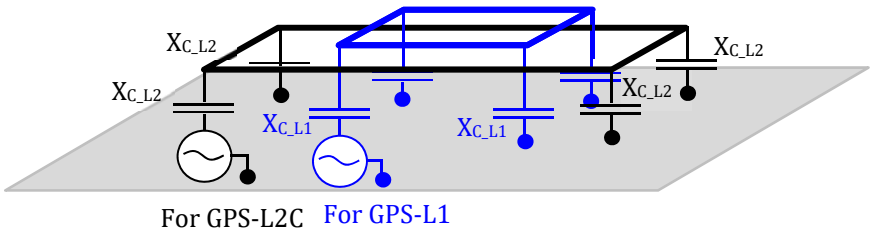


Figure 4.17: Schematic representation of the double-ring antenna concept for dual-band reception of GPS-L1 and -L2C signals.

Each metal frame of the double-ring concept is provided with a separate excitation point, ensuring a path separation for two different signals (L1 and L2C).

In what follows, two realizations of the double-ring antenna concept will be discussed. Both also include an aerial for satellite broadcasting by the reason that this service is also widely used in automotive applications, already mentioned before. Moreover, the aerials for GPS and SDARS are in the similar mounting condition,

namely they are mounted on top of the conducting plane, which can be considered as an optimal position for both radiators.

### 4.3.2 Double-ring Aerial for GPS-L1 and -L2 Services in Combination with Antenna for SDARS at Common Footprint

Herein, a double-ring antenna for operation in L1 and L2 bands of a GPS service is combined with an antenna for satellite broadcasting in a concentric way. The metal structure for SDARS is placed into the middle of the double-ring aerial for GPS. Such a combination with a common footprint provides a space-efficient use of the available mounting volume.

All radiators of the module are made by a scarabaeus design, as can be noticed in Figure 4.18. The metal parts are lifted and fixed in a plastic holder by their lower parts (by their horizontal plates). The overall dimensions of the module including the supporting element are 60 mm by 60 mm and 10 mm.

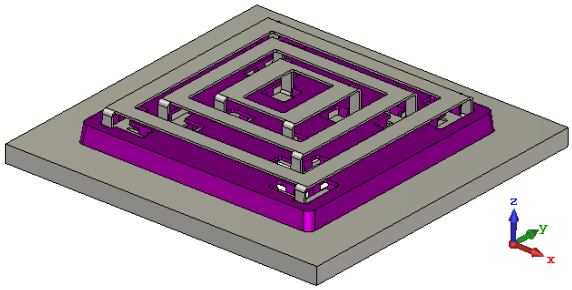


Figure 4.18: Simulation model of the double-ring GPS antenna combined with an antenna for SDARS at common footprint.

The outer frame for the GPS-L2C signal is the lowest and the widest metal part of the combination. It is 53 mm in width and length, and its height amounts to 7.5 mm. The second large metal frame is another element of the double-ring aerial for GPS-L1. Its dimensions are 37 mm x 37 mm x 9 mm. The GPS-L1 frame is enclosed by the ring for GPS-L2C. In the middle of the double-ring GPS antenna, an aerial for reception of satellite broadcasting is located. This radiator is the narrowest and highest part of the module. It has a length and width of 20 mm, and the height is 10 mm.

Like other satellite antennas in this thesis, each part of the combination needs to be additionally matched to a 50-Ohm signal line. Corresponding matching networks are made in a similar manner to those of the antennas discussed above in this

section. Accordingly, each antenna part of this module shows demanded impedance matching within the required frequency band according to the simulation results given in Figure 4.19.

Decoupling between the parts of the double-ring GPS antenna and the aerial for satellite broadcasting is sufficient for the proper function of these receiving antennas. Thus, in Figure 4.19-b transmission coefficients between GNSS and SDARS radiators are below -35 dB within the GPS-L2C band. At the frequencies of L1 signal, it is around 10 dB higher, which is still a very low value (it amounts -25 dB). Within the SDARS band, the port isolation between the double-ring aerial for navigation and the SDARS antenna is below -20 dB (for the metal part for reception of GPS-L2C signal) and below -16 dB (for the element for GPS-L1) at all frequencies of the corresponding services. Transmission coefficients between the frames of the double-ring aerial for navigation are around -15 dB and approximately -25 dB within the GPS-L2C and -L1 bands, respectively. The first value can be improved by increasing the separation between the frames and by further lowering the outer element for GPS-L2C. However, the latter option leads to the narrowing of the operational bandwidth of the antenna part for GPS-L2C.

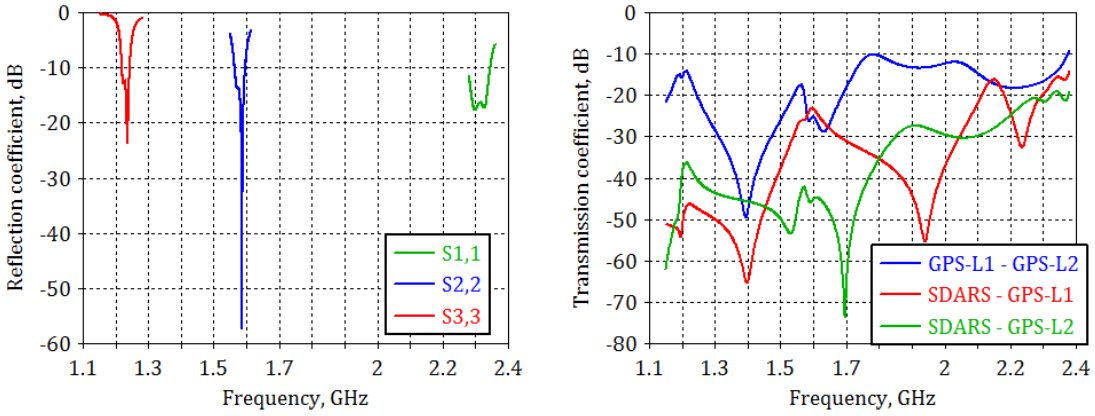


(a) Reflection coefficient.

(b) Transmission coefficient.

Figure 4.19: Simulation results of the combination of the double-ring aerial for GPS with the antenna for SDARS at common footprint.

The calculated gain in the far-field zone of the double-ring antenna for the GPS service in L1 and L2 bands is depicted in Figure 4.20-a,b for the carrier frequencies of each signal. At both frequencies, the RP for RHCP gain is plane-symmetrical with main radiation near to zenith as it is demanded. The cross-polarized signal is discriminated by more than 20 dB in zenith and by around 10 dBic at elevation angles

±60° at both carrier frequencies. The XPD level at the band limits of L1 signal is around 8 dBic. In the L2 band, this value is 2 dBic lower (it is 6 dBic) due to the extremely low profile of the radiator, which results in a narrow bandwidth in terms of XPD.

The GPS-L2C receiving part of the double-ring antenna provides more gain in zenith than that for the GPS-L1 at their corresponding frequencies. These values are 7.1 dBic and 5.5 dBic, respectively. By contrast, the 3-dB beam width is wider at the GPS-L1 carrier frequency than that at the GPS-L2C (approximately 80° for L2 and around 100° at L1 frequency). These differences are fully expected, and they are caused by the different degree of the shortening [73]. Thus, the top frame of the double-ring antenna for the L1 signal has a perimeter of 0.78·λ while the perimeter of the top element for L2C signal is 0.87·λ. Accordingly, the first top element is 20% smaller than a conventional resonance loop antenna of 1·λ perimeter. The second ring is even 13% smaller than this loop. Therefore, according to the scarabaeus concept, both elements of the double-ring aerial have obtained additional shortening capacitors ($X_{C\_L1}$ and $X_{C\_L2}$ in Figure 4.17). The larger these capacitances, the greater the portion of the current that passes through them and consequently the smaller the part of the current that remains on the top frame. Thus, in RP, some gain reduction in zenith and gain increase at angles between approximately 15° and 90° (and between -15° and -90°) can be observed.

The aerial for satellite broadcasting provides an LHCP gain of around 2.6 dBic within elevation angles of ±65°, as Figure 4.20-c shows, where the RP of the SDARS antenna from the combination is given for the SDARS mid-band frequency. The cross-polarization (RHCP) is discriminated by nearly 22 dB in zenith and by more than 10 dB at a wide sector of the elevation (within ±50°). However, high co-polarized gain in zenith and at angles near to zenith is typical for the ring-shaped antennas with shortening, whereby this SDARS antenna of the combination possesses only 2.6 dBic LHCP gain in zenith and near to it. Such a low gain is a result of mutual coupling between the aerial for satellite broadcasting and the element for GPS-L2C of the double-ring antenna for navigation. Since the outer element is meant to operate at frequencies from 1217 MHz to 1237 MHz as a frame antenna, its electrical size is $1 \cdot \lambda_{GPS\text{-}L2C}$ (perimeter) at these frequencies, including considering the shortening. However, this frame also acts at the frequency 2332 MHz (the SDARS mid-band frequency) as a loop antenna with an electrical size of nearly $2 \cdot \lambda_{SDARS}$ (in perimeter). This part of the double-ring antenna has a strong effect on the radiator for SDARS since it encloses the latter, forming a disturbing outer metal boundary that is additionally in resonance. By contrast, the double-ring radiator for GPS is not influenced

by the aerial for satellite broadcasting since the latter is located in its centre, where no field is produced by the double-ring aerial.

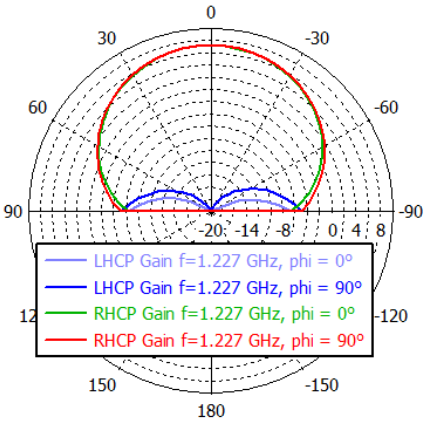


(a) GPS antenna's part for L2C band.

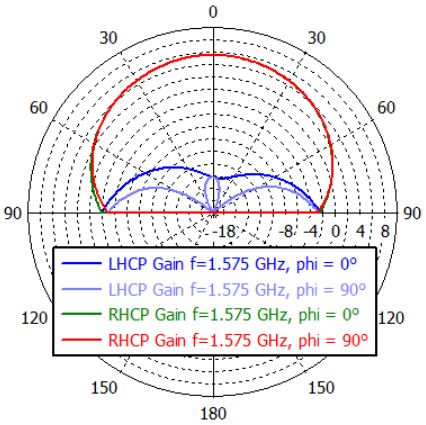


(b) GPS antenna's part for L1 band.

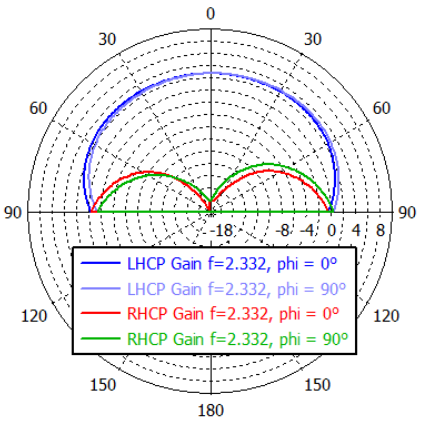


(c) SDARS antenna.

Figure 4.20: Conical cuts of the simulated RP (gain) of the antennas from the combination.

Clearly, the SDARS antenna has to be separated from the double-ring antenna for navigation in L1 and L2 bands. The results of this investigation are described in the following subsection.

### 4.3.3 Double-ring Aerial for GPS-L1 and -L2 services in Combination with Spatially-Separated Antenna for SDARS

This subsection shows a possible solution to reduce the impact of the double-ring radiator for navigation on the ring antenna for satellite broadcasting. This solution comprises the spatial separation of these aerials. Thus, the SDARS radiator is distanced by 45 mm from the double-ring GPS antenna (measured between their geometrical centres). The simulation model of this combination is shown in Figure 4.21.

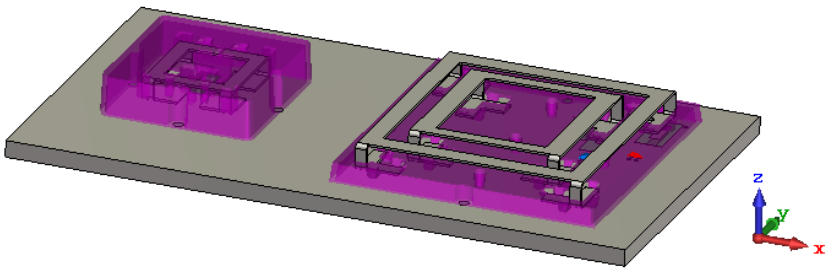


Figure 4.21: Simulation model of the spatial combination of the double-ring GNSS antenna with the aerial for SDARS.

The overall dimensions of the double-ring antenna for GPS remain unchanged, although the widths of the parts of theirs frames and the shortening capacitors were adjusted for new conditions. Additionally, the structure has obtained an ESD protection cover with fine walls.

The SDARS antenna is made by the scarabaeus principle. It has a low profile according to the investigations discussed in subsection 4.1. Thus, the aerial is 20 mm in both width and length, as well as 7 mm high. The radiator for satellite broadcasting has a separate plastic cover for protection from ESD, which is used simultaneously as a fixation element for the metal part. The aerial is lifted and suspended on hooks and clamped by four corner elements for its precise mounting. There are also two inner columns with steps that secure the distance between plates of the shortening capacitances. Therefore, the ESD protection cover can be advantageously used as a reliable holder.

In the simulation, all antennas of the module have a demanded matching to their 50 Ohm by using simple matching networks. The reflection coefficient of the double-ring aerial is below -14 dB within the L1 band and lower than -10 dB at L2C frequencies (Figure 4.22-a). For the SDARS antenna, the reflection coefficient is below -12 dB within the whole operational band of satellite broadcasting. Noticeably in this

combination, isolation between the ports of the antennas – especially between the elements of the double-ring GPS aerial and the radiator for the SDARS – is much higher than in the previous combination with a common footprint. It is concluded from the low transmission coefficient for the corresponding bands, which is shown in Figure 4.22-b. Accordingly, transmission coefficients between the SDARS radiator and the double-ring structure for GPS are below -48 dB at both GPS-L1 and -L2C band and below -30 dB within the SDARS operational bandwidth. Transmission between the elements of the double-ring radiator for GPS is slightly higher due to their close placement. These values are below -15 dB in the GPS-L2C band and lower than -10 dB in the GPS-L1 band, which are still acceptable.

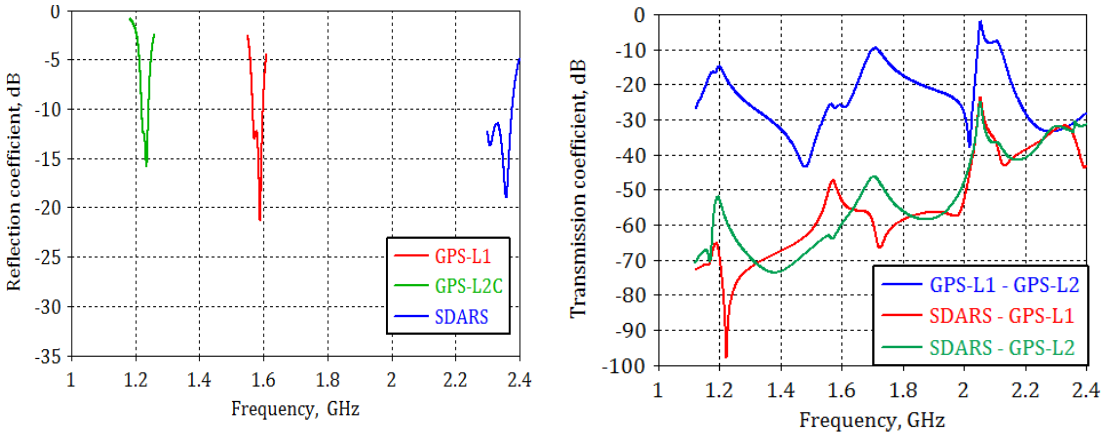


(a) Reflection coefficient.

(b) Transmission coefficient.

Figure 4.22: Simulation results of the combination of the double-ring aerial for GPS with the spatially-separated antenna for SDARS.

Due to the spatial separation, the antenna for SDARS yields the demanded form of RP with an excellent LHCP gain, as Figure 4.23-a shows. The LHCP gain in zenith amounts to 5.7 dBic, while the RHCP gain is suppressed by more than 25 dBic at the SDARS mid-band frequency. At the band limits, the XPD level is around 14 dBic (Figure 4.23-b), which is fully sufficient.

Despite high decoupling between the antennas for satellite reception, slight non-symmetry appears in the RP of the SDARS aerial, caused by the presence of the relatively large GPS structure from one side and the proximity of the plate's boundary from the other side.

The out-of-band reception of VP waves is well suppressed, as is seen in the low values of VP gain out of the SDARS band at three example elevation angles, which are given in Figure 4.23-c. Along with the high suppression of the VP signals outside

the operating band, the antenna provides good reception of VP signals from terrestrial repeaters of satellite broadcasting, showing sufficient values of VP realized gain: 4 dBi at an elevation angle of 30°, 3 dBi at 60° and 90°. These values are near to those of the low-profile aerials for SDARS presented in subsection 4.1.

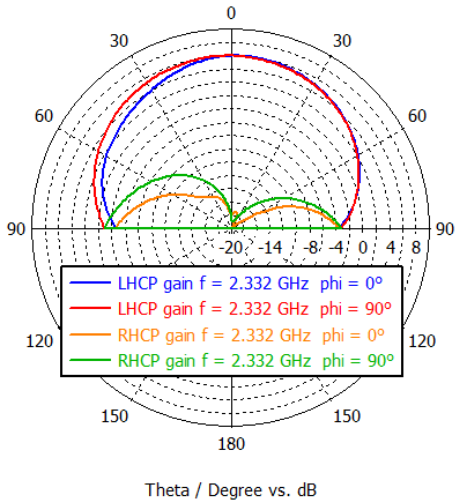


(a) Conical cut of RP (gain) at SDARS mid-band frequency, 2332 MHz.

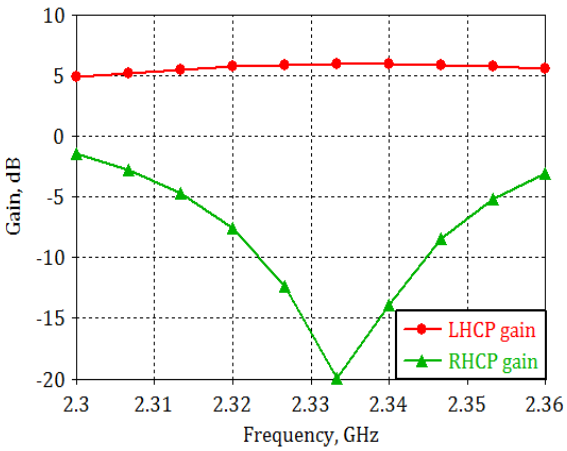


(b) RHCP and LHCP gain in zenith.

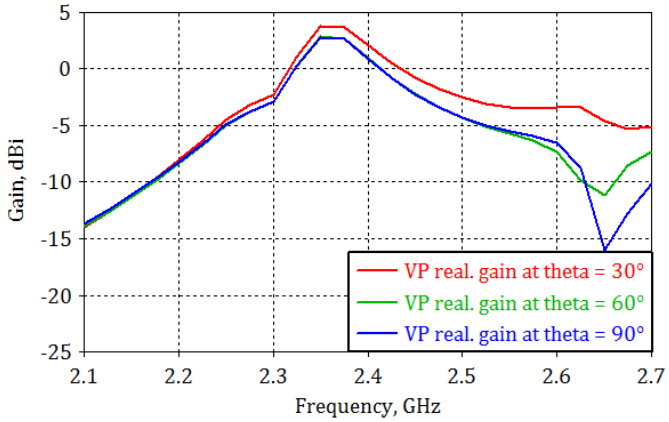


(c) VP gain at elevation angles 30°, 60° and 90°.

Figure 4.23: Simulated RP (gain) of the aerial for SDARS from the spatial combination with the double-ring GNSS antenna.

The double-ring antenna for navigation from this combination reveals almost the same radiation properties as from the previous case when it was combined with the SDARS radiator at a common footprint. The maximum RHCP gain at both L1 and L2C frequencies occurs in zenith and amounts to 5.5 dBic and 7 dBic, respectively.

The co-polarized gain is above 0 dBic even at elevation angles up to ±65° (for both carrier frequencies). The cross-polarization is discriminated by around 25 dBic in zenith for both bands, by more than 10 dBic within angles ±60° at L1- and within ±70° at L2C-carrier frequencies. At the limits of both bands, the XPD level is slightly lower. It is equal to around 8 dB for L1 signal and nearly 5 dBic for the L2C case.

The discussed double-ring antennas and their combinations can be successfully used in such mounting situations where the height is restricted while there is a lot of space in width and length. However, the use of the second metal frame leads to a higher degree of tolerance due to the manufacturing inaccuracy. Furthermore, a single-ring solution will be presented for simultaneous reception of the GPS service in L1 and L2 bands. The proposed technique eliminates production of the second ring, although it implies a further circuitry for the dual-band performance.

## 4.4 Single-ring GNSS Antenna for Simultaneous Dual-band Operation in L1 and L2 Bands

In the current subsection, a new antenna concept for a dual-band operation at L1 and L2C signals of the GPS service is presented and the simulation results of an antenna sample are shown. The proposed technique involves the use of only a single ring for signal reception in both frequency bands. The dual-band operation is achieved by implementing a special circuitry, as will be shown in the following.

### 4.4.1 Concept for Dual-Band Operation

As a base for the design of the metal structure, the scarabaeus concept was chosen [76], [77], which was also considered to design the antennas in this section above, in [47] and some other investigations.

The antenna is made in the form of a table with a rectangular table-top and four legs at each corner. Each corner leg of the metal structure ends with a parallel capacitor of the same value (Figure 4.24-a), working as an element that compensates the size reduction of the top element (loop). The value of the capacitor defines the operation frequency of the aerial. With the change of the parallel capacitance, only the resonance frequency of the aerial changes, while its radiation properties remain almost unaffected (concerning the resonance frequency).

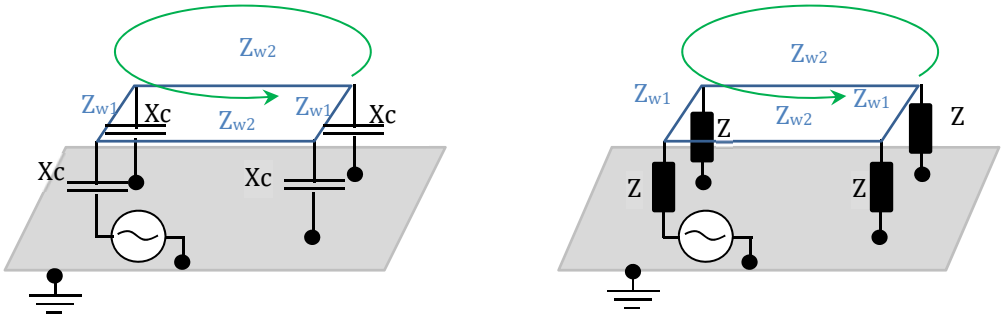


(a) Single-band operation.

(b) Dual-band operation.

Figure 4.24: Schematic representation of the loop antenna with shortening elements.

An antenna with parallel capacitors of the fixed value obtains only single resonance. In order to obtain an aerial with two resonances, the loading capacitor was replaced with a frequency-dependent network that has appropriate impedances at the required frequencies, i.e.

$$\Im\{Z(\omega)\} = \begin{cases} X_{C1} & at \quad 1.227 \quad GHz \\ X_{C2} & at \quad 1.575 \quad GHz \end{cases}. \tag{14}$$

The higher the frequency, the smaller the parallel capacitance (the higher capacitive reactance $X_C$) that is required as long as the metallic part of the antenna remains unchanged. This statement is concluded from the fact that the geometrical dimensions of the top element are constant whereas its electrical size (in terms of wave length) is frequency depended. With the increase in frequency (or decrease in the wave length), its electrical dimensions rise and consequently lower the value of the capacitances is needed to compensate the shorted length of the loop.

The requirements above are satisfied by a parallel resonant circuit included in series with a capacitor. An input impedance of this substitutional network with ideal components is described in a first approximation by equation (15).

$$Z(\omega) = -j\frac{\omega^2(L_{res}C_{res} + L_{res}C_{serial}) - 1}{\omega C_{serial}(\omega^2 L_{res}C_{res} - 1)}. \tag{15}$$

The network delivers negative values of the reactance in GPS-L1 and L2 frequency bands that reveal a capacitive behaviour. At the frequency of 1.575 GHz, the

reactance is lower than that at 1.227 GHz, which is the goal of the current network synthesis.

Equation (15) is only a rough approximation of the substitutional network considered since it does not include any parasitic effects, albeit which appear in the praxis. In the next subsection, some of these effects will be discussed.

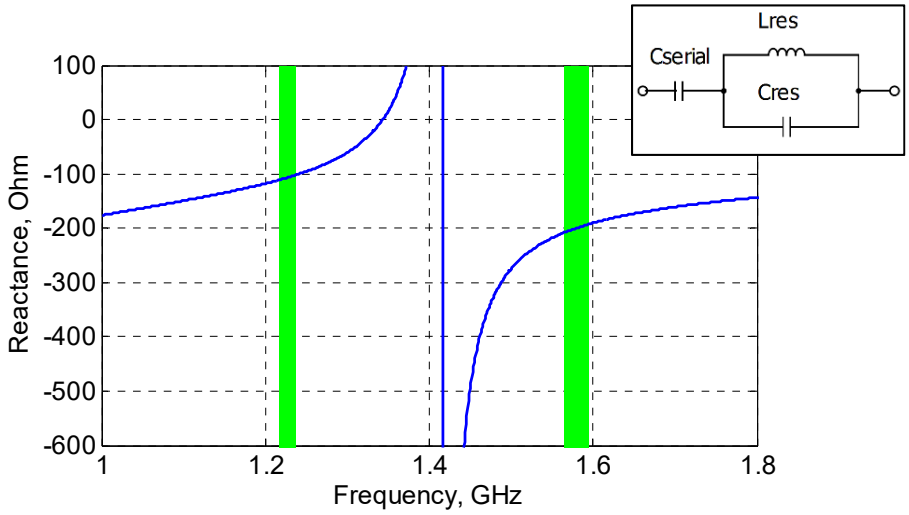


Figure 4.25: Graphical representation of the reactance produced by the substitutional network (green: GPS-PPS in L1 and L2 bands).

As far as the antenna structure has four corner vertical elements, there are four substitutional networks needed, one for each part. The networks can be either identical, or identical in pairs at the diagonal legs. The latter option gives an opportunity to reach better values of XPD at either L1 or at L2C frequencies with almost no influence on the XPD value at another (L1 or L2C) GPS frequency, whereas the change in the width of the ring's parts affects the performance of the aerial within both bands.

Next, two possibilities for implementing the described concept will be considered and their functionality will be derived by means of the simulation.

### 4.4.2 Antenna Design

In the simulation model, some simplifications were introduced. Thus, the antennas' models were placed on an infinite conducting plane and the properties of the required metals (brass – for the antenna part, and copper – metallization of the circuit board) were replaced with PEC. Other materials such as FR-4 and plastic were modelled corresponding to the real one, including power losses.

## *Metal Part and Network*

Metal parts of the dual-band antennas are designed of a 0.5 mm thick sheet.

The top elements are made in the form of a rectangle hollowed in the middle, which is held by four vertical columns (legs), one at each corner according to the scarabaeus concept. Herein, two possible embodiments of the principle for the dual-band operation will be discussed and two samples as well as their simulation results will be shown. The main distinction of these two examples comprises the different implementation of the substitutional network for the dual-band performance. Network No 1 is built exclusively of the discrete components (Figure 4.26-a), whereas network No 2 is made in a way to maximize the stability of its properties by replacing the discrete components with constructions that admit much lower deviations from the nominal values (Figure 4.26-b).

The vertical elements of the antenna structure with the exclusively discrete components are put partially through a circuit board for the fixation of the aerial. The resonance network is printed on top of the circuit board, as can be seen in Figure 4.26-a. Such an antenna structure is mechanically stable, and it is easy to manufacture although the tolerances in the values of the discrete components will lead to some deviations in the operational frequencies from the demanded one of the samples being produced in mass. Therefore, another way of the network realization was investigated.

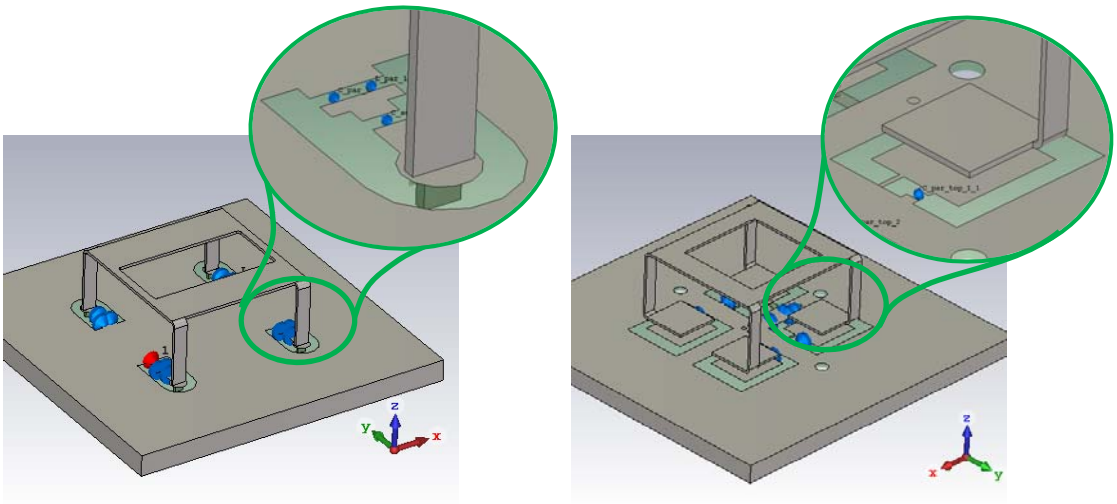

(a) Resonance network is made of discrete components.

(b) Resonance network is made of elements with high stability of their properties.

Figure 4.26: Simulation models of the dual-band GNSS aerials. Discrete components are represented by blue arrows.

The simulation model of this solution is shown in Figure 4.26-b. There is a metal structure lifted above the ground plane on a definite height; thus, a small horizontal plate and the corresponding outcut area in the top metallization of the circuit board build a parallel plate air-filled capacitor, which is the first element of the substitutional network for the dual-band operation. Furthermore, a resonance network follows, which comprises an ideal discrete capacitor and a metal line cut from the circuit board's top metallization. There are four identical substitutional networks for dual-band operation, one at each antenna leg.

There are additional parasitic elements in such an embodiment of the principle for dual-band performance for the scarabaeus antenna. Thus, between the outcut pad for the serial capacitor and the top metallization of the circuit board, which surrounds this pad, a parasitic capacitance appears as well as a parasitic inductance. The value of these elements can be roughly estimated by considering the structure as a part of a lossless coplanar waveguide (CPW) and thus by using equations derived in [78], [79] and [80]. The pad, a lossless CPW that is equivalent to the pad and its elementary equivalent circuit are shown in Figure 4.27. As far as the cut areas (slots) in the circuit board are oriented in pairs along x- and y-axes, they build two CPW that are included in parallel to each other (Figure 4.27-b).

Although this rough approximation does not consider any corner effects, it offers a good picture about the parasitic effects in the pad.

The capacitance per unit length for each infinite-ground CPW is derived from its characteristic impedances and the effective dielectric constants according to [78], as

$$\varepsilon_{re} = 1 + \frac{1}{2}(\varepsilon_r - 1)\frac{K(k_2)}{K'(k_2)}\frac{K'(k_1)}{K(k_1)}, \tag{16}$$

$$Z_0 = \frac{30\pi}{\sqrt{\varepsilon_{re}}}\frac{K'(k_1)}{K(k_1)}, \tag{17}$$

where: $\frac{K(k)}{K'(k)}$ is a ratio of the complete elliptical integral of the first kind and its complement of the variable *k*;

$k_1 = \frac{a}{b}$ ,

$$k_2 = \frac{\sinh(\pi a/2h)}{\sinh(\pi b/2h)},$$

*a, b, h* are dimensions of CPW (see Figure 4.27-b)

According to the relations from [80], capacitance and inductance per unit length are calculated by the equations below:

$$L' = \frac{Z_0\sqrt{\varepsilon_{re}}}{c}, \tag{18}$$

$$C' = \frac{\sqrt{\varepsilon_{re}}}{c \cdot Z_0}, \tag{19}$$

where *c* is the speed of light in vacuum.

Figure 4.27-c shows a simple equivalent circuit for including the parasitic inductance and capacitance for each CPW-similar structure – which are estimated by the calculation above – in the full scheme for the network.

A full equivalent circuit of the substitutional network for the dual-band operation is determined as shown in Figure 4.28 In this scheme, $C_{paras1}$ is the parasitic parallel capacitance that appears between the small horizontal plates (parts of the

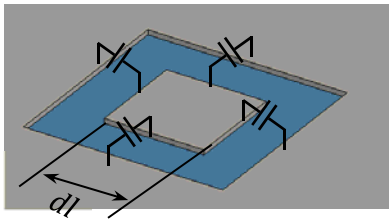


(a) Pad of dimensions $dl_1$ x $dl_2$.

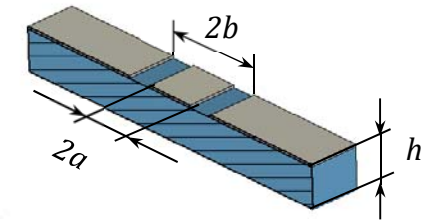


(b) Equivalent CPW structure for the pad. Case 1: $2a = dl_1$; case 2: $2a = dl_2$.

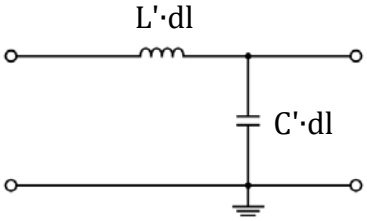


(c) Elementary equivalent circuit for a lossless TEM line of length dl.

Figure 4.27: Picture of pad, its representation as CPW and equivalent circuit of lossless CPW.

antenna metal structure) and the ground plane, $C_{serial}$ is a capacitance of the parallel plate air-filled capacitor, $C_{res}$ and $L_{res}$ are parameters of the network for the dual-band performance of the antenna. The parameters $L_{paras}$ and $C_{paras2}$ are capacitance and inductance caused by the CPW-like parts. They can be roughly estimated by means of (18) and (19), taking into account the physical dimensions of the pad. Therefore, $C_{paras2}$ comprises two included in parallel per unit capacitances of CPW with strips of length $dl_1$ and $dl_2$, whereas $L_{paras}$ must be taken only once since there is only one inductive constituent in the wave's path between the vertical leg and the point where the resonance network is printed.

The parasitic parallel capacitance $C_{paras1}$ between the small horizontal plates of the aerial and the ground plane is around 0.1 pF. The capacitance $C_{serial}$ of the parallel plate air-filled capacitor is nearby 0.6 pF. The series inductance $L_{paras}$ caused by the horizontal length of the air-filled capacitor is in the range of 1.2 nH. The parallel capacitance $C_{paras2}$ between the outcut pad and the surrounding ground plane is nearly 0.7 pF and the parameters $C_{res}$, $L_{res}$ of the inserted parallel resonant circuit for the dual-band performance of the antenna are approximately 2 nH and 2 pF, respectively. Further small parasitic effects occur in the inductive line (stray capacitance) as well as the discrete capacitor. Their influence was determined by means of the measurement and subsequently compensated through optimization in the laboratory.

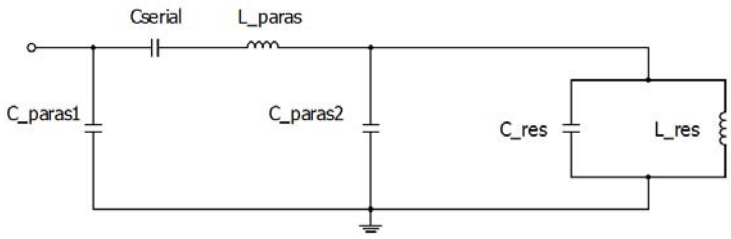


Figure 4.28: Full equivalent circuit of the lossless network for the dual-band operation.

Noticeably, parasitic capacitance $C_{paras1}$ has a tremendous influence on the radiation efficiency of the complete structure (the metal part together with the resonant networks) since it blocks a power transfer through the network.

## *Fixation Techniques for the Metal Part*

As can be inferred from the view of the metal structure given Figure 4.29, it needs some supporting element. Furthermore, two different fixation techniques will be discussed and the simulation results of two antenna models will be shown.

A simulation model of an antenna with a bottom-side fixation technique (the technique is also used in [34]) is shown in Figure 4.29-a. There, the metal part is clamped at the bottom side by a socket, whereby the antenna feet stand on the plastic supports and are caught by the plastic clamps. This aerial structure is suitable for the modules that contain two and more radiators combined under a common ESD protection cover; otherwise, an additional housing for each antenna has to be designed. For the stand-alone case, a new top-side fixation technique shown in Figure 4.29-b has a great advantage over the bottom-side fixation type. By this type of the fixation, a metal part is clipped into an ESD protection cover and is suspended by the top rectangular element. The housing contains additional corner and upper clamps for the antenna mounting. Four corner elements help to exactly position the radiator in the cover. Two inner columns with ledges, and the hooks assign the suspension height of the metal part. Thus, the ESD protection cover works simultaneously as a dependable holder.

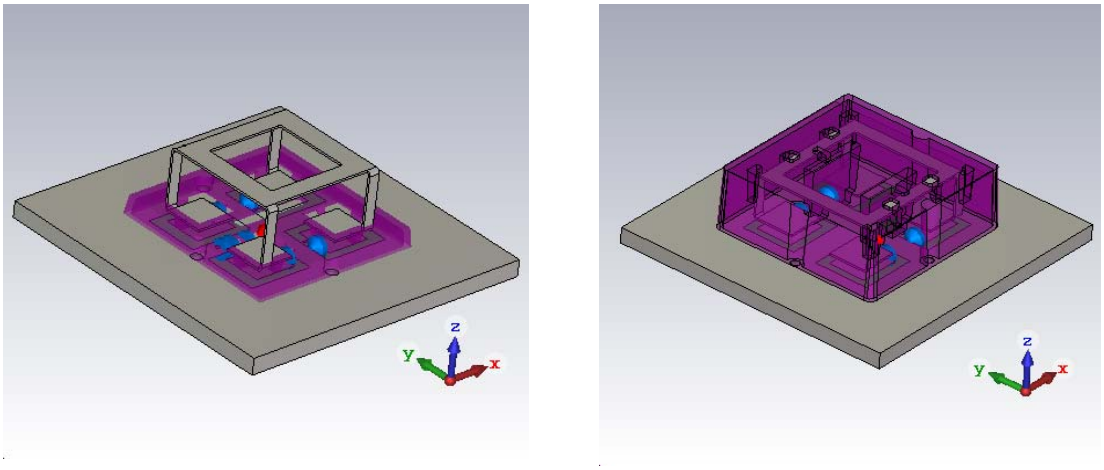


(a) GNSS antenna with fixation from the bottom side.

(b) GNSS antenna with fixation from the top side.

Figure 4.29: Simulation models of dual-band antennas with different fixation techniques.

The antennas have slightly different dimensions. The first aerial is 29.2 mm by 26.2 mm and 16.3 mm, while the second one is by 2 mm lower and a slightly wider (it is 31 mm x 29 mm x 13 mm). The overall dimensions of the antennas are enlarged by their supporting elements. The radiator structure with the bottom-side fixation is 40 mm wide, 40 mm in length and 16.3 mm high. The antenna construction with the top-side fixation type has sizes of 43 mm x 43 mm x 15 mm. Both aerials are compact relative to their operational frequencies.

### *Design Procedure*

For both antennas of two fixation techniques described above, the design procedure includes the same steps.

First, an overall dimension of the complete structure (including supporting elements) has to be defined based on the available space. Subsequently, a metal structure must be optimized for the best value of XPD at L1 frequency. The shortening capacitances obtained should be noted. Afterwards, by keeping permanent the ratio of widths of the perpendicular loop parts, the required values of the capacitances at the L2C frequency have to be found. Based on the values obtained of the required capacitive reactance and in accordance with the scheme depicted in Figure 4.28, the substitutional networks must be calculated and then pre-simulated in a program for a circuitry design. After the pre-calculation and pre-simulation, the sizes of the capacitive plates of the metal part need additional changes corresponding to the obtained values of the serial capacitance ($C_{serial}$ in Figure 4.28) and the substitutional networks have to be applied to each antenna foot. The obtained simulation model requires slight optimization to obtain the best possible values of XPD at the required L1 and L2C frequencies as far as some simplifications in the formulas and equivalent circuits were introduced. The simulations show that deviances between pre-calculated models and the simulated one are fully acceptable (for example, $C_{res}$ has deviation of $\Delta$ = 1.6 pF – difference between pre-calculated and simulated values).

## 4.4.3 Simulation Results

Both optimized antennas provide a dual-band reception of the L1 and L2C signals. The antenna with bottom-side fixation (BSF) has the best performance at the L2C frequencies and acceptable one at L1-SPS frequencies, while the antenna with top-side fixation (TSF) was optimized vice versa, i.e. for the best possible accomplishment at the frequencies of L1 signal and for a good performance at the frequencies of the L2C signal. As can be seen in Figure 4.30, the impedances of the GNSS antenna with BSF at L1 frequencies build a loop, whereas those of the antenna with USF has a sharp bend, which indicates the strong resonance and thus the best achievable values of RHCP gain and XPD.

The antenna with BSF has maximum RHCP directivities of 5.5 dBic at 1227 MHz and 1575 MHz; cross-polarization is discriminated by approximately 18 dBic at 1227 MHz and by around 11 dBic at 1575 MHz (Figure 4.31-a). The radiation efficiency of the antenna amounts to nearly -0.2 dB within the L2C frequency range and around -0.6 dB at GPS-SPS frequencies. The radiation patterns have the demanded

hemispherical form with main radiation of the RHCP waves in zenith (Figure 4.31-c, d). The sections of RPs at 1227 MHz and 1575 MHz show a near plane symmetry, whereby only slight deviations occur.

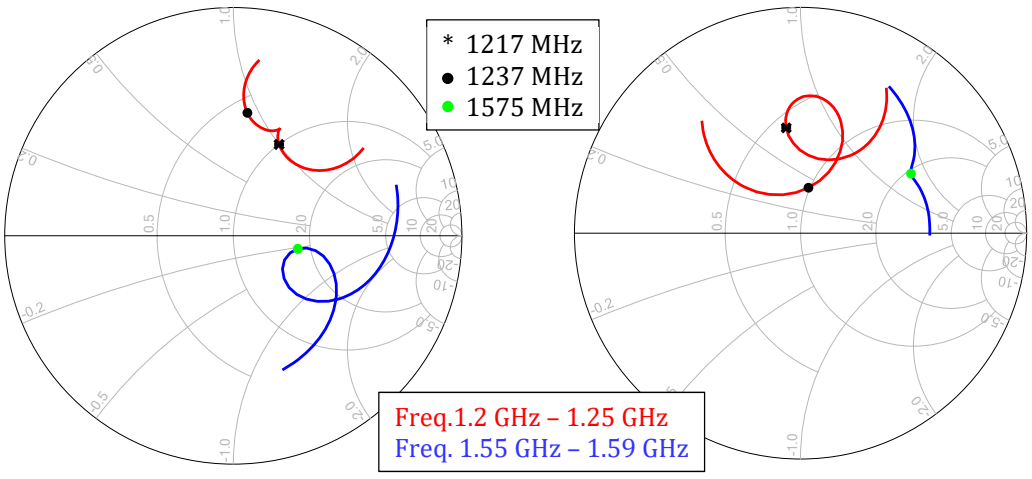


(a) Antenna with BSF. (b) Antenna with TSF.

Figure 4.30: Impedance curves of the GNSS dual-band antennas with different fixation.

The antenna with TSF has nearly the same values of the RHCP directivity at the required frequencies as the previous antenna, while at 1575 MHz the RHCP directivity in zenith is even better and amounts to 6.2 dBic (Figure 4.32-b, c). XPD at the frequencies of L1-SPS is more than 16 dBic, while at the L2C frequencies the XPD values are between 4.2 dBic and 10.2 dBic, which is still an acceptable level for the reliable operation of the accessory service in the L2 band.

The dual-band GNSS antenna with the top-side fixation technique was combined in one module with the antenna for the reception of satellite broadcasting signals with improved out-of-band reception. A slight adjustment of each antenna for the best performance in the combination case was necessary, since the properties of every antenna change with the change in the close environment.

Simulated and measured results and some design aspects of this satellite antenna module are presented in the following subsection.

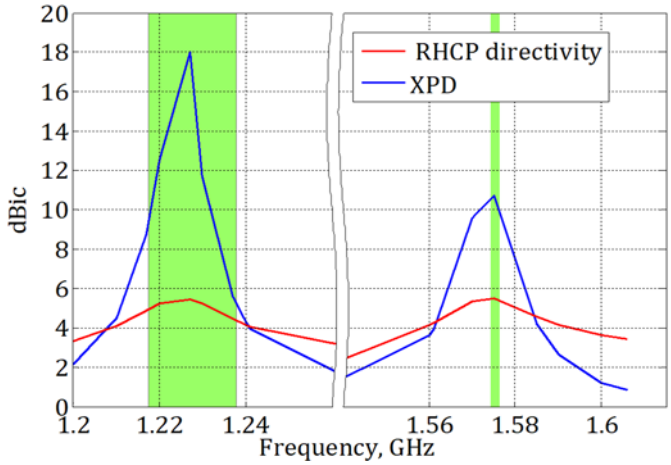


(a) Directivity and XPD in zenith.

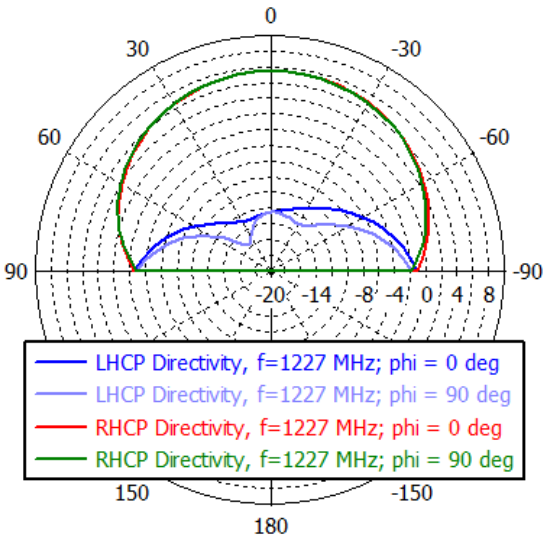


(c) Great circle cuts of the radiation patterns at 1227 MHz.

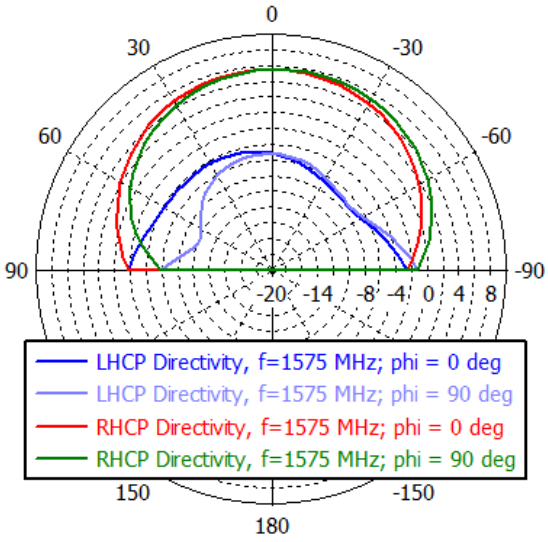


(d) Great circle cuts of the radiation patterns at 1575 MHz.

Figure 4.31: Simulated radiation properties of the antenna with bottom-side fixation.

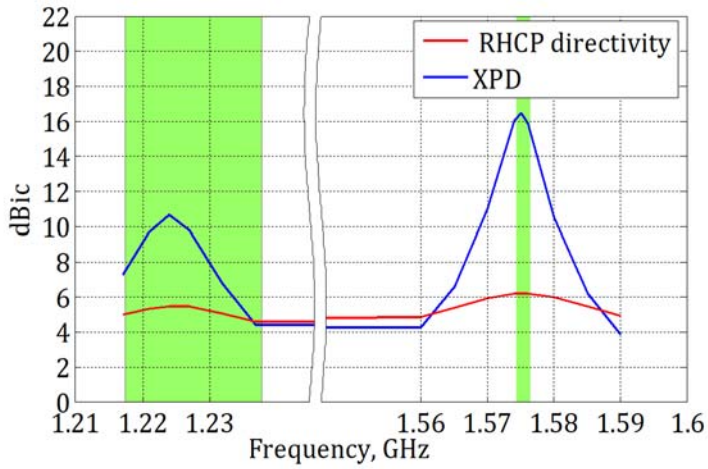


(a) Directivity and XPD in zenith.

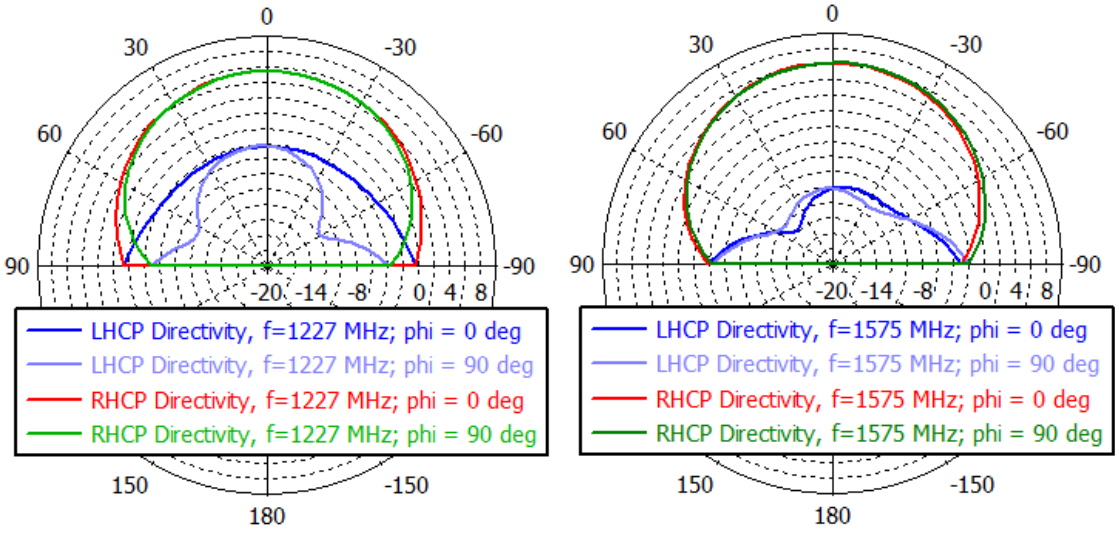


Theta / Degree vs. dBi

(b) Great circle cuts of the RPs at 1227 MHz.

Theta / Degree vs. dBi

(c) Great circle cuts of the RPs at 1575 MHz.

Figure 4.32: Simulated radiation properties of the antenna with upper-side fixation.

## 4.5 Single-Ring Antenna for Operation in L1 & L2 Bands Combined with Aerial for SDARS

A compact dual-band antenna for global navigation systems and a small-size antenna for satellite broadcasting with improved out-of-band signal rejection are combined with each other in a module.

The antenna for GNSS receives GPS L2C, L1, GLONASS and BeiDou-2 signals and it can be applied for a system based on the new L1C signal. Furthermore, it is applicable for the local navigation satellite system from Japan (QZSS) as far as this system operates at the same signal types and frequencies as GPS. The antenna possesses high RHCP gain, while cross-polarized (LHCP) gain is strongly discriminated.

The antenna for SDARS covers all required frequencies providing high LHCP gain and high discrimination of RHCP waves. It is able to receive vertically-polarized signals from the terrestrial repeaters of SDARS and it also has low interference with the terrestrial cellular communication services.

### 4.5.1 Design Aspects

The antennas were built (Figure 4.33-b) in compliance with a simulation model (Figure 4.33-a). They are located on a common circuit board with a separation of 65 mm between their centres.

#### *Antenna for Positioning Services*

A metal part of the GNSS antenna is 31 mm in length, 29 mm in width and 13 mm high. It is made of a metal sheet by a punch-bending process. This receiving element is suspended on hooks, which are parts of a plastic ESD protection cover. By this type of the fixation, a metal part is clipped into an ESD protection cover and suspended by the top receiving element and exactly positioned at each corner by means of plastic elements, which are made in the housing.

The overall dimensions of the antenna structure determined by the housing are 43 mm x 43 mm x 14.5 mm.

A three-component substitutional network is realized in a way to maximize the stability of its properties by replacing discrete components by constructions with lower tolerances. A serial capacitor is realized in the form of an air-filled parallel plate capacitor. It is built of a small plate – which is a part of the metal antenna structure – and a metal area cut from a top metallization of a circuit board. The small plate is bent towards the inside of the table-formed metal. The capacitor is included in

series with a parallel resonance LC-circuit formed of a discrete capacitor and of an inductance. The latter is made as a line cut from the top metallization of the board. The parasitic capacitance and inductance can be calculated as shown in section 4.4.

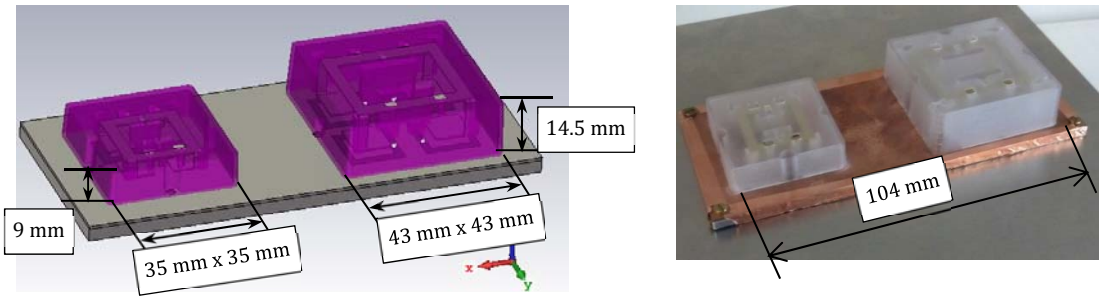


(a) Simulation model. (a) Functional sample.

Figure 4.33: Combination of the antenna for GPS-L1&L2/GLONASS/BeiDou-2 and the antenna for SDARS [76].

The antenna is capacitively fed from one leg. Its input impedances within the GPS L1 and L2 bands lead to higher reflection coefficients than required. Therefore, a dual-band matching network is applied to the GNSS antenna, whose scheme is shown in Figure 4.34.

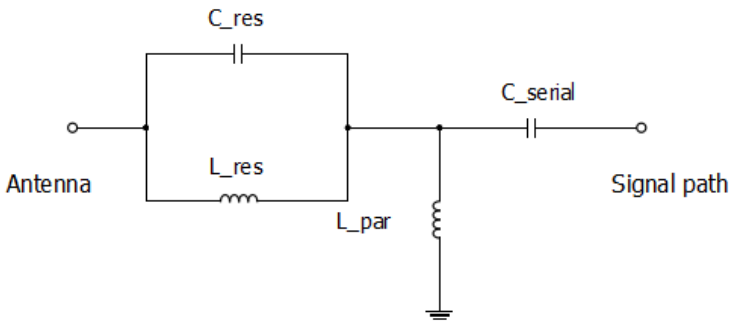


Figure 4.34: Scheme of the matching network for dual-band GNSS antenna.

A first component from the antenna's side is a parallel resonance circuit, which is included in series with the antenna feed. The resonance circuit adds some inductance to the impedances at both L1 and L2 frequencies, wherein an inductive effect of the network at the L1 frequency is stronger than that at another frequency, thus resulting in shifting the antenna's impedance at L1 towards the second point (impedance at the L2 frequency), as is schematically represented in Figure 4.35. Since the

antenna impedances ($Z_A$) at the L1 and L2 frequencies have almost the same values of the real parts, both points are almost overlapping.

After the resonance circuit, a parallel inductance a serial capacitor follows, which possess nearly the same values at both frequencies under the consideration, so that both impedance points turn together towards the 50 Ohm as shown in Figure 4.35.

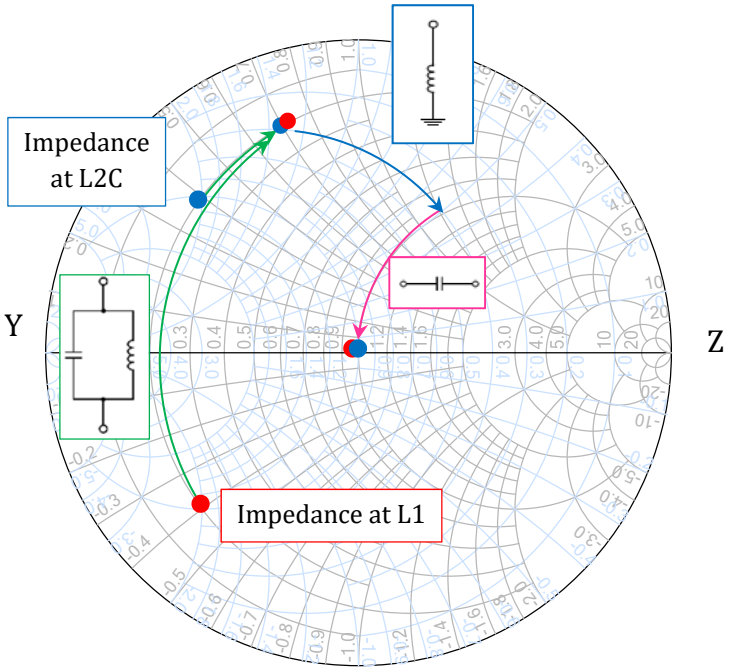


Figure 4.35: Scheme of the dual-band matching procedure.

The matching network is realized by high-quality discrete components, and it is printed on the bottom side of the circuit board.

## *Antenna for SDARS*

The antenna for SDARS has the same structure as the antenna for positioning services. The shortening capacitors are realized by small plates parallel to the ground – which are the parts of the metal construction – and the metal top of the circuit board building parallel plate air-filled capacitors. Due to these capacitors, the antenna sizes are only 20 mm x 20 mm x 7 mm.

The antenna is clipped into an individual plastic ESD protection cover and fixed in it by the same technique as the other antenna of the module. The ESD protection cover increases the antenna's overall size to 35 mm x 35 mm x 9 mm.

The SDARS antenna is capacitively fed through one of the legs. On this leg, instead of shortening parallel capacitor, a serial capacitor is built. The capacitor is used

as part of the matching network, which also contains an elongation line and a parallel inductance. Both are realized based on micro strip lines printed on the bottom side of the circuit board.

### 4.5.2 Simulation and Measurement Results

Simulation and measurement results appear in good correlation with each other, as seen in Figure 4.36, where impedance curves of the antenna for satellite broadcasting with matching circuit and the antenna for global positioning systems without matching network are presented [76]. The simulated and measured impedances of the SDARS antenna on the frequencies between 2.32 GHz and 2.345 GHz are almost the same, whereas only a small difference is seen, which is caused by a tolerance in the production and slight distinction between the properties of simulated and real materials.

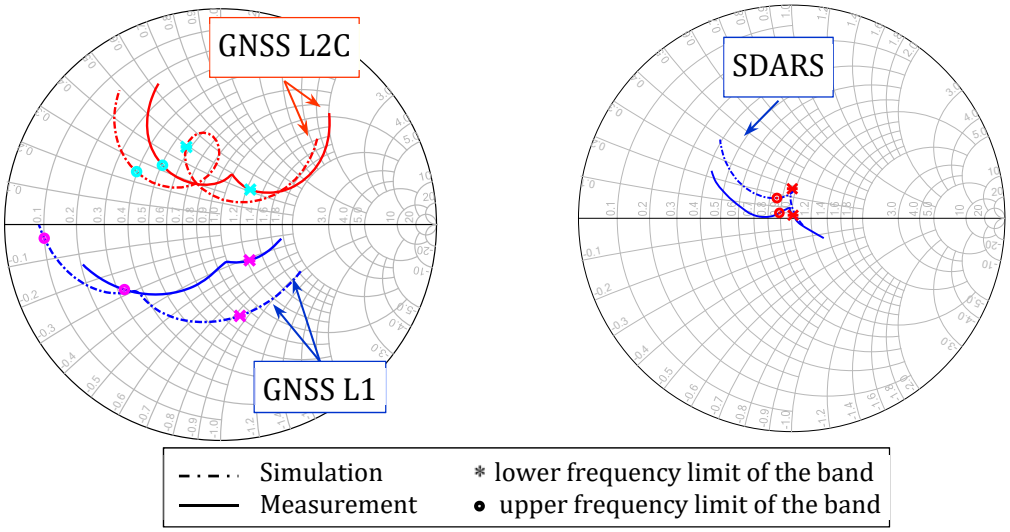


Figure 4.36: Impedance curves of the simulation model and the functional sample of the antennas from the module (GNSS antenna is without matching circuit).

The behaviour of the simulated impedance curve of the antenna for GNSS in L1 frequency band is very similar to the one measured with the difference that the real parts of the simulated impedances are lower those from the measurement. In the L2 band, the difference between the simulated and measured results is greater, alt-

hough evidence of similarity can be found. The discrepancy between the measurement and simulation can be explained by some inaccuracy in the manufacturing and tolerances in the discrete components.

Clearly, the GNSS antenna of the module needs matching. With the applied matching network, it possesses a reflection coefficient below -10 dB in both GPS L1 and L2 ranges. The reflection coefficients are lower than -10 dB even on operation frequencies of BeiDou-2 and GLONASS services (Figure 4.37).

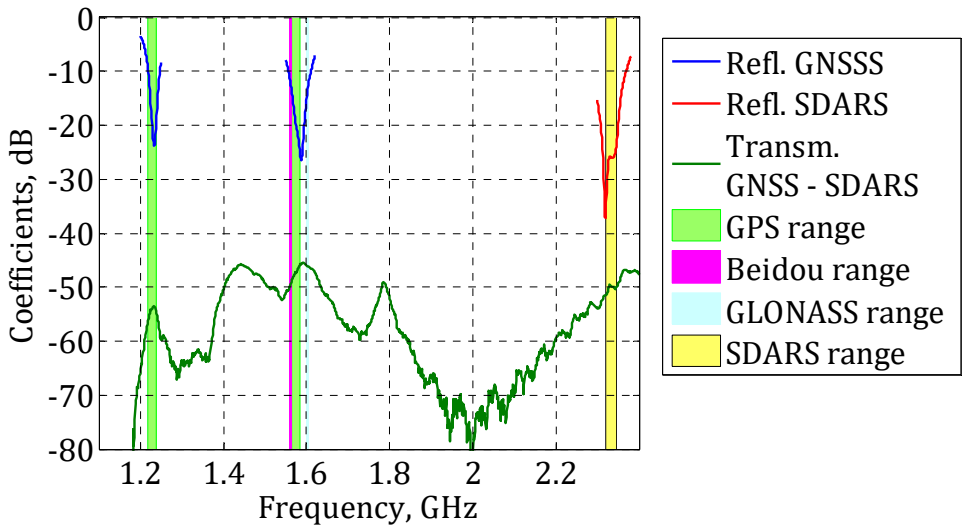


Figure 4.37: Reflection and transmission coefficients of the antennas in the module.

The antenna for SDARS is perfectly matched with the output line. The reflection coefficient within the SDARS frequency range is below -24 dB (Figure 4.37).

The satellite antennas are electrically invisible to each other. Transmission coefficients between them are below -45 dB at all frequencies between 1.1 GHz and 2.4 GHz (Figure 4.37).

## *Antenna for Positioning Services*

The radiation pattern of the antenna for the positioning system has a pronounced RHCP behaviour (Figure 4.38). Within the GPS L2C band, a cross-polarization discrimination is more than 26 dBic at the carrier frequency and around 5 dBic and 6 dBic at the lower and upper boundaries, respectively. At the GPS-SPS frequencies of L1 band, the cross-polarization is discriminated by more than 16 dBic and on those of the PPS service it is not lower than 8 dBic (at the lower boundary) and 12 dBic (at the upper boundary). The antenna possesses a sufficient level of XPD, including at the frequencies of BeiDou-2 and GLONASS services. Within the BeiDou-2

frequency band, the XPD level varies between 6 dBic and 7.6 dBic, while at GLONASS frequencies it ranges from 6 dBic to 4.2 dBic. As is clear from Figure 4.38, the simulation and measurement show similar results. The GNSS antenna obtains hemispherical RP with the main reception in zenith as it is specified.

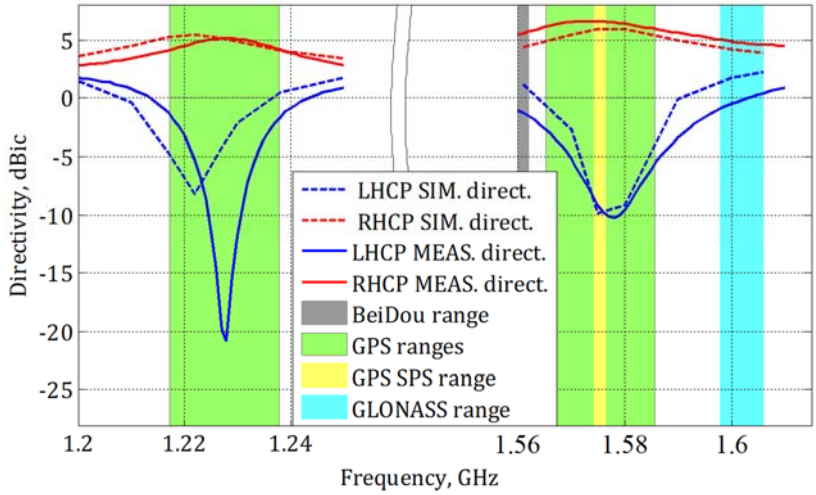


Figure 4.38: RHCP and LHCP directivities in zenith of the GNSS dual-band antenna.

At the GPS L1, the carrier frequency RP of the antenna is almost symmetrical with slight deviations, as seen in Figure 4.39, where twelve great circle cuts of RP at the GPS frequencies of L1 and L2 band are presented. The maximum realized gain (RG) in zenith is 4.5 dBic. Within elevation angles of ±30°, the realized gain is more than 2.5 dBic; moreover, it is even positive at angles of -50° and 50°.

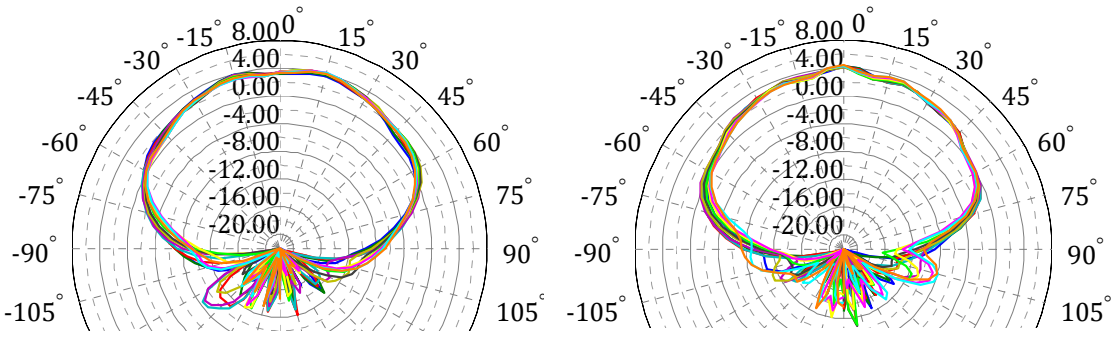


(a) GPS-L2C carrier frequency 1.227 GHz.

(b) GPS-L1 carrier frequency 1.575 GHz.

Figure 4.39: Great circle cuts of RP (RHCP RG) for azimuthal angles from 0° to 180° with 15° step of the GNSS antenna.

The RP at the GPS L2C carrier frequency is also nearly symmetrical. In zenith, a small recess can be seen. The realized gain at this angle is approximately 3.5 dBic, which is still a very good value for the stable reception. The maximum realized gain appears at angles of -15° and +15° and attains 4.15 dBic. Similar to the RP on the frequency of 1.575 GHz, the realized gain is more than 2.5 dBic at elevation angles of ±30° and it is above 0 dBic at angles of ±60°.

The antenna shows good properties at the frequencies of BeiDou-2 service (Figure 4.40-a). Deviations only become more visible at higher elevation angles (between 45° and 90°), while at lower angles from -30° to +30° – which are more important – RP is nearly symmetrical. The maximum realized gain is in zenith and amounts to 3.2 dBic. It declines to 1.5 dBic at angles of -30° and +30° and to –1 dBic on average at angles of -60° and +60°. These values show that the antenna is able to provide a reliable reception of BeiDou-2 signals.

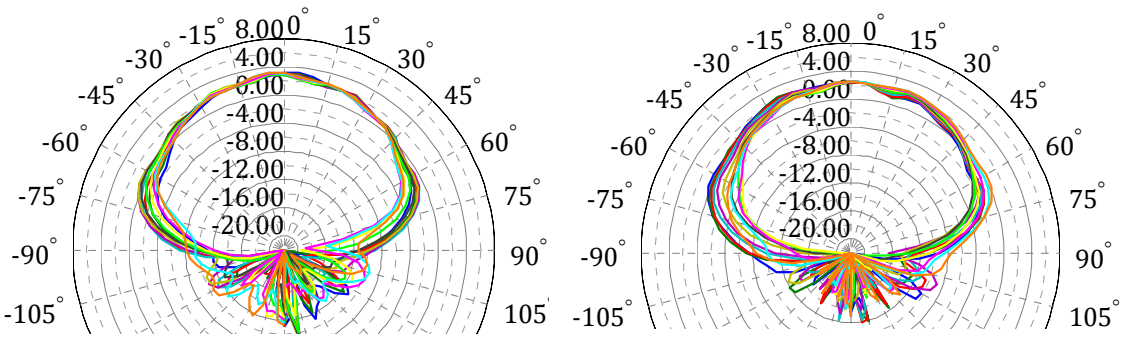


(a) BeiDou-2 carrier frequency 1.561 GHz. (b) GLONASS mid-band frequency 1.602 GHz.

Figure 4.40: Great circle cuts of RP (RHCP RG) for azimuthal angles from 0° to 180° with a 15° step of the GNSS antenna of the module.

At the GLONASS frequencies, the ripples become apparent (Figure 4.40-b). Nevertheless, the antenna possesses sufficient gain. The realized gain at the GLONASS mid-band frequency is 2.64 dBic in zenith (maximum) and around 1 dBic on average at angles of -30° and +30°.

The GNSS antenna has acceptable values of total radiation efficiency at L1- and L2-frequencies of the GPS service as well as at the frequencies of BeiDou-2 and GLONASS services, amounting on average to -2 dB (or 63%).

## *Antenna for Satellite Broadcasting*

The antenna for satellite broadcasting has nearly constant directivity in zenith of around 5.5 dBic over all required frequencies (Figure 4.41-a) [76]. The cross-polarization (i.e. RHCP) is discriminated by more than 34 dBic at the mid-band frequency of the SDARS range and by around 14 dBic at the lower and upper frequency boundaries. The simulation shows the same results except for XPD at 2.332 GHz, where it is 9 dBic lower than that of the measurement.

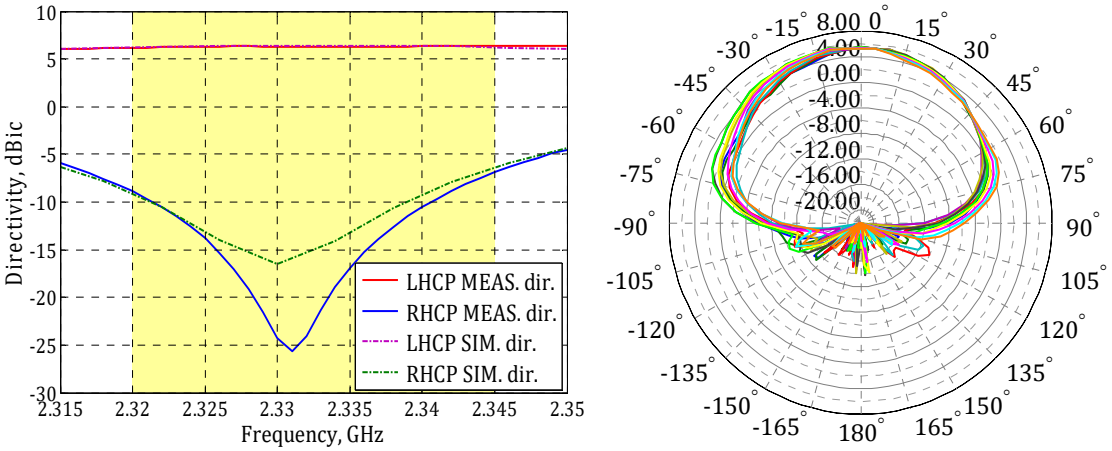


(a) RHCP and LHCP directivities in zenith.

(b) LHCP RG at 2.332 GHz.

Figure 4.41: Radiation properties of the antenna for satellite broadcasting of the module.

The RP of the antenna for satellite broadcasting at the SDARS mid-band frequency has hemispherical form with the maximum gain of 5.8 dBic in zenith (Figure 4.41-b). There is some asymmetry in the RP, caused by the presence of the relatively large GNSS antenna structure. Despite this, the antenna reaches high values of the average gain. Within elevation angles of ±40°, the average over azimuth realized LHCP gain ranges between 3.2 dBic (at -40° and +40°) and 5.8 dBic (at $\theta$ = 0°).

The antenna for satellite broadcasting ensures a reliable reception of the SDARS signals from terrestrial repeaters. Its average over azimuth vertically-polarized (VP) gain at an elevation angle of 30° is around +1 dBi, while at 60° it is slightly below 0 dBi and at 90° it is approximately -6 dBi (Figure 4.42).

At the same time, out-of-band reception is low. The VP realized gain of the antenna for satellite broadcasting at LTE frequencies between 1.8 GHz and 2.155 GHz is much lower than -10 dBi. At 2.4 GHz, the VP average over azimuth realized gains are -1.4 dBi at the elevation angle of $\theta$ = 30°, while they are -2.8 dBi at the angle of $\theta$

= 60° and -7.5 dBi at $\theta$ = 90°. These values smoothly decrease towards the frequency of 2.69 GHz by approximately -4 dBi at all three elevation angles (Figure 4.42). Thus, the SDARS antenna has sufficiently high passive rejection of VP signals of terrestrial communication, which can even be improved by implementing additional filters.

Despite the lossy plastic housing, the antenna for satellite broadcasting of the module shows relatively high efficiency of -1 dB (or 80%).

The antenna module is cost efficient in production due to the use of economical materials, easy manufacturing of antennas' metal parts by a punch-bending process and a special design of the ESD protection covers, which enables using them as holders for the antennas' metal parts. The required networks are constituted of elements with low tolerance, whereby only a few discrete components are used.

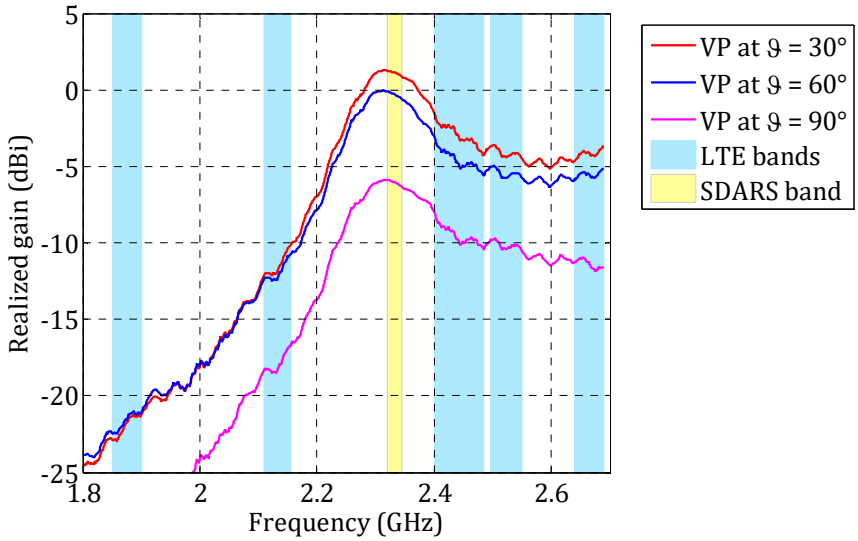


Figure 4.42: Vertically-polarized averaged over azimuth realized gain of the antenna for SDARS.

The compact design with an overall size of 43 x 104 x 14.5 mm$^3$ of the passive structure enables easy integration into various mounting positions at the car.

***Summary***

In this section, an interoperability of scarabaeus antennas for satellite signal reception has been investigated. Herein, the scarabaeus design was modified and optimized for the current requirements of the navigation service and satellite broadcasting. Thus, the aerial for SDARS was lowered to enhance its resistance against strong terrestrial interferers, such as Wi-Fi and cellular base stations. This low pro-

file (of 7.5 mm height) antenna shows excellent suppression of the VP waves at frequencies outside the SDARS band, while it keeps the demanded LHCP and VP gain within the operational bandwidth of satellite broadcasting.

For reception of the future interoperable L1C signal and all currently-available GNSS in the L1-band, the wide-band scarabaeus antenna was introduced. Although this aerial is slightly larger than its former version – which is presented in [73] – it perfectly fits underneath the restricted plastic cover by using the new fixation technique for the metal part of this antenna type, which implies utilization of the housing as the supporting element. Since GNSS will be extended by operation in the L2 band for more accurate positioning – including for civil purposes – their receiving systems have to be enhanced for dual-band performance. Therefore, for simultaneous operation in L1 and L2 bands, the scarabaeus antenna was equipped with the special network, which enables its resonance within two separated frequency bands.

Discussion of the combinations of the SDARS antenna – which allows high rejection of the out-of-SDARS-band waves – with the GNSS antennas for dual-band reception closed the current section.

The section also covered the theory of the dual-band performance for the antenna of the scarabaeus design.

The common antenna module includes radiators for both terrestrial and satellite services. Therefore, in the next chapter, the combinations of the aerials of these two different types will be considered. Thus, the antennas for cellular communication from section 3 have been combined with the aerials for satellite signal reception of the scarabaeus concept. The results of such an investigation will be shown further in subsections 5.3 and 5.5.

Furthermore, in subsection 5.4, the investigation of the combination of the compact GNSS with the helical antenna for AM/FM will be reported.

# Chapter 5

# Antenna Combinations for Terrestrial and Satellite Services for Roof-Top Mounting on Car

The previous sections have incorporated the detailed discussion of the terrestrial antennas for the cellular communication service based on LTE technology and satellite antennas for the reception of SDARS and GNSS on vehicles. In the current section, combinations of the antennas of these two types underneath a common housing will be described. The modules were designed for several shapes of the cover for the roof-top mounting position. Although this mounting is the most appropriate location for each antenna, such a dense placement of the radiators in the modules sets a serious hindrance since mutual coupling appears between the transmitting antennas for mobile communication and the sensitive antennas for satellite signal reception. The section is focused on such interference between the aerials in the combinations, as well as the ways in which to reduce it.

First, a combination of a 3D aerial for cellular communication with an antenna for satellite radio broadcasting and an aerial for global navigation systems will be presented and simulation and measurement results will be given. Furthermore, its elaborated version will be discussed, which has been extended with a helical antenna for the reception of terrestrial radio. Since the newest release of the LTE communication technology implies the use of MIMO, clearly the above modules have to be enhanced with the second LTE antenna to enable the MIMO performance. The results of a brief investigation of this problem will also be provided in this section.

A combination of an antenna for navigation services with an aerial for terrestrial broadcasting and its amplifier will close the chapter. In the last module, a circuit board for the amplifier is vertically located in the centre of the GNSS aerial and both are protected by an extremely small conical cover.

All antenna modules were simulated by both time and frequency domain solvers of CST Microwave Studio, since different problems were set, i.e. field calculation of the wide-band LTE antenna made of a pure metal and a field calculation of the narrow-band satellite antennas – which comprises both metal and plastic parts – as well as a calculation of interference between these antennas. In order to solve the first task (simulation of the wide-band antennas), the calculation in the time domain was chosen since it provides precise results along with very short simulation time for a large number of frequency samples for the far-field calculation (more than 50 samples). It is well suited for the antenna models with a wide operational bandwidth that comprise a metal only. Satellite antennas were simulated in the frequency domain because this method delivers highly precise results for the structures with a narrow frequency bandwidth and for such excellent results – which are shown in the previous chapters and will be shown further – the simulation duration is fully acceptable (it amounts about 8 – 12 minutes for simulation at infinite plane). The interaction between the antennas was calculated in the time domain, which provides sufficient results of a three-port simulation in a wide bandwidth with acceptable simulation time (of around 15 minutes). The high degree of the correlation between the simulation and measurement results can be observed in the figures given below; for example, in Figure 5.4, Figure 5.9 and Figure 5.25.

## 5.1 Principle of Combination of Antennas for Satellite and Terrestrial Services

Antennas for the reception of terrestrial and satellite signals – which were discussed above – can be successfully combined with each other by putting the terrestrial monopole-like antenna into the centre of the satellite ring-shaped antenna. This particular location is allowed by the antennas' architectures. Moreover, it is also highly advantageous from an electrical perspective, since there are almost no fields in the middle point of the loop, as concluded from the results of the near-filed simulation for scarabaeus antenna given in [73]. This property is explained by the following.

On the simple resonance loop, electric current with sinusoidal distribution (there is one sine wave of the current which fully fits in the loop's structure) is flowing in the horizontal plane, which produces an electric far field with a hemispherical radiation pattern. However, in the near-field zone, another effect is observed. The antipodal points of the circular frame contain the particles with the charge of the same amplitude and with a phase difference of 180° due to the sinusoidal distribution with the wave period of π. Consequently, the antipodal fragments of the loop

produce the near fields of the same amplitude but with the totally opposite phase, which leads to their destructive develop in the centre of the loop in the near-field zone. However, there is some residual field due to path and consequently phase difference due to the propagation of the electric fields.

There is one more reason for the good decoupling of the loop antenna from the monopole that is placed in its centre. The electric current in the monopole passes through the vertical path, causing a VP electric far field, whereas that of the loop antenna is flowing in horizontal direction. Therefore, the pure monopole antenna and the pure loop antenna are highly decoupled. The isolation between the monopole with the roof capacitance and the table-formed loop antenna (scarabaeus) is slightly lower since some vertically-flowing currents occur in the satellite aerial and some horizontal currents are present in the terrestrial radiator (Figure 5.1). These electric flows – which are moving on one antenna – are easily coupled by another aerial of the combination due to their closeness and the existence of both vertical and horizontal fragments in the architectures of the aerials.

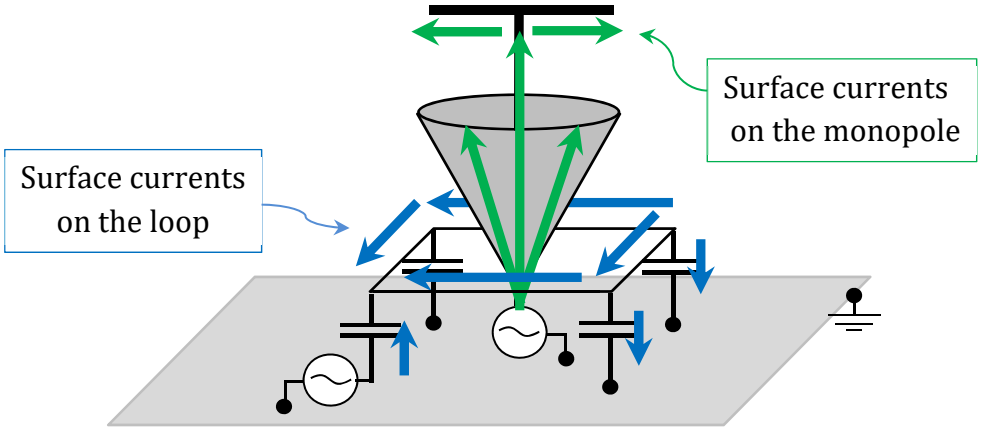


Figure 5.1: Schematic representation of the combination of terrestrial and satellite antennas.

The following subsection reports about the results of an investigation on a combination of the wide-band 3D antenna for cellular communication (with possible exploitation at LTE) with the antennas for satellite signal reception of the scarabaeus concept.

## 5.2 Antenna Module for LTE Communication, Navigation System and Satellite Broadcasting

In the module, a 3D antenna for cellular communication is combined with two ring antennas, one for navigation (GPS-L1 and Galileo services) and another for satellite broadcasting (SiriusXM service) [3]. The cellular aerial can even be used for LTE communication if the module were extended by the second LTE antenna (such research is reported in subsection 5.4); therefore, further in the text it is called "LTE antenna", corresponding to its potential functionality.

The antennas are designed to be placed underneath an ESD protection cover with a maximum height 55 of mm and a length of 96 mm. Its width is 2 mm at the top and increases to 8 mm at the height of 35 mm and up to 50 mm at the height of 13 mm. Furthermore, the width of the footprint of the ESD protection cover changes towards the front, from 53 mm to 26 mm. The module is covered by an outer large design cover. The front side of the module contains the antenna for the GPS-L1/Galileo service. At the rear side at a distance of 53 mm from the GNSS antenna (between centres), the radiators for LTE and SDARS are located. The antenna for mobile communication is put into the centre of the SDARS aerial. Such an arrangement allows achieving a high decoupling along with a small mounting volume.

### *Designs Aspects of Antennas for Satellite Signal Reception*

***Antennas for GPS-L1/Galileo services and for SDARS*** are based on the loop antenna concept presented in [47], [81] and section 4, which are designed for the corresponding operational frequencies and demanded polarizations.

### *Designs Aspects of LTE Antenna for Module*

***The antenna for LTE communication*** is made based on the concept described in section 3. It is a combination of a cone antenna with a capacitively-loaded quarter-wave monopole with a common driving point.

For this module, several realizations of the 3D concept were considered and investigated. As an initial architecture, the 3D antenna shown in Figure 3.12 was chosen. Its high-frequency part (the cone) is made from the sloped strips and the low-frequency part (the monopole with the roof capacitance) is realized from two metal strips that hold the capacitive top load. Since the cellular antenna has to be located in the centre of the aerial for satellite radio, a small fragment of the lower part of the initial architecture was modified into a flat plate that conducts the current from the

excitation port to the point, where the structure starts its shaping into the 3D body. Moreover, the aperture angles of the conical part and the roof of the new antenna are much narrower than that of the aerial shown in section 3 due to the different shape of the cover. A functional demonstrator of the described antenna is shown in Figure 5.2-a. This antenna occupies all available height (53 mm), but it is only 30 mm long. Reasonably, the aerial needs an additional matching network for the LTE low band. In order to reach the required decoupling of at least 20 dB from the aerial for satellite broadcasting, the 3D radiator with the two-wire monopole was constructed from very tight strips – which are maximum 1 mm wide – which certainly makes it extremely fragile, as can be noticed in Figure 5.2-a. Therefore, further investigations were conducted.

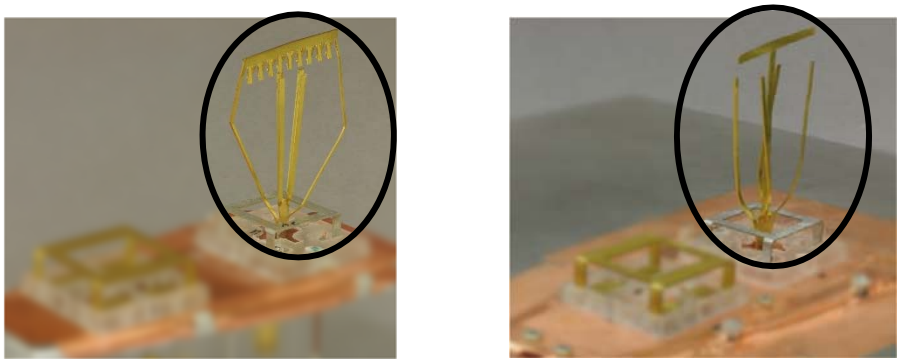

(a) Realization 1 (with two-wire monopole). (b) Realization 2 (with single-wire monopole).

Figure 5.2: Different realizations of 3D antenna for LTE cellular communication for the combination with antennas for satellite signal reception

The second realization of the 3D LTE antenna concept is depicted in Figure 5.2-b. In this version, a cone-shaped part for the LTE upper frequencies is made by four strips bent in alternating way to form a half-parted tulip [3]. The quarter-wave monopole with the roof capacitance is realized like a T-shaped monopole with only single vertical strip (the single-wire monopole). The monopole's inductive part and each strip of the cone are around 2 mm wide. The low and high parts start their shaping outside the antenna for satellite reception by their lifting up to the height of 11 mm. Similar to version 1, there is only a flat lengthening metal part in the centre of the SDARS antenna. The modified $\lambda/4$-monopole allows reaching high decoupling from the satellite aerial, at the centre of which the antenna for LTE is placed, together with the improved mechanical stability of the 3D architecture.

The antenna structure admits using the ESD protection cover as a stabilizing element. An inner part of this cover is very narrow at the top side with only 1 mm in width, whereby the roof capacitor of the antenna is reliably fixed between the walls

of the cover. Additionally, the upper parts of the arms of the cone follow the form of the ESD protection cover and thus the antenna part for the LTE upper frequencies is caught by the cover. Accordingly, the aerial for cellular communication based on the LTE technology is sufficiently stable even if the metal thickness of only 0.4 mm is chosen.

In order to fulfil demands on matching to the 50-Ohm path, the LTE antenna of version 2 also requires a simple matching network as the antenna of version 1. This network comprises an LC-serial resonant circuit, which is included parallel to the antenna feed. It acts only at the LTE lower frequency band and has almost no influence on the antenna's impedance at frequencies between 1427 MHz and 2700 MHz.

### 5.2.1 Simulation and Measurement Results

In the following, simulation and measurement results of the 3D LTE antenna version-2 combined with the antennas for satellite broadcasting and for navigation system – which are shown in Figure 5.3 – will be discussed.

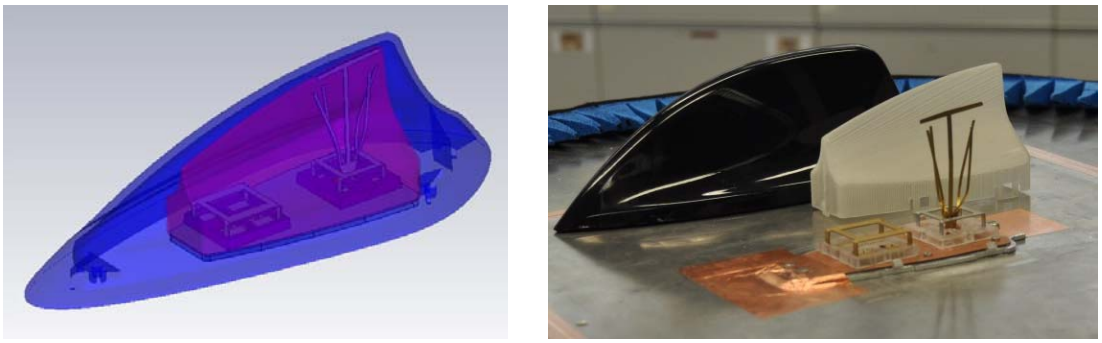

(a) Simulation model. (b) Functional sample.

Figure 5.3: Functional sample of the antenna module for mobile communication and satellite signal reception.

For the more careful simulation, two different simulation methods (time and frequency domain) were used. Therefore, the obtained simulated results appear in good agreement with the measured one, as can be noticed in Figure 5.4, for example.

The simulated and measured impedance curves of the antenna for LTE communication are very similar to one another, as well as those of the satellite antennas of the module. In Figure 5.4-a, it can be observed that the built matching network has a stronger effect on the impedances of the LTE antenna at frequencies between 700 MHz and 960 MHz than the simulated one. This difference can be easily explained

by the slight inaccuracy of the manufacturing of the antenna structure itself and by deviations of the values of the discrete components used.

In Figure 5.4-b, c, the measured curves are slightly turned up on the Smith chart, caused by the discrepancies between the properties of the substrate in the simulation model and the manufacturing, as well as the tolerances in the components.

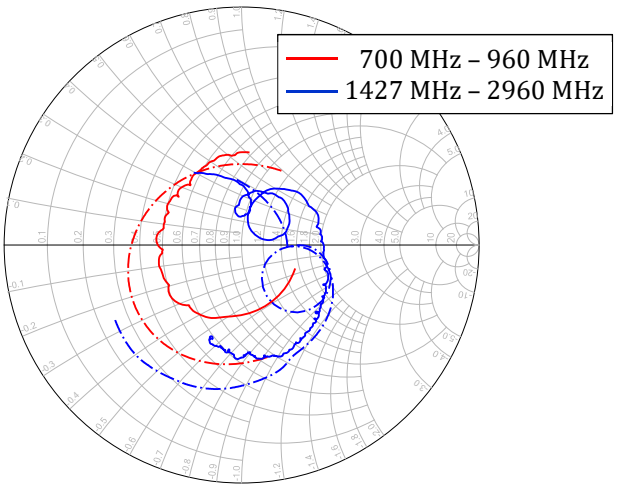


(a) Antenna for LTE cellular communication.

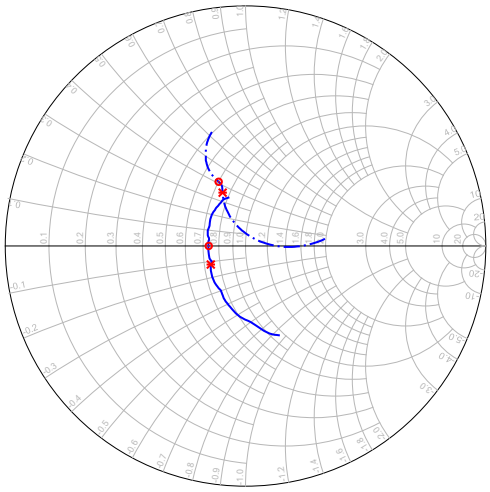

(b) Antenna for SDARS;
freq. 2.25 GHz – 2.4 GHz

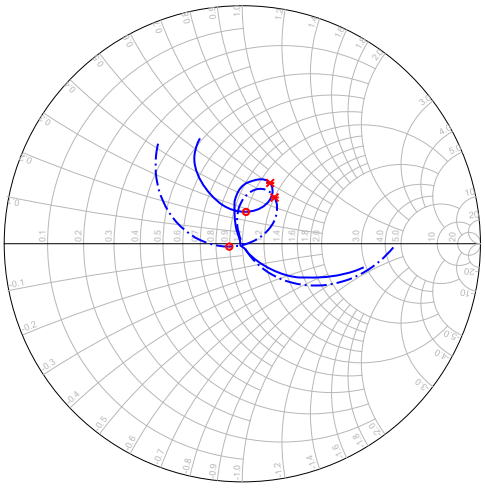

(c) Antenna for GPS-L1/Galileo;
freq. 1.5 GHz – 1.61 GHz

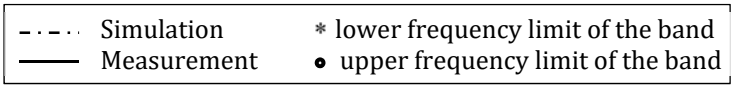


Figure 5.4: Simulated and measured impedance curves of the antennas in the module.

In order to reach better values of the reflection coefficient – especially for the satellite antennas – the realized matching networks of all antennas of the module after the first measurement (the results are shown in Figure 5.4) were slightly tuned. After the readjustment, the antennas for satellite signal reception obtained reflection coefficients lower than -20 dB, which means almost perfect impedance matching the 50-Ohm signal path. The antenna for LTE cellular communication has reflection coefficients around -7 dB within the LTE lower and upper frequency ranges and below -8 dB at the LTE middle frequencies (Figure 5.5).

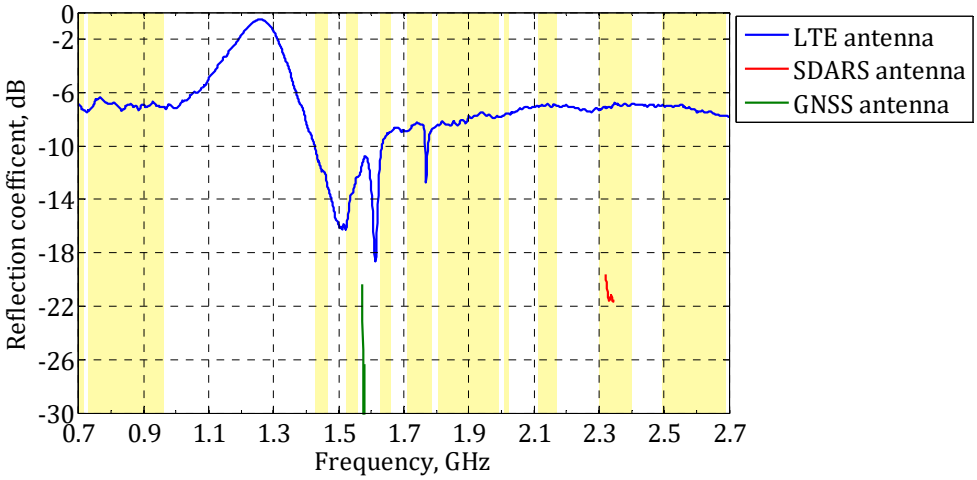


Figure 5.5: Reflection coefficient of the antennas in the module.

The total radiation efficiencies of all antennas in the module are around -1.9 dB on average over the corresponding operational frequencies.

Figure 5.6 shows horizontal and vertical sections of the radiation patterns for different frequencies of the antenna for the LTE service from the module. The conical cuts are made at three elevation angles: 65°, 75° and 85° (counted from zenith). In these figures, it can be seen that the MBD of the RP turns upwards. This is explained by an influence of the ground plane with finite dimensions. This effect is stronger at frequencies between 698 MHz and 1500 MHz, so MBD turns more to the upside and occurs at an elevation angle around 65°. At frequencies between 1.5 GHz and 2.7 GHz, MBD is at an elevation angle of approximately 75°. The effect of a finite ground plane on the radiation pattern of terrestrial antennas is described in detail in 3.3.3 and [2].

At the lower LTE frequencies, the LTE antenna acts like a monopole with a roof capacitor and provides an omnidirectional RP without any deviation (Figure 5.6).

The maximum achievable realized gain at the example frequency 850 MHz is approximately 3 dBi.

At frequencies between 1427 MHz and 2700 MHz, where the conical part of the 3D antenna dominates, the radiation pattern of the LTE aerial also obtains omnidirectional properties. The maximum realized gain at 2.6 GHz reaches a value of 5.2 dBi. The deviation is around ±2 dBi.

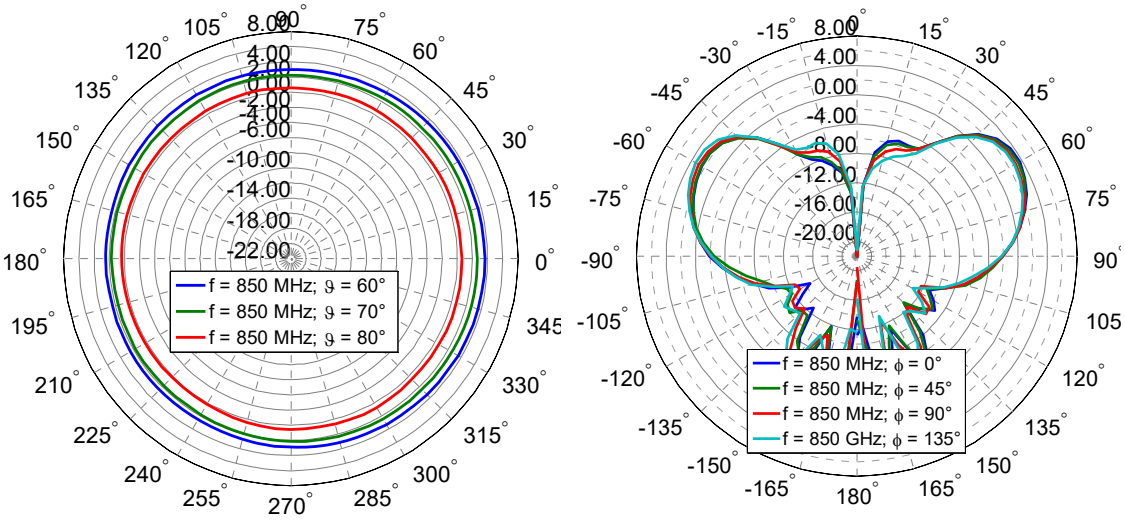


(a) Conical cuts at 850 MHz.

(b) Great circle cuts at 850 MHz.

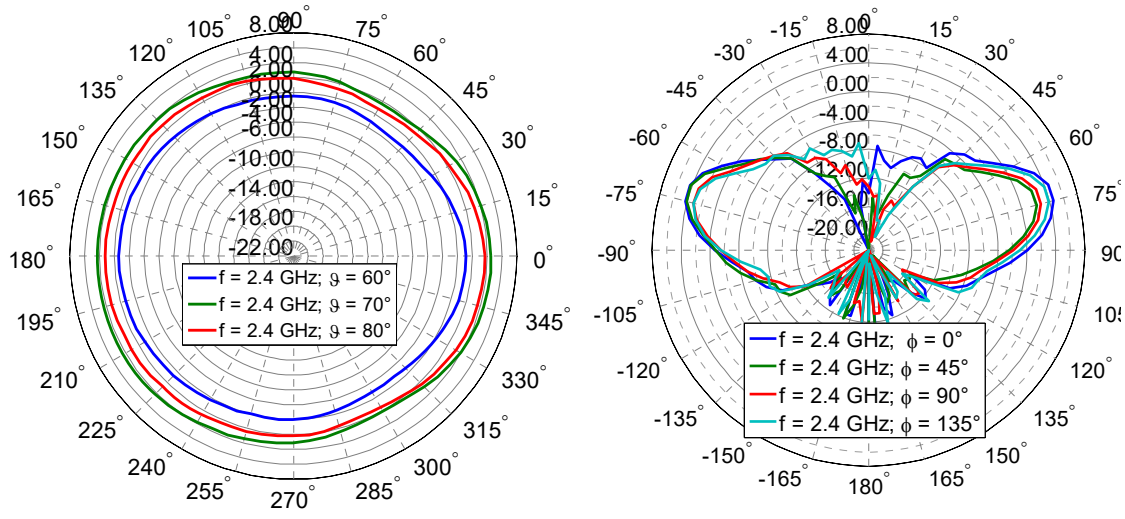


(c) Conical cuts at 2.4 GHz.

(d) Great circle cuts at 2.4 GHz.

Figure 5.6: Sections of RPs of the LTE 3D antenna of the module.

In Figure 5.7, the linear realized gain of the antenna for LTE service (on average over azimuth) is compared with the one of four λ/4-monopoles. The monopoles are designed for different frequency bands corresponding to the required LTE frequencies. This comparison shows that the antenna for the LTE service provides the realized gain of only 0.9 dBi lower than that of the reference monopoles, even though the antenna operates at a wider frequency band covering all frequency bands of the four quarter-wave monopoles, and the height of the antenna is lower than that of the monopole for frequencies below 1 GHz.

The antenna for GNSS at the GPS-L1 carrier frequency achieves a maximum RHCP realized gain of 5.75 dBic in zenith, as Figure 5.8-a shows. Even at elevation angles of ±45°, the antenna possesses the realized gain of 2 dBic. Cross-polarization is discriminated by more than 12 dBic in zenith and at the elevation angles up to ±40°. Noticeably, there are some distortions in RP of the GNSS antenna. The reduced gain occurs at an elevation of 65° and at azimuthal angles between 150° and 195°. This is the sector where the LTE antenna is located looking from the GNSS aerial's side.

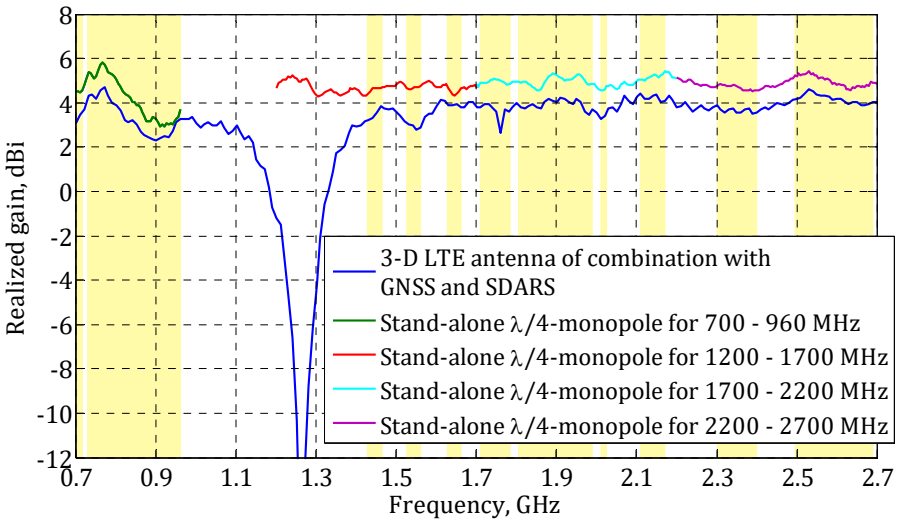


Figure 5.7: Linear average over azimuth realized gain of the LTE antenna of the module.

By contrast, the radiation pattern of the radiator for satellite radio obtains a nearly symmetrical form. The view of both RPs appears to be in good correlation with the measured decoupling, which will be discussed in the following. The transmission coefficient between LTE and SDARS antennas is better than -20 dB at 2332 MHz, whereas the one between LTE and GNSS radiators is only -10 dB at the GPS-L1/Galileo frequency of 1575 MHz.

The antenna for SDARS obtains the demanded form of the radiation pattern and almost fulfils the requirements to the LHCP realized gain. Its maximum value at the mid-band frequency occurs in zenith and reaches 3.82 dBic (Figure 5.8-b). Cross-polarization is discriminated by more than 14 dBi at elevation angles between -50° and +50°.

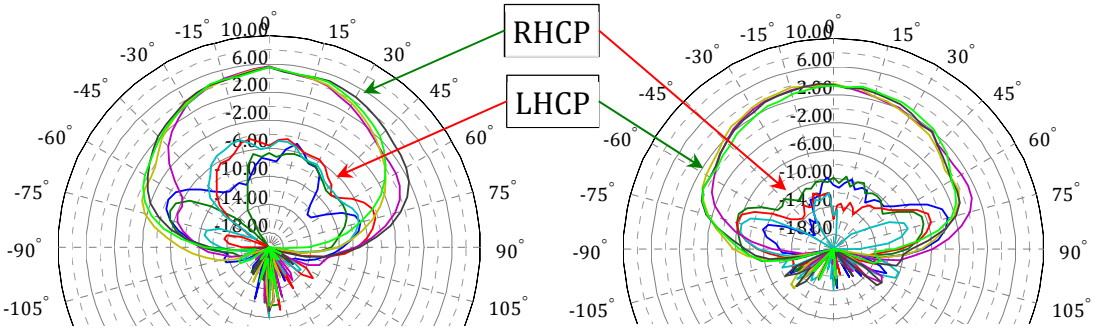


(a) Antenna for GPS-L1/Galileo. Great circle cuts at 1575 MHz for φ = 0°, 45°, 90°, 135°.

(b) Antenna for SDARS. Great circle cuts at 2332 MHz for φ = 0°, 45°, 90°, 135°.

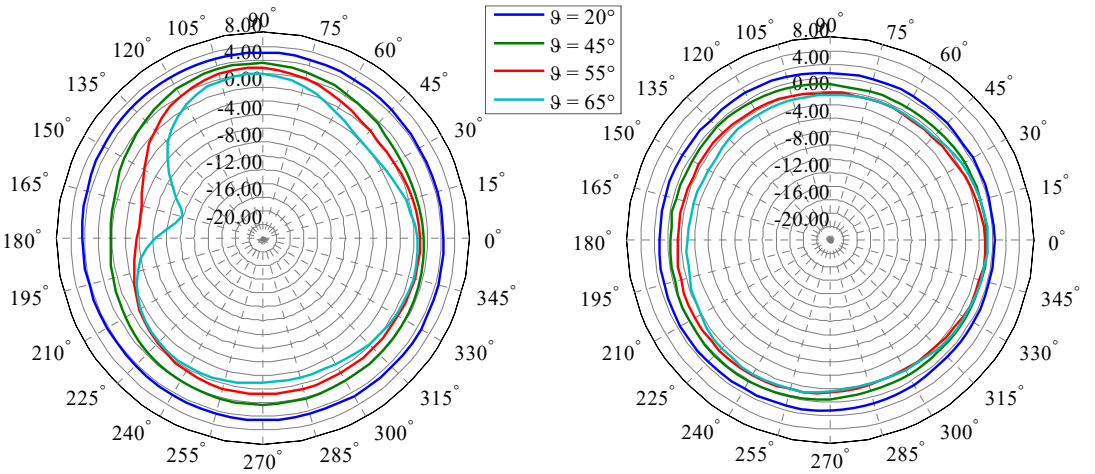


(c) Antenna for GPS-L1/Galileo. Conical cuts at 1575 MHz.

(d) Antenna for SDARS. Conical cuts at 2332 MHz.

Figure 5.8: Radiation pattern (realized gain) of the satellite antennas of the module.

### 5.2.2 Isolation between Terrestrial and Satellite Antennas and Ways to Reduce it

The measured power transmission between the antennas in the module was accurately predicted by the simulation, whose results appears to be in good agreement with the measured one (Figure 5.9).

Despite the close arrangement, the antennas achieve the proper isolation between their feeding ports at almost all LTE frequencies (Figure 5.9-b).

As far as the antenna for the LTE service is placed in the middle of the aerial for SDARS, port coupling between these two antennas is low. At almost all operation frequencies of the LTE radiator, the isolation with the antenna for SDARS is more than 20 dB [3].

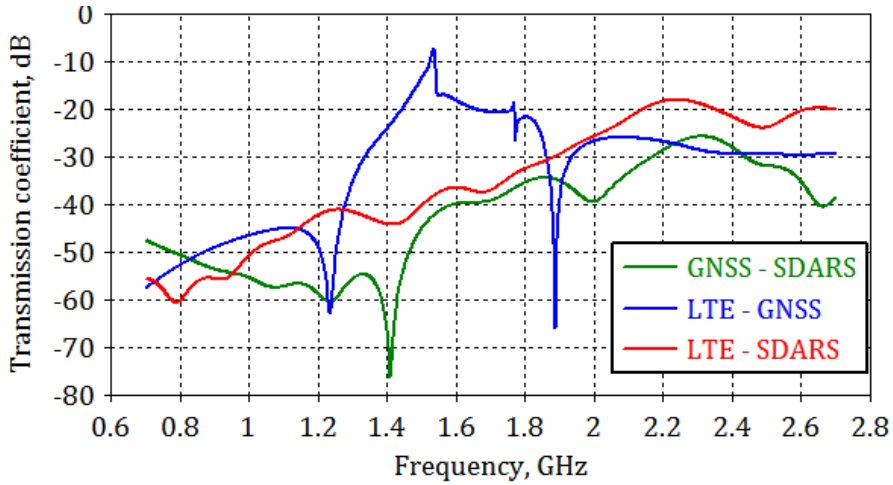


(a) Simulated results.

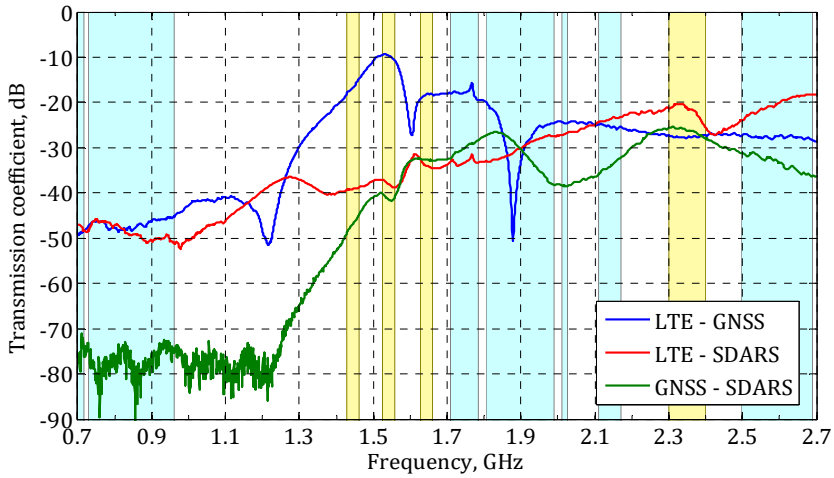


(b) Measured results.

Figure 5.9: Transmission between antennas in the module (blue: LTE frequencies in North Atlantic Region, yellow: other LTE bands).

Moreover, the isolation between the antennas for GNSS and LTE in most of the LTE ranges is greater than 20 dB, whereas only at the frequencies from 1525 MHz to 1559 MHz this value decreases down to 10 dB. Such a small value is caused by the inconvenient position of the LTE antenna relative to the GNSS antenna. At this location, the LTE antenna is no longer invisible for the GNSS aerial since it is not located in the phase centre of this antenna [34].

Even in this case when the antennas for GNSS and SDARS are aligned along one path, they are almost electrically invisible for each other, whereby the decoupling is more than 25 dB at their operation frequencies.

In order to improve isolation between the antenna for the terrestrial LTE service and the radiators for the satellite services in the module, further investigations were conducted by means of ADS, program for the circuit simulation. Better decoupling has been reached by implementing the filters, which is a common technique for the manufacturers of automotive antennas. For this purpose, S-parameters of SAW filters are used, which are available at [82].

Band-pass filters are applied to the aerials for SDARS and GNSS according to their operation frequencies (Figure 5.10). As an additional element, a band-stop filter for the GPS-L1/Galileo frequency in the signal path of the radiator for LTE is used as far as there is no LTE service around the GPS frequency (from 1560 MHz to 1625 MHz).

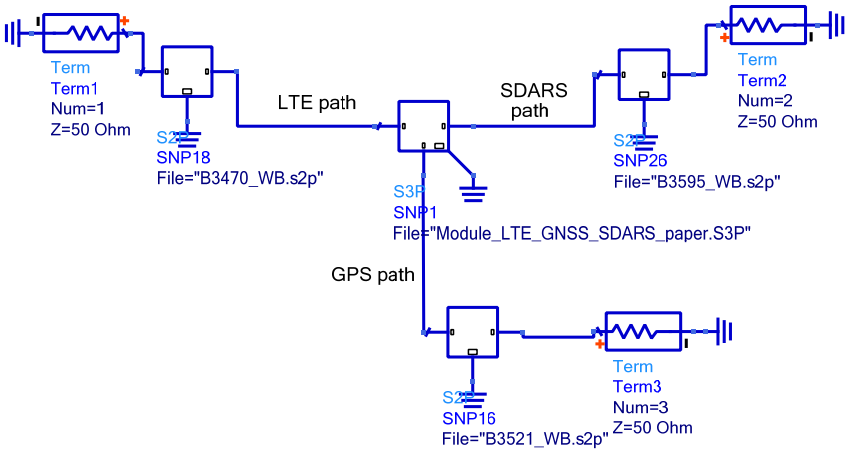


Figure 5.10: Simulation model of the antenna module with applied filters in ADS environment.

After the filters on surface acoustic waves (SAW) were applied, the antennas in the module keep sufficient matching to 50 Ohm, which can even be improved by a

readjustment. Reflection coefficients of the aerials for satellite broadcasting and navigation are below -10 dB. The radiator for the LTE service has a reflection coefficient lower than -6 dB at almost all operating frequencies.

In Figure 5.11, an improved decoupling between the antennas in the module is shown. The isolation between the GNSS aerial and the radiator for LTE was noticeably increased and amounts to 35 dB in the worst case [3]. The decoupling between the antennas for LTE and SDARS is also enhanced to 25 dB in the worst case.

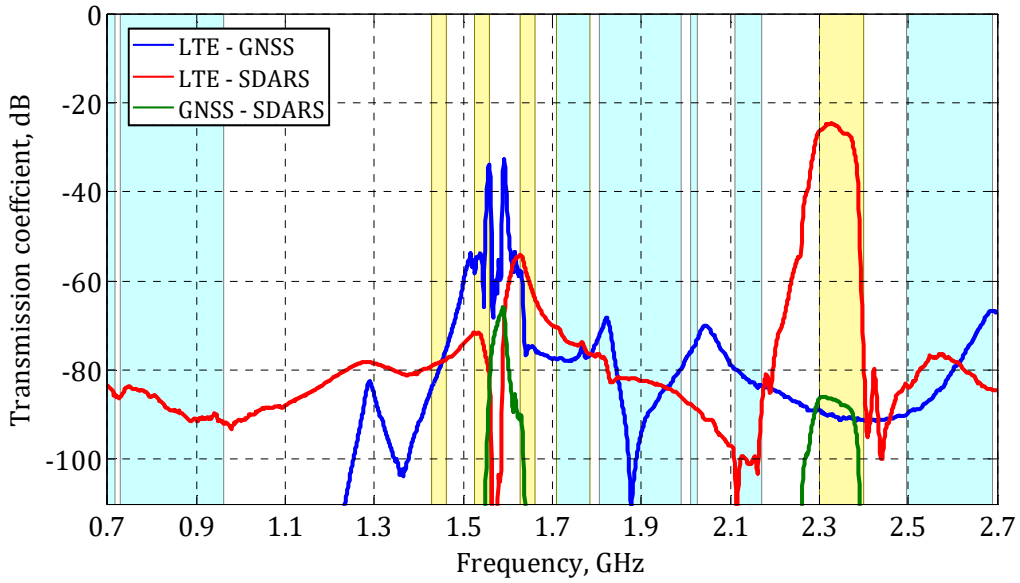


Figure 5.11: Decoupling in the module of antennas for LTE, SDARS and GPS/Galileo. Simulation results with applied SAW filters.

Therefore, by applying the band-rejection filter for GPS-L1 frequency to the LTE path, the strong LTE signals will no longer suppress weak satellite signals in the GPS-L1/Galileo signal path.

Next, we discuss the results of an investigation of an extended version of the antenna module presented in this subsection.

## 5.3 Antenna Module for LTE Communication, Navigation Services and Satellite and Terrestrial Broadcasting

In the current subsection, a combination of antennas for satellite services and LTE cellular communication extended by an antenna for terrestrial broadcasting will be considered.

The antennas for GNSS (GPS/Galileo/GLONASS), SDARS and LTE are placed underneath a plastic housing, while the antenna for the AM/FM/DAB service is outside the cover and it is connected to the LTE antenna via a connection pad in the housing [83]. The mounting volume under the cover has a maximum length of 90 mm, width at the footprint of 46 mm, and the maximum height is 53 mm (Figure 5.12). As a typical shark-fin-formed cover, it has a relative narrow top part that widens towards the ground plane. The height of the cover decreases towards the front as well as the width of the footprint.

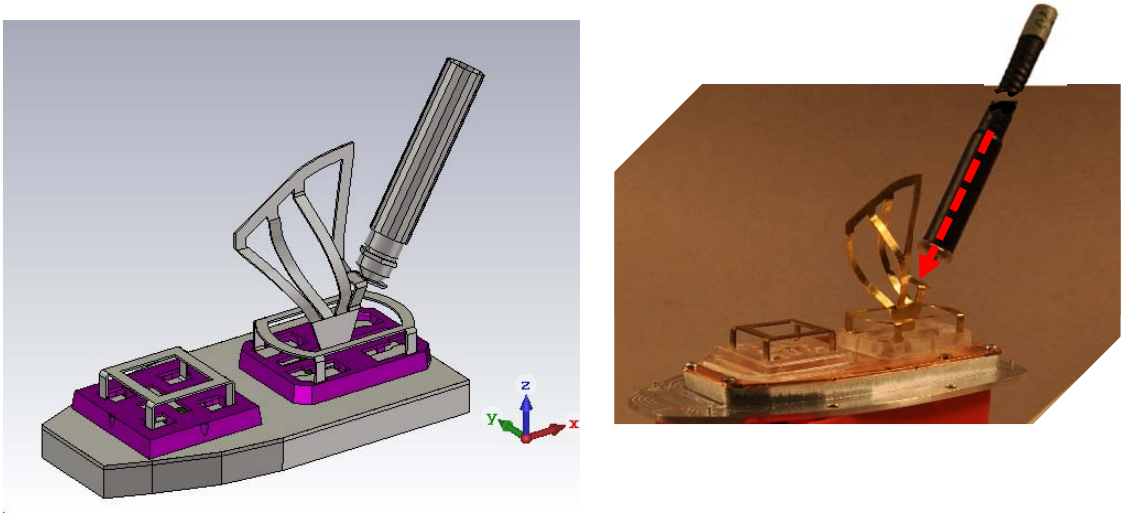


(a) Simulation model.

(b) Photograph of the functional sample (is to be used with plastic cover).

Figure 5.12: The LTE 3D antenna connected with the AM/FM antenna and combined with antennas for satellite reception.

At the higher rear part of the module, the antenna for LTE cellular communication is placed, to which the antenna for terrestrial broadcasting is connected via the metal adapter, which is built in into the cover. Both antennas are located in the centre of the aerial for GNSS. In the front side of the module, the antenna for the reception of satellite broadcasting is positioned. The distance between centres of the satellite antennas as well as between centres of the SDARS aerial and LTE radiator is 45 mm, the greatest possible value limited by the cover's dimensions.

The feeding of the antennas is realized at the bottom side of the circuit board by semi-rigid 50-Ohm coaxial cables, as has been done in all antenna modules described in this thesis.

## *Design Aspects of 3D Antenna for LTE Mobile Service*

The design principle of the radiator for LTE cellular communication is similar to that described in section 3. However, the low and high-frequency parts of the current aerial are connected to each other, forming a single construction that is near to the conical antenna. The cone is made of four strips, which are connected to the common upper part. Identically to the previous LTE antennas, this antenna is cut from one metal sheet and can be produced by a single push-stamping process.

The 3D antenna was designed to be set into the centre of the table-formed aerials for the satellite service. Therefore, its lower part (marked in blue in Figure 5.13) is flat, which enables a lower influence on the satellite aerial, located under the LTE antenna. In the lower part of the radiator's structure, additional corner elements are designed for better stabilization by bending these elements in opposite directions.

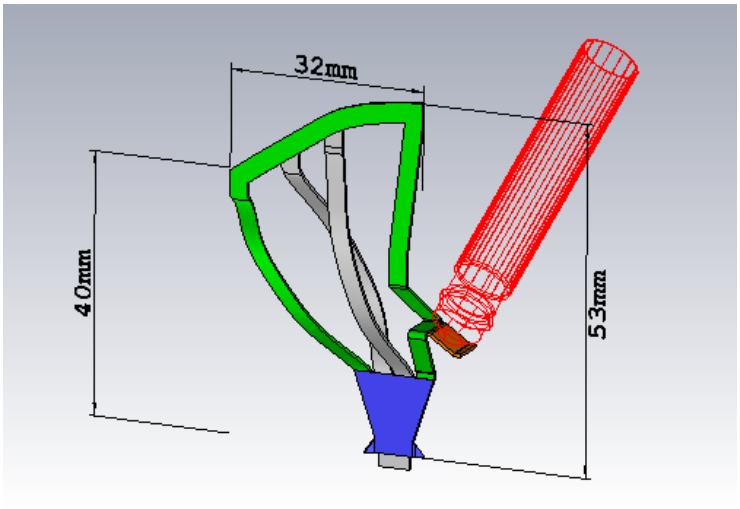


Figure 5.13: Simulation model of 3D LTE antenna of the module.

An outer loop (green in Figure 5.13) together with two wires in the antenna centre (grey in Figure 5.13) and with the flat plate form a cone-shaped monopole, which acts at frequencies between 970 MHz and 2700 MHz. In order to join the LTE structure with the antenna for AM/FM, a connection pad (marked in brown in Figure 5.13) was constructed. Mechanical stability and a proper connection of the pad to the metal adaptor for the antenna for terrestrial radio is secured by the outer loop of the LTE radiator.

A sleeve of the antenna for terrestrial broadcasting (red lines in Figure 5.13) functions as an elongation of the 3D LTE antenna and allows covering the lower LTE frequencies down to 700 MHz.

The 3D structure is 32 long and maximum 12 mm wide, its maximal height is 53 mm at the rear and reduces towards the front side to 40 mm.

### *Antenna for Reception of Terrestrial Broadcasting Signals*

For the reception of AM/FM/DAB signals, an active helical rod antenna is used, which is capacitively coupled with its excitation point (CCHA). Its concept and realizations are described in [84], [85] and [86]. In order to improve a decoupling to the LTE aerial at the LTE lower frequencies, CCHA was extended with third fragment of a different pitch [87].

The simulation model of the helical antenna includes only a metal sleeve, which has the main effect on the aerials for satellite signal reception since it is located in close proximity to them. The helical part itself almost does not affect the simulation accuracy as far as the modified antenna for AM/FM is highly decoupled from other antennas of the module.

### *Antennas for Satellite Signal Reception*

For the reception of satellite signals, two table-formed antennas – one for SDARS and one for GNSS – are utilized, which are designed by the ring antenna concept described above and in [73].

The antenna for SDARS has overall dimensions of 20 mm x 20 mm x 10 mm. It is located in the front side of the combination, as Figure 5.12 shows.

The GNSS antenna was specially designed for the large structures, which are being put in its centre. A top element of the antenna has a nearly elliptical form with a maximum length of approximately 35 mm and a width of 22 mm. The height of the radiator is kept at 10 mm. This aerial for GNSS is placed in the rear side of the module around the antenna for LTE cellular communication and radiator for terrestrial broadcasting (Figure 5.12).

## 5.3.1 Measurement Results

The antennas were measured in the presence of all other aerials of the module. The measurement setup is described in appendixes A.1 and A.2.

The LTE antenna (with the helical radiator, which has been connected to it) achieves demanded impedance matching to the 50-Ohm line at almost all operational frequencies of LTE service without use of any matching network. Within the LTE lower frequency range, the antenna structure reaches reflection coefficients below -6 dB. Only at the frequencies between 700 MHz and 738 MHz are they between

-6 dB and -4 dB due to the insufficient electrical height (< λ/4) of the radiator at these frequencies. Within the LTE middle and upper frequency ranges, reflection coefficients are even below -11 dB (Figure 5.14).

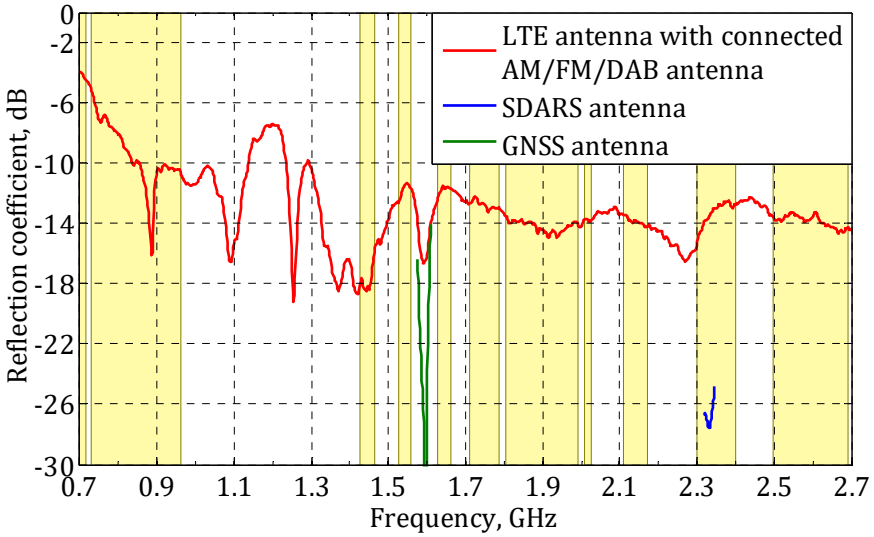


Figure 5.14: Reflection coefficients of the antennas in the module.

The SDARS antenna is perfectly matched to the 50-Ohm line, which is indicated by a low reflection coefficient of below -25 dB. The aerial for the navigation systems has the required level of the reflection coefficient, which is lower than -14 dB at GPS, Galileo and GLONASS operational frequencies.

## *Radiation Properties of the Antennas from the Module*

The sections of PR of the antenna for LTE mobile communication with the connected antenna for terrestrial broadcasting show that the structure obtains properties like monopoles as long as these monopoles are matched to the 50-Ohm signal path at different frequencies, which is not possible for a single monopole. The antenna possesses an omnidirectional RP with deviations from the circular form of nearby ±0.5 dBi (at 850 MHz) and ±1.2 dBi (at 2.4 GHz), as can be noticed in Figure 5.15-a, c. The maximum realized gain of 4 dBic occurs at lower elevation angles of 60° and 70° at frequencies of 850 MHz and 2.4 GHz, respectively.

In the radiation pattern, undesired minor lobes appear at lower elevation angles close to zenith. The level of these minor lobes rises with the frequency increase, as can be observed in Figure 5.15-b, d. The undesired lobes are caused by the large height of the 3D helical antenna construction, as long as the 3-D structure and the sleeve of CCHA build a large monopole-like structure of 72 mm height (Figure 5.16). The influence of the antenna height on the form of its RP can be explained by the example of a thin monopole, which is vertically placed above the infinite-ground plane. The higher the monopole, the narrower the main beam of its RP in the vertical

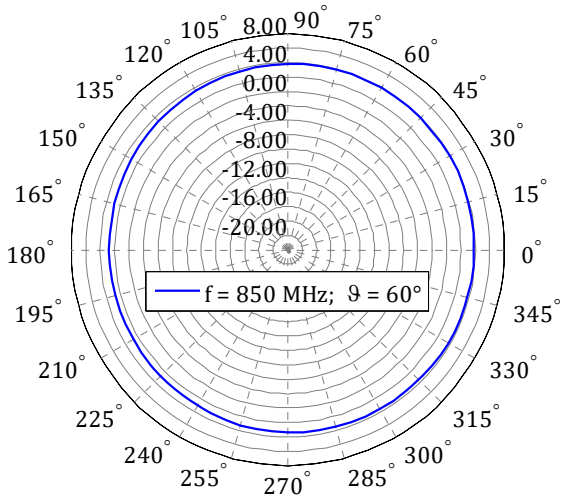


(a) Conical cut in MBD, 850 MHz.

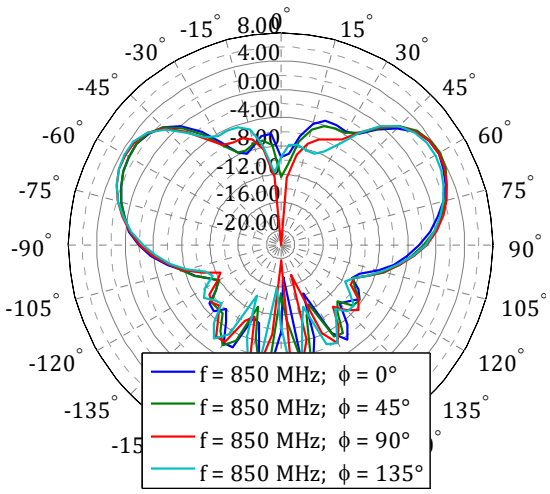


(b) Great circle cuts, 850 MHz.

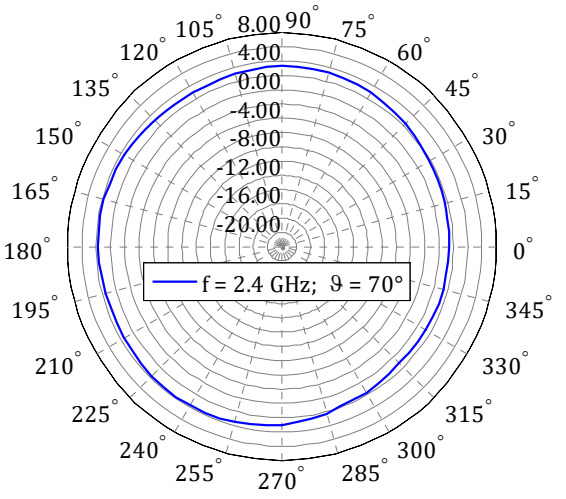


(c) Conical cut in MBD, 2.4 GHz.

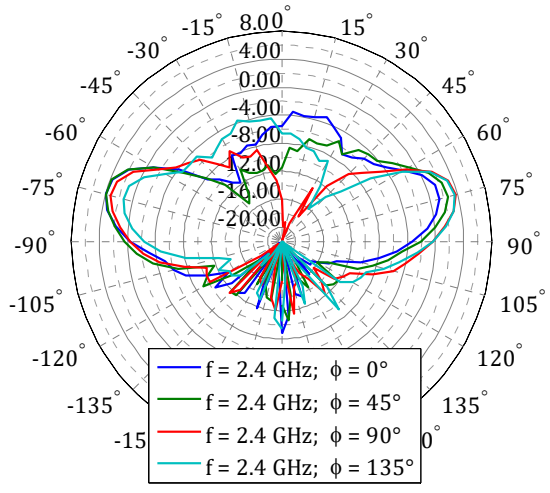


(d) Great circle cuts, 2.4 GHz.

Figure 5.15: Sections of RP (realized gain) of LTE antenna.

plane and the higher the minor lobes. The increase of the monopole's height leads to the change of the current distribution on it, which in turn causes mirror lobes and narrowing of the main beam in the elevation plane. This property corresponds to the typical behaviour of the monopole [54] and it is also valid for all monopole-like aerials and 3D antenna.

The effect of the antenna height can be observed in Figure 5.18, where averaged over azimuth realized gains of the large antenna construction (3-D antenna is combined with CCHA) are compared with those of the 3-D LTE antenna (described in section 3).

As already mentioned in section 3, the dual-band 3D aerial comprises two parts for different frequency ranges, so that the monopole-like structure of 54 mm (Figure 5.16) acts at frequencies from 700 MHz to 960 MHz, while the cone-shaped structure works at frequencies between 1447 MHz and 2700 MHz. Therefore, the antenna height is always around one-quarter of the wave lengths (including taking into account the roof capacitance) over the complete LTE frequency ranges, which provides λ/4-monopole-like radiation patterns without any radiation/reception in zenith and with poor reception at angles near to zenith, as seen in Figure 5.17.

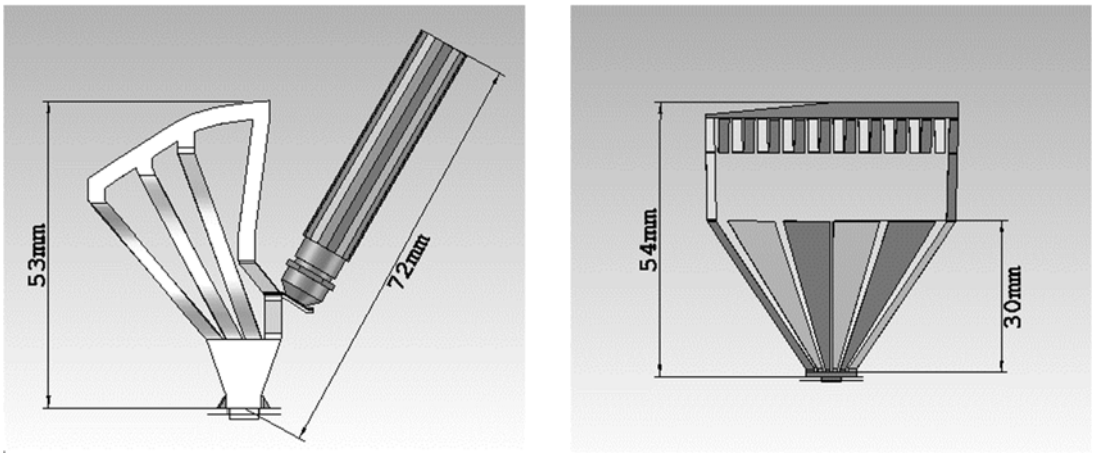


(a) Single-band 3-D/sleeve antenna construction.

(b) Dual-band 3-D antenna structure.

Figure 5.16: Simulation models of the LTE 3-D antennas.

On the contrary, the whole structure of the single-band 3-D antenna with the connected to it sleeve of CCHA (3-D/sleeve construction) acts within complete LTE ranges with the same physical height but with an electrical height, which changes over the frequency. Therefore, at 850 MHz, the 3-D/sleeve antenna construction's

height is around 0.25·λ, whereas at the higher frequency of 2.4 GHz its height amounts to 0.6·λ.

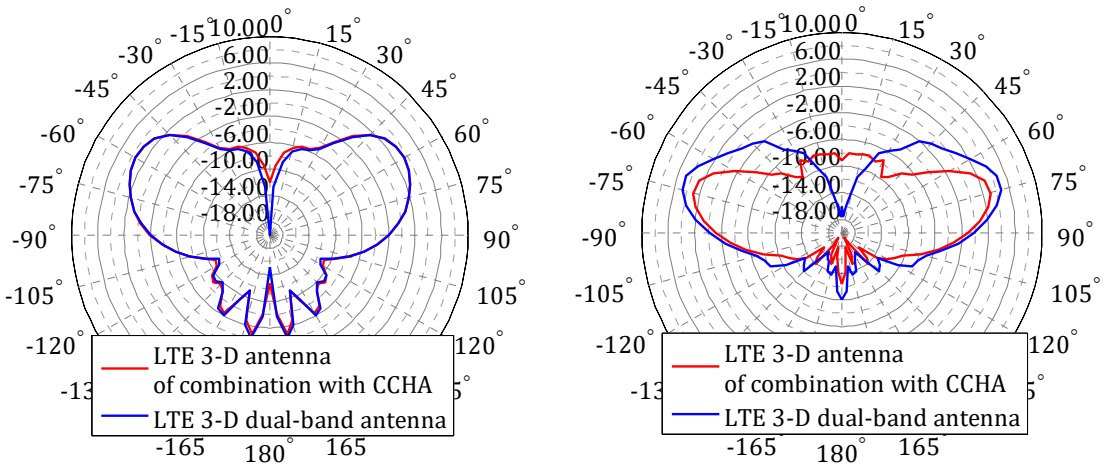


(a) 850 MHz. (b) 2.4 GHz.

Figure 5.17: Comparison of RPs (realized gain, average over azimuth) of the 3-D stand-alone antenna and the 3-D antenna combined with CCHA.

At 850 MHz, the 3-D/sleeve antenna construction has almost the same realized gain and the form of RP as the dual-band 3-D antenna (Figure 5.17-a), since the heights of both antennas are around 0.25·λ. At the frequency of 2.4 GHz in RP of the 3-D/sleeve antenna of the combination, the minor lobes appear with a level of -10

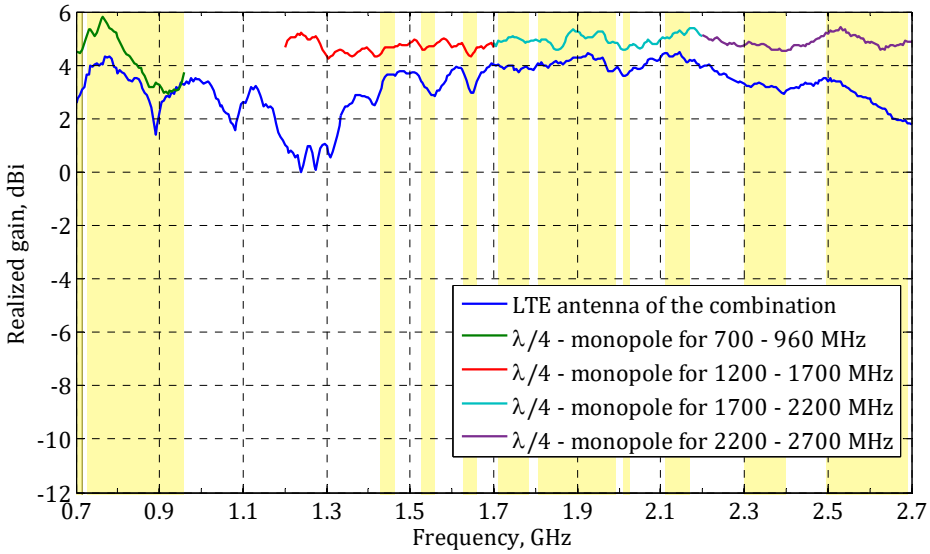


Figure 5.18: Measured realized gain (average over azimuth) of the LTE 3-D antenna with the CCHA connected to it in comparison with the reference monopoles.

dBi, which is nevertheless acceptable. Noticeably, the main beam narrows in the elevation plane.

The LTE 3-D antenna with the CCHA connected to it has realized gain on average only 1.7 dBi lower than that of the four reference monopoles measured under the ideal conditions (Figure 5.18). The radiator is applicable at all LTE frequencies between 700 MHz and 2.7 GHz with the realized gain of approximately 3.7 dBi (on average) and total radiation efficiency of around -1.8 dB.

## *Antennas for Satellite Signal Reception*

Figure 5.19 shows that the radiation patterns of both satellite antennas of the combination are noticeably affected by the large 3-D/helical structure.

The influence of the construction of two terrestrial antennas on RP of the aerial for SDARS becomes apparent in a slight inclination of the main beam towards the driving direction. The realized LHCP gain of the antenna for SDARS amounts to approximately 4 dBic in zenith and is not lower than 2 dBic within the elevation angles of ±45 (Figure 5.19-c) with XPD of around 12 dBic in zenith at the mid-band frequency. The total radiation efficiency is on average -1.9 dB.

The radiation properties of the GNSS antenna are more strongly influenced by the LTE-AM/FM/DAB antenna construction than that of the SDARS aerial. In Figure 5.19, large deformations of RPs can be noticed (Figure 5.19-a, b) at the GNSS frequencies. At 1575 MHz, the realized gain of the antenna is approximately 1.8 dBic in zenith with XPD of around 12 dBic. At the higher elevation angles between 45° and 90°, the antenna's co-polarized realized gain increases up to 5 dBic, whereas the XPD level decreases. At the GLONASS mid-band frequency, the RP for co-polarized realized gain is closer to the circular form than that at GPS-L1 frequency. The maximum RG in zenith is almost 3.5 dBic. The total radiation efficiency of the aerial at GPS-L1/Galileo frequencies is approximately -1.3 dB. Within the GLONASS frequency range, it is higher and amounts to -0.7 dB on average.

## *Decoupling in the Module*

The antennas in the module are well isolated from each other, as is noticeable in Figure 5.20. Transmission between the antenna for SDARS and the LTE 3-D aerial (together with CCHA connected to it) is lower than -20 dB at the LTE operational frequencies of North Atlantic Region (NAR), which are marked in blue in Figure 5.20. Transmission coefficients between the LTE 3-D antenna and the GNSS aerial are below -20 dB at the GPS-L1/Galileo frequency and even below -30 dB within the GLONASS operational frequency bands.

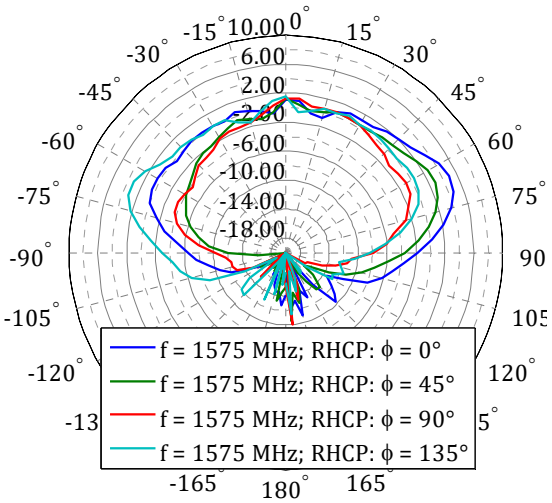


(a) GPS-L1/Galileo carrier frequency.

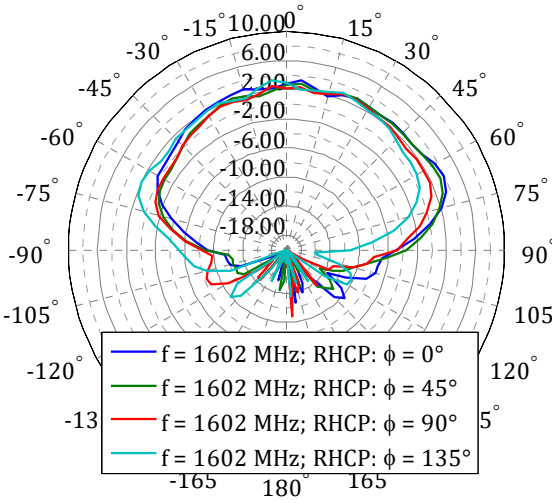


(b) GLONASS mid-band frequency.

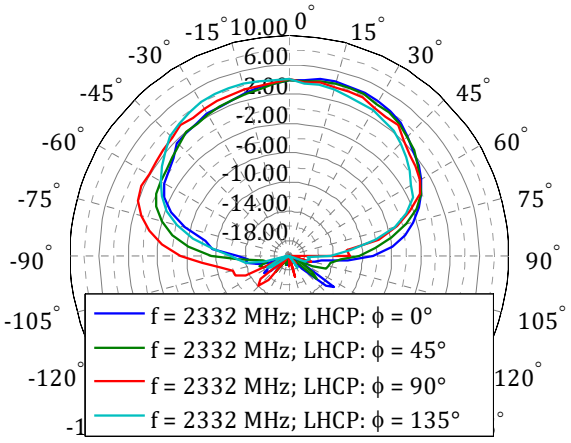


(c) SDARS mid-band frequency.

Figure 5.19: Great circle cuts of RPs (realized gain) of the satellite antennas of the module.

Obviously, there is the same trend in the decoupling between the cellular antenna and the aerials for satellite reception like in the first module, which is presented in subsection 5.2. Overall, transmission between these aerials is very low, except for those satellite antennas located aside the terrestrial one. Thus, for the module from the previous subsection – where the GPS antenna is placed aside the LTE radiator – cross-talk between the antenna for navigation and the radiator for cell-phone service is around -10 dB at the GPS frequencies. In the combination of the current subsection – where the antenna for satellite broadcasting is aside the one

for cellular communication – transmission between the LTE antenna and the aerial for the SDARS is slightly higher than for other aerials of the module (-15 dB).

The satellite antennas are highly decoupled one from another, obtaining values of the transmission coefficient lower than -33 dB (at 1575 MHz) and below -15 dB at 2332 MHz.

If there is a higher decoupling required between the antenna for cellular communication and the satellite antennas, cross-talk between them can be improved (i.e. reduced) by applying band-pass filters to satellite antennas' paths, which is a commonly-used technique.

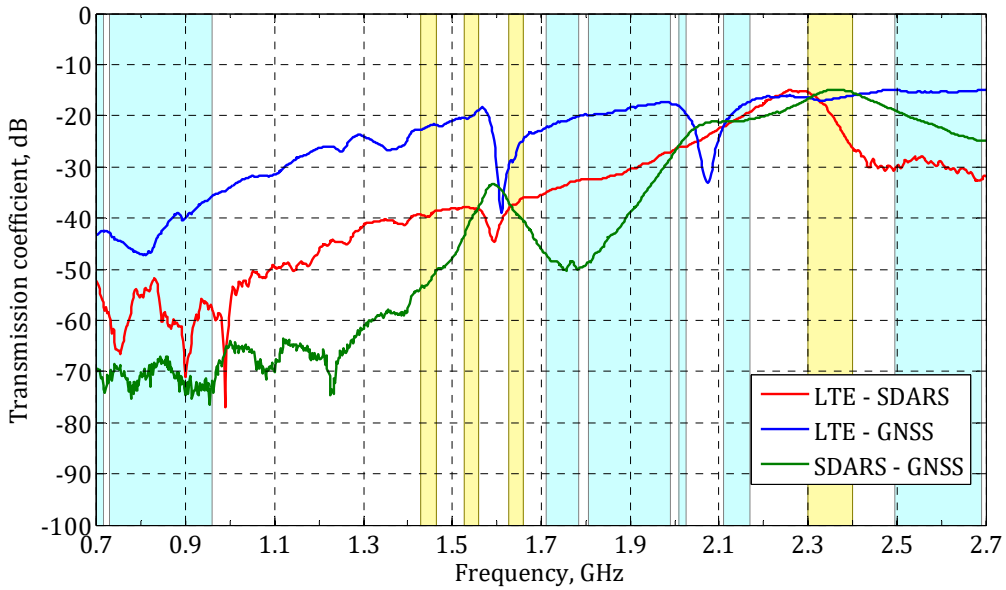


Figure 5.20: Decoupling between the antennas in the module (blue: LTE in Noth Atlantic Region, yellow: other LTE frequencies).

The discussion in the subsections above has focused on the interaction of one 3-D antenna for the cellular communication with several aerials for reception of different satellite services on the vehicle. In the following, we will consider an interference between two 3-D antennas for LTE MIMO and an aerial for reception of the signals from satellite broadcasting as an example, since the cellular communication based on the LTE technology involves using at least 2x2 MIMO to enable the declared high data rates.

## 5.4 Investigation of Cross-Talk between 3-D Antennas for LTE MIMO and Aerial for Satellite Reception

This subsection briefly reports about an investigation of interaction between two LTE antennas for MIMO and a single antenna for reception of satellite radio. The results of this research allow estimating the changes that would happen if the antenna modules above gained an extension for LTE performance, i.e. the second wideband 3-D antenna for MIMO.

The module under research includes two identical 3-D antennas for LTE MIMO, one in the front side and another one in the rear side of the module (considering the orientation of the car and driving direction), which are separated by 60 mm between their feeding points [88]. Since the chosen plastic cover has a shark-fin shape with the slightly smaller height in the front side and the larger height at the rear side, the front-side aerial (left-side in Figure 5.21) is lowered by further 1 mm in the socket, while keeping a safe distance to the conducting bottom side of the chassis.

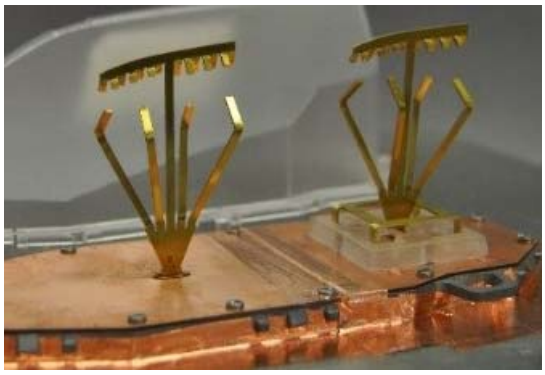

Figure 5.21: 3-D antennas for LTE MIMO combined with the SDARS antenna.

The LTE radiators are constructed in the same manner as the one from subsection 3.3. They have obtained a pyramidal bottom side and an overall narrow design to enable their combination with scarabaeus aerials. Due to the very restricted width (max. 15 mm) and length (35 mm) along with the low height (max. 53 mm for the rear-side antenna and 52 mm for the front-side one), the radiators require additional networks to be matched to 50-Ohm signal paths. After applying these simple networks for the LTE low band (the circuits are similar to that of the aerial from 5.2), the antennas for the cellular communication show sufficient reflection coefficients of around -7 dB at operational frequencies [88].

In the rear side of the module, a 7.5 mm-high antenna for satellite radio is placed enclosing one of the LTE radiators. The scarabaeus antenna with bottom-side fixation is constructed in the same way as the samples of subsection 4.1. Like these antennas, it possesses high discrimination of the signals from the terrestrial interferes and simultaneously it shows high performance for the satellite radio. It also needs a simple matching network, like other scarabaeus antennas. Accordingly, the SDARS aerial reaches an excellent reflection coefficient of lower than -20 dB within the demanded band.

Isolation between the MIMO antennas of the 3-D concept appears to be in strong correlation with that depicted in Figure 3.27. Thus, in the LTE low range, the transmission coefficient for the LTE radiators is below -6 dB. For the LTE middle and high frequency ranges, it is better than -15 dB, since the electrical separation (in terms of wave length) is notably higher than for the frequencies of the LTE low range. This value is even better than the one from Figure 3.27 due to the larger separation of the antennas' feed points in this module and larger distance between the sides of the radiators (around 30 mm in the current sample).

There is a high decoupling of better than 20 dB (Figure 5.22) between the SDARS receiving antenna and the rear-side LTE antenna, which is located in its centre. Such low cross-talk is ensured by the fact that the loop does not receive any waves in its centre, which is seen from the near-field pattern and by different orientation of the electric current on these radiators, as already mentioned in 5.1.

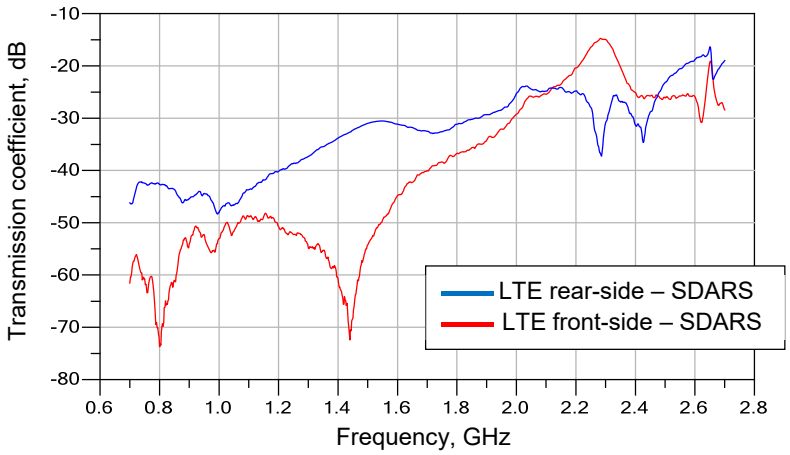


Figure 5.22: Transmission coefficient between LTE antennas and satellite antenna.

The transmission coefficient between the satellite antenna and the LTE radiator – which is placed aside the SDARS aerial – is around -15 dB at the SDARS frequency

(Figure 5.22), which is insufficient for the reliable functionality of the sensitive antenna for satellite signal reception. In such a location, an increase in the spatial separation will help to reduce the impact of the strong signals from the front-side LTE radiator on the SDARS aerial. Another way to reduce the cross-talk between these antennas is to implement band-rejection filters by the same technique as described in subsection 5.2. In this case, a band-rejection filter for the frequencies from 2.32 GHz to 2.345 GHz has to be integrated into the signal path of the LTE radiator, which is located aside the SDARS antenna. This option is fully acceptable since there is no LTE service at the frequencies between 2.3 GHz and 2.4 GHz in NAR where satellite broadcasting is in use, and such a combination with the SDARS aerial will be utilized only in NAR.

This investigation shows that there is no hindrance to enhance the antenna modules from sections 5.2 and 5.3 with the second cellular antenna to enable the use of the LTE service. Notably, the LTE radiators will need additional band-rejection filters for those frequencies where the neighbour satellite antenna operates to prevent the LTE 3-D aerials from receiving the weak satellite signals and reduce the functionality of the antennas for satellite reception in this way.

Besides complicated multi-antenna systems of more than three aerials, there is a demand for two-antenna solutions that combine aerials for satellite signal reception and terrestrial services. In what follows, an investigation of a combination of a compact antenna for satellite reception and an aerial for AM/FM in an extremely restricted mounting volume will be discussed.

## 5.5 Compact Antenna Module for Reception of Navigation Services and Terrestrial Broadcasting

Sometimes access to a simple set of services is preferred, which is normally limited to two or three. In this case, a few antennas for them can be hidden underneath a restricted housing, which is much smaller than a typical shark-fin-formed cover. These changed conditions set further challenges for the antenna design, such as creating extremely compact aerials and ascertaining the best arrangement of the radiators in combination to reduce their impact on one another. In the current subsection, the results of one such study will be shown.

In the following, a very compact antenna for the navigation in combination with a radiator for terrestrial broadcasting – which is meant to be mounted on the roof top – will be discussed [89], [90].

### 5.5.1 Design of Compact Antenna Module

The compact GNSS antenna is integrated underneath a small housing with a maximum length of 49 mm and a width of 40 mm on the chassis level, while the maximum height of the cover is 40 mm. On top of the cover, a radiator for AM/FM/DAB-L is set via a metal adapter. In order to effectively utilize the volume underneath the cover, an amplifier for the aerial for terrestrial broadcasting has been realized on a vertical FR-4 plate, which is put in the centre of the GNSS antenna (Figure 5.23-b).

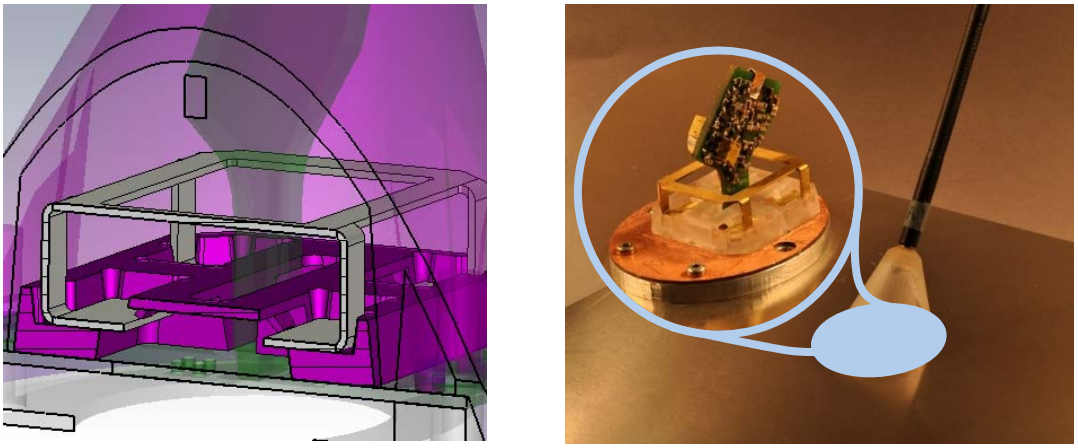

(a) Vertical section of the simulation model. (b) Functional demonstrator.

Figure 5.23: GNSS antenna with AM/FM/DAB-L radiator and its amplifier in the centre.

For the reception of terrestrial broadcasting signals, an active rod antenna (CCHA) together with its high-impedance amplifier (HIA) is used. The radiator is extremely low profile. Its height amounts only 18 mm, thus fulfilling the requirements regarding compactness. The amplifier is printed on a circuit board with a special form. It is very narrow at the lower part (7 mm wide) and the width increases smoothly towards the upper part. Such a special design reduces the influence of the vertical circuit board on the GNSS antenna. Due to the small area of the plate, the components of the amplifier are closely packaged by taking into account the fact that the largest components must be distanced from the metal part of the aerial for the navigation, which is a further solution to reduce the impact of HIA on the GNSS antenna.

The design principles of the ultra-short rod aerial concept and HIA are shown in [84] and [91].

The GNSS antenna is made of a single metal sheet, which is bent in a way to obtain a rectangle loop held by four flat pillars. Each of the pillars ends with a small horizontal plate that represents a capacitor to the ground. In order to define the distance from the small plates to the ground plane, a plastic socket is used. In Figure 5.23-a, it can be noticed that the parallel plate capacitor is filled particularly with the plastic, which perceptibly increases the resulting capacitance of the shortening capacitor and thus allows designing a very compact antenna. From (21) and (22), if half of the volume between the plates will be filled with the plastic, the resulting capacitance will be nearly doubled or will increase by the value calculated by (20).

$$\frac{2 \cdot \varepsilon_{r\_air}}{\varepsilon_{r\_air} + \varepsilon_{r\_plastic}}, \tag{20}$$

where: $\varepsilon_r$ - relative permittivity of the filling material ($\varepsilon_{r\_plastic}$ of polycarbonate at 1575 MHz is around 2.6; $\varepsilon_{r\_air}$ of the air is approximately 1).

Accordingly, due to the parallel including, the resulting capacitance is

$$C_{resulting} = C_{air\_filled} + C_{plastic\_filled}, \tag{21}$$

where $C_{air\_filled}$ – capacitance of a parallel plate air-filled capacitor, F,
$C_{plastic\_filled}$ – capacitance of a parallel plate plastic-filled capacitor, F.

In order to roughly calculate the values of these capacitances, the common formula (22) for the parallel plate capacitors can be applied. Although it does not consider the corner effects, this equation gives a reliable estimation of the capacitances' value and consequently the required geometrical dimensions of the small plates.

$$C = \frac{S \cdot \varepsilon_0 \cdot \varepsilon_r}{d}, \tag{22}$$

where $\varepsilon_0$ – dielectric constant, F/m,
$\varepsilon_r$ – relative permittivity of the filling material,
$S$ – square of the plates for the corresponding filling, m$^2$,
$d$ – distance between the plates, m.

By using this technique, the top part of the aerial obtains very low dimensions of only 25 mm to 20 mm (length to width). It is lifted by the plastic part to the height of 10 mm. The plastic socket slightly increases the footprint to 29 mm x 26 mm.

### 5.5.2 Antenna Simulation and Measurement

The simulation model of the combination does not contain CCHA and the circuitry of HIA on the vertical plate by reason of the simulation duration. Instead of the circuitry, the vertical plate is covered double-side by the metal that is connected to the conducting ground plane. Nevertheless, the simulation delivers sufficiently accurate results so that only a slight tuning of the manufactured sample to the demanded resonance frequency is required. The similarity of the simulation and measurement results are shown in Figure 5.24-a, where the impedance curves are depicted for the simulation model with the introduced simplifications and that of the functional sample after the adjustment, which is measured together with the active rod antenna and its amplifier on the assembled circuit board.

The measurement results show very good impedance matching to the 50-Ohm signal path within a wide-frequency band: for the -10 dB level of reflection coefficient, the bandwidth is approximately 60 MHz and the antenna provides a fine matching condition with values lower than -20 dB of reflection within a 32 MHz frequency band (Figure 5.24-b).

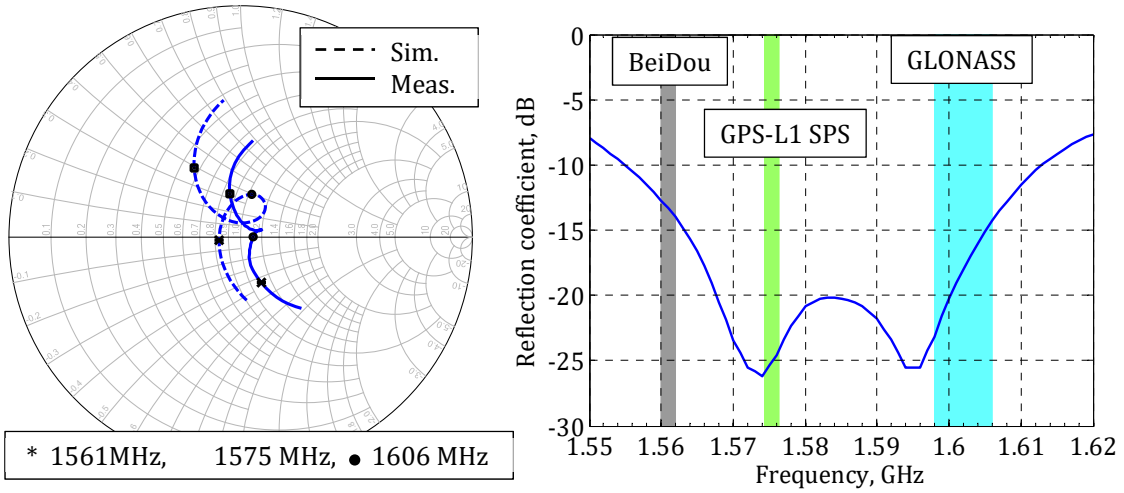


(a) Impedance curves freq. 1.55 GHz – 1.62 GHz.

(b) Reflection coefficient (measured).

Figure 5.24: Impedance properties of the GNSS antenna of the combination.

The RHCP realized gain in zenith ($\theta$ = 0°) of the GNSS antenna reaches values of 4.3 dBic at the frequency of 1.575 GHz and obtains at least 3.6 dBic at the highest GLONASS frequency of 1.606 GHz (Figure 5.25). The realized gain of a cross-polarization (LHCP) is approximately -7 dBic at 1.575 GHz and it is not greater than -3

dBic at 1.606 GHz. Accordingly, the cross-polarization is discriminated by 11 dBic at 1575 MHz and by 7 dBic on average over the GLONASS operation frequency bands (1602 ±3.73 MHz).

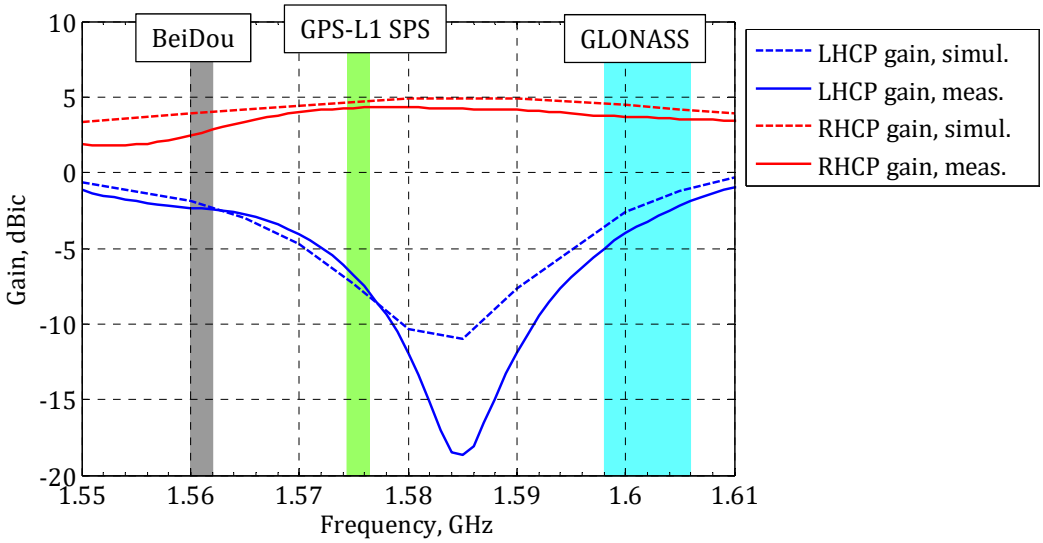


Figure 5.25: Simulated and measured gains (RHCP and LHCP) in zenith of the GNSS antenna of the module.

Great circle cuts of the radiation pattern of the GNSS antenna at the GPS-L1, Galileo, BeiDou-2 and GLONASS frequencies are presented in Figure 5.26. The antenna yields an almost plane-symmetrical RP with slight deviations, which are mainly caused by the vertical plate of HIA (see section 4.2). At elevation angles of ±60°, it achieves positive realized gain and at elevation angles of ±30° it obtains more than 2 dBic. These results show that the loop antenna can not only be combined with a complex terrestrial antenna in its centre, but even under such complicated conditions it shows superior characteristics compared to single patch antennas with a similar footprint, even if these are measured under ideal conditions [21].

The antenna possesses total radiation efficiency of around -2 dB on average over its operational frequencies. As can be noticed, this value is almost 1 dB lower than the total radiation efficiencies of other table-formed antennas described in this thesis, which indicates additional losses in the structure. These losses are caused by the polycarbonate filling between the plates of the shortening capacitances.

Consequently, the reduction of the antenna dimensions by the increased values of the shortening capacitances leads to a decrease in the antenna efficiency, as expected. This trend is also observed by the example of the low-profile antenna for

SDARS, which is discussed in section 4. The functional sample of 10 mm height obtains a radiation efficiency of around -0.5 dB [73], while the lower one (of 7.5 mm

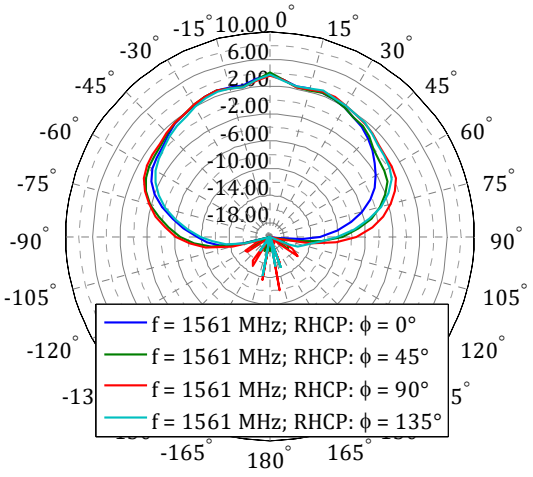


(a) BeiDou-2 carrier frequency, 1561 MHz.

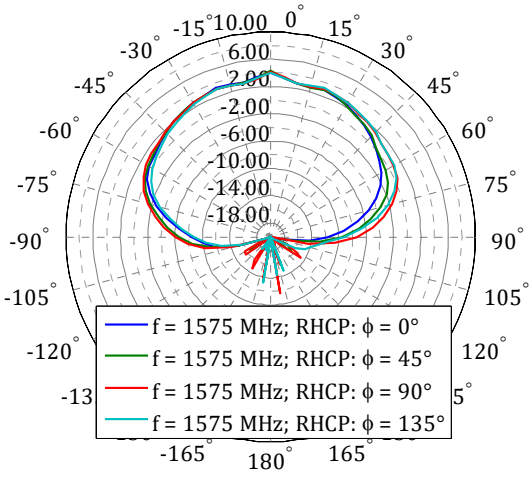


(b) GPS-L1 and Galileo carrier freq., 1575 MHz.

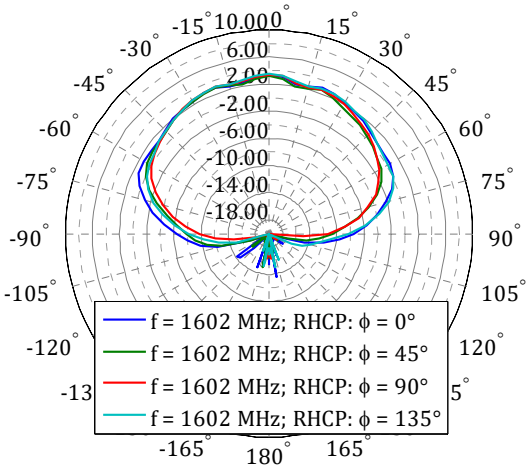


(b) GLONASS mid-band frequency, 1602 MHz.

Figure 5.26: Great circle cuts of RP (realized gain) of the GNSS antenna.

height) with the larger plates' square of the shortening capacitances reaches the lower value of -1 dB (see section 4), considering that the shortening capacitances of both samples are realized in the form of the parallel plate capacitors with air filling and both antennas have the same footprint.

Even in such restricted volume and in combination with the large radiator for terrestrial broadcasting and its amplifier in the centre, the interoperable GNSS antenna for all common navigation services shows its high performance. It ensures a stable reception of GPS, BeiDou-2, Galileo and GLONASS signals in the L1 frequency band due to high realized gain (more than 2 dBic within ±30°) in required elevation angles together with sufficient total radiation efficiency of around -2 dB and perfect matching to the 50-Ohm signal path with a reflection coefficient below -12.5 dB.

***Summary***

The investigations performed show that the radiators of the 3-D LTE concept can be successfully combined with the antennas of scarabaeus type underneath a common housing with the strictly-limited volume. Thus, such combinations allow covering a wide spectrum of services with only single module. However, the dense placement of the aerials in these modules poses a problem of mutual coupling between the radiators, which becomes evident in undesired mutual effects, such as blocking of the sensitive satellite antennas by strong antennas for cellular communication, especially if the latter are in transmitting mode. In this section, several combinations of antennas for cellular communication, navigation, satellite radio and terrestrial broadcasting have been discussed and the ways to increase decoupling between the ports of the antennas included in these modules have been shown. These combinations are designed for the roof-top mounting.

A trend of totally or partially hiding antennas underneath a car's surface has recently been observed. Therefore, some research regarding the functionality of antennas for satellite reception in hidden positions has been carried out, whereby the results of two such studies will be discussed in the following.

# Chapter 6

# Compact Satellite Antenna Modules for Blade Mounting on Cars

Along with the use of shark-fin-formed covers for an antenna hiding in a roof-top mounting position on a car, a blade mounting is widely implemented. Through this mounting, an antenna module is hidden in a cavity that is usually made in a car roof or trunk lid. The module is covered by a flat plastic cover, which follows the form of the car's body so that it is completely invisible (Figure 6.1). Since in such a mounting the aerials are confined from the sides, their performance is substantially deteriorated at elevation angles near to the horizon, while at angles near to the zenith the radiators operate sufficiently well. Therefore, the blade mounting is well suited for the antennas for satellite signal reception due to their hemispherical RP with main reception at near-to-zenith elevation angles. However, antennas for terrestrial services can also be mounted in the hidden position, as done by the authors of [92].

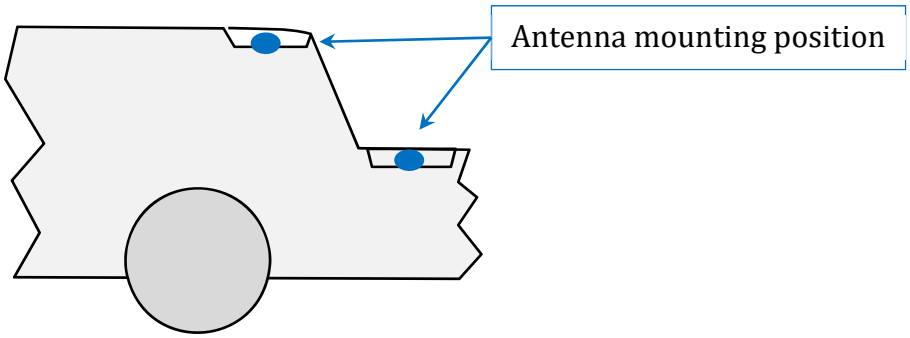


Figure 6.1: Schematic representation of an example of an antenna blade mounting.

In the current chapter, hidden satellite antenna modules will be considered. The discussion will start with a stand-alone hidden SDARS antenna and will be contin-

ued with a compact module of two antennas for the reception of the satellite broadcasting that form a diversity module for more reliable reception in the Rayleigh fading scenario (for example, while driving underneath a dense foliage) [93], [94].

## 6.1 Hidden Antenna for SDARS with Improved Out-of-Band Signal Rejection

Hereafter, the low-profile antenna for a hidden roof-mounting will be discussed. Its simulation model and a photograph of the functional demonstrator are shown in Figure 6.2.

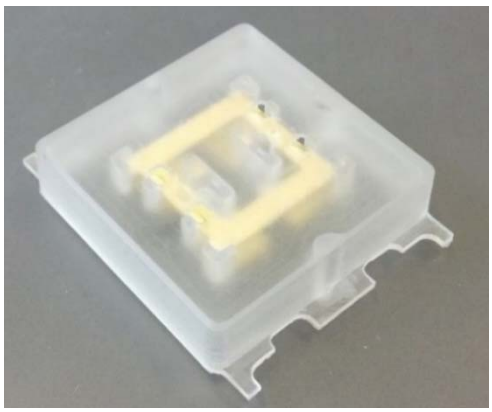

(a) Functional sample.

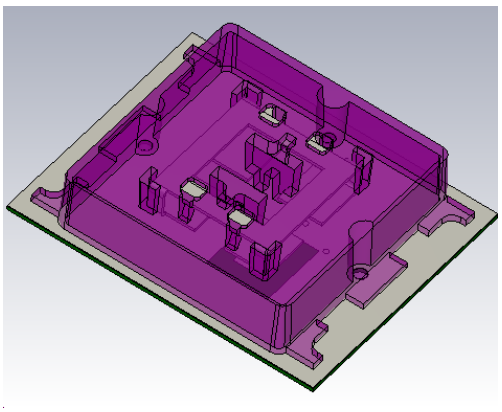

(b) Simulation model (the cavity is hidden).

(c) Antenna in the hidden position.

Figure 6.2: SDARS antenna of 7 mm height for a blade mounting.

The antenna metal part is only 7 mm high and 20 mm x 20 mm in width and length. The table-formed metal part is protected from ESD by a plastic cover, the special design of which allows its use as a supporting element for the antenna (it is

outlined in dark in Figure 6.2-b). The metal part is suspended in the cover on four plastic hooks constructed in pairs at the opposite sides. The suspension height and the distance from the feet to the ground plane are exactly defined by two inner columns and ledges on them. Additionally, the antenna is precisely positioned by means of four guiding elements at each corner. This fixation technique eliminates the production of an additional supporting plastic element, thus reducing the complexity of the structure as well as the manufacturing costs. Moreover, there is no plastic between the small horizontal plates and the conducting plane due to the top-fixation and consequently there is some reduction in thermal losses in the parallel capacitances.

The full height of the antenna underneath the ESD protection cover is 9 mm. Such a low profile enables its location in different hidden positions, like a roof-top or trunk-lid mounting in a cavity. From the top side, the antenna is covered by a flat robust plastic plate, which follows the roof profile without any protrusion from the car's exterior.

The measurement results of the functional demonstrator appear to be in strong correlation with the simulated one observed in Figure 6.3-a. Both simulated and measured impedance curves contain a point of inflection, which indicates the antenna resonance. Noticeably, the resonance (operation) frequencies of the manufactured aerial and its simulation model slightly differ one from another, although the difference only amounts to 15 MHz. This and other discrepancies are caused by

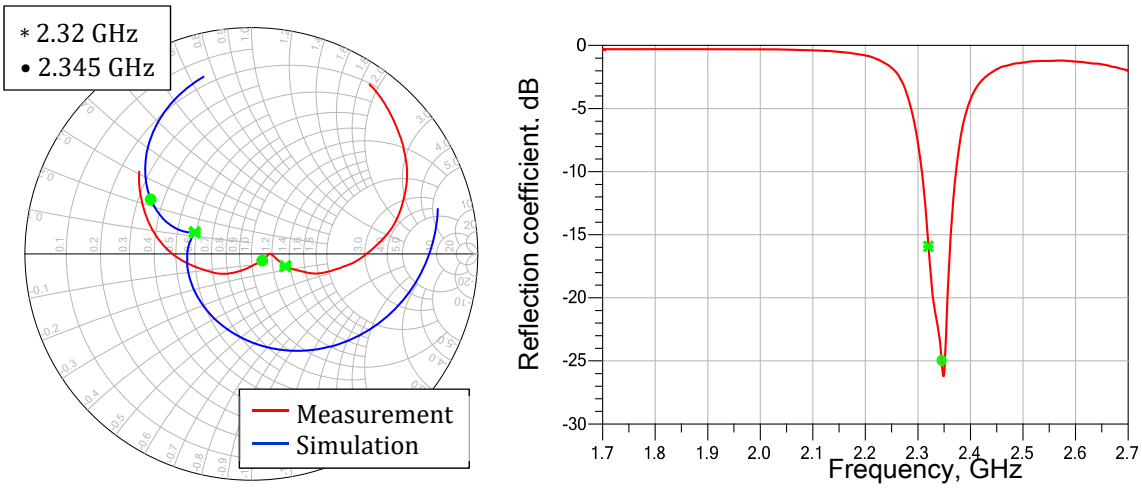


(a) Simulated and measured impedance curves (from 2.2 GHz to 2.4 GHz).

(b) Measured reflection coefficient.

Figure 6.3: Impedance characteristics of the low-profile antenna for SDARS service (7 mm height).

some simplifications made in the simulation model. Thus, there are no screws in the simulation model and the opening for the antenna mounting has an ideal rectangular form with the constant distance to the aerial, whereas it is non-homogeneous in the praxis. The discrepancy between the simulated and measured curves is also caused by tolerances in the utilized materials.

Obviously in Figure 6.3-a, the loop of the impedance curve is greater than the that of the SDARS antenna samples discussed in section 4.1, which proves the statement about the improvement of the out-of-SDARS-band signal rejection by lowering the radiator's height.

Despite the adverse mounting position in the cavity, the antenna still shows good radiation properties. The form of the radiation pattern is hemispherical and symmetrical as demanded, as can be seen in Figure 6.4-a. The LHCP realized gain is only 0.5 dBic lower than demanded by the provider of the satellite broadcasting.

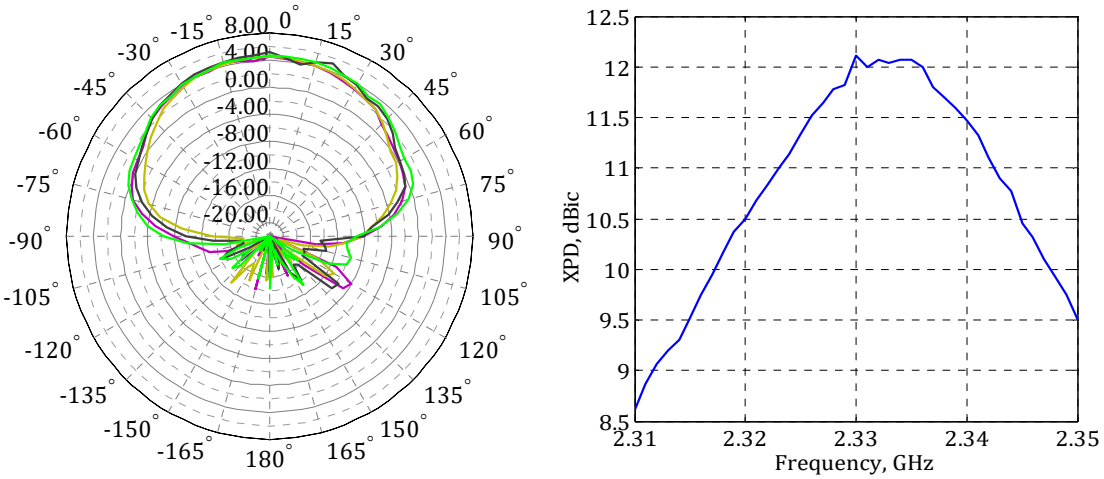


(a) Conical cuts of RP (LHCP realized gain) at 2.332 GHz.

(b) Cross-polarization discrimination.

Figure 6.4: Radiation properties of the low-profile antenna for SDARS in hidden position.

Cross-polarization is discriminated by 12 dBic at SDARS mid-band frequency and it is not lower than 10.5 dBic at the range limits. The operational bandwidth in terms of the acceptable XPD level (at 10 dB level) is around 33 MHz. This is sufficient to compensate possible frequency shifts caused by external factors and production tolerances since the bandwidth of SDARS is 25 MHz.

The hidden SDARS antenna reveals high filtering properties, rejecting the out-of-band VP signals. The VP realized gain at the frequency 2.4 GHz is below -2 dBi at

an elevation angle of 30°, -3 dBi at 60° and -9 dBi at 90° (Figure 6.5). These values are even 3-5 dBi lower at frequencies between 2.41 GHz and 2.7 GHz.

At the same time, the aerial reliably receives the VP signals from terrestrial repeaters of the satellite broadcasting within the band. As Figure 6.5 shows, the VP realized gain in-SDAR-band is around 1.5 dBic at an elevation angle of 30°, near -0.5 dBic at 60° and -7 dBic at 90°.

The antenna obtains sufficient total radiation efficiency of -1.4 dB on average over the operational frequencies. This value is 0.4 dB lower than that of the SDARS antenna for the roof-top mounting (see section 4.1) due to the disadvantageous mounting in the deepening.

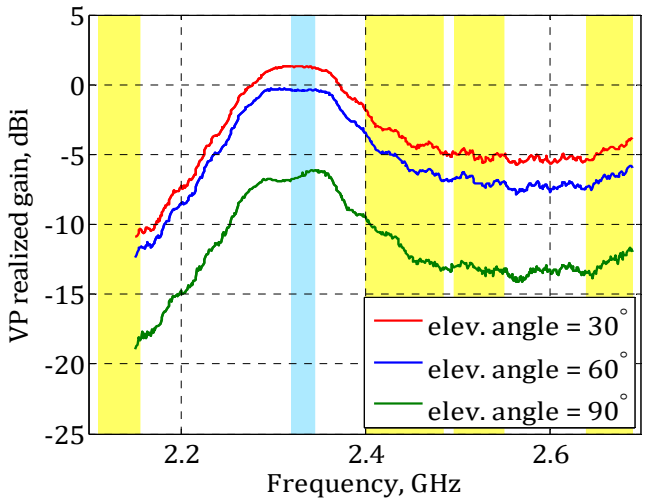


Figure 6.5: Measured VP realized gain of the low-profile hidden antenna for SDARS (blue – SDARS range, yellow – LTE frequencies).

Although stand-alone antennas are well suited for the satellite signal reception in Line-of-Sight, they cannot provide a stable reception while driving underneath a dense foliage. Therefore, deep signal fails occur, causing even long mutes in the radio. In order to enhance the function of the stand-alone aerials for the satellite broadcasting, further antennas with another form of RP can be inserted in the module to form a pattern and maximum-ratio-combining diversity [95], [74].

The next subsection discusses an investigation of a diversity module hidden in the extremely small cavity for reception of the satellite broadcasting.

## 6.2 Hidden Compact SDARS Diversity Antenna Module

Herein, a diversity combination will be discussed, which has been designed for the hidden mounting in a very small cavity of 40 mm x 40 mm. The current research is based on the diversity concept published in [95]. There two aerials of the scarabaeus principle were combined with the same footprint. The combination is meant to be located on the top of the conducting plane and occupies the volume of 45 mm x 45 mm x 10 mm. In the current work, a much compacter solution for the hidden mounting is proposed.

The diversity module is formed by two antennas for the reception of satellite broadcasting with the different shape of RP forming a diversity. The aerials are combined by a design with a common footprint: in the centre of an outer antenna – which is much larger – a smaller antenna is located. The inner radiator is a ring-shaped antenna with a hemispherical radiation pattern. Some variations of this aerial type are discussed in section 4.1, [34] and [73]. The outer radiator is a loop antenna of the second resonance order with toroidal RP.

The overall dimensions of the antenna module together with an ESD protection cover and plastic supporting element are 39 mm x 39 mm x 12 mm. The radiators are extremely small: the inner aerial is only 15 mm x 16.5 mm x 10 mm, the outer antenna is maximum 37 mm in width and length and 8.6 mm high to enable their mounting in a square cavity with the side length of 40 mm.

The outer antenna is designed by a concept of a frame antenna of the second resonance order [73], along the structure of which two wave lengths of the current flow in contrast to the inner antenna, where only one wave length fits. The top element (ring) has taken a near octagonal shape with eight segments, which are identical in quartets (one by one). Each segment ends with a shortening capacitor, which is realized by a parallel plate air-filled capacitor in a similar way as the shortening capacitors of the inner antenna.

The current distribution along the ring antenna of the second order leads to the toroidal RP with MBD at an 70° elevation angle, while the compact antenna of the first order possesses hemispherical RP with the main radiation near zenith. Thus, these two antennas build a pattern diversity with high gain in zenith and at elevation angles between 0° and ±50°, which is provided by the ring antenna of the first order (main antenna), and with a strengthened reception at angles from 50° to 70° (and from -50° to -70°), which is enabled by the ring antenna of the second order (auxiliary antenna).

The simulation model and the functional demonstrator are shown in Figure 6.6. Here, the diversity module is lowered by 7 mm in the cavity, so that the module protrudes by only 5 mm above the plate (Figure 6.6-c). From the top side, the combination is hidden by a flat design cover and is mounted in an outcut in the roof of a car, as shown in Figure 6.1.

The waves that are coupled by the first-order ring antenna from the free space propagate further through one of its legs to its separate 50-Ohm output. At the antenna feed leg, a simple matching network is realized, which comprises a serial capacitor and a parallel inductor made in a similar manner as the networks in section 4.1. The same is valid for the ring antenna of the second resonance order.

The hidden diversity module was realized according to the CAD model, which was designed and calculated in CST Microwave Studio. The combination was measured under the conditions described in appendixes A.3 and A.4.

Despite the very small overall sizes, the main antenna shows a reliable performance within the whole SDARS frequency range. Its LHCP gain in zenith reaches 4.7

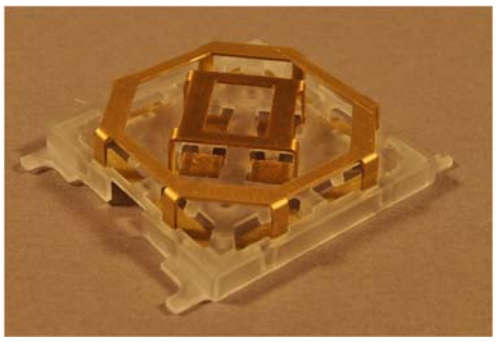

(a) Functional sample.

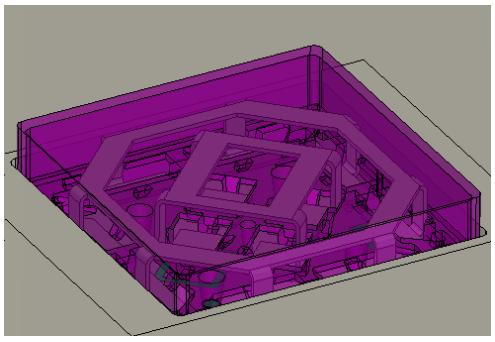

(b) Simulation model.

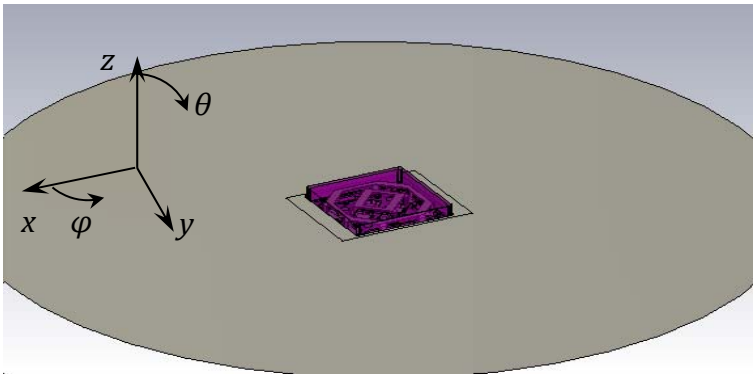


(c) Simulation model in the hidden position.

Figure 6.6: Compact SDARS diversity antenna module for a blade mounting.

dBic, while its cross-polarized gain (RHCP) is discriminated by around 26 dBic at the mid-band frequency and is not lower than 14 dBic at the band limits (Figure 6.7-a).

In Figure 6.7-b, it can be noticed that the radiation pattern of the antenna at the SDARS mid-band frequency is almost symmetrical, whereby only slight deviations appear at the elevation angles near to the horizon. The same is valid for all frequencies between 2.32 GHz and 2.345 GHz.

The reflection coefficients of the antenna within the SDARS frequency band are below -12 dB, as demanded from the matching to the 50-Ohm feeding line. The main antenna possesses relatively good radiation efficiency, which amounts to -1.2 dB. This value is slightly reduced by the mismatch loss to -1.4 dB (total radiation efficiency) on average over the operational frequencies.

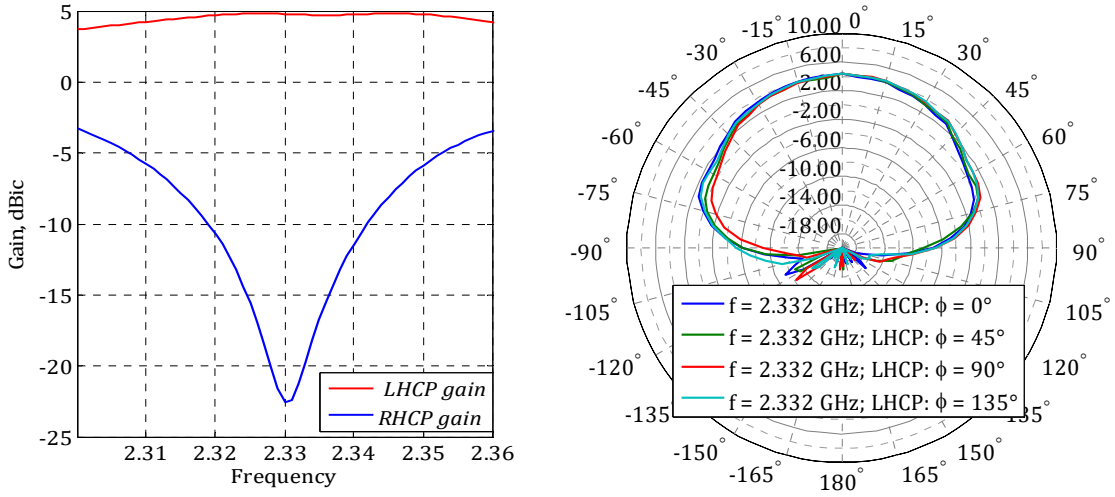


(a) Gain in zenith.

(b) Conical cuts of RP (gain) at 2.332 GHz.

Figure 6.7: Radiation properties of the main antenna of the diversity module.

The auxiliary antenna can be used within either Sirius or XM band parts due to the extremely low sizes and consequently the narrow bandwidth. The considered antenna for the diversity system is adjusted for the XM segment with operational frequencies between 2.335 GHz and 2.345 GHz, since the main part of the SDARS GEO satellites broadcast the radio signals at these frequencies.

In contrast to the double-ring diversity module mounted above – the conducting plane [73] – the integration of this antenna combination into a cavity leads to surface currents along the cavity's edges, which causes a more inhomogeneous behaviour in azimuth. The deviations in radiation pattern are obvious and amount to 6 dB in MBD (70°) in the worst case, as Figure 6.8 shows. The non-symmetry of RPs is caused by different conditions for the segments of the second-order ring antenna.

Thus, four segments are located along the walls of the cavity, whereas other four segments "smooth" over the edges of the cavity. Such different conditions lead to the different types of the waves' coupling by the metal ring and thus the different forms of the RP's fragments.

The maximum LHCP gain in MBD amounts to around 3 dBic at three example frequencies, at which the radiation patterns by gain are depicted (Figure 6.8). Cross-polarization discrimination on average over azimuth (for elevation angle 70°) is around 2 dBic at the frequencies of the XM segment.

The radiation efficiency is -2 dB on average over operational frequencies due to the very small size of the antenna, especially in terms of the corresponding wave length (the circumference of the ring in only 0.57λ instead of the required 2λ length).

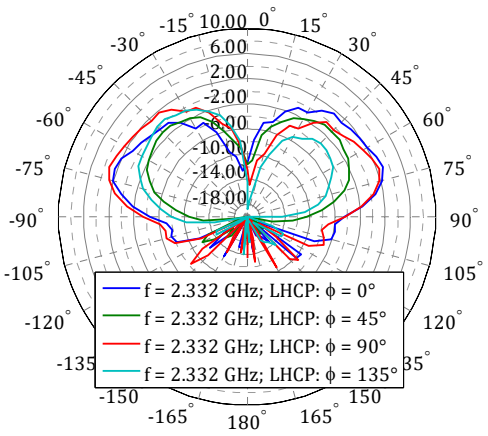


(a) 2.332 GHz (XM lower frequency limit).

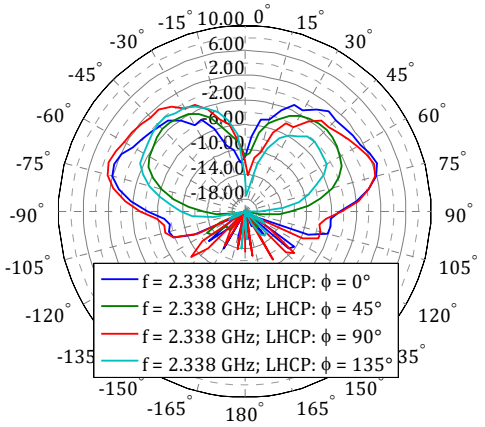


(b) 2.338 GHz (XM mid-frequency).

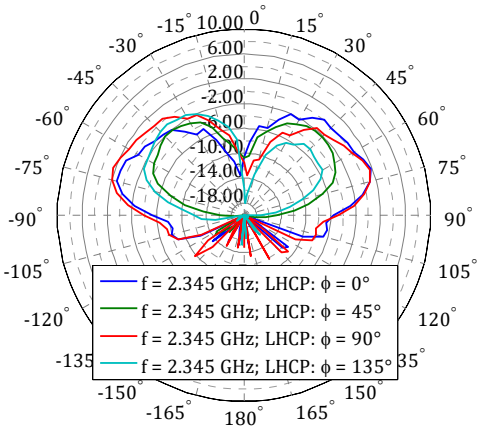


(c) 2.345 GHz (XM upper frequency limit).

Figure 6.8: Conical cuts of RP (gain) of the auxiliary antenna from the SDARS diversity set.

The value of the total realized efficiency is lowered by the mismatch losses, which can be reduced by the further adjustment of the existing matching network.

This antenna diversity set can be used in a scan/phase diversity system, as described in [96]. In the diversity system according to this principle, the phases of the output signals – which come from both antennas – are aligned by the power combiner to reach the new output signal with significantly improved SNR.

In Figure 6.9, the enveloping curves of the superposed gains of the antennas in the module are shown for the case when the phases of the signals coming from both aerials are in the best-phase situation provided that the amplifiers of both antennas insert the same noise (has the same noise figure). During the evaluation of the diversity-RP, the phase of the signal received by the main antenna was considered to be constant (of 0°), while that from the auxiliary aerial was continually changing to scan for the best case.

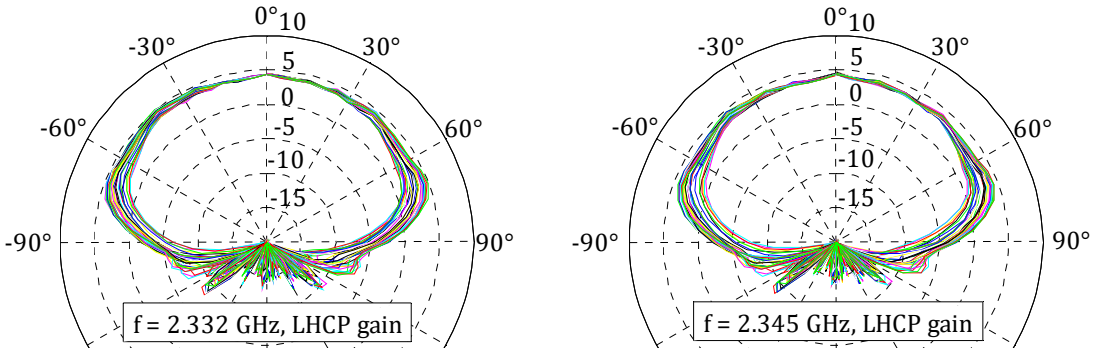


(a) 2.332 GHz (b) 2.345 GHz

Figure 6.9: Conical cuts of RPs (summed LHCP gains) at φ from 0° to 360° with 5° step.

As Figure 6.9 shows, deviations from the symmetrical form in the radiation pattern are much smaller than those in RP of the second-order ring antenna. It indicates some smoothing effect of the main antenna (ring antenna 1st order).

Noticeably, the antenna diversity combination obtains maximum LHCP gain of near 4 dBic at elevation angles of up to ±75° at both example frequencies of the XM segment, which is approximately 4.5 dBic greater than the LHCP gain of the main antenna only. This high gain of the diversity combination contributes to more reliable reception of the signals transmitted by the GEO satellites even at elevation angles close to the horizon.

Obviously, to obtain a dependable diversity function of the aerials in the combination, these antennas must be highly isolated from one another. In the discussed module, the cross-talk between the main and the auxiliary antennas is better than -

15 dB even in such a dense placement. Since both antennas operate only in receiving mode, this value sufficient to consider the aerials as separate parts of the system.

Thus, the discussed antenna combination – which is built by the principle of the pattern diversity – can be successfully used to improve the satellite signal reception on cars, especially while driving under a dense foliage or in other shadowing scenarios as well as in Line-of-Sight.

***Summary***

The scarabaeus antenna for SDARS with improved rejection of LTE and Wi-Fi-2.4GHz signals operates well even when partially hidden in a deepening in the car's surface. The antenna shows excellent gain in zenith and sufficient one at angles near to the horizon. Its performance can be successfully enhanced by adding a second antenna (scarabaeus antenna of the second resonance order) to form a diversity. By using this technique, reception of satellite radio even while driving underneath dense foliage or if the satellites appear near the horizon is significantly strengthened, as shown in this chapter.

# Conclusion and Work Outline

The thesis encloses investigations on a broadband antenna for cellular communication on LTE technology for automotive application. The research was conducted starting from the theory thought simulation to realization of functional demonstrators in different operation scenarios: in stand-alone case, in a MIMO module and in combinations with radiators for other services like terrestrial radio, navigation and satellite broadcast.

The researched aerial for LTE (so called Nefer-antenna) consists of two structures, which are joined together at an excitation point, for two different frequency bands covering the frequencies of LTE low, middle and upper bands. There are a monopole-like part for frequencies from 698 MHz to 960 MHz and a cone-shaped structure for frequencies between 1500 MHz and 2690 MHz. These parts do not almost interfere one with another due to the high-omic behaviour outside their operational bands (except for some high-order modes).

This antenna for cellular communication shows nearly the same realized gain within the mentioned frequency ranges as a set of four quarter-wave monopoles, which were designed for distinct frequencies corresponding to the required LTE bands. Even though the aerial is only 53 high - that is by 20 mm lower than the reference monopole for the LTE low band - it is well-matched to a 50-Ohm feeding line showing input reflection coefficient below -6 dB without applying an additional matching circuit. The special 3-D design enables easy manufacturing by push-stamping, high reproducibility along with high stability of the construction.

The applicability of the 3D LTE antenna on automobiles was proven via the simulation of the radiator being placed on the roof of a common car (rear side). Although there are some fails of around ±2 dB in the simulated RP, such deviations from omnidirectional form cannot be avoided since they are caused by the car's body and the high elevation above the earth surface. Overall, the 3-D LTE antenna shows good performance in the roof-top mounting.

The aerial has strong potential to be used in modern LTE systems. However, some further investigations on its bandwidth extension are required due to the recent developments of LTE communication, particularly the use of new bands like 3400 MHz – 3800 MHz.

Since LTE implies the use of at least 2 x 2 MIMO, two aerials of the 3D principle were combined in a module, forming a MIMO system at the user end. The radiators provide reliable MIMO performance, showing low correlation and enough mean throughput of 25 Mb/s (for 2012) during a drive test in the real-time scenario. These

antennas appear in very low correlation between one another (correlation factor is below 30 % for low band and better than 5 % at LTE middle and upper frequencies) providing true MIMO function.

At the same time, the 3D Nefer-radiators are relatively compact and have a flexible shape, which can be adjusted to new mounting conditions. This allows placing other antennas underneath the same cover, such as compact satellite antennas of scarabaeus principle for GNSS and SDARS. The most appropriate placement is to put a 3D antenna for cellular communication into the centre of a scarabaeus antenna for satellite signal reception. These combinations were described in section 5. In this special arrangement, the 3D radiator and the scarabaeus aerial are well decoupled from one another due to the special near-field pattern of the scarabaeus antenna, namely there is no field in its phase centre (near to its geometrical centre inside the frame). Moreover, there are different directions of the currents flowing on both antennas. On the frame aerial, mainly horizontal currents are flowing, while along the 3-D LTE structure mainly vertical currents are distributed. The high decoupling also becomes apparent in the absence of any distortion in RPs, especially in that of the antenna for satellite reception, which is more sensitive (Figure 5.8-b, d).

In those combinations where a 3D radiator for cellular communication is located aside a scarabaeus antenna (LTE and GPS antennas of the module in section 5.2), mutual coupling between them is much higher than in former case. It becomes obvious in relatively high transmission coefficients at the operational frequencies of the frame aerial and in the distortion of its RP. The problem of low port isolation can be solved by applying additional filters at the LTE antennas, which block the radiator for the reception of GNSS signals (in case a 3D Nefer-antenna and a GNSS aerial are spatially separated). The results of such investigations were shown in subsection 5.2. Transmission between these antennas was reduced from -10 dB to -60 dB, which is a perfect value. However, the shape of the radiation pattern is still distorted. It indicates a necessity for further research to reduce the mutual coupling between the 3-D LTE radiator and the neighbour scarabaeus antenna for satellite signal reception.

The same technique can be applied in the modules that contain a 3-D LTE radiator and an antenna for satellite radio that is placed aside from it, since there is no cellular service within the SDARS band as well as within the GPS one.

The 3-D antennas from these two combinations are broadband and therefore can be used in LTE systems but these modules must be equipped by a second radiator for mobile phone since the LTE communication uses MIMO. An investigation of a MIMO of two 3-D radiators in combination with an antenna for satellite radio reception has shown that there is no hindrance for such extension.

Thus, the investigated 3D radiators for the cellular communication – which is based on LTE technology – can be successfully combined in a multi-antenna system with the scarabaeus aerials for satellite signal reception.

Alongside with the main topic on antennas for cellular communication, some researches on scarabaeus aerials for satellite reception were conducted. These investigations were required because of the recent developments in navigation – like opening of the GPS-L2C band for civil use and development of an interoperable L1C-singal – and due to the strengthened requirements on decoupling from the terrestrial interferers.

Close allocation of the frequencies of cellular communication and satellite radio poses an additional challenge on high isolation between the antennas for these services. In the thesis, the results of research on satellite antenna with the reduced out-of-band reception of VP waves have been reported. The aerial is designed due to the scarabaeus principle by using its particularities to form a demanded RP with low gain at the incidence angles of the interfering terrestrial waves.

The thesis also encloses further research on scarabaeus antennas for the current GNSS, which can be used in current multi-antenna modules. Thus, wide-band antennas and dual-band aerials for the simultaneous reception in L1 and L2 bands were investigated.

For reception of the future interoperable L1C signal and all currently-available global navigation systems in the L1-band, a wide-band scarabaeus antenna was designed. It perfectly fits underneath the restricted plastic cover by using the new fixation technique for the metal part of this antenna type, which implies utilization of the housing as a supporting element. Such fixation provides the maximum efficient use of the available volume which is usually strictly limited.

Since GPS for civil use will be next extended by operation in the L2 band for more accurate positioning, their receiving systems have to be enhanced for dual-band performance. Therefore, for simultaneous operation in L1- and L2-bands, two different concepts on base of the scarabaeus principle were considered. There are a double-ring and a single-ring designs. The double-ring radiator contains two metal frames, each for a certain band, whereas a single-ring antenna utilize only one frame and a special network, which enables its function within two distinct frequency bands. The radiators of both design principles show their good performance and, consequently, can be used in new dual-band systems for navigation.

Both concepts of scarabaeus antennas with dual-band performance can be successfully applied for precise positioning. They even have a potential for being used

in systems for autonomous driving. However, the concepts need further investigations to improve the axial ratio bandwidth to enable stable reception of the required signals and reject undesired and even dangerous one.

For enhancing resistance of an antenna for satellite radio against strong terrestrial interferers, such as WLAN and cellular base stations, some researches were conducted. Thus, an aerial for satellite radio has gained a low profile which helps to decrease reception of signals outside its operational bandwidth. This antenna shows an excellent suppression of the VP waves at frequencies outside that of satellite radio, while it keeps the demanded performance at the required frequencies. Its function has been further enhanced by adding a second antenna (scarabaeus antenna of the second resonance order) to form a diversity. By using this technique, reception of satellite radio even while driving underneath dense foliage has been significantly strengthened.

Thus, the results of the investigations conducted during the postgraduate work can be applied in wide area of automotive antennas.

# Appendix

# A.1 Key Antenna Characteristics

In order to describe antennas' performance, a special terminology has been introduced by several committees working on a standardization in the antenna field. In this thesis, terminology adopted by the IEEE society and published in IEEE Standard for Definitions of Terms for Antennas (IEEE Std 145™-2013) has been used.

Below, some of the most relevant terms for the description of the antennas in this thesis are given. There are operational bandwidth, efficiency, polarization, radiation pattern, directivity, gain and realized gain, antenna impedance matching and mutual coupling between antennas in the module.

Let us consider the antenna in a receiving mode, when it couples electromagnetic waves from the free space. Due to reciprocity of the passive antenna parts, all characteristics described below are also valid for the antenna in transmitting mode. In this mode, high-frequency modulated signals come from a transmitter through a feed line into the antenna, and afterwards the antenna radiates electromagnetic waves caused by modulated signal.

### *Antenna Impedance and Reflection Coefficient*

An antenna ***input impedance*** is "the impedance presented by an antenna at its terminals" [97]. In common cases, it comprises resistance (includes radiation and loss resistances) and reactance.

In order to provide a maximum possible power transfer from the antenna to the receiver, the input impedance of the antenna has to be the same as the impedance of a transmission line connected to the antenna terminals. In order to assess the losses caused by reflections at the antenna terminals, a ***reflection coefficient*** is applied. It is a ratio between amplitude of the wave passed though the joint point to that of the reflected one. Often in the communication, the reflection coefficient is referred to 50 Ohm.

### *Mutual Coupling and Mutual Effect*

A ***mutual coupling*** is "interactions of an antenna with one or more other antennas", which results in ***mutual coupling effects***: "the changes in the radiation

pattern and impedance of the antenna due to mutual coupling" [97]. The mutual effects have a destructive behaviour, and thus the mutual coupling has to be kept as low as possible or even improved.

## *Efficiency*

***Antenna radiation efficiency*** is the ratio of the net power delivered through the antenna to the receiver to the total power accepted by the antenna from the free space. Radiation efficiency describes how much power has been dissipated in the antenna itself (in conductive and dielectric parts). Radiation efficiency reduced by mismatch losses is called ***realized radiation efficiency*** (or *total radiation efficiency*) [97].

## *Polarization*

Antenna polarization is defined as the polarization of the wave transmitted or received by the antenna. The behaviour of an extremity of the vector of electrical field ($\bar{E}$) at a fixed location in space determines polarization of the wave.

There are *elliptical* polarization, *linear* (*horizontal – HP, and vertical – VP)* polarization and *circular* polarization with the left-hand (LHCP) or right-hand (RHCP) rotation of the vector $\bar{E}$.

The required polarization is called a co-polarization. A polarization orthogonal to the demanded one is defined as a cross-polarization. In order to value the superiority of the co-polarized waves over the cross-polarized, the term ***cross-polarization discrimination (XPD)*** is used. It is a difference between co- and cross-polarized gains or directivities of the antenna in a specified direction.

## *Directivity, Gain, Realized Gain*

***Directivity*** (*D* in Figure A.1) of the antenna (in a given direction) is the ratio of the radiation intensity accepted by the antenna in a given direction to the radiation intensity averaged over all directions. [97]. If the direction is not specified, the direction of maximum radiation intensity is implied. Directivity characterizes degree of an advantage in accepted power due to directional properties of the antenna comparing with an isotropic radiator [98]. Often a *partial directivity* (directivity for a given polarization) is a point of interest.

***Gain*** (*G* in in Figure A.1) is a "ratio between a radiation intensity in a given direction and a radiation intensity that would be produced if the power accepted by

the antenna were isotopically radiated" [97]. Gain does not include losses due to polarization and impedance mismatch, although it includes losses in the antenna itself caused by lossy conductive and dielectric materials. Similar to the directivity, there is a *partial gain for the certain polarization*.

In common cases, an antenna has some mismatch with a feeding line that causes return losses (mismatch losses). Antenna gain reduced by impedance mismatch is called ***realized gain*** (*RG* in Figure A.1) [97].

## *Radiation Pattern*

An ***antenna radiation pattern*** (or antenna pattern) is defined as a "spatial distribution of a quantity that characterizes the electromagnetic field generated by an antenna…" [97]. Radiation pattern (RP) is a mathematical or graphical representation of the dependence of the electric field, directivity or gain on azimuthal ($\varphi$) and elevation angles ($\theta$, here is counted from zenith), which is usually denoted as $f(\theta, \varphi)$.

In order to obtain a better picture about radiation capability of the antenna, often sections of the radiation pattern are shown. A horizontal section of the far-field radiation pattern ($\theta$ angle is a specified constant, φ is a variable) is called a *conical cut*. The path formed by the number of points for which φ is a specified constant and $\theta$ is a variable – i.e. a vertical section – is called a *great circle cut*. The conical cut at the elevation angle $\theta$ = 90° is also a *great circle cut* [97].

## *Overview of Antenna Properties*

Antenna radiation characteristics can be summarized by a diagram depicted in Figure A.1 [97].

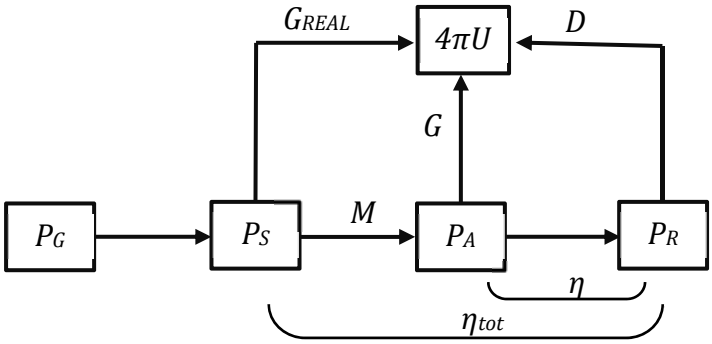


where:
- $P_G$ – power, available from generator
- $P_S$ – power to matched transmission line
- $P_A$ – power accepted by antenna
- $P_R$ – power radiated by antenna
- M – reflection coefficient
- G – gain
- $G_{real}$ – realized gain
- D – directivity
- U – radiation intensity
- $\eta$ – radiation efficiency
- $\eta_{tot}$ – total realized efficiency.

Figure A. 1: Overview of the antenna parameters [97].

# A.2 Calculation of Antenna Far Field

This calculation procedure and introduced approximations are valid for linear antennas with continuous current distribution $I_V(x,y,z)$ which is assumed to be known.

### 1. Magnetic vector potential

$$\underline{\hat{V}}(\vec{r}) = \frac{\mu}{4\pi}\iiint I_V \cdot \frac{e^{-jkR}}{R}dv,$$

where $R$ – distance to an observation point (Figure A.2); according to the Fraunhofer approximations: $R = R$ – for amplitude term; and $kR = k(r - \hat{r}_A \cdot \boldsymbol{r})$ – for phase term, where $\boldsymbol{r}$ is a unit vector which depends on antenna orientation.

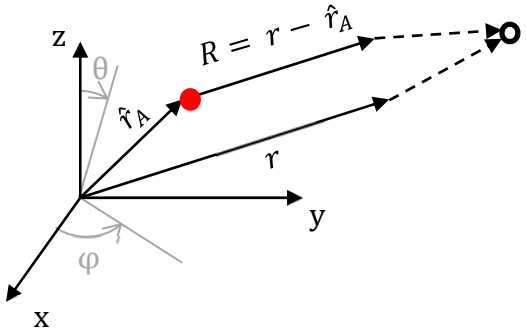


● Antenna position; ○ Observation point in far filed.

Figure A.2: Coordinate system for representation of radiation fields.

### 2. Magnetic and electric field intensity

$$\underline{\hat{H}}(r,\theta,\varphi) = \frac{1}{\mu_0} rot\left(\underline{\hat{V}}(r,\theta,\varphi)\right).$$

$$\underline{\hat{E}}(r,\theta,\varphi) = \frac{1}{j\omega\varepsilon_0} rot\left(\underline{\hat{H}}(r,\theta,\varphi)\right).$$

# A.3 Impedance Measurement Setup

Reflection and transmission coefficients, as well as antennas' impedances, of the antenna modules were measured by means of a 4-port network analyser.

For the measurement of LTE antennas and modules which includes LTE radiators, a circular metal plate of 80 cm in diameter with absorbing material along the edge is utilized as a ground plate. For the measurement of the aerials for a satellite signal reception, a metal plate with sizes 30 cm x 30 cm is used. Dimensions of both metal plates are chosen to be near or greater than wavelength at the operational frequencies of the antennas to be measured.

Antennas and combinations under the test are placed into the centre of the corresponding ground plate and are fed from the bottom side through 50-Ohm coaxial cables, so that the feeding cables are electrically invisible for the antennas under the test.

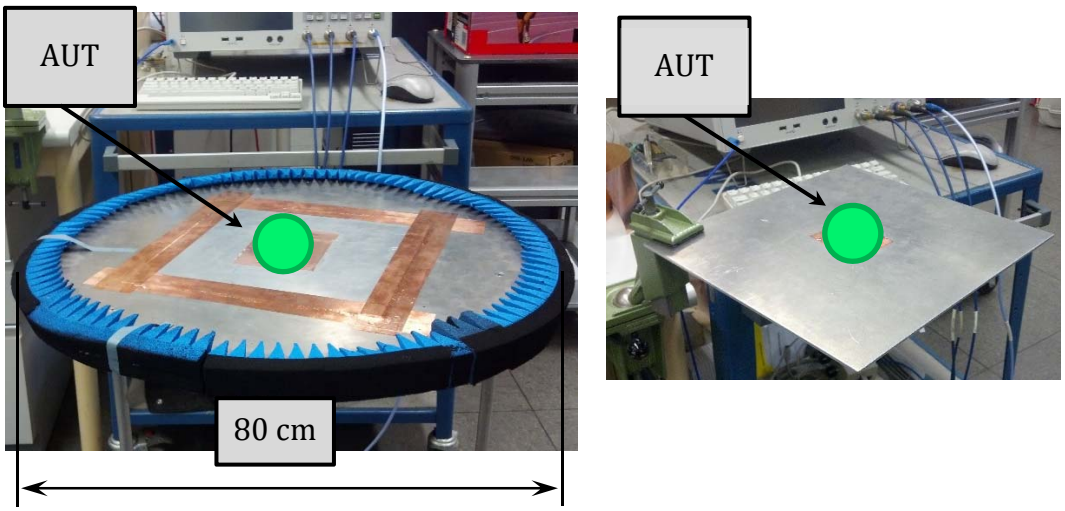


(a) Plate for LTE antennas' measurements.

(b) 30 cm x 30 cm ground plate for satellite antenna measurements.

Figure A.3: Impedance measurement set up.

# A.4 Measurement Setup in Anechoic Chamber

Antenna measurements were executed in an anechoic chamber of the Institute of High Frequency Technology and Mobile Communication of the University of the Bundeswehr, Munich, which is shown in Figure A.4-b.

The anechoic chamber is covered with an absorbing material and is equipped with a necessary measurement sets allowing measurements at the frequencies from 700 MHz up to 40 GHz.

As a transmitting antenna, one of two changeable horn antennas are used for two wide frequency bands. One antenna operates at the frequencies from 700 MHz to 10.5 GHz and another radiator functions at the frequencies between 10.5 GHz and 40 GHz.

On a receiving side, an antenna under the test (AUT) is meant to be placed on a circular ground plane with bent edges and 1.2 m in diameter. Distance between transmitting and receiving antennas is chosen to be 5.45 m (Figure A.4-a). Thus, the antennas under the test are measured directly in the far-field region without need of further near- to far-field transformation.

In order to get accurate measurement results, the anechoic chamber as well as the used 50-Ohm coaxial cables are calibrated, and correction coefficients are implemented during an evaluation procedure.

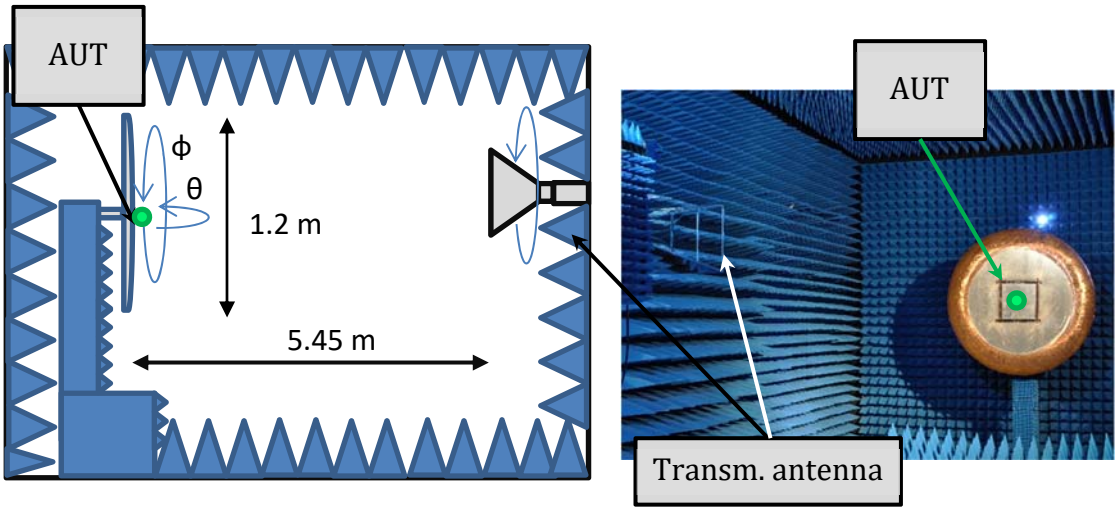


(a) Schematic representation. (b) Photograph.

Figure A.4: Anechoic chamber for antenna measurement.

# List of Figures

# List of Tables

# References


[1] "Deutsches Museum. Verkehrszentrum," 2017. [Online]. Available: http://www.deutsches-museum.de/en/verkehrszentrum/exhibitions/hall-ii-travel/.

[2] I. Goncharova and S. Lindenmeier, "A High–Efficient 3–D Nefer–Antenna for LTE Communication on a Car," *The 8th European Conference on Antennas and Propagation (EuCAP 2014),* 2014.

[3] I. Goncharova and S. Lindenmeier, "A High Efficient Automotive Roof-Antenna Concept for LTE, DAB-L, GNSS and SDARS with Low Mutual Coupling," *European Conference on Antennas and Propagation ,* 2015.

[4] S. Jimaa, K. K. Chai, Y. Chen and Y. Alfadhl, "LTE-A an Overview and Future Research Areas," *Second International Workshop on the Performance Enhancement in MIMO-OFDM Systems,* 2011.

[5] S. Kanchi, S. Sandlilya, D. Bhosale, A. Pitkar and M. Gondhalekar, "Overview of LTE-A Technology," *Global High Tech Congress on Electronics (GHTCE 2013),* 2013.

[6] J. Wannstrom, "LTE-Advanced," 2013. [Online]. Available: http://www.3gpp.org/technologies/keywords-acronyms/97-lte-advanced.

[7] I. Poole, "Resources of analysis for electronics engineers," [Online]. Available: http://www.radio-electronics.com/info/cellulartelecomms/lte-long-term-evolution/lte-frequency-spectrum.php.

[8] S. DiPierro, R. Akturan and R. Michalski, "Sirius XM Satellite Radio System Overview and Services," *5th Advanced Satellite Multimedia Systems Conference and the 11th Signal Processing for Space Communications Workshop,* 2010, IEEE.

[9] "Official U.S. Government information about the Global Positioning System (GPS) and related topics," [Online]. Available: http://www.gps.gov.

[10] *Global Positioning System Standard. Positioning Service Performance Standard,* Department of Defense of the USA, 2008.

[11] *Interface Specification IS-GPS-200,* Global Positioning Systems Directorate. Systems Engineering & Integration , 2013.

[12] " Information-Analytical Center Federal Space Agency," [Online]. Available: https://www.glonass-iac.ru/GLONASS/.

[13] "European Global Navigation Satellite System Agency,," [Online]. Available: http://www.gsa.europa.eu.

[14] "BeiDou. Navigation Satellite System," [Online]. Available: http://en.beidou.gov.cn/.

[15] *BeiDou Navigation Satellite System. Signal in Space. Interface Control Document.,* China Satellite Navigation Office, 2012.

[16] *Signal in Space Interface Control Document,* European GNSS (Galileo) Open Service, 2015.

[17] "Interface Specification IS-GPS-800," 2013.

[18] V. Rabinovich, N. Alexandrov and B. Alkhateeb, Automotive Antenna Design and Application, Boca Raton, London, New York: CRC Press Taylor & Francis Group, 2010.

[19] B. D. Pell, E. Sulic, W. S. T. Rowe, K. Ghorbani and S. John, Advancemnents in Automotive Antennas, New Trends and Developments in Automotive System Engineering, InTech, Available at: https://www.intechopen.com/books/howtoreference/new-trends-and-developments-in-automotive-system-engineering/advancements-in-automotive-antennas, 2011.

[20] M. Pannozzo, M. Busa, E. Toniolo, L. S. Drioli and D. Zamberlan, "State of the Art review for Automotive Satellite Antennas," *5th Advanced Satellite Multimedia System Conference (ASMA) and the 11th Signal Processing for Space Communication Workshop,* 2010.

[21] E. Levine, "A Review of GPS Antennas," *Consumer Electronics Times,* vol. Vol. 3, pp. PP. 233-241, July 2014.

[22] S. Lindenmeier and S. Senega, "Satellite Antennas on Vehicles," in *Handbook of Antenna Technologies*, Springer Science+Business Media, 2016.

[23] J.-H. Lu, H.-M. Chin and Z.-W. Lin, "Planar Monopole Antenna with Triple-band Operation for LTE/WLAN MIMO System," *International Conference on Computational Electromagnetics (ICCEM),* pp. 318 - 319, 2017.

[24] J.-H. Lu and Y.-Y. Lee, "Planar compact triple-band monopole antenna for IEEE 802.16 m worldwide interoperability for microwave access system," *IET Microwaves, Antennas and Propagation,* pp. 1045 - 1054, 2011.

[25] J.-H. Lu and Y.-Y. Lee, "Planar C-shaped Monopole Antenna with Multi-band Operation for WiMax System.," *Antenna and Propagation Society International Symposium (APSURSI),* 2010 .

[26] G. Zhou, "A Non-Uniform Pitch Dual Band Helix Antenna," *International Symposium on Antennas and Propagation,* pp. 274 - 277, 2000.

[27] A. Friedrich, B. Geck, O. Klemp and H. Kellermann, "On the Design of a 3D LTE Antenna for Automotive Applications based on MID Technology," *European Microwave Conference,* pp. 640 - 643, 2013.

[28] B. Sanz-Izquierdo, J. Heirons and N. Acharya, "Inkjet Printed and Folded LTE Antenna for Vehicular Application," *European Microwave Conference,* pp. 88 - 91, 2016.

[29] N. Guan, H. Tayama, M. Ueyama, Y. Yoshijima and H. Chiba, "A Roof Automobile Module for LTE-MIMO Antennas," *IEEE-APS Topical Conference on Antennas and Propagation in Wireless Comunication,* pp. 387 - 391, 2015.

[30] Z. D. Liu, P. S. Hall and D. Wake, "Dual-frequency planar inverted-F antenna," *IEEE Transactions on Antennas and Propagation,* pp. 1451 - 1458, 1997.

[31] C. R. Rowell and R. D. Murch, "A compact PIFA suitable for dual-frequency 900/1800-MHz operation," *IEEE Transaction on Antennas and Propagation,* pp. 596 - 598, October 1988.

[32] K. L. Chung, K. H. Man, H. K. Kan and W. Y. Tam, "A Compact Wideband PIFA," *Asia-Pacific Microwave Conference (APMC),* 2008.

[33] R. Kronberger, H. Lindenmeier, L. Reiter and J. Hopf, "Multiband Planar Inverted-F Car Antenna for Mobile Phone and GPS," *Antennas and Propagation Society International Symposium,* pp. 2714 - 2717, 1999.

[34] J. Kammerer and S. Lindenmeier, "A new Compact Antenna Combination with high Efficiency for Reception of SDARS and GPS Signals," *Antenna and Propagation Society International Symposium (APSURSI 2012),* 2012.

[35] G. Panther, "Patch Antennas for the New GNSS," available at: http://gpsworld.com/wirelesspatch-antennas-new-gnss-12552/, 2012.

[36] S. X. Ta, I. Park and R. W. Ziolkowski, "Dual-band wide-beam crossed asymmetric dipole antenna for GPS applications," *Electronics Letters,* 6th December 2012.

[37] U. U. Hussine, Y. Huang and C. Song, "A New Circularly Polarized Antenna for GNSS Applications," *European Conference on Antenna and Propagation,* 2017.

[38] J. Lei, G. Fu and Y. Hao, "Wideband Printed Tapering Quadrifilar Helical Antenna for GNSS," *European Conference on Antenna and Propagation,* 2015.

[39] C. Lu, J. Shen, Y. Cao, F. Meng and T. Yin, "Novel Dual-Band and Dual Circularly Polarized Microstrip Antenna,," *Antenna Propagation Symposium,* 2015.

[40] Y.-Q. Zhang, L. Yang, S.-X. Gong and X. Li, "Wide-Band Circularly Polarized Antenna for Dual-Band GPS Receiver," *International Symposium on Antennas, Propagation and EM Theory (ISAPE),* pp. 62 - 65, 2012.

[41] Y.-Q. Zang, X. Li, L. Yang and S.-X. Gong, "Dual-Band Circularly Polarized Annular-Ring Microstrip Antenna for GNSS Applications," *IEEE Antenna and Wireless Propagation Letters,* pp. 615 - 618, 2013.

[42] M. Chen, "A Compact Dual-Band GPS Antenna Design," *IEEE Antenna and Wireless Propagation Letters,* pp. 245 - 248, 2013.

[43] H. Lindenmeier, J. Hopf and L. Reiter, "Low Profile SDARS-Antenna with Diversity Functionality," *IEEE International Symposium on Antennas and Propagation,* 2002.

[44] J. F. Hopf, L. M. Reiter and S. M. Lindenmeier, "Crossed Frame Antenna for Automotive Application for the New US Satellite Digital Audio Radio Service (SDARS)," *9th European Conference on Wireless Technology,* pp. 8 - 11 , 2006.

[45] D.-C. Chang and J.-H. Chen, "2.3 GHz Antenna with both LHCP and LP for SDARS," *Antennas and Propagation Society International Symposium* , 2003.

[46] B. Lee, C. Jung, B. Yu, K. Kong, N. Choi, F. J. Harackiewicz, I. Lee, S. Cho, M.-J. Park and Y.-S. Chung, "Design concept of compact antenna for SDARS application," *Electronic Letters,* pp. 845 - 846, 2007.

[47] J. Kammerer and S. Lindenmeier, "A compact car antenna with high efficiency for reception of heo- and geo- satellites signals," *IEEE International Symposium on Antennas and Propagation (APSURSI),* p. 1205 – 1206, July 2011.

[48] G. Saala and S. Lindenmeier, "Compact circular polarized antenna for mobile reception of radio signals transmitted by geostationary satellites," *2010 European Microwave Conference (EuMC),* pp. 1465 - 1468, 2010.

[49] G. Saala, D. Müller, J. Hopf and S. Lindenmeier, "Antenna with Optimized Pattern for Simultaneous Reception of Terrestrial Signals and Signals of Geostationary Satellites," *Advances in Radio Science, Vol. 8,* pp. 37 - 42, 2010.

[50] N. Guan, H. Chiba, Y. Yamaguchi, Y. Niihara and H. Tayama, "A Flat Roof Automobile Antenna Module for LTE, GPS and SDARS Applications," *IEEE-APS Topical Conference on Antennas and Propagation in Wireless Communication (APWC),* pp. 11 - 14, 2014.

[51] J. Kammerer, L. Reiter and S. Lindenmeier, "Automotive Hexband Antenna for AM/FM/GPS/SDARS and AMPS/PCS1900 Cell Phone in an only 65 mm high Housing," *Radio and Antenna Days of the Indian Ocean (RADIO 2012),* 2012.

[52] J. Hopf, L. Reiter and S. Lindenmeier, "Compact Multi-Antenna System for Cars with Electrically Invisible Phone Antennas for SDARS Frequencies," *INICA 2007,Internationale ITG-Conference on Antennas,* 2007.

[53] P.-S. Kildal, Foundations of Antenna Engineering: A Unified Approach for Line-of-Sight And Multipath, Gothenburg, Sweden: Kildal Antenn AB, 2015.

[54] C. A. Balanis, Antenna theory. Analysis and Design. Fourth eddition, Hoboken, New Jersey: John Wiley & Sons. Inc., 2016.

[55] M. M. Weiner, Monopole Antennas, New York: Marcel Dekker, Inc., 2003.

[56] K. W. Kark, Antennen und Strahlungsfelder, Wiesbaden: Vieweg+Teubner, 2010.

[57] N. I. Khan, A. Azim and S. Islam, "Radiation Characteristics of a Quarter-Wave Monopole Antenna above Virtual Ground," *Journal of Clean Energy Technologies, Vol. 2,* pp. 339-342, October 2014.

[58] E. Stirner, Antennen. Band1: Grundlagen, Heidelberg, Germany: Dr. Alfred Hüthig Verlag GmbH, 1984.

[59] T. L. Simpson, "The Theory of Top-Loaded Antennas: Integral Equations for the Currents," *IEEE Transactions on Antennas and Propagation, Vol. Ap.-19,* pp. 186-190, March 1971.

[60] A. d. Wunsch and S.-P. Hu, "A Closed-Form Expression for the Driving-Point Impedance of the Small Inverted L Antenna," *IEEE Transactions on Antennas and Propagation,* pp. 236 - 242, February 1996.

[61] A. Andújar, J. Anguera, C. Pauente and A. Pérez, "On the Radiation of the L-shaped Wire Antenna," *Progress In Electromagnetics Research, Vol. 6,* pp. 91-105, 2009.

[62] S. Pradas and R. W. P. King, "Experimental Study of Inverted L-, T-, and related Transmission-Line Antennas," *Journal of Research of the National Bureau of Standards,* pp. 449 - 454, September-October 1961.

[63] G. Arfken, Mathematical Methods for Physicists, San Diege: Academic Press, 1985.

[64] P. M. Morse and H. Feshbach, Methods of Theoretical Physics, New York: McGraw Hill, 1953.

[65] Jahnke-Emde-Lösch, Tafeln höherer Funktionen, Stuttgart: Teubner, 1966.

[66] R. Kühn, Mikrowellenantennen, Berlin: VEB Verlag Technik, 1964.

[67] "www.leiton.de," [Online].

[68] M. Bueno Diez, P. Plitt, W. Pascher and S. Lindenmeier, "Antenna Placement and Wave Propagation for Car-to-Car Communication," *European Microwave Conference (EuMC),* 2015.

[69] R. Walter, Zweiband-3D-LTE-Antenne mit einer Bauhöhe von 53 mm, Masterarbeit, Universität der Bundeswehr, München, 2012.

[70] S.-C. Chen, Y.-S. Wang and S.-J. Chung, "A Decoupling Technique for Increasing the Port Isolation Between Two Strongly Coupled Antennas," *IEEE Transactions on Antennas and Propagation, Vol. 56, No. 12,* pp. 3650 - 3658, December 2008.

[71] B. K. Lau and J. B. Andersen, "Simple and Efficient Decoupling of Compact Arrays With Parasitic Scatterers," *IEEE Transactions on Antennas and Propagation, Vol. 60, No. 2,* pp. 464 - 472, February 2012.

[72] T. Lankes, P. Turban and F. Mierke, "Evaluation and Optimization of LTE MIMO Antenna Configurations in Automotive Environment," *European Conference on Antenna and Propagation (EuCAP 2014),* pp. 1100 - 1104, 2014.

[73] J. Kammerer, Kompakte Ringantennen für satellitengestützte und terrestrische Übertragungsdienste im Fahrzeug, Dissertation, Universität der Bundeswehr, München, 2014.

[74] D. Müller, Kompakte Diversity-Antennen für den mobilen Empfang von Satellitensignalen, Dissertation, Neubiberg, Deutschland, Universität der Bundeswehr München, 2010.

[75] D. Müller, S. Senega and S. Lindenmeier, "Compact 3-Antenna Diversity Set foe HEO and Geo Satellite System with Terrestrial Repeaters," *IEEE Antennas and Propagation Society International Symposium ,* 2010, Toronto Canada.

[76] I. Goncharova and S. Lindenmeier, "A Compact Satellite Antenna Module for GPS, Galileo, GLONASS, BeiDou and SDARS in Automotive Application," *European Conference on Antennas and Propagation (EUCAP),* pp. 3639 - 3643, 2017.

[77] I. Goncharova and S. Lindenmeier, "A Compact Satellite Antenna Module for GPS, Galileo, GLONASS, BeiDou and SDARS in automotive application," *IET Microwaves, Antennas & Propagation,* pp. 445 - 451, 2018.

[78] K. Chang, Encyclopedia of RF and Microwave engenireeng, John Wiley & Sons Inc., 2005.

[79] S. Bedair and I. Wolf, "Fast, Accurate and Simple Approximate Analytic Formulas for Calculating the Parameters of Supported Coplanar Waveguides for (M)MIC's," *IEEE Transactions on Microwave Theory and Techniques. Vol. 40,* Januar 1992.

[80] P. Russer, Electromagnetics. Microwave Circuits and Antenna Design for Comminication Engineering, Artech House, 2006.

[81] H. Ristau, Kompakte Diversity-Kombination aus zwei Empfangs-Antennen für Satelliten-Radio-Dienste, Masterarbeit, Universität der Bundeswehr, München, 2011.

[82] "EPCOS-TDK Europe," [Online]. Available: https://en.tdk.eu/.

[83] I. Goncharova, A. Böge, L. Reiter and S. Lindenmeier, "Combinations of Antennas with High Efficiency for LTE Mobile Services," *3. Workshop Automotive Antennas (WSAA),* 2015.

[84] A. Negut, Ultra Short Multiband AM/FM/DAB Active Antennas for Automotive Application, Dissertation, Universität der Bundeswehr, München, 2011.

[85] L. Reiter, A. Böge and S. Lindenmier, "A new low-cost active rod antenna for automotive reception of all terrestrial audio broadcast services,"

*European Conference on Antennas and Propagation EuCAP 2014,* pp. 2981 - 2984, 2014.

[86] A. Negut, L. Reiter, j. Hopf and S. Lindenmeier, "Performance of a 20 cm Short Active AM/FM Monopole Antenna for Automotive Application," *European Conference on Antennas and Propagation, EUCAP 2009,* pp. 2708 - 2712, 2009.

[87] A. Böge, Unobstrusive Active Mutiband Car Antennas for Reception of Terrestrial Broadcasting Services, Dissertation, in publishing, 2018.

[88] S. Lindenmeier, I. Goncharova, S. Hastürkoğlu and M. Bueno Diez, "Antennas for terrestrial Communication in Vehicles and their Interaction with Antennas for Satellite Services," *IEEE-APS Topical Conference on Antennas and Propagation in Wireless Communications (APWC),* pp. 334 - 337, 2017.

[89] I. Goncharova and S. Lindenmeier, "An interoperable antenna for GPS and GLONASS services on a car," *Antenna Propagation Symposium and National Radio Science Meeting (APS/URSI),* pp. 15 - 16, 2015.

[90] S. Lindenmeier, I. Goncharova, S. Matthie and S. Senega, "Reception Systems with Compact Ring-Antenna Structures for GNSS and BGAN," *IEEE MTT-S International Microwave Symposium Workshop,* 2017.

[91] A. Böge, J. Kotschor and S. Lindenmeier, "Adaptive Switchable FM/DAB Windscreen Antenna Matched with a High-Impedance Amplifier," *European Conference on Antenna and Propagation (EuCAP),* 2016.

[92] S. Hastürkoğlu and S. Lindenmeier, "A wideband automotive antenna for actual and future mobile communication 5G/LTE/WLAN with low profile," *European Conference on Antennas and Propagation,* pp. 602 - 605, 2017.

[93] S. Lindenmeier, L. Reiter, D. Barie and J. Hopf, "Antenna Diversity for Improving the BER in Mobile Digital Radio Reception Especially in Areas with Dense Foliage," *International ITG-Conference on Antennas, INICA2007,* 2007.

[94] S. Senega, A. Nassar and S. Lindenmeier, "Compact Scan Phase Antenna Diversity System for High Driving Speeds," *Proceedings of the 18th European Microwave Week,* pp. 1459 - 1462, 2015.

[95] S. Senega, J. Kammerer and S. Lindenmeier, "Scan-phase antenna diversity for digital satellite radio (SDARS) in a single automotive side mirror," *The 8th European Conference on Antennas and Propagation (EuCAP 2014),* pp. 3255 - 3259, 2014.

[96] S. Senega, D. Muller, D. Barie, L. Reiter, J. Hopf and S. Lindenmeier, "Investigation on the combination of a scan/phase antenna diversity system with a novel diversity antenna set," *Antenna and Propagation Society International Symposium, APSURSI,* 2009.

[97] *IEEE Std 145™-2013,* IEEE Standard for Definitions of Terms.

[98] J. Shifrin, Antennas, Kharkiv, Ukraine, 1976.